DRAFT VERSION SEPTEMBER 30, 2015
Preprint typeset using LaTeX style emulateapj v. 5/2/11

arXiv:1509.08468v1 [astro-ph.GA] 28 Sep 2015

GALAXY MERGERS DRIVE SHOCKS: AN INTEGRAL FIELD STUDY OF GOALS GALAXIES

J. A. RICH [1,2], L. J. KEWLEY[3] & M. A. DOPITA[3,4]

(Dated: September 30, 2015)
Draft version September 30, 2015

ABSTRACT

We present an integral field spectroscopic study of radiative shocks in 27 nearby ultraluminous and luminous infrared galaxies (U/LIRGs) from the Great Observatory All-sky LIRG Survey, a subset of the Revised Bright Galaxy Sample. Our analysis of the resolved spectroscopic data from the Wide Field Spectrograph (WiFeS) focuses on determining the detailed properties of the emission line gas, including a careful treatment of multi-component emission line profiles. The resulting information obtained from the spectral fits are used to map the kinematics of the gas, sources of ionizing radiation and feedback present in each system. The resulting properties are tracked as a function of merger stage. Using emission line flux ratios and velocity dispersions, we find evidence for widespread, extended shock excitation in many local U/LIRGs. These low-velocity shocks become an increasingly important component of the optical emission lines as a merger progresses. We find that shocks may account for as much as half of the Hα luminosity in the latest-stage mergers in our sample. We discuss some possible implications of our result and consider the presence and effects of AGN on the spectra in our sample.

Subject headings: galaxies: active, interactions, ISM, starburst

1. INTRODUCTION

As gas rich starburst galaxies and massive mergers, ultraluminous and luminous infrared galaxies (U/LIRGs) in the local universe provide valuable insight and context for phenomena that impact galaxy formation and evolution at high redshift. ULIRGs, with total $L_{IR}/L_{\odot} > 10^{12}$ are overwhelmingly represented by systems in the latest stages of a merger between two gas-rich galaxies (Sanders et al. 1988; Veilleux et al. 1995; Murphy et al. 1996; Genzel et al. 1998; Rigopoulou et al. 1999; Scoville et al. 2000; Kewley et al. 2001b; Spoon et al. 2006; Desai et al. 2007). The strong infrared luminosity (L_{IR}) in local LIRGs is powered by star formation and in some cases AGN, both driven by galaxy mergers and interactions. LIRGs ($L_{IR}/L_{\odot} > 10^{11}$) in the high redshift Universe may commonly be mergers, as supported by observational evidence of disturbed morphologies in Submillimetre Galaxies (SMGs) and an increase in merger activity with redshift (Blain et al. 2002; Dasyra et al. 2008; de Ravel et al. 2009; Bundy et al. 2009). In the local Universe, however, a significant fraction ($\sim 20-40\%$) of LIRGs show little or no evidence of ongoing or past strong interactions (Ishida 2004, Howell et al. in prep). In order to fully understand the processes that govern star formation and black hole assembly a clear and complete picture of the evolution U/LIRGs in the local Universe is essential.

Integral field spectroscopy (IFS) furnishes one of the most powerful tools for the study of nearby U/LIRGs. Through its ability to both spatially and spectrally map a galaxy, it provides a wealth of spatially resolved information tracing the kinematics of the gas and stars, variations in the radiation field and sources of ionizing photons, metallicity and chemistry in the ISM, maps of extinction and gas flows.

IFS studies in recent years have enabled the discovery of extended shock excitation in several nearby galaxies, notably in U/LIRGs and other massive galaxies. Monreal-Ibero et al. (2006) identified extended LINER-like emission resulting from shocks in a small sample of ULIRGs. Sharp & Bland-Hawthorn (2010) found widespread shock-excitation in the extended emission associated with outflows in a study of several galactic wind-bearing galaxies. A larger IFS study found a significant fraction of tidally induced shock excitation in nearby LIRGs (Monreal-Ibero et al. 2010). Farage et al. (2010) discovered extended shocks caused by gas accreting on to a giant brightest cluster galaxy (BCG). Finally, Rich et al. (2010) found extended shock excitation caused by a galactic wind in the M82-like galaxy NGC 839 and widespread shocks in the late-stage LIRG mergers NGC 3256 and IC 1623 (Rich et al. 2011). In Farage et al. (2010), Rich et al. (2010) and Rich et al. (2011), new slow shock models were employed to analyze the shocked gas. In all of the above cases, shock excitation exhibits characteristics of extended LINER-like emission with broadened line profiles.

The shock excitation seen in the LIRGs NGC 839, NGC 3256 and IC 1623 is associated with moderately broadened emission line profiles and enhanced emission line ratios of lower ionization species such as [SII]$\lambda\lambda 6717, 6731\AA$ and [OI]$\lambda 6300\AA$ (Monreal-Ibero et al. 2010; Rich et al. 2011). The shocks themselves are due to major gas flows caused by the merger process. During a major merger, gas is driven inwards by tidal forces, which can result in shock excitation (e.g. Farage et al. 2010). This infalling gas fuels massive bursts of star formation and AGN activity which in turn drive massive galactic outflows and further shocks into the ISM and beyond. In an effort to determine the contribution from shocks in U/LIRGs and the relationship between shocks and merger progress, we have searched for similar signatures in a larger IFS sample of 10 nearby U/LIRGs (Rich et al. 2012). We find many of the galaxies in our sample, especially those in later-

jrich@ipac.caltech.edu
[1] IPAC, California Institute of Technology, 1200 E. California Blvd., Pasadena, CA 91125
[2] Observatories of the Carnegie Institution of Washington, 813 Santa Barbara St., Pasadena, CA 91101
[3] Research School of Astronomy and Astrophysics, Australian National University, Cotter Rd., Weston ACT 2611, Australia
[4] Astronomy Department, Faculty of Science, King Abdulaziz University, PO Box 80203, Jeddah, Saudi Arabia

stage mergers, exhibit evidence of significant ongoing shock excitation in their optical spectra. To characterize the relative contribution from shocks throughout the merger process, we extend and expand upon the analyzes from our previous work in Rich et al. (2010, 2011) with a sample of U/LIRGs covering the entire merger sequence.

This paper presents a comprehensive study of the emission line properties of the Wide Field Spectrograph (WiFeS) Great Observatory All-Sky LIRG Survey (GOALS) sample (WiGS), with an emphasis on understanding the shock emission observed. The sample, observations and analysis are described in Sections 2 and 3. The emission line ratio maps and diagnostic diagrams for the sample are discussed in Section 4. A summary of the velocity dispersion distributions for the WiFeS GOALS sample is given in Section 5. Section 6 summarizes the various diagnostics as a function of merger stage. The total contribution from shocks as a function of merger stage, the potential impact of shock excited gas on observational interpretation, and the potential overlap with AGN/composite galaxies is discussed in Section 7. Our conclusions are presented in Section 8.

We use the cosmological parameters assumed in the summary of the GOALS sample Armus et al. (2009), based on the five-year WMAP results Hinshaw et al. (2009): H_0=70 km s^{-1}Mpc^{-1}, Ω_V=0.72, and Ω_M=0.28.

2. SAMPLE, OBSERVATIONS AND DATA REDUCTION

Our targets are U/LIRGs drawn from the Great Observatory All-Sky LIRG Survey (GOALS) sample (Armus et al. 2009). GOALS is a multi-wavelength survey of the brightest 60μm extragalactic sources in the local universe ($log(L_{IR}/L_{\odot}) > 11.0$) with redshifts z < 0.088. GOALS is a complete subset of the IRAS Revised Bright Galaxy Sample (RBGS) (Sanders et al. 2003). Objects in GOALS cover the full range of nuclear spectral types and interaction stages and may serve as useful analogs for comparison with high-redshift galaxies.

The GOALS U/LIRGs represent an entire array of merger stages from isolated starburst systems to massive post-mergers as well as galaxies in compact groups. The GOALS systems include starburst galaxies, AGN, composite systems, LINERs and E+a galaxies. While the ULIRGs in GOALS are composed entirely of major mergers, the lower luminosity LIRGs represent a variety of systems-some past or future ULIRGs, others simply undergoing intense bursts of star formation driving up the infrared luminosity temporarily (Ishida 2004; Armus et al. 2009). Our sample consists of targets observable from the south.

2.1. *Observations*

Our observations were conducted with the Wide Field Field Spectrograph at the Mount Stromlo and Siding Spring Observatory 2.3m telescope. WiFeS is a, dual beam, image-slicing integral field unit (IFU) described in detail by Dopita et al. (2007) and Dopita et al. (2010). We have previously presented analysis of smaller portions of the WiFeS GOALS dataset in Rich et al. (2010, 2011, 2012). In short, a single pointing from our dataset provides a data cube $25'' \times 38''$, sampled with $1''$ spaxels in double binning mode. The typical seeing was $\sim 1.5''$. The setup used for our observations produces a spectral coverage of 3700-5700 Å for the blue spectra, at a spectral resolution of R$\sim$ 3000 (100 km s^{-1}) and 5700-7000 Å for the red spectra at a resolution of R$\sim$ 7000 (40 km s^{-1}). Thus, the data have sufficient spectral resolution in the red to allow detailed dynamical studies, while the total wavelength coverage (3700-7000 Å) is sufficient to support excitation and chemical abundance analyzes.

The data were taken over 5 separate observing runs in July, August and September 2009 and March and May 2010. Observations were begun shortly after the instrument was commissioned, prior to the availability of nod-and-shuffle mode. Hence data taken in 2009 are taken primarily in classical observing mode with separate observations of the sky throughout each evening, while observations carried out in 2010 primarily use nod-and-shuffle mode for sky subtraction. Table A.1 lists the systems and dates observed, with the number of individual WiFeS pointings and total exposure times for each pointing, divided among two to five exposures. Figure A1 shows our WiFeS pointings overlaid on Digitized Sky Survey (DSS) images for each system listed in Table A.1. We observe a total of 27 GOALS systems with a wide variety of properties described in section 2.3. Observations were generally aligned and/or mosaiced to cover the entire galaxy or galaxies in each system.

2.2. *Data Reduction*

The data were reduced and flux calibrated using the WiFeS pipeline, briefly described in Dopita et al. (2010), which uses IRAF routines adapted primarily from the Gemini NIFS data reduction package. Cosmic ray removal was performed on the raw data frames prior to reduction with the "dcr" routine (Pych 2004).

The bias subtraction is somewhat complicated by the use of quad-readout with four amplifiers on each ccd to decrease chip read-out time. Additionally, there is a slight slope and instability in the bias across each region of the chip. Bias frames are taken immediately before and after each set of observations and a 2-D fit of the surface is subtracted from the temporally nearest object data in order to avoid adding additional noise to the data. Any resulting residual is accounted for with a fit to unexposed regions of the detector.

Quartz lamp flats are used to account for the response curve of the chip and twilight sky flats are used to correct for illumination variation along each of the slitlets. Spatial calibration is carried out by placing a thin wire in the filter wheel and illuminating the slitlet array with a continuum lamp. This procedure defines the center of each slitlet. The individual spectra have no spatial distortion because the camera corrects the small amount of distortion introduced by the spectrograph. Thus only low-order spatial mapping of the slitlets is required.

Wavelength calibration is performed using CuAr and NeAr arc lamp observations to provide sufficient lines in both the blue and red arms of the camera. Arc lamp data were taken in between sets of object exposures. Each of the 25 slitlets is then rectified by the pipeline into a full data cube (one for each camera) sampled on a common wavelength scale.

Telluric absorption features were removed from the resulting red data cubes using observations of B-stars or featureless white dwarfs (typically also used as flux standards) taken at similar air mass. The effects of differential atmospheric refraction are calculated and corrected by the pipeline for the blue data cubes.

Flux calibration of each individual data cube was carried out using flux standards observed throughout each night. Standard stars are taken from the WiFeS observing manual (Bessell 1999). Individual data cubes were flux calibrated using the standards observed nearest in time and air mass.

The individual data cubes are binned by 2 pixels in the spa-

tial direction to increase signal to noise and produce square spatial pixels (spaxels) 1″x 1″. Observations taken in march 2009 were binned during the data reduction process, observations taken in May 2009 and later were binned on-chip. Typical seeing achieved at SSO during our observations is $\sim 1.5''$, with some variation, on par with the spaxel size for our data cubes. Individual data cubes thus consist of 25x38 1″square spaxels, producing over 900 spectra. In practice, a few rows of spaxels are trimmed from the top and bottom of the individual cubes, corresponding to the edges of the slitlets.

Finally, the individual reduced, flux-calibrated data cubes are median combined and sampled to a common spatial grid using overlapping features found in each pointing. This is done for both single pointing and for mosaiced observations. Combined data cubes were aligned astrometrically by comparing a pseudo 'r-band' image generated using the red spectrum from each spaxel with either DSS R-band or HST data when available.

2.3. *The WiFeS GOALS Sample*

In all, 27 systems comprising nearly 40 individual galaxies were observed. THe sample was selected to cover a range of infrared luminosities, merger stages and nuclear activity. Basic sample properties are shown in Table 1.

The final sample comprises 4 ULIRGs and 23 LIRGs. This represents a slightly larger fraction of ULIRGs than the GOALS sample itself, which has 23 ULIRGs and 198 LIRGs. We apply the merger stage classification used in Yuan et al. (2010), adopted from Veilleux & Rupke (2002). Isolated systems ("iso") have no neighbors within a projected distance of 100 kpc, wide pairs ("a") are separated by a distance of greater than 10 kpc, close pairs ("b") are separated by less than 10 kpc and latest-stage, coalesced mergers are a combination of the original 'diffuse', 'compact' and 'old' merger class ("cde")-defined by an increase in compactness in K-band and decreasing to no evidence of any tidal features. This somewhat coarse sampling of the merger process is necessary given the small number in each class: two isolated systems, five wide pairs, ten close pairs and nine late-stage mergers. None the less, we are still able to trace bulk changes in the properties of our sample as a function of merger stage. Individual notes about each system are provided in the appendix.

To avoid contamination by AGN ionization in our analysis of shocks, four galaxies with strong optical, mid-IR and X-ray AGN signatures are removed from the various merger stage bins and treated separately. The isolated galaxy IRAS F21453-3511, the closely interacting pair IRAS F23128-5919 and the coalesced mergers IRAS 13120-5453 & F16164-0746 are all dominated by an AGN, as detected via [Ne V] in mid-IR Spitzer spectroscopy (Petric et al. 2011) and X-ray color/spectroscopy from Chandra observations (Farrah et al. 2007; Iwasawa et al. 2009, 2011). These galaxies are not included in their respective merger classes for the analysis of shocks for the remainder of the paper. The possibility of lower-level AGN activity in other systems is further discussed in Section 7.3.

Once the AGN are removed, there are three isolated galaxies ("iso"), four close pairs ("a"), nine close pairs ("b") and seven coalesced systems ("cde"). The average $\log(L_{IR})$ for the four classes are $11.37 \pm 0.04, 11.37 \pm 0.26, 11.62 \pm 0.23 and 11.85 \pm 0.33 L_{\odot}$ respectively, and $11.86 \pm 0.4 L_{\odot}$ for the four AGN.

3. DATA ANALYSIS

Table 1
WiFeS IFU GOALS Sample (WIGS)

IRAS Name (a)	$L_{IR}/L_{\odot}$ (b)	z (c)	pc/″ (d)	Merger Stage (e)
F01053-1746	11.71	0.0201	399	b
F02072-1025	11.01	0.0129	256	a
F06076-2139	11.65	0.0374	742	b
08355-4944	11.62	0.0259	543	cde
F10038-3338	11.78	0.0341	707	cde
F10257-4339	11.64	0.0094	185	b
F12043-3140	11.43	0.0232	517	b
F12592+0436	11.68	0.0375	784	cde
13120-5453	12.32	0.0308	653	cde
F13373+0105	11.62	0.0226	502	a
F15107+0724	11.35	0.0130	308	iso
F16164-0746	11.62	0.0272	588	cde
F16399-0937	11.63	0.0270	584	b
F16443-2915	11.37	0.0209	465	a
F17138-1017	11.49	0.0173	392	cde
F17207-0014	12.46	0.0428	878	cde
F17222-5953	11.41	0.0208	456	iso
17578-0400	11.48	0.0140	322	a
F18093-5744	11.62	0.0173	383	b
F18293-3413	11.88	0.0182	401	b
F18341-5732	11.35	0.0156	344	iso
F19115-2124	11.93	0.0487	976	b
F20551-4250	12.06	0.043	860	cde
F21330-3846	11.14	0.0191	400	b
F21453-3511	11.42	0.0162	341	iso
F22467-4906	11.84	0.0430	853	cde
F23128-5919	12.06	0.0446	884	b

(a) IRAS identifier from Sanders et al. (2003); Armus et al. (2009) (b) $\log(L_{IR}/L_{\odot})$ (Sanders et al. 2003; Armus et al. 2009) (c) systemic redshift (Sanders et al. 2003) (d) Spatial Scale (e) Veilleux & Rupke (2002) Merger Stage, taken from Yuan et al. (2010) where possible.

The key data products required for our work are accurate emission line fluxes and emission line kinematics at the highest possible spatial resolution, with as few confounding spectroscopic fitting parameters as possible. In order to tailor the final data product derived from the cubes to the needs of the analysis, in-house IDL routines combined with existing IDL software were used to analyze the spectra from each final data cube.

3.1. *Spectral Fitting*

Each data cube was analyzed using the UHSPECFIT software package (Rupke et al. 2010; Rich et al. 2010; Zahid et al. 2011). The WiFeS UHSPECFIT package cycles through the red and blue cubes for a single object, fitting the blue and red spectra from a given spaxel simultaneously. For each spectrum, the package performs an initial fit to the continuum and emission lines, checks whether any emission is found in the strongest lines (Hα and [NII]) and if so performs a second, final fit using the first fit as input estimators. After fitting every spectrum in the data cube in this fashion, the final data prod-

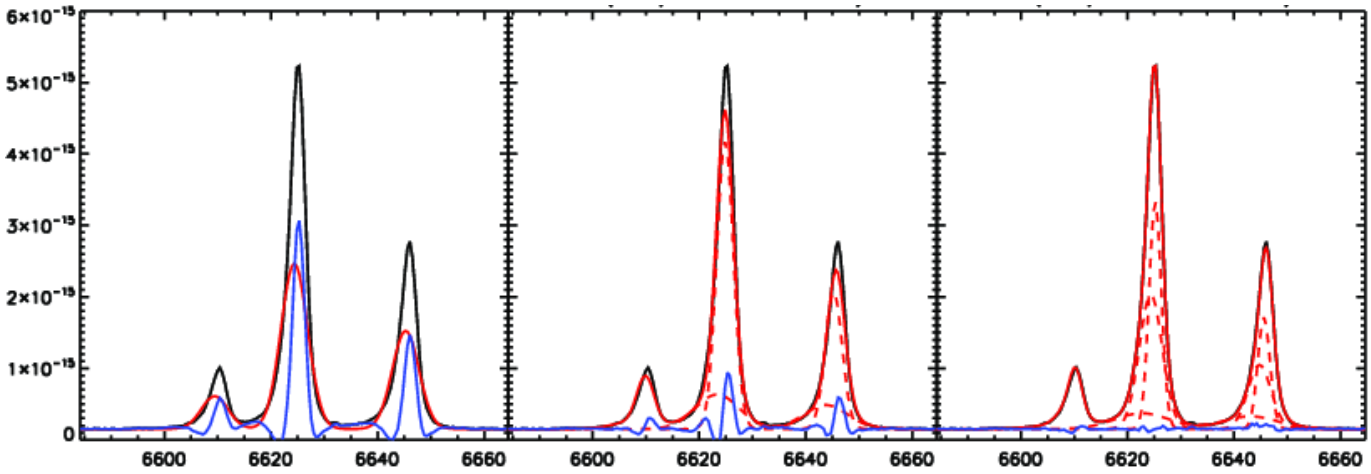

Figure 1. : Example of one, two and three component fits applied to the [NII]+Hα complex prior to fitting the entire spectrum. This is an example of a spaxel from IRAS F10257-4339 where a 3-component fit was chosen. The black line represents the data, the red line the best fit and the blue line the residuals. Individual components are plotted with a dashed red line.

uct is a data structure with spectral fits as well as all of the parameters necessary to reconstruct the emission line component fits for each line of each spectrum, as well as the errors on those parameters. The details of the fitting routine are further described in the following subsections.

3.2. *Continuum Fitting*

The first step in fitting a spectrum in all cases was to fit and subtract a stellar continuum using stellar population synthesis models from González Delgado et al. (2005). This is done in order to obtain a pure emission line spectrum while accounting more accurately for stellar features that underlie the emission lines in several systems. An IDL routine, IBACKFIT (Moustakas & Kennicutt 2006), fits a linear combination of stellar templates to the stellar continuua. IBACKFIT employs a least-squares analysis using the Levenberg-Marquardt algorithm via MPFIT (Markwardt 2009). IBACKFIT was applied in each case only to the blue spectrum, which holds the majority of the stellar spectral features in the WiFeS data. The best-fitting combination of templates was then combined with a functional fit and extrapolated to the entire data cube. No information from stellar template fitting (i.e. stellar population age, metallicity, etc.) was derived for the work in this paper.

3.3. *Emission Line Fitting*

The continuum-subtracted spectrum is then fit with several gaussian emission lines using routines built using the MPFIT package. The list of emission lines is chosen by the user prior to running UHSPECFIT. The emission lines fit in the WiFeS GOALS data include [OII] 3727,3729Å, Hϵ, Hδ, Hγ, Hβ, [OIII] 4959,5007Å, [OI] 6300,6364Å, [NII] 6548,6583Å, Hα and [SII] 6717,6731Å. The [OII] and [SII] doublet flux ratios were allowed to vary within the upper and lower theoretical limits and the flux ratios of the [OIII], [OI] and [NII] doublets were fixed to their prescribed theoretical values (i.e. Osterbrock 1989). Emission line gaussian peaks are constrained to be greater than or equal to zero.

One, two or three Gaussian components are fit to every emission line, to account for the complex line profiles seen in several of the WiFeS GOALS systems. Prior to running UHSPECFIT on a galaxy, mpfit was used to fit one, two and three gaussian components to the [NII]+Hα lines. An example of this process is given in Figure 1. Each resulting one, two and three gaussian component fit was checked by eye. Upon inspection, the best fit was chosen based on both quantitative comparison of the respective χ^2 as well as a qualitative assessment of the goodness of fit and consistency with features in surrounding fits within a single galaxy, similar to the method employed by Westmoquette et al. (2011, 2012).

If the χ^2 does not markedly improve when an extra gaussian component is added, fewer components are used to avoid over-fitting the emission lines. Consideration is also given to emission line fits in neighboring spaxels within a single cube when choosing whether to add additional gaussian components. The best fit emission line widths and redshifts are then passed to UHSPECFIT, which holds them fixed while simultaneously varying the remaining parameters. The resulting emission line fits to the rest of the spectrum were then again inspected by eye to ensure poorly and erroneously fit lines are rejected. This method resulted in more reliable, consistent fits with UHSPECFIT.

All emission lines are fit simultaneously, but the redshift and velocity width of each gaussian component are fixed to be the same value for every emission line. The relative velocities are fixed separately for the red and blue data cubes to allow for variation in wavelength calibration and resolution between the red and the blue spectra. This assumption implies that the line-emitting gas in a single spaxel is produced in the same region (e.g. Kewley et al. 2001b). Figure 2 shows an example of a successful multi-component emission line fit to key diagnostic lines in a single spectrum.

The errors in the parameters used in fitting the emission lines are calculated by the fitting code, which includes propagation of the variance spectra. The parameters include the gaussian widths (velocity dispersions) ratio of dispersions between the blue and red spectra, individual gaussian peaks, redshift and any slight deviation between the blue and red wavelength calibrations.

3.4. *Data Products*

Once a galaxy has been run through UHSPECFIT, we generate maps of the recessional velocity, velocity dispersion and emission line fluxes of each emission line component as well as maps of the total emission line flux of several strong lines. In addition to manual inspection of the emission line fits, a final S/N of 5 is used as a cutoff to create the total flux maps and a S/N of 3 cutoff as measured between component peaks

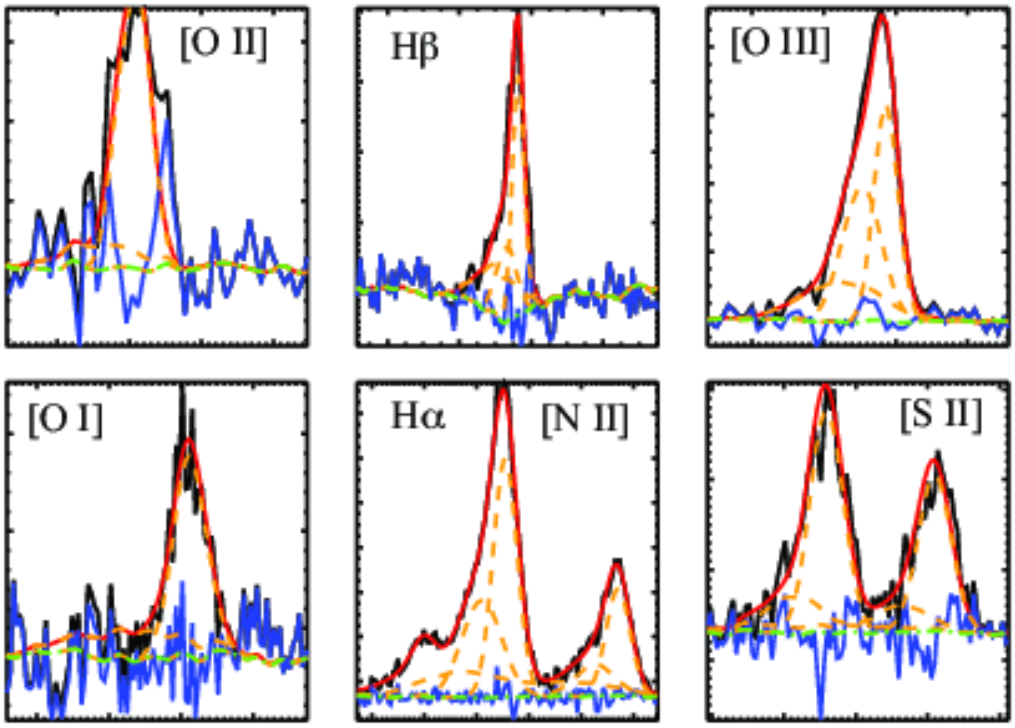

Figure 2. : Example of a 3-component fit to a spectrum from a single spaxel in IRAS F23128-5919. Several strong emission lines are shown. The total fit is plotted in red over the data in black, individual emission components are orange dashed lines, the continuum fit is a green dashed line and the residual fit between the total fit and the emission fit is shown in blue. The individual component (orange lines) for the [NII] 6548 line have been removed to decrease confusion.

and continuum noise is applied to the individual component maps. In all, $\sim 10,000$ spectra are analyzed in this paper, with $\sim 17,000$ individual gaussian components above the S/N cut-off. This corresponds to about 2100 individual gaussian components in the "iso" galaxies, 3300 in "a", 8300 in "b", 1300 in "cde" and 1750 in the AGN. The lower number of gaussian components in the cde bin despite the higher number of galaxies reflects both the small spatial extent of the emission line gas and the higher average distance to the coalesced merger galaxies.

4. EMISSION LINE GAS PROPERTIES

Our emission line maps and diagrams provide an overview of the distribution of spaxels spaxels dominated by enhanced low ionization species emission as well as some indication of the underlying power source and metallicity. For our purposes, the maps and diagnostic diagrams are most useful in spatially separating regions dominated by HII-region emission, shock emission and AGN emission. The observed emission line ratios are governed by the overall flux of ionizing photons, the hardness of the radiation field and the metallicity of the gas. By taking emission-line ratios that are sensitive to abundance and with a variety of ionization potentials, the source of ionizing radiation can be determined (e.g. Baldwin et al. 1981; Veilleux & Osterbrock 1987; Kewley et al. 2001a; Kauffmann et al. 2003; Kewley et al. 2006). With a harder radiation field than young stars or radiative shocks, AGN-ionized gas has generally higher log([OIII]/Hβ) emission line ratios than HII-region and shock emission, with log([OIII]/Hβ) of order unity to a factor of several times unity. HII-regions exhibit a range of emission line ratios, with low ionization species-to-Hα ratios (log([NII]/Hα)<-0.4, log([SII]/Hα)<-0.3 and log([OI]/Hα)<-1.0). HII-regions show a large range of log([OIII]/Hβ) emission line ratios (log([OIII]/Hβ from -1.0 to 0.8 from high to low abundance respectively) as a result of less efficient cooling leading to higher ionization parameters and thus higher [OIII]/Hβ. Shocks with velocities of $\sim 100 - 200$ km s^{-1}, on the other hand correspond to enhancements in lower ionization lines ([NII], [SII], [OI]), and some enhancement in [OIII]/Hβ in higher metallicity systems (Rich et al. 2011).

4.1. *Distinguishing Power Sources*

Both the distribution of line ratios and the values of the line ratios themselves provide useful information about the source(s) of ionizing radiation in a galaxy. Emission line ratio maps are generated using the total line fluxes spaxel by spaxel, which effectively traces the dominant power source. Line ratio diagnostic diagrams provide a more detailed perspective of the sources of ionizing radiation at work in a given system (Baldwin et al. 1981; Veilleux & Osterbrock 1987; Kewley et al. 2001a; Kauffmann et al. 2003; Kewley et al. 2006). When combined with the spatial information from the line ratio maps, a clear picture of one or more power sources present in a galaxy is revealed.

Figure 3 shows how the diagrams and line ratios maps appear for three systems with very different sources of ionizing radiation. Some of the galaxies in our sample appear to be dominated entirely by HII region emission, with no indication of any other source of ionizing radiation. IRAS F17222-5953 is a good example of such a system, as seen in Figure 3. The line ratios fall entirely within the HII-region portion of the diagnostic diagram. The [OIII]/Hβ and [NII]/Hα ratios fall as a function of radius due to the presence of a metallicity gradient (Rich et al. 2012). The gradient and line ratios are

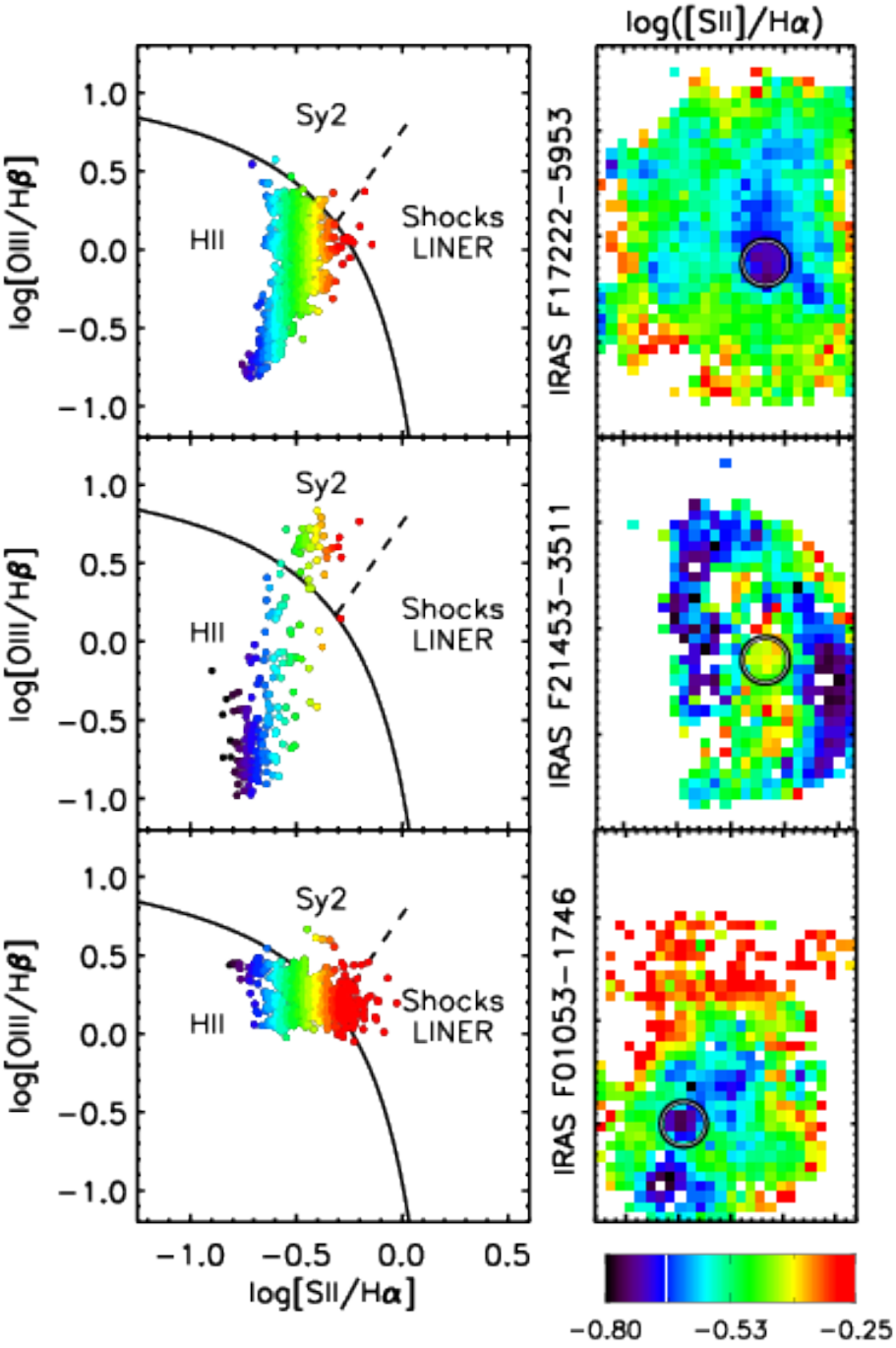

Figure 3. : Example line ratio diagnostic diagrams and maps from IRAS F17222-5953, F21453-3511 and F01053-1746. Points in the diagnostic diagrams are color coded with respect to the [SII]/Hα values shown in the line ratio maps. The center of each galaxy, corresponding to the peak in R-band emission, is marked with a circle in the line ratio map for reference. IRAS F17222 is dominated by star formation, F21453 is an AGN blended with star formation (Davies et al. 2014) and F01053 is a mixture of radiative shocks and star formation (Rich et al. 2011). These three galaxies are chosen to show key features of galaxies in our sample with each source of ionizing radiation. The remaining diagnostic diagrams and maps are shown in the appendix.

entirely consistent with other star forming galaxies (Kewley et al. 2010; Rupke et al. 2010).

Some of the galaxies in our parent sample exhibit a blend of strong AGN activity blended with star formation. IRAS F21453-3511, shown in Fig. 3, is a good example of this behavior. The diagnostic diagrams in these galaxies have very strong [OIII]/Hβ , moving into the Seyfert/AGN portion of the diagnostic diagram. Line ratio maps tend to show the highets emission line ratios in the nucleus, corresponding to the AGN, decreasing with distance from the nucleus (Davies et al. 2014; Leslie et al. 2014).

Finally, some galaxies show evidence of star formation blended with composite/LINER-like emission. This is shown in figure 3 with the close pair IRAS F01053-3511, which shows extended LINER-like emission well outside the nuclear regions, which are dominated primarily by star formation. Extended composite/LINER emission alone, however, does not confirm the presence of shocks (Rich et al. 2010, 2011). Extended low-ionization emission regions (LIERs) can be caused by a number of mechanisms, including heating by post-AGB stars Sarzi et al. (2010); Annibali et al. (2010); Eracleous et al. (2010) and diffuse ionized emission (e.g. Blanc et al. 2009).

4.2. *Line Ratio Maps*

Example emission line ratio maps are shown in Figure 3, with the remaining galaxy emission-line maps given in the Appendix. Emission line ratio maps are generated using the total line fluxes spaxel by spaxel, which effectively traces the dominant power source. For instance, in Figure 3 large portions of the merging system IRAS F01053-1746 are dominated by emission line ratios consistent with star formation while there is evidence of enhanced emission line ratios in areas of lower Hα surface brightness (as traced by the contours). As is noted in Rich et al. (2011), even in some portions of IRAS F01053-1746 dominated by HII region emission there may be a contribution to the emission from shocks that can be separated kinematically, but the total flux will show HII region-like line ratios overall.

Systems dominated entirely by HII region emission include IRAS F13373+0105 W & E, IRAS F17222-5953, IRAS F16443-2915 N & S. These systems exhibit line ratios consistent with HII region emission (see also section 4.2) across the entire line ratio map, with no indication of any other significant source of ionizing flux.

In some systems the line ratio map provides an immediate indication that there may be an AGN present. In systems with a strong AGN, the nuclear regions tend to be dominated by strong line ratios in every map, including [OIII]/Hβ . We are able to resolve and separate regions of star formation and AGN ionization in the maps of IRAS F21453-3511 and IRAS F23128-5919, both of which show a combination of Seyfert II nuclei and ongoing star formation (Davies et al. 2014; Leslie et al. 2014).

In many of the emission line maps, galaxies show enhanced low-ionization line ratios away from the nucleus and in inter-galaxy regions with HII-region like line ratios in the nuclear regions: this radial rise in line ratios is opposite to the drop in line ratios seen in AGN-dominated systems. As shown in Rich et al. (2010, 2011), underlying shock excitation combined with a lower contribution from star formation with increasing radius reveals itself as stronger low-ionization line ratios away from the nucleus. Some examples include IRAS F12043-3140, IRAS F15107+0724, IRAS F17138-1017, IRAS F20551-4250 and IRAS F21330-384 In some cases this may be enhanced by galactic winds (Sharp & Bland-Hawthorn 2010), as in IRAS F02072-1025 and IRASF F10257-4339 (Rich et al. 2010, 2011). Dust lanes also serve to bury ongoing star formation, enhancing shock-like line ratios, shock-like ratios. especially where shocks are caused by outflowing gas, the passage of dense clouds of gas through a substrate of more diffuse ISM, or through cloud-cloud collisions. This is evident in IRAS F01053-1746, IRAS F10257-4339 and IRAS F18293-3413. Some of the latest stage mergers are entirely dominated by enhanced line ratios consistent with shock excitation, such as IRAS F12592+0436 and IRAS F22467-4906. Shocks are not restricted to portions of the galaxy dominated by shock emission, however, and can be spread across merging galaxies even where the optical emission is dominated by star formation (Rich et al. 2011).

4.3. *Line Ratio Diagnostic Diagrams*

Line ratio diagnostic diagrams provide a more detailed perspective of the sources of ionizing radiation at work in a given system (Baldwin et al. 1981; Veilleux & Osterbrock 1987; Kewley et al. 2001a; Kauffmann et al. 2003; Kewley et al. 2006). When combined with the spatial information from the line ratio maps, a clearer picture of the combined power sources is revealed. Figure 3 shows example line diagnostic diagrams using the total emission line flux for three galaxies with disparate sources of ionizing radiation including star forming regions, AGN and radiative shocks. The diagrams for the remaining 30 data cubes, including diagrams with individual line components rather than total flux, are shown in the appendix.

Traditionally, emission line ratio diagnostic diagrams have been applied to nuclear spectra of U/LIRGs to investigate the presence of AGN (e.g. Yuan et al. 2010). Systems with resolved AGN activity provide a good example of the power of IFS. IRAS F21453-3511 has a cluster of spaxels in the AGN portion of all three diagnostic diagrams corresponding to the central regions seen in the emission line ratio maps. The rest of the spaxels form a sequence stretching towards the HII region portion of the diagnostic diagrams as the line ratios decrease away from the nucleus.

The combination of line ratio maps and diagnostic diagrams provides a way to disambiguate the difference between AGN enhanced emission and shock enhanced line ratios. Rich et al. (2010, 2011) discuss in detail this method for the systems IRAS F02072-1025, F01053-1746, F10257-4339 but the same effect can be seen in, for example, IRAS F12043-3140 and IRAS F21330-3846. The latter two systems show a sequence of spaxels in the line diagnostic diagrams indicating enhanced line ratios consistent with some contribution from non-HII region emission. The enhanced line ratios in the emission line maps of these systems are not consistent with AGN but with shock excitation due to the merger process.

As described in Rich et al. (2011), the presence of slow shocks leads to LINER-like line ratios in the diagnostic diagrams. The [SII]/Hα and [OI]/Hα ratios in particular are enhanced in the presence of shocks due to their low ionization potential, as is seen in great detail in IRAS F01053-1746 and F10257-4339 (Rich et al. 2011). LINER-like line ratios are seen in extranuclear regions in some other systems as well (e.g. IRAS F20551-4250). Two of our systems, IRAS F13373+0105 and F18341-5732 exhibit evidence of nuclear LINER activity, which are more likely associated with the traditional low-luminosity AGN explanation for LINER emis-

sion, whether it be photo-excited (Ferland & Netzer 1983; Halpern & Steiner 1983; Ho 1999; Kewley et al. 2006; Ho 2009; Eracleous et al. 2010) or shock excited (Fosbury et al. 1978; Baldwin et al. 1981; Dopita et al. 2015).

The underlying metallicity of the gas also affects the line ratios seen in the diagnostic diagrams. IRAS F17222-5953 and 13373+0105 W are good examples of this effect: both galaxies have an intrinsic metallicity gradient which create the sequence of values seen in the [NII]/Hα diagrams (Rich et al. 2012). Most of the galaxies that show HII region emission have spaxels that correspond to intrinsically high metallicity gas, with the exceptions being IRAS F01053-1746 and F18093-5744 C&N.

5. VELOCITY DISPERSIONS

Velocity dispersion provides a separate, independent test for the presence of shock emission (Rich et al. 2011). Here we examine the velocity dispersions of the emission line gaussian components. Velocity dispersions associated with HII regions are typically a few tens of km s^{-1}, while low-velocity shocks and AGN line profiles can have velocity dispersions in excess of 100 km s^{-1} (Epinat et al. 2010; Rich et al. 2011). In their discussions of the high velocity dispersions in the SINS sample, Genzel et al. (2008) note that the turbulent star formation, shocks and stellar feedback can drive up velocity dispersion as well (Efstathiou 2000; Silk 2001; Monaco 2004; Thompson et al. 2005; Dib et al. 2006). This is consistent with the correlation between average velocity dispersion and star formation surface density seen in, for instance, the sample of Green et al. (2010).

5.1. *Dispersion Distributions*

We analyze the distribution of velocity dispersions fit to the individual components in each system. An example histogram of velocity dispersions is shown in Figure 4, with the remaining systems shown in the Appendix. The dispersion distribution is shown as both the fraction of the total number of profiles at a given σ and as a fraction of the total $F_{H\alpha}$ in a given velocity bin. All gaussian components detected in at least one emission line are included in the velocity dispersion distribution histograms.

In systems mainly dominated by star formation (e.g. IRAS F16443-2915 N/S, F17222-5953) the majority of the velocity dispersions are consistent with the expected σ of a few tens of km s^{-1}. As noted in Rich et al. (2010, 2011), galaxies with a significant contribution from shocks show a significant contribution between σ=100-200 km s^{-1}, consistent with the shock velocities derived from line ratios (e.g. IRAS F01053-1746, F02072-1025, F10257-4339, Rich et al. 2010, 2011). Many galaxies also exhibit a significant number of components with σ between 40-90 km s^{-1}, likely consistent with disc turbulence. The galaxies in our sample that show unambiguous AGN signatures also show some contribution at significantly higher velocity dispersions, of 300-600 km s^{-1}.

5.2. *Line Ratios and Velocity Dispersion*

In their lower spectral resolution IFS survey of U/LIRGs, Monreal-Ibero et al. (2006, 2010) established a correlation between velocity dispersion and emission line ratio, which they attributed to shocked gas components. In Rich et al. (2011) we see the same correlation for IRAS F01053-1746 and F10257-4339, consistent with the other signatures of shock excitation (Rich et al. 2011).

Nearly all of the galaxies in the WiFeS GOALS sample which have line profiles fit with elevated velocity dispersion components reproduce this enhancement in [NII]/Hα, [SII]/Hα and [OI]/Hα with respect to velocity dispersion, regardless of the excitation mechanism. The exceptions to this rule appear to be IRAS F18093-5744 C & S. IRAS F18093-5744 C in particular shows the opposite trend: a component with elevated velocity dispersion and correspondingly lower [NII]/Hα, [SII]/Hα and [OI]/Hα ratios. IRAS F18093-5744 C is a compact Wolf-Rayet galaxy with the emission driven by young, bright stars (Kovo & Contini 1999; Fernandes et al. 2004). Our data show two narrow components with an underlying broad component seen in the σ vs. ratio diagrams. This broader component is elevated in [OIII]/Hβ, and can be seen in the diagnostic diagram in the Appendix, corresponding to lower metallicity gas, consistent with the analysis in Fernandes et al. (2004).

6. MERGER PROGRESS

All line diagnostic methods described in section 5 have been applied to each galaxy in our sample. We now track how they change, if at all, as a function of merger evolution. We group spaxels from galaxies in each of the four merger stages as outlined in section 2. The four positively identified AGN are placed in a separate group. We now examine the overall shape of the line ratio diagnostic diagrams, velocity dispersion distribution and σ vs. line ratio diagrams for each merger stage.

6.1. *Diagnostic Diagram Evolution*

Figure 5 shows the three diagnostic diagrams for each merger group and the AGN. The points are generated using the total flux line ratios in each spaxel for every galaxy in a given merger class. In the case of the close pair stage, the data points are somewhat dominated by IRAS F01053-1746 & F10257-4339, but the other individual galaxies in this merger stage group have line ratios that fall in consistent regions of the diagnostic diagram. The AGN stage is likewise dominated by IRAS F21453-3511 and F23128-5919 which have comparatively spaxels in their diagnostic diagrams, though the relatively fewer points from the other two AGN are again consistent.

The overall shape of the diagnostic diagrams shows an increasing number of spaxels in the 'composite' region of the [NII]/Hα line ratio diagnostic diagram in later merger stages. This result is consistent with the work of Yuan et al. (2010) which shows an increasing fraction of composite behavior with merger stage.

There is a much narrower range of spaxels in the HII region portion of the [NII]/Hα diagram for the "cde" galaxies, which is primarily a result of the flattening and dilution of metallicity gradients as mergers progress: we discuss this effect further in Rich et al. (2012). The same effect is seen in individual systems in the "b" stage.

6.2. *Velocity Dispersion Evolution*

As in the case of line ratio evolution with merger stage, there is also clear evidence of an corresponding evolution in the observed velocity dispersion. In Figure 7, we show the change in the overall velocity dispersion distribution as a function of merger stage. The isolated systems are dominated primarily by narrow HII region-like velocity dispersions, though there is a tail of higher dispersion spaxels corresponding to some turbulence and the LINER emission in

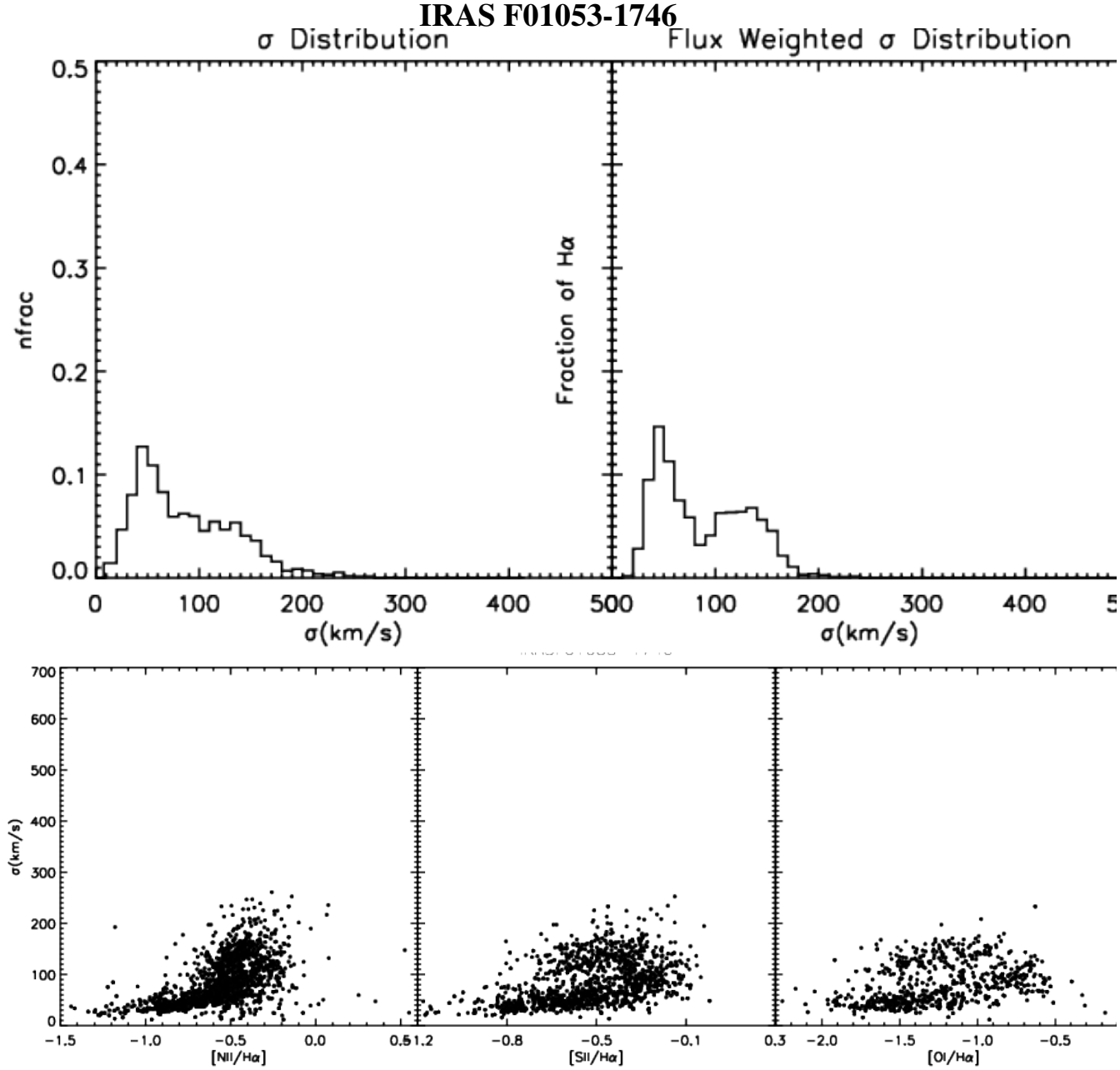

Figure 4. : Velocity dispersion distribution and comparison with line ratios. The top left panel shows the histogram for the fraction of the total number of components for a given velocity dispersion The top right panel shows a similar histogram, but with the fraction of the total Hα flux for a given velocity dispersion. Systems with a stronger contribution from shocks show a larger fraction of $\sigma \gtrsim$90 km s^{-1}. The bottom three panels show various diagnostic emission line ratios vs. velocity dispersion. Lower emission line ratios are, on average, dominated by lower-σ star forming regions. The same diagrams for the remaining portion of the sample are in the Appendix.

IRAS F18341-3413. In the widely separated pairs the peak in both number of profiles and total Hα flux shifts slightly to the right and the tail of broader spaxels grows, indicating an increase in turbulent star formation. Figure 7 compares the velocity dispersion distribution for the isolated, "cde" and AGN systems. The AGN galaxies show a stronger high-σ component above 350 km/s that is not seen in the other distributions.

In the closely interacting pairs, the shape of the dispersion distribution begins to change significantly: a strong tail of higher σ line profiles is seen in both fractional number and total F_{Ha}. This is consistent with the increase in outflows as the merger progresses, as seen in previous IFU studies (Rich et al. 2011; Soto et al. 2012; Genzel et al. 2014; Arribas et al. 2014; Ho et al. 2014; Wild et al. 2014), and in section 5 above. At the latest merger stages, the velocity dispersion distribution is fairly flat from narrow to broad line components, indicating a significantly increased contribution from turbulent star formation and shocks in the emission line gas.

Figure 8 shows the evolution of the line ratio versus σ with merger stage. The overall shape of the diagrams tells the same story as the diagnostic diagrams and velocity dispersion distributions taken together: There is an overall trend in the to-

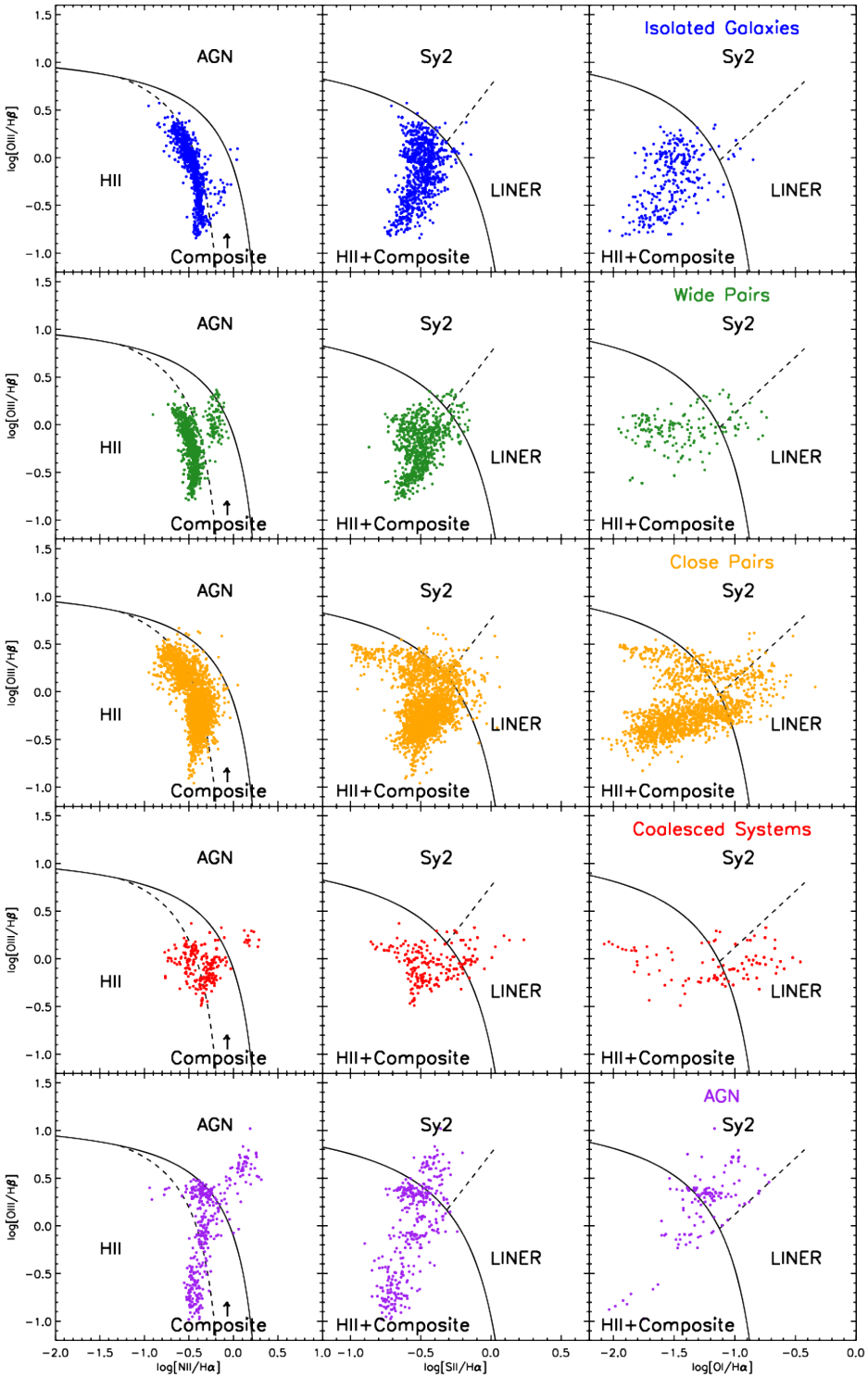

Figure 5. : Line ratio diagnostic diagrams created using all spaxels from every galaxy in each merger class. In blue are isolated systems, green are widely separated pairs ("a"), orange are close pairs ("b"), red points are coalesced galaxies ("cde") and the bottom diagrams with purple points are the four AGN galaxies. Kewley et al. (2006) classifications are shown on each diagram.

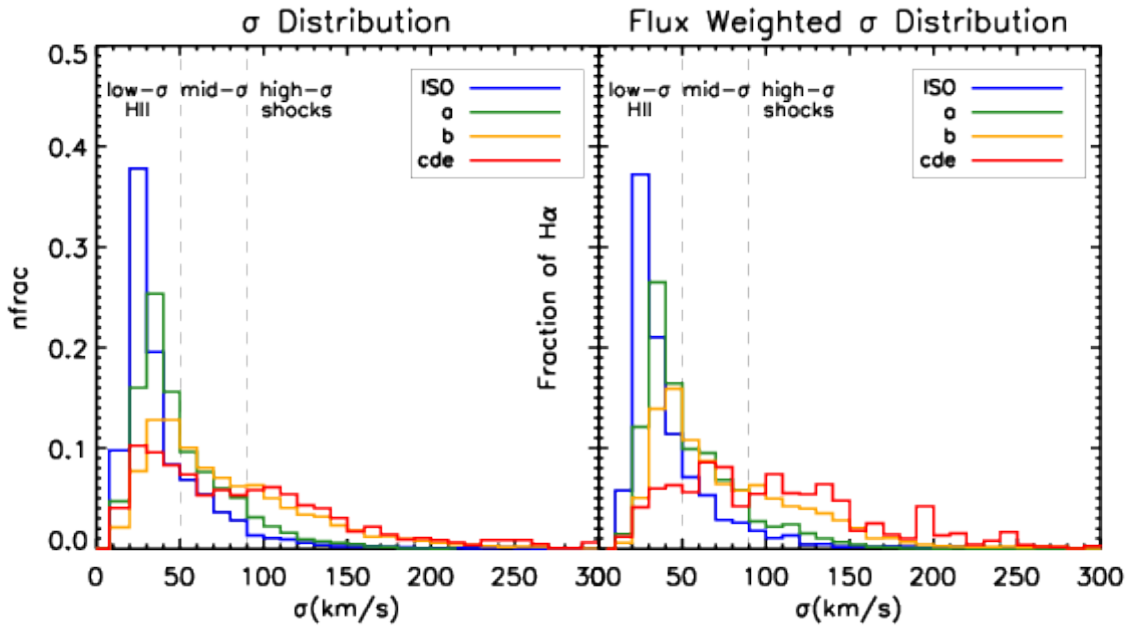

Figure 6. : Velocity dispersion distribution histograms for each merger class. As in Figure 4, the fractional number of profiles is shown in the left panel and flux-weighted σ distribution in the right panel.

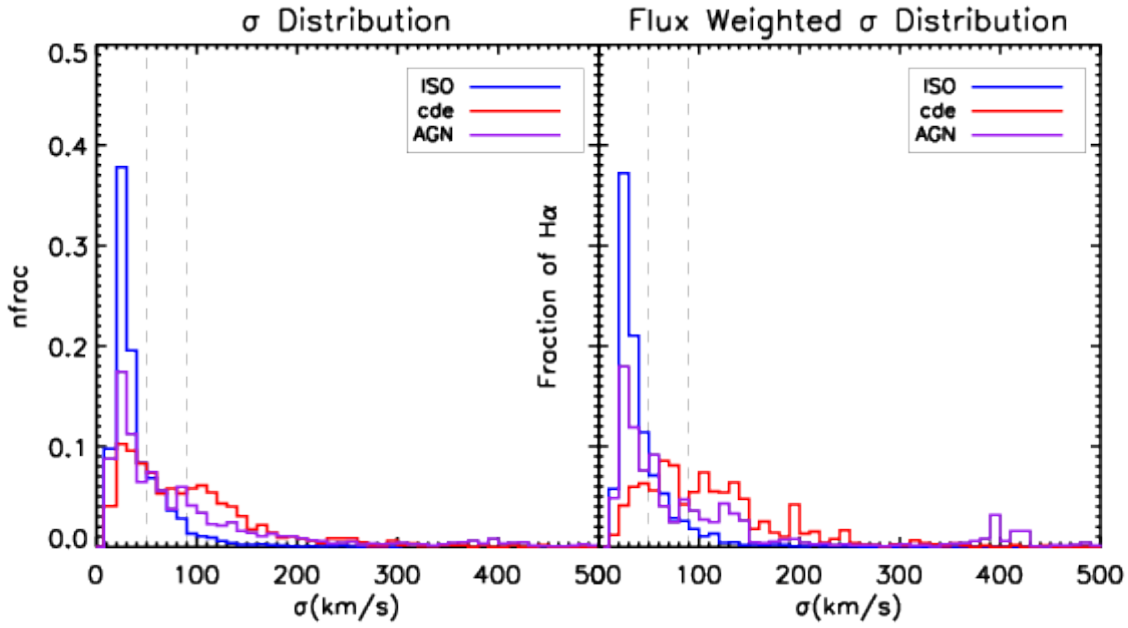

Figure 7. : Line ratio vs. σ as in Figure 6, but for isolated galaxies, coalesced mergers and the four AGN. Note that this figure is extended to a higher value of σ than Figure 6.

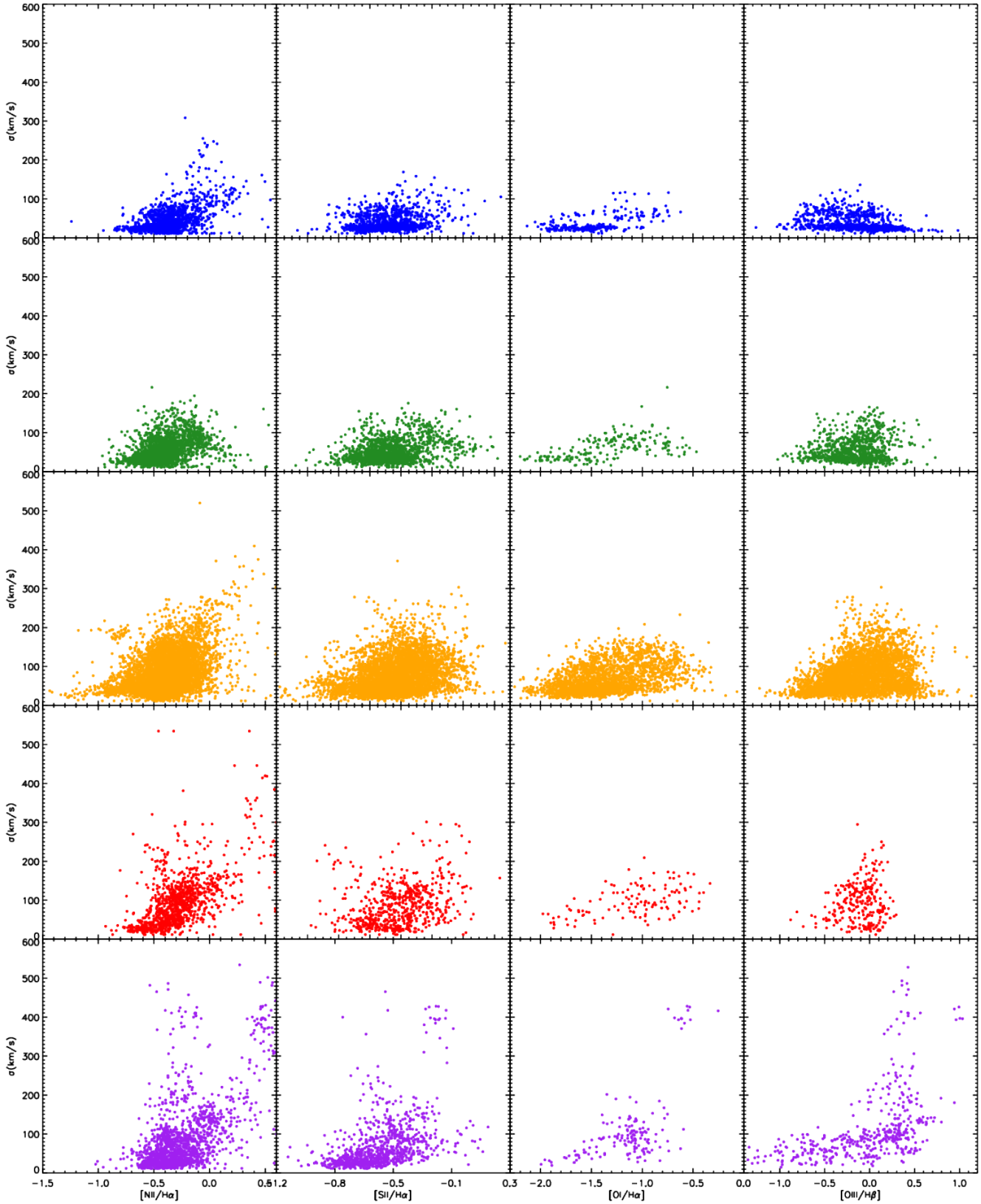

Figure 8. : Line ratio vs. σ as in Figure 4, for each merger stage, with "iso, a, b, cde" and AGN represented by blue, green, orange, red and purple from top to bottom respectively.

tal number of spaxels with enhanced velocity dispersion and emission line ratio as a function of merger stage.

The AGN show a bimodal distribution in the line ratio vs. σ, owing mainly to the difference in line ratio values at high velocity dispersion between IRAS F21453-3511 and F23128-5919 which dominate these figures. This is likely due to a difference in metallicity between the AGN-illuminated gas in the two systems.

7. DISCUSSION

In the absence of an AGN, a relative increase in the velocity dispersion and shift of the strong emission line ratios in the diagnostic diagram towards the LINER region is indicative of gas excited by slow shocks (Monreal-Ibero et al. 2006, 2010; Rich et al. 2010, 2011). Moreover, high-σ and LINER-like line components are not restricted to the nuclear regions of our non-AGN systems, again consistent with widespread shock excitation caused by merger-driven gas flows as the source of ionization for the observed emission (Monreal-Ibero et al. 2010; Rich et al. 2011, see also individual system notes in appendix). We therefore interpret the overall relative increase in velocity dispersion, particularly in the absence of any detectable influence from an AGN, as an increased relative contribution from slow shock excitation in our sample and discuss the relative strengths of each velocity component in our sample.

7.1. *Shock Fraction and Merger Stage*

With the simple correlations established in the previous sections, σ can be used as a proxy for the total contribution from HII region emission, turbulent star formation and shocks. The histograms of the distribution of σ discussed in section 5 and shown in Figures 6 and 7 allow us to establish approximate cutoffs between the three components. For the discussion here we establish an upper limit of σ=50 km s^{-1} for pure HII region emission and σ >90 km s^{-1} for spaxels that are primarily dominated by shock excitation in the absence of an AGN.

Figure 9 shows the change in the total fraction of $F_{H\alpha}$ in each component as a function of merger stage. The fraction in each component is the total of the profiles in each merger stage bin. There is a minimal flux-weighted contribution of a few percent from a higher σ, shock-dominated component in the three isolated galaxies and in the widely separated pairs in our sample. The turbulent, mid-range σ component increases as the galaxies begin to interact, but stays roughly flat throughout the merger process. Most interestingly, however, is the rapid increase in a high-σ component from wide to close pairs and from close pairs to late-stage mergers. By the "cde" stage, just over half of the total $F_{H\alpha}$ we measure lies in high velocity dispersion line emission.

The low-σ component is consistent with the velocity dispersions seen in star forming regions, while the mid-σ component is likely associated with regions of more turbulent star formation seen in strongly star bursting systems (e.g. Green et al. 2010). The highest observed velocity dispersions, above 90 km s^{-1}, are caused by even more turbulent activity in the ISM of U/LIRGs. The most likely culprit is shocks caused by merger-driven gas flows, such as galactic winds (e.g. Armus et al. 1989, 1990; Sharp & Bland-Hawthorn 2010; Rich et al. 2010). These lower velocity shocks exhibit velocity dispersions consistent with the outflow velocity and the observed high-σ gas, on the order of 100-200 km s^{-1}(Rich et al. 2010, 2011). The high-σ component observed in our systems

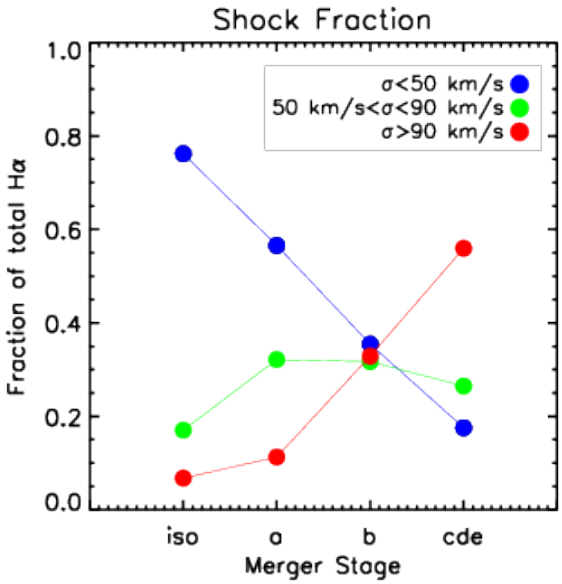

Figure 9. : Here the contribution from shocks is traced by the overall velocity dispersion distribution. In each merger stage bin, the total fraction of Hα flux within each velocity dispersion range is calculated. Cutoffs of σ=50 and 90 km s^{-1} are chosen to distinguish between HII region velocity dispersions, more turbulent dispersions, and shock-dominated dispersions. These values are consistent with the overall distribution of spaxels seen in Figure 6

is also correlated with elevated emission line ratios, as seen by Monreal-Ibero et al. (2010) and consistent with the radiative spectra of gas ionized by shocks. This combined elevation in emission line ratios and velocity dispersions increases as a function of merger stage, and in the 7 latest merger-stage systems, there appears to be a significant contribution to the optical spectra from merger-induced shocks.

There is the possibility of contribution from a less luminous AGN (classical LINER), which can similarly increase observed emission line ratios and velocity dispersions. The spatial and spectrally resolved information provided by our IFS observations, however, show not only elevated σ and line ratios in the nuclear regions, but at many kpc from the nucleus, more consistent with widespread shocks (see Appendix C). We discuss further possible contamination from AGN in section 7.2.

7.2. *AGN Diagnostics and Contamination*

The conclusion that the composite spectra we observe are due to shocks assumes that there is no appreciable contribution to the optical spectra from an AGN. Although we have excluded the four AGN-dominated galaxies from our merger stage discussion, there remains the question of any low-level AGN contribution to the optical spectra in some of our systems. This is of somewhat more of a concern in the latest-stage mergers in our sample, as the optical emission is concentrated primarily in the nuclear regions. Although none of the galaxies in the merger sample have detectable [Ne V] emission in the mid-IR, this does not necessarily rule out the possibility of a lower-luminosity AGN (Petric et al. 2011). Further, not all of the galaxies in our sample have been observed with Chandra, and some systems that have been observed with Chandra but show X-ray emission consistent with

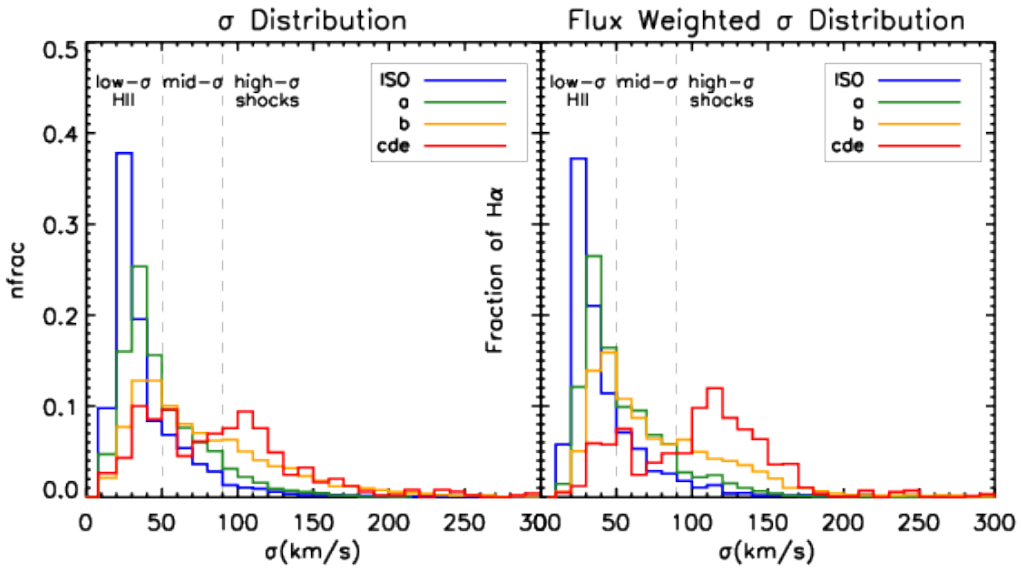

Figure 10. : Reproduction of Figure 7 with low 6.2μm PAH equivalent width galaxies excluded from "cde". In this case, only three galaxies remain in the "cde" bin, IRAS F12592+0436, F17138-1017 and F22467-4906.

intense star formation may still harbor compton-thick AGN (Iwasawa et al. 2009, 2011).

Another measure of AGN activity that can be derived from the mid-IR data is 6.2μm PAH equivalent width (eqw). In AGN dominated spectra the hot dust continuum depresses the 6.2μm eqw and the PAHs that generate the feature are apparently destroyed in the EUV photon field (Genzel et al. 1998; Lutz et al. 1999; Rigopoulou et al. 1999; Sturm et al. 2000; Armus et al. 2007; Desai et al. 2007; Wu et al. 2009; Fu et al. 2010; Petric et al. 2011). Stierwalt et al. (2013) determined 6.2μm PAH eqw values from nuclear spectra for the entire GOALS sample, setting a value eqw$>0.54\mu$m for galaxies that are dominated by starburst and eqw<0.27 for galaxies dominated by an AGN. Galaxies with eqw values that fall between these values are considered composite systems.

To make a more conservative estimate of the shock fraction in the late stage mergers galaxies with 6.2μm PAH eqw $<0.54\mu$m are removed from the "cde" bin (these include IRAS 08355-4944, F10038-3338, F17207-0014 and F20551-4250, with 6.2μm PAH eqw of 0.19, 0.03, 0.31 and 0.10μm). This leaves 3 coalesced mergers, IRAS F12592+0436, F17138-1017 and F22467-4906 which have eqw of 0.55, 0.68 and 0.45μm respectively. The total number of components with Hα above the S/N cutoff in these three galaxies is $\sim$ 490. The new velocity dispersion distribution and shock fraction are shown in Figures 11 and 12. Interestingly, when the potential low-luminosity AGN bearing galaxies are excluded the fraction of emission from broad, slow-shock dominated velocity dispersion components goes up, moving from roughly 55% to nearly 70% of the observed Hα flux. In Fig. 10 IRAS F17138-1017 is classified as a composite system, while F12592+0436 and F22467-4906 host extended LINER-like emission, though in the complete absence of any indication of AGN activity these three systems are clear examples of shock-driven LIER hosts, with LIER emission contaminating and in some cases dominating the observable optical emission line gas.

7.3. *Prevalence of Shocks and Energy Budget*

Our results indicate an overall increase in the total contribution from shocks to the global optical spectra of middle and late stage merging U/LIRGs. The U/LIRGs in the WiFeS GOALS sample contain buried star formation that is so extinguished as to be unobservable at optical wavelengths, which may account in part of the relative increase from non-HII region emission to the total observed emission line flux.

A prime example of this is IRAS F01053-1746, which has an extended shock-like region in the optical cospatial with a strong IR source indicative of buried star formation (Howell et al. 2010; Rich et al. 2011). Indeed, as noted in Rich et al. (2011), the total luminosity of the shocks in IRAS F01053-1746 is a negligible fraction of the bolometric luminosity, though they can still act as a means of removing energy from the infalling gas over the time scale of the merger process.

Regardless, the *observable* optical emission in our sample shows a combination of HII-region emission and ionization by slow shocks, increasing as a function of merger stage. This combination manifests in some systems as a "composite" spectrum, though in this case "composite" means starburst+shocks rather than starburst+AGN. Indeed, in Rich et al. (2014) we showed that when only nuclear spectra are considered, 75% of the "composite" galaxies in our sample are composite simply due to a sizable contribution from shocks to their emission line spectra.

8. SUMMARY

We have analyzed WiFeS optical integral field spectroscopic data cubes of 27 systems from the GOALS sample, 23 of which are a combination of at least two interacting galaxies, ranging from widely separated pairs approaching first pericenter to coalesced systems on their way to becoming elliptical merger remnants. Our analysis focuses on continuum-subtracted emission line gas, in particular through a decomposition of individual emission line profiles into one, two or three distinct kinematic components. We use the results of our emission line fits to create line ratio maps, line diagnostic diagrams and velocity dispersion distributions for each individual galaxy observed. We consider Hα-flux weighted line

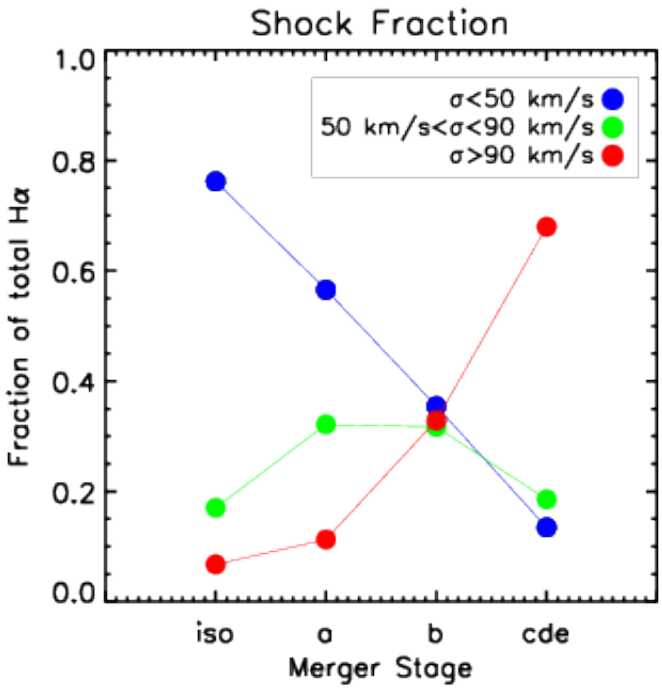

Figure 11. : Reproduction of Figure 9 with low 6.2μm PAH equivalent width galaxies excluded from "cde", as in Fig. 12. component velocity dispersion distributions to avoid overweighting regions of low-surface brightness emission. The results from each galaxy are placed into bins according to merger stage and the evolution of the emission line ratios and velocity dispersions are tracked as a function of merger progress. Our main conclusions are:

- Isolated systems and wide pairs are dominated primarily by HII-region emission ($\sim$75% and $\sim$55% of Hα emission respectively), with line profiles primarily σ of a few tens of km s^{-1}.
- All interacting systems exhibit emission with slightly higher velocity dispersions (50$<\sigma<$90 km s^{-1}), likely associated with turbulent star formation (e.g. Genzel et al. 2008; Green et al. 2010. This component makes up roughly 30% of the total observed Hα flux throughout the merger process.
- Closely interacting pairs and coalesced mergers show a strong σ component above 100 km s^{-1} and an increasingly dominant contribution contribution from composite and LINER-like emission line ratios. In the absence of an AGN, we assume the broadened σ component above 90 km s^{-1} is tracing an increasing fractional contribution from shocks, passing 50% of the total observed Hα flux in the coalesced mergers.

We consider the IFS data of 4 AGN-dominated systems in our sample separately. The AGN dominant systems are detected in [Ne V] in the mid-IR and show AGN-like X-ray colors and spectra in Chandra and XMM-Newton data (Petric et al. 2011; Iwasawa et al. 2011; Franceschini et al. 2003). We consider the role that less dominant AGN may play in the latest stage mergers in our system by using the mid-IR diagnostic 6.2μm PAH eqw as a proxy for AGN activity. Our conclusions are:

- The 4 AGN show a significant component at σ of 300-500 km s^{-1} and emission line ratios clearly approaching and entering the Seyfert region of the emission line diagnostic diagrams. The AGN also contain shock-like velocity dispersions, driven either by the AGN itself, galactic winds (observed in blue-shifted Na D absorption) or merger-induced gas flows
- When the low 6.2μm eqw coalesced mergers are removed from the non-AGN sample, the shock-like high-σ component increases to 70% of the observed Hα emission in the remaining three systems. Stierwalt et al. (2013) note that some galaxies show strong evidence for enhanced H_2 emission due to starburst-driven outflows and shocks rather than AGN, with correspondingly low PAH 6.2μm eqw, lending further ambiguity to the picture.

Spatially resolved spectroscopy is clearly a powerful tool for distinguishing non-AGN composite emission, particularly in systems where widespread shocked ISM is expected due to a powerful starburst or an ongoing gas-rich interaction. Recent multi-wavelength studies of systems from the GOALS sample and elsewhere have shown promising routes to further study the impact that shocks have on the environment of U/LIRGs (Mazzarella et al. 2012; U et al. 2013; Inami et al. 2013). New surveys of hundreds and thousands of galaxies with IFU spectroscopy, namely CALIFA, SAMI and MaNGA Sánchez et al. (2012); Croom et al. (2012); Bundy et al. (2015) are revealing a complex mix of forces at work in less luminous galaxies, including LINER excitation in non-mergers caused by shocks as well a warm ionized interstellar medium heated by old stars and UV photons that escape HII regions (Arribas et al. 2014; Ho et al. 2014; Belfiore et al. 2015). The combination of complementary, resolved multi-wavelength data that probes the multiple sources of activity will be the key to understanding the complex interplay between star formation, shocks, AGN and the ISM in galaxies throughout the universe

The authors acknowledge ARC support under Discovery project DP0984657. This research has made use of the NASA/IPAC Extragalactic Database (NED) which is operated by the Jet Propulsion Laboratory, California Institute of Technology, under contract with the National Aeronautics and Space Administration. This research has also made use of NASA's Astrophysics Data System, and of SAOImage DS9 (Joye & Mandel 2003), developed by the Smithsonian Astrophysical Observatory.

REFERENCES

Alonso-Herrero, A., Rieke, G. H., Rieke, M. J., & Scoville, N. Z. 2002, AJ, 124, 166
Annibali, F., Bressan, A., Rampazzo, R., Zeilinger, W. W., Vega, O., & Panuzzo, P. 2010, ArXiv e-prints
Armus, L., Heckman, T. M., & Miley, G. K. 1989, ApJ, 347, 727
—. 1990, ApJ, 364, 471
Armus, L., et al. 2007, ApJ, 656, 148
—. 2009, PASP, 121, 559
Arribas, S., & Colina, L. 2003, ApJ, 591, 791
Arribas, S., Colina, L., Bellocchi, E., Maiolino, R., & Villar-Martín, M. 2014, A&A, 568, A14
Arribas, S., Colina, L., Monreal-Ibero, A., Alfonso, J., García-Marín, M., & Alonso-Herrero, A. 2008, A&A, 479, 687
Baldwin, J. A., Phillips, M. M., & Terlevich, R. 1981, PASP, 93, 5
Belfiore, F., et al. 2015, MNRAS, 449, 867

Bessell, M. S. 1999, PASP, 111, 1426
Blain, A. W., Smail, I., Ivison, R. J., Kneib, J.-P., & Frayer, D. T. 2002, Phys. Rep., 369, 111
Blanc, G. A., Heiderman, A., Gebhardt, K., Evans, II, N. J., & Adams, J. 2009, ApJ, 704, 842
Bundy, K., Fukugita, M., Ellis, R. S., Targett, T. A., Belli, S., & Kodama, T. 2009, ApJ, 697, 1369
Bundy, K., et al. 2015, ApJ, 798, 7
Chien, L.-H., & Barnes, J. E. 2010, MNRAS, 407, 43
Cluver, M. E., et al. 2010, ApJ, 710, 248
Croom, S. M., et al. 2012, MNRAS, 421, 872
Darling, J., & Giovanelli, R. 2002, AJ, 124, 100
Dasyra, K. M., Yan, L., Helou, G., Surace, J., Sajina, A., & Colbert, J. 2008, ApJ, 680, 232
Davies, R. L., Rich, J. A., Kewley, L. J., & Dopita, M. A. 2014, MNRAS, 439, 3835
de Ravel, L., et al. 2009, A&A, 498, 379
Desai, V., et al. 2007, ApJ, 669, 810
Dib, S., Bell, E., & Burkert, A. 2006, ApJ, 638, 797
Dopita, M., Hart, J., McGregor, P., Oates, P., Bloxham, G., & Jones, D. 2007, Ap&SS, 310, 255
Dopita, M., et al. 2010, Ap&SS, 95
Dopita, M. A., Pereira, M., Kewley, L. J., & Capaccioli, M. 2002, ApJS, 143, 47
Dopita, M. A., et al. 2015, ApJ, 801, 42
Efstathiou, G. 2000, MNRAS, 317, 697
Elmegreen, D. M., & Elmegreen, B. G. 2006, ApJ, 651, 676
Epinat, B., Amram, P., Balkowski, C., & Marcelin, M. 2010, MNRAS, 401, 2113
Eracleous, M., Hwang, J. A., & Flohic, H. M. L. G. 2010, ApJ, 711, 796
Farage, C. L., McGregor, P. J., Dopita, M. A., & Bicknell, G. V. 2010, ArXiv e-prints
Farrah, D., et al. 2007, ApJ, 667, 149
Ferland, G. J., & Netzer, H. 1983, ApJ, 264, 105
Fernandes, I. F., de Carvalho, R., Contini, T., & Gal, R. R. 2004, MNRAS, 355, 728
Fosbury, R. A. E., Mebold, U., Goss, W. M., & Dopita, M. A. 1978, MNRAS, 183, 549
Franceschini, A., et al. 2003, MNRAS, 343, 1181
Fu, H., et al. 2010, ApJ, 722, 653
Genzel, R., et al. 1998, ApJ, 498, 579
—. 2008, ApJ, 687, 59
—. 2014, ApJ, 796, 7
González Delgado, R. M., Cerviño, M., Martins, L. P., Leitherer, C., & Hauschildt, P. H. 2005, MNRAS, 357, 945
Green, A. W., et al. 2010, Nature, 467, 684
Grimes, J. P., Heckman, T., Strickland, D., & Ptak, A. 2005, ApJ, 628, 187
Guillard, P., Boulanger, F., Cluver, M. E., Appleton, P. N., Pineau Des Forêts, G., & Ogle, P. 2010, A&A, 518, A59
Haan, S., et al. 2011, AJ, 141, 100
Halpern, J. P., & Steiner, J. E. 1983, ApJ, 269, L37
Henkel, C., & Wilson, T. L. 1990, A&A, 229, 431
Hinshaw, G., et al. 2009, ApJS, 180, 225
Ho, I.-T., et al. 2014, MNRAS, 444, 3894
Ho, L. C. 1999, Advances in Space Research, 23, 813
—. 2009, ApJ, 699, 626
Howell, J. H., et al. 2010, ApJ, 715, 572
Imanishi, M., Nakagawa, T., Shirahata, M., Ohyama, Y., & Onaka, T. 2010, ApJ, 721, 1233
Inami, H., et al. 2013, ApJ, 777, 156
Ishida, C. M. 2004, PhD thesis, UNIVERSITY OF HAWAI'I
Iwasawa, K., Sanders, D. B., Evans, A. S., Mazzarella, J. M., Armus, L., & Surace, J. A. 2009, ApJ, 695, L103
Iwasawa, K., et al. 2011, A&A, 529, A106
Joye, W. A., & Mandel, E. 2003, in Astronomical Society of the Pacific Conference Series, Vol. 295, Astronomical Data Analysis Software and Systems XII, ed. H. E. Payne, R. I. Jedrzejewski, & R. N. Hook, 489–+
Kauffmann, G., et al. 2003, MNRAS, 346, 1055
Kewley, L. J., Dopita, M. A., Sutherland, R. S., Heisler, C. A., & Trevena, J. 2001a, ApJ, 556, 121
Kewley, L. J., Groves, B., Kauffmann, G., & Heckman, T. 2006, MNRAS, 372, 961
Kewley, L. J., Heisler, C. A., Dopita, M. A., & Lumsden, S. 2001b, ApJS, 132, 37
Kewley, L. J., Rupke, D., Jabran Zahid, H., Geller, M. J., & Barton, E. J. 2010, ApJ, 721, L48
Kim, D.-C., Sanders, D. B., Veilleux, S., Mazzarella, J. M., & Soifer, B. T. 1995, ApJS, 98, 129
Kovo, O., & Contini, T. 1999, in IAU Symposium, Vol. 193, Wolf-Rayet Phenomena in Massive Stars and Starburst Galaxies, ed. K. A. van der Hucht, G. Koenigsberger, & P. R. J. Eenens, 604–+
Leslie, S., Rich, J., Kewley, L., & Dopita, M. 2014, ArXiv e-prints
Lutz, D., Veilleux, S., & Genzel, R. 1999, ApJ, 517, L13
Markwardt, C. B. 2009, in Astronomical Society of the Pacific Conference Series, Vol. 411, Astronomical Society of the Pacific Conference Series, ed. D. A. Bohlender, D. Durand, & P. Dowler, 251–+
Martin, J. M., Bottinelli, L., Dennefeld, M., Gouguenheim, L., Handa, T., Le Squeren, A. M., Nakai, N., & Sofue, Y. 1988, A&A, 195, 71
Mazzarella, J. M., et al. 2012, AJ, 144, 125
Medling, A. M., et al. 2015, MNRAS, 448, 2301
Monaco, P. 2004, MNRAS, 352, 181
Monreal-Ibero, A., Arribas, S., & Colina, L. 2006, ApJ, 637, 138
Monreal-Ibero, A., Arribas, S., Colina, L., Rodríguez-Zaurín, J., Alonso-Herrero, A., & García-Marín, M. 2010, A&A, 517, A28+
Moustakas, J., & Kennicutt, Jr., R. C. 2006, ApJS, 164, 81
Murphy, Jr., T. W., Armus, L., Matthews, K., Soifer, B. T., Mazzarella, J. M., Shupe, D. L., Strauss, M. A., & Neugebauer, G. 1996, AJ, 111, 1025
Nardini, E., Risaliti, G., Salvati, M., Sani, E., Imanishi, M., Marconi, A., & Maiolino, R. 2008, MNRAS, 385, L130
Osterbrock, D. E. 1989, Astrophysics of gaseous nebulae and active galactic nuclei (University Science Books)
Pereira-Santaella, M., Diamond-Stanic, A. M., Alonso-Herrero, A., & Rieke, G. H. 2010, ApJ, 725, 2270
Pérez-Montero, E., & Contini, T. 2009, MNRAS, 398, 949
Peterson, B. W., et al. 2012, ApJ, 751, 11
Petric, A. O., et al. 2011, ApJ, 730, 28
Phillips, M. M., Charles, P. A., & Baldwin, J. A. 1983, ApJ, 266, 485
Poggianti, B. M., & Wu, H. 2000, ApJ, 529, 157
Ptak, A., Heckman, T., Levenson, N. A., Weaver, K., & Strickland, D. 2003, ApJ, 592, 782
Pych, W. 2004, PASP, 116, 148
Rich, J. A., Dopita, M. A., Kewley, L. J., & Rupke, D. S. N. 2010, ApJ, 721, 505
Rich, J. A., Kewley, L. J., & Dopita, M. A. 2011, ArXiv e-prints
—. 2014, ApJ, 781, L12
Rich, J. A., Torrey, P., Kewley, L. J., Dopita, M. A., & Rupke, D. S. N. 2012, ApJ, 753, 5
Rigopoulou, D., Spoon, H. W. W., Genzel, R., Lutz, D., Moorwood, A. F. M., & Tran, Q. D. 1999, AJ, 118, 2625
Rothberg, B., & Fischer, J. 2010, ApJ, 712, 318
Rupke, D. S., Veilleux, S., & Sanders, D. B. 2005a, ApJS, 160, 115
—. 2005b, ApJS, 160, 115
Rupke, D. S. N., Kewley, L. J., & Chien, L. 2010, ArXiv e-prints
Rush, B., Malkan, M. A., Fink, H. H., & Voges, W. 1996, ApJ, 471, 190
Sánchez, S. F., et al. 2012, A&A, 538, A8
Sanders, D. B., Mazzarella, J. M., Kim, D., Surace, J. A., & Soifer, B. T. 2003, AJ, 126, 1607
Sanders, D. B., Soifer, B. T., Elias, J. H., Madore, B. F., Matthews, K., Neugebauer, G., & Scoville, N. Z. 1988, ApJ, 325, 74
Sani, E., et al. 2008, ApJ, 675, 96
Sarzi, M., et al. 2010, MNRAS, 402, 2187
Scoville, N. Z., et al. 2000, AJ, 119, 991
Sharp, R. G., & Bland-Hawthorn, J. 2010, ApJ, 711, 818
Silk, J. 2001, MNRAS, 324, 313
Soto, K. T., Martin, C. L., Prescott, M. K. M., & Armus, L. 2012, ApJ, 757, 86
Spoon, H. W. W., et al. 2006, ApJ, 638, 759
Staveley-Smith, L., Norris, R. P., Chapman, J. M., Allen, D. A., Whiteoak, J. B., & Roy, A. L. 1992, MNRAS, 258, 725
Stierwalt, S., et al. 2013, ApJS, 206, 1
Sturm, E., Lutz, D., Tran, D., Feuchtgruber, H., Genzel, R., Kunze, D., Moorwood, A. F. M., & Thornley, M. D. 2000, A&A, 358, 481
Thompson, T. A., Quataert, E., & Murray, N. 2005, ApJ, 630, 167
U, V., et al. 2013, ApJ, 775, 115
Väisänen, P., Ryder, S., Mattila, S., & Kotilainen, J. 2008a, ApJ, 689, L37
Väisänen, P., et al. 2008b, MNRAS, 110
Veilleux, S., Kim, D., Sanders, D. B., Mazzarella, J. M., & Soifer, B. T. 1995, ApJS, 98, 171
Veilleux, S., & Osterbrock, D. E. 1987, ApJS, 63, 295
Veilleux, S., & Rupke, D. S. 2002, ApJ, 565, L63
Westmoquette, M. S., Clements, D. L., Bendo, G. J., & Khan, S. A. 2012, MNRAS, 424, 416

Westmoquette, M. S., Smith, L. J., & Gallagher, III, J. S. 2011, MNRAS, 414, 3719
Wild, V., Rosales-Ortega, F., Falcón-Barroso, J., et al. 2014, A&A, 567, A132
Wu, Y., Charmandaris, V., Huang, J., Spinoglio, L., & Tommasin, S. 2009, ApJ, 701, 658
Yuan, T., Kewley, L. J., & Sanders, D. B. 2010, ApJ, 709, 884
Zahid, H. J., Kewley, L. J., & Bresolin, F. 2011, ApJ, 730, 137

APPENDIX

A. NOTES ON INDIVIDUAL SYSTEMS AND MAPS

This appendix contains brief notes about each system from our sample and a reproduction of Figures 3 and 4 for every system in the WiFeS GOALS sample. This includes digitized sky survey (DSS) R-band or *HST* ACS I-band images matching the field of view of the WiFeS GOALS observations combined with emission line ratio maps, emission line ratio diagnostic diagrams, velocity dispersion distribution histograms, velocity dispersion v. emission line ratio diagrams and maps of the distribution of low, mid and high-σ velocity components. We also include a table detailing the observation program for the WiFeS GOALS sample, as well as DSS R-band finder images with individual WiFeS pointings overlaid. Some of the notes on individual systems are adapted from those already published in (Rich et al. 2012).

IRAS F01053-1746 (IC 1623) This system contains two very closely interacting spiral galaxies. It is kinematically very complex and exhibits evidence of widespread radiative shocks (Rich et al. 2011). The eastern system is very intensely star-forming as seen in the infrared (e.g. Howell et al. (2010)), but is so enshrouded in dust that our optical spectra do not trace any of the buried star-formation.

IRAS F02072-1025 (NGC 839) This system is described in great detail in Rich et al. (2010). It is a nearly edge-on starburst galaxy in a compact group (HCG 16). Our emission line maps trace the shocks associated with the starburst-driven outflow and we see evidence of a post-starburst E+A spectrum in portions of the galaxy.

IRAS F06076-2139 Arribas et al. (2008) describe this ULIRG in great detail in their IFS study of ULIRGs. They determined that the system consists of two galaxies that may never merge given their significantly different velocities, though they are interacting as evidenced by a ring of Hα emission (Elmegreen & Elmegreen 2006; Arribas et al. 2008). Our velocity dispersion and line ratio data imply the northern galaxy is dominated by star formation, with some amount of composite ratios and σ in the southern galaxy. The southern galaxy in this closely interacting pair has a fairly low 6.2μm PAH eqw, which also corresponds to enhanced [NII]/Hα in our maps.

IRAS 08355-4944 While *HST* I-band images show remnant tidal tails extending nearly 20 kpc, only the central 5 kpc or so appears to harbor the entirety of the intense ongoing star formation in this system. Our spectra are dominated by HII region emission, with evidence in some portions of the system of a blue-shifted component with low-velocity shock-dominated line ratios which could be associated with a galactic wind. This is in agreement with the IFS observations of Monreal-Ibero et al. (2010).

IRAS F10038-3338 (ESO 374-IG032) This post-merger exhibits significant ongoing star formation in its southwestern tidal arm unlike the two other coalesced systems in our sample. The total line emission in this region is much weaker than in the nucleus, inducing a large uncertainty in the extinction map and [OII] lines, creating the discrepant values seen in the metallicity gradients for this galaxy (Rich et al. 2012). This system hosts an OH megamaser and has soft x-ray emission, all consistent with the advanced stage of merging and increasingly intense nuclear starburst (Henkel & Wilson 1990; Staveley-Smith et al. 1992; Darling & Giovanelli 2002; Iwasawa et al. 2009). Our spectra also show evidence for extended off-nuclear shock emission dominating in areas where there is little to no evidence of ongoing star formation, consistent with the IFU observations of Monreal-Ibero et al. (2010).

IRAS F10257-4339 (NGC 3256) This advanced merger is the nearest galaxy in our sample (z$\sim$ 0.0094) and is well studied. As with IRAS F01053-1746, one of the galaxies in IRAS F10257-4339 is very extinguished. The second, buried system and its nucleus are revealed at longer wavelengths, south of the main optical nucleus (Alonso-Herrero et al. 2002; Rothberg & Fischer 2010). The gas and tidal tails in this system extend 10's of kpc from the nuclear regions (e.g. Rothberg & Fischer 2010). Our IFU mosaic covers only the central 6 kpc, though this appears to be the physical extent of most of the ongoing star formation in this system. NGC 3256 also shows evidence for widespread shocks in our data and is discussed alongside IC 1623 in Rich et al. (2011).

IRAS F12043-3140 (ESO 440-IG058) This pair of closely interacting galaxies is poorly studied and there exists no higher spatial resolution imagery to examine. The DSS image, though, shows tidal features indicative of the ongoing interaction. Our IFS data indicate a combination of ongoing star formation and shocked gas, seen in the diagnostic diagrams as HII-region + composite spaxels and with a tail out to σ $\sim$200 km s^{-1}in the velocity dispersion distribution. Our map shows the enhanced ratios seem to form a cone extending to the north and south of the southern galaxy, and agrees with the IFU observation of (Monreal-Ibero et al. 2010). The overlap in the two galaxies and the lower S/N of our data make it difficult to discern if this is indeed associated with an outflow from the southern galaxy.

IRAS F12592+0436 (CGCG 043-099) This late-stage merger is very dusty and subsequently the blue data are mostly too low S/N to measure any emission in single spaxels. The red data indicate low line ratio and σ gas in a tidal tail indicative of star formation and higher line ratio and σ data toward the nucleus. Our nuclear spectrum indicates composite behavior dominated by shocks. Poggianti & Wu (2000) found balmer emission and absorption indicative of star formation, with no indication of Seyfert behavior. X-ray and IR data indicate a galaxy with ongoing star formation and no indication of an AGN, consistent with our results (Rush et al. 1996; Petric et al. 2011; Stierwalt et al. 2013).

IRAS 13120-5453 This nearby ULIRG is dominated by AGN emission at all wavelengths. X-ray data indicate an AGN signature Iwasawa et al. (2009, 2011) and mid-IR PAH values and [Ne V] are consistent with a galaxy dominated by an AGN (Farrah et al. 2007; Pereira-Santaella et al. 2010; Petric et al. 2011). Our optical IFS data are quite consistent with this picture: the strongest emission we detect is dominated by Seyfert-like ratios in the diagnostic diagrams, and the velocity dispersion distribution shows a contribution a high-σ component in the nuclear regions of 300-400 km s^{-1}in addition to the lower $\sim$100 km s^{-1}component.

IRAS F13373+0105 W (NGC 5257) Although NGC 5257 and its equal mass partner NGC 5258 are still widely separated and retain much of their structure, they exhibit interaction features including tidal tails and a bridge between the two galaxies. The spiral arms show regions of strong star formation with some signatures of post-starburst populations away from the nucleus. The nuclear regions of NGC 5257 are dominated by an older stellar population as the intense nuclear starburst associated with the later stages of major mergers has not yet begun. The extinction is higher in the nuclear regions and the measurable line-ratios place the nucleus in the composite region of the standard diagnostic diagrams, indicating possible LINER activity-previous nuclear observations and integrated spectrophotometry are consistent with the higher nuclear extinction and overall line ratios we observe (Veilleux et al. 1995; Kewley et al. 2001b; Moustakas & Kennicutt 2006).

IRAS F13373+0105 E (NGC 5258) NGC 5258 is a near-twin to NGC 5257 in mass and luminosity. Our spectra indicate higher extinction and a flatter gradient, though the extent of measurable HII-region metallicities is smaller than in NGC 5257. Again similar to NGC 5257 the nuclear region of NGC 5258 is dominated by older stars and very little line-emission and there is some evidence of younger post-starburst populations away from the nucleus. The strongest line emission is associated with the knot of star formation to the southwest of the nuclear region.

IRAS F15107+0724 (CGCG 049-057) This galaxy bears a low-luminosity OH megamaser (Martin et al. 1988), and was classified as an HII-region galaxy by (Kim et al. 1995; Veilleux et al. 1995). Our IFS data are dominated primarily by an older stellar population in the blue, with the emission lines primarily indicative of ongoing star formation plus some composite contribution, likely shocks given the velocity dispersion distribution and relatively high 6.2μm PAH eqw value of 0.51μm (Stierwalt et al. 2013). An *HST* NICMOS H-band image is the highest resolution data available, showing what appears to be a relatively undisturbed spiral disc (Haan et al. 2011). This is in keeping with it's status as a isolated galaxy (Yuan et al. 2010).

IRAS F16164-0746 This coalesced merger is AGN dominated in the X-ray and mid-IR (Iwasawa et al. 2009, 2011; Petric et al. 2011). Our optical spectra show rotation and a narrow and a broad component, consistent with star formation and shocks, though our line ratio map shows a composite spectrum. Our data do not have sufficient S/N to detect [OIII]/Hβ where the other line ratios increase towards the nucleus, where more LINER-like ratios dominate (Veilleux et al. 1995). Our nuclear spectrum is somewhat ambiguous, indicating composite, SB and Seyfert-like spectra with [OIII]/Hβ near unity.

IRAS F16399-0937 This close-merger pair shows HII-region+composite emission and a velocity dispersion distribution dominated by star formation. The emission line ratio map indicates a ring of star forming gas surrounding the northern nucleus. The northern nucleus has much stronger emission line ratios, though very few spaxels are detected in both [OIII]and Hβ . The composite nuclear spectrum of the northern nucleus has [OIII]/Hβ near unity, indicating LINER-like emission. This may be associated with shocks, possibly caused by an outflow. There is some indication of broad blue wings in the Na D profile possibly associated with such an outflow (e.g. Rupke et al. 2005a), though no fit was performed.

IRAS F16443-2915 N&S (ESO 453-G005) This widely separated pair of galaxies appear to be completely dominated by star formation. The emission line ratio maps are dominated by HII emission and the velocity dispersions in both systems are primarily a few tens of km s^{-1}. The southern galaxy does show a larger turbulent component approaching σ $\sim$100 km s^{-1}, but neither indicates any shock component. These galaxies show no apparent signs of interaction, though the available imaging data are low resolution.

IRAS F17138-1017 Our observations of this coalesced merger are consistent with the IFS observations of Monreal-Ibero et al. (2010). The central regions of the galaxy are dominated by star formation, with an underlying shock-like velocity dispersion component. In the outer portions of the galaxy, our line ratios are also consistent with a dominant contribution from shocks both in line ratio and velocity dispersion. There is no indication of any AGN activity at any wavelength, with a very high 6.2μm PAH eqw of 0.68μm (Stierwalt et al. 2013).

IRAS F17207-0014 This ULIRG is the second brightest in the GOALS sample, behind only MRK 231. Despite its high L$_{IR}$, the X-ray data from Chandra and XMM are apparently dominated by the starburst (Franceschini et al. 2003; Iwasawa et al. 2011). The 6.2μm PAH eqw is low (0.3μm), though there is no detected [Ne V] emission (Petric et al. 2011; Stierwalt et al. 2013). Arribas & Colina (2003) carried out early IFS observations of this system and suggest that this ULIRG is not evolving into a QSO. Our data show composite-like line ratios,though the overall velocity dispersion distribution is quite high, with σ exceeding 100 km s^{-1}in nearly all measurable spaxels. Rupke et al. (2005a,b) detect blue shifted Na D absorption consistent with a galactic wind, which we also see in our data. In a recent study, Medling et al. (2015) analyzed the nuclear region in great detail with AO-aided near-IR IFU data which also shows evidence of outflow-driven shocks. Taken all together, the data indicate an intense starburst with a galactic wind driving low velocity shocks.

IRAS F17222-5953 (ESO 138-G027).—This system is more akin to a typical, non-interacting, strongly starbursting spiral galaxy in our sample. It is in the vicinity of a few other galaxies, including the similarly bright ESO 138-G026, but even the

nearest galaxy is at a projected distance of over 100 kpc and IRAS F17222-5953 is not yet interacting with any of these systems. Our IFU data applied to the [NII]/Hα v [OIII]/Hβ BPT diagram show a clean curve following the shape of the SDSS sequence of local star forming galaxies (e.g. Kewley et al. (2006)), but with a slight apparent shift in total [NII]/Hα . We interpret this shift as an overall nitrogen enhancement (Pérez-Montero & Contini 2009).

IRAS 17578-0400 There is very little information available about this system in the literature. Our data are very low S/N in the blue, though the binned nuclear spectrum is indicative of pure star formation. This is consistent with the [NII] and [SII]/Hα line ratios and the velocity dispersion distribution, which shows little to no indication of any appreciable non-HII region component and a rotation-dominated velocity field.

IRAS F18093-5744 N (IC 4687) We classify this galaxy as a close merger; in fact it is a member of a triplet. IC 4687 is undergoing a close merger with the less massive starburst IC 4686, classed as a Wolf-Rayet galaxy by Kovo & Contini (1999); Fernandes et al. (2004). IC 4687 itself is a is also in a wide merger with the equally massive spiral IC 4689. The archived *hst* images of IC 4687 show a complex morphology tangled up with IC 4686: gas and dust from IC 4687 appear to be obscuring the less massive system. Our IFU data cover the entirety of IC 4686/4687 and the metallicities we measure are consistent with the expected metallicties in the outskirts of IC 4687 as extrapolated from the gradient we present in this paper as well as a low-metallicity, flattened gradient in IC 4686. The kinematic information from our data also indicates that we are indeed seeing gas from both systems.

IRAS F18093-5744 S (IC 4689) This spiral galaxy is slightly less massive and luminous than IC 4687 and less well-observed, though it is still intensely star forming (Howell et al. 2010). It is less morphologically disturbed than the other two interacting galaxies IC 4686/4687, though its gradient is quite flattened already according to our observations (Rich et al. 2012). Although it is widely separated from IC 4687, we include it as part of the closely interacting system of IRAS F18093-5744.

IRAS F18093-5744 C (IC 4686) IC 4686 is a compact strongly star-bursting galaxy with Wolf-Rayet features in its spectrum (Kovo & Contini 1999; Fernandes et al. 2004). As noted in Rich et al. (2012), this galaxy shows a strong moderate σ component with lower line ratios. This may be due to the very compact nature, causing an overlap in the kinematics that may require a higher-component line fit or higher resolution spectroscopy than have been considered in this thesis.

IRAS F18293-3413 The IR-bright source in this galaxy is the northern, highly extinguished galaxy. K-band data from NIRC and *HST* NICMOS show very buried spiral structure (Väisänen et al. 2008a; Haan et al. 2011). The southern galaxy appears elliptical, with our IFS spectra having no detectable emission line gas and a continuum indicative of an old stellar population. The northern galaxy is dominated by star formation with some contribution from shocks in the outskirts of the galaxy. The study of Chandra observations by Iwasawa et al. (2009, 2011) shows resolved soft X-ray emission possibly associated with an outflow, but with no indication of an AGN.

IRAS F18341-5732 (IC 4734) Like IRAS F17222-5953, this isolated galaxy is in the vicinity of a few other luminous galaxies, but is not yet undergoing any interactions. Our nuclear spectra are dominated by a LINER combined with an aging stellar population. The strongest sites of star formation are where the bar in this galaxy meet the spiral arms, evidenced by the two strong clumps of HII-region like spaxels seen in the line-ratio and metallicity. Hα imaging by Dopita et al. (2002) shows further knots of star formation along the spiral arms and our nuclear spectra also show signs of an aging stellar population in the nucleus of IC 4734.

IRAS F19115-2124 (ESO 593-IG 008) Väisänen et al. (2008b) analyze the morphology of this close pair in detail using Adaptive Optics K-band images and suggest the possibility of a triple-galaxy interaction. Kinematic modelling can be satisfied by an interacting pair, however, and indicates that though this system is classified as a 'close pair', it is actually just entering first pericenter (Josh Barnes, private communication). The metallicity gradient in this system, however, has already flattened considerably (Rich et al. 2012).

IRAS F20551-4250 (ESO 286-IG019) This late stage merger shows ambiguous AGN signatures. The Chandra X-ray data show extended soft emission inconsistent with AGN (Ptak et al. 2003; Grimes et al. 2005; Iwasawa et al. 2009, 2011), but (Franceschini et al. 2003) classify the galaxy as an AGN based on the XMM data. There is no [Ne V] detection in the mid-IR, though the 6.2 μm PAH eqw is very low (0.1μm) more consistent with AGN emission (Petric et al. 2011; Stierwalt et al. 2013). Imanishi et al. (2010); Sani et al. (2008); Nardini et al. (2008) also claim signs of a heavily obscured AGN with IR data. Our IFS data are dominated by a post-starburst spectrum and composite LINER emission, with the emission line velocity dispersion distribution centered around 100 km s^{-1}and trailing to 300 km s^{-1}. The emission line maps show the lowest emission line ratios near the nucleus with increasing ratios further away, more consistent with shock excitation in the optical rather than a low-luminosity AGN. The Na D absorption line profile in this galaxy also appears to have broad blue wings consistent with an outflow (e.g. Rupke et al. 2005a), though no fit to the complex was performed. Our observations are in agreement with previous optical spectra of the nucleus, classified as HII-dominated (Veilleux et al. 1995; Kewley et al. 2001b), coupled with extended shock excitation.

IRAS F21330-3846 (ESO 343-IG013) This closely interacting pair shows tidal tails in the available DSS image. Our IFS data show both discs are dominated primarily by HII emission. The line ratio diagnostic diagrams show a composite component, which corresponds primarily to the outskirts of the outskirts of the northern galaxy. The ionized emission between the two

systems is also higher line ratio and velocity dispersion than the discs, consistent with shock excitation possibly caused directly by the interaction, as seen in systems like Stephan's Quintet and the Taffy Galaxies (Cluver et al. 2010; Guillard et al. 2010; Peterson et al. 2012) as opposed to outflow-driven shocks.

IRAS F21453-3511 (NGC 7130) NGC 7130 is an isolated face-on spiral galaxy with a previously observed Seyfert 2 nucleus (Phillips et al. 1983). The AGN dominates the mid-IR spectra in the nucleus and is detected in x-ray as well (Petric et al. 2011; Iwasawa et al. 2011). Because of it is nearby and nearly uninclined, our IFS spectroscopy resolve well the AGN and starburst component in this galaxy showing spiral arms dominated by star formation and a strong Seyfert component in the nucleus. The distribution of spaxels in the diagnostic diagram and the line ratio maps show this well, and agree with Monreal-Ibero et al. (2010) who also observed this system. Na D absorption shows a blue-shifted component which may be due to an AGN-driven outflow. Further analysis of the WiFeS data for NGC 7130 is presented in Leslie et al. (2014).

IRAS F22467-4906 (ESO 239-IG002) The nuclear regions of this compact late-stage merger have very high [NII]/Hα and [SII]/Hα line ratios, with moderate [OIII]/Hβ ratios indicating composite/LINER behavior. The nucleus also shows a post-starburst spectrum in the blue, with older stellar features in the tidal debris to the southeast of the nucleus. There is some detection of low-level HII-region like emission in the tidal arm to the SE as well, likely similar to the star formation in IRAS F10038-3338, likely related to the shock-induced star formation in NGC 7252 described by Chien & Barnes (2010). The Chandra data show a point-like source detected in the hard band, while the soft X-rays extend to the N and S and the overall hardness of the X-ray data are not consistent with an AGN (Iwasawa et al. 2011). There is a very broad blue shifted Na D absorption feature indicating an outflow which may be driving shocks in the is galaxy. The velocity dispersion distribution seems consistent with low velocity shocks with some high-velocity components, but the limited spatial resolution of our data in this system make this more difficult to discern.

IRAS F23128-5919 (ESO 148-IG002) The nuclei in this closely interacting ULIRG are separated by a projected distance of about 4 kpc and show distinctly different properties in our spectra. The northern nucleus has line ratio and velocity dispersion values consistent with star formation. The southern nucleus is about three times brighter in at 24μm and hosts an X-ray and IR detected AGN (Franceschini et al. 2003; Petric et al. 2011; Iwasawa et al. 2011), which are mirrored in the enhanced composite/Seyfert line ratios and broadened velocity dispersions seen in our IFS diagnostic diagrams and emission line maps. The emission line components associated with the composite/Seyfert emission show broad velocity dispersions of 200-400 km s^{-1}, though there is still a significant contribution below 100 km s^{-1}, likely due to the ongoing star formation in both nuclei. The broad component shows signs of rotation while the underlying narrow component seems to show none, indicating most of the narrow emission may be coming from the non-AGN galaxy. We do not detect a blue-shifted component in fits to the Na D component. Further analysis of the WiFeS data for ESO 148-IG002 is presented in Leslie et al. (2014).

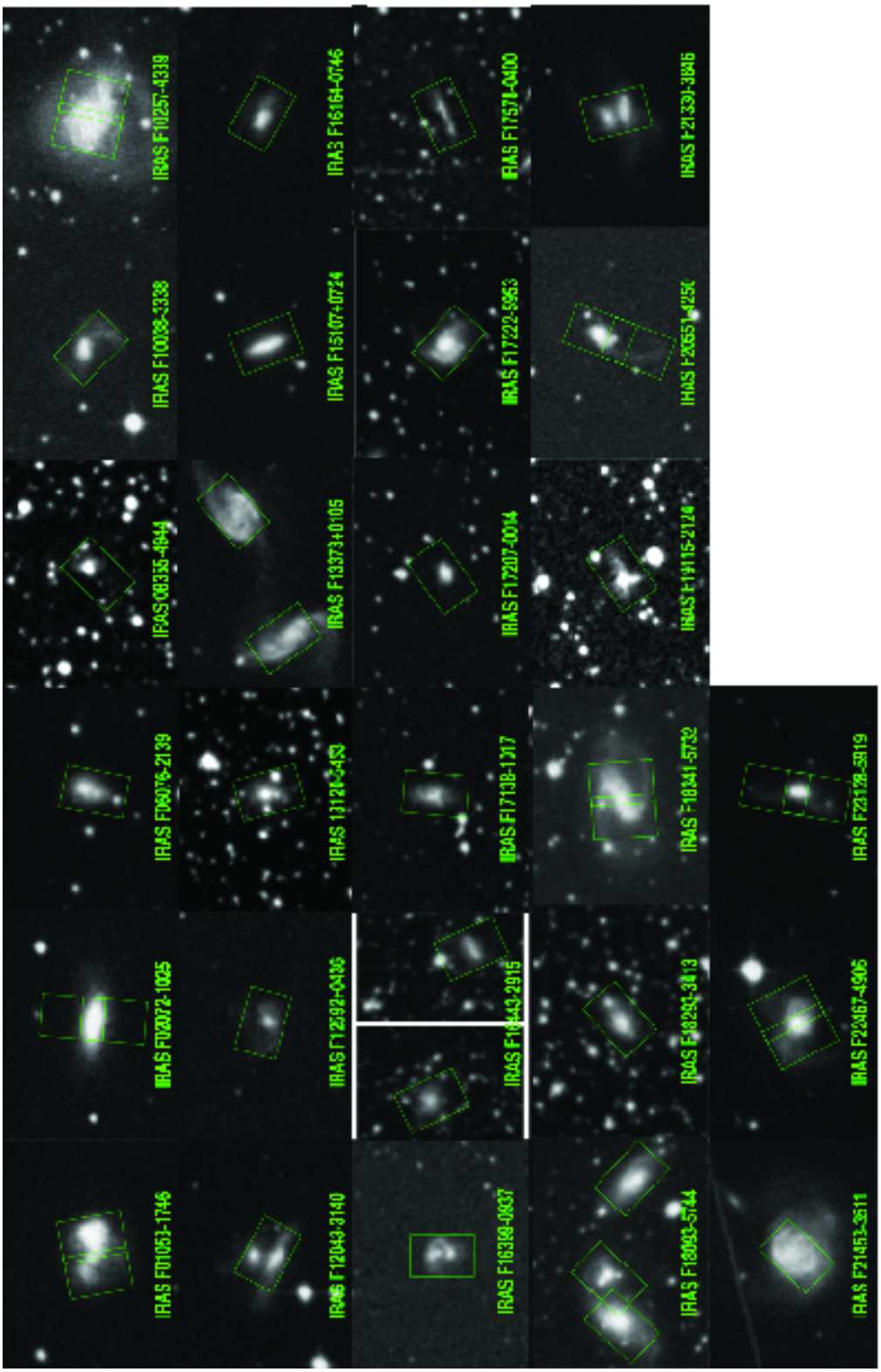

Figure A0. : DSS R-band images with individual WiFeS pointings overlaid in green. Coordinates for the pointings are given in Table A.1

Table A1
WiFeS Observations

IRAS Name (a)	Optical ID (b)	Observation Date (c)	Pointing center (J2000) (d)		PA° (e)	Exp. (f)
F19115-2124	ESO 593-IG008	2009 Jul 26	19h14m30.8s	−21d19m05s	305	120m
F16443-2915	ESO 453-G005	2009 Jul 28	16h47m31.1s	−29d21m22s	115	67m
		2009 Jul 28	16h47m29.5s	−29d19m07s	115	67m
F23128-5919	ESO 148-IG002	2009 Jul 28	23h15m47.1s	−59d03m25s	173	67m
		2009 Aug 14, 15	23h15m46.7s	−59d03m00s	173	59m
F18293-3413	-	2009 Aug 14	18h32m41.1s	−34d11m26s	130	84m
F20551-4250	ESO 286-IG019	2009 Aug 15	20h58m26.7s	−42d39m00s	160	100m
		2009 Aug 15	20h58m27.5s	−42d39m23s	160	100m
F18341-5732	IC 4734	2009 Aug 18	18h38m24.5s	−57d29m27s	10	60m
		2009 Aug 18	18h38m27.0s	−57d29m28s	10	60m
F22467-4906	ESO 239-IG002	2009 Aug 18	22h49m40.6s	−48d51m00s	30	40m
		2009 Aug 18	22h39m39.0s	−48d50m51s	30	40m
F02072-1025	NGC 839	2009 Aug 18	02h09m42.6s	−10d10m49s	350	40m
		2009 Aug 18	02h09m42.8s	−10d11m13s	350	40m
F21330-3846	ESO 343-IG013	2009 Aug 20	21h36m10.7s	−38d32m38s	15	80m
F01053-1746	IC 1623	2009 Aug 20	01h07m46.8s	−17d30m25s	10	40m
		2009 Aug 20	01h07m48.3s	−17d30m29s	10	40m
F21453-3511	NGC 7130	2009 Sep 18	21h48m19.6s	−34d57m08s	130	60m
F06076-2139	-	2010 Mar 12, 13	06h09m45.9s	−21d40m30s	170	60m
08355-4944	-	2010 Mar 14, 15	08h37m02.2s	−49d54m36s	135	80m
13120-5453	-	2010 Mar 14, 16	13h15m06.3s	−55d09m26s	15	95m
F10257-4339	NGC 3256	2010 Mar 15	10h27m51.9s	−43d54m10s	165	60m
		2010 Mar 15	10h27m50.1s	−43d54m15s	165	60m
F13373+0105	Arp 240	2010 Mar 15, 16	13h39m52.8s	+00d50m26s	35	60m
		2010 May 7	13h39m57.8s	+00d49m56s	130	50m
F10038-3338	ESO 374-IG032	2010 Mar 16	10h06m04.5s	−33d53m10s	45	60m
F12592+0436	CGCG 043-099	2010 Mar 16	13h01m50.3s	+04d20m04s	75	40m
F12043-3140	ESO 440-IG058	2010 May 7, 8	12h06m51.7s	−31d56m55s	60	100m
F16164-0746	-	2010 May 7	16h19m11.6s	−07d54m03s	60	75m
F18093-5744	IC 4687	2010 May 7, 13	18h13m40.1s	−57d43m28s	50	116m
		2010 May 9	18h13m40.2s	−57d44m56s	140	109m
		2010 May 8, 9, 15	18h13m38.9s	−57d43m56s	50	60m
F16399-0937	-	2010 May 10	16h42m40.3s	−09d43m15s	0	90m
F17138-1017	-	2010 May 12, 17	17h16m35.8s	−10d20m40s	175	175m
F15107+0724	CGCG 049-057	2010 May 12, 13	15h13m13.0s	+07d13m31s	20	75m
17578-0400	-	2010 May 13	18h00m32.1s	−04d00m55s	115	75m
F17222-5953	ESO 138-G027	2010 May 14	17h26m43.2s	−59d55m57s	45	75m
F17207-0014	-	2010 May 15	17h23m22.1s	+00d16m59s	315	75m

(a) IRAS identifier from Sanders et al. (2003); Armus et al. (2009) (b) Optical counterpart from Armus et al. (2009) (c) Observation Dates (d) center of pointing (e) Position Angle, degrees E of N (f) Total pointing exposure time in minutes

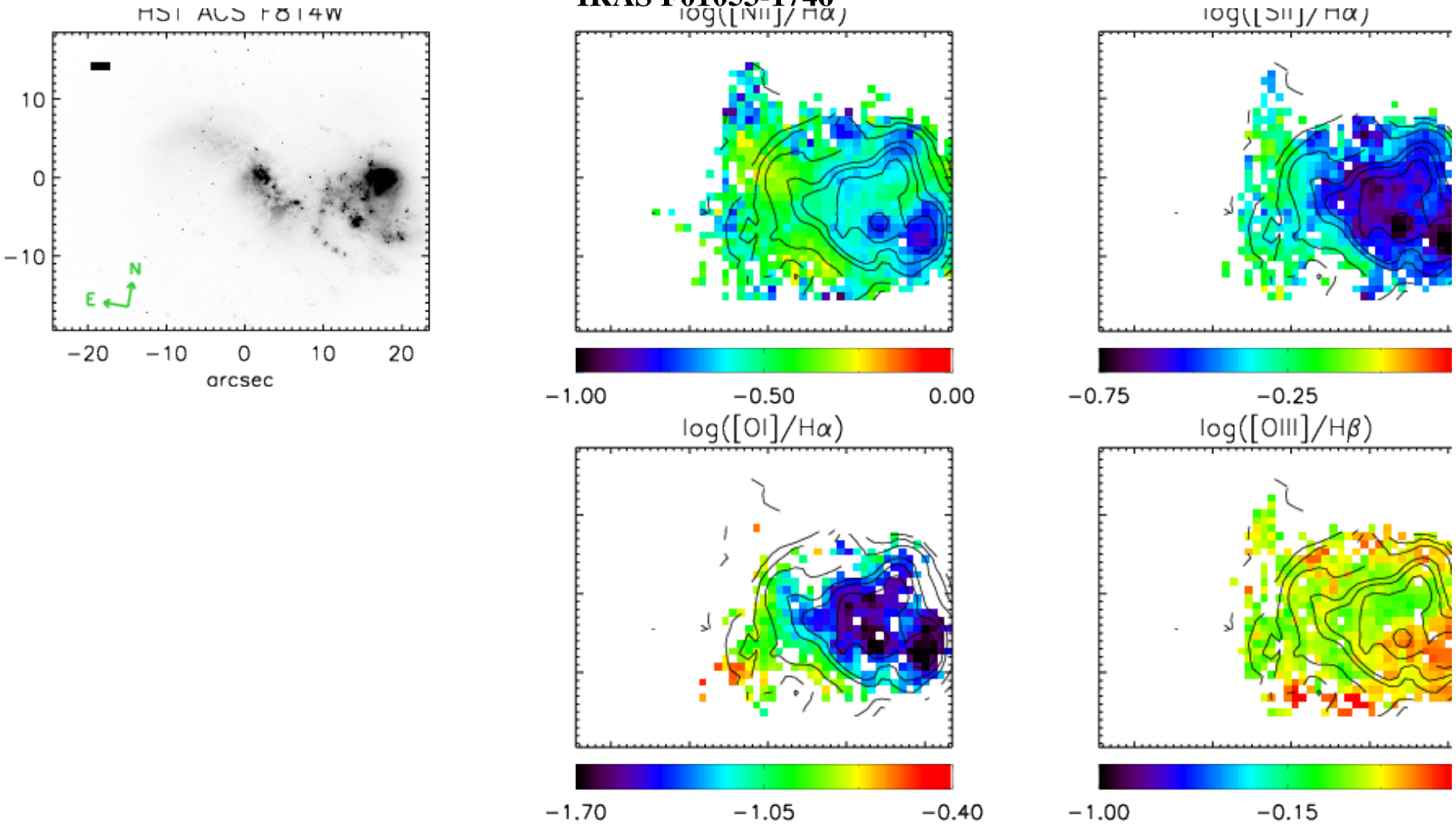
IRAS F01053-1746
HST ACS F814W
10
0
−10
N
E
−20
−10
0
10
20
arcsec
log([NII]/Hα)
−1.00
−0.50
0.00
log([SII]/Hα)
−0.75
−0.25
log([OI]/Hα)
−1.70
−1.05
−0.40
log([OIII]/Hβ)
−1.00
−0.15

Figure A1. :

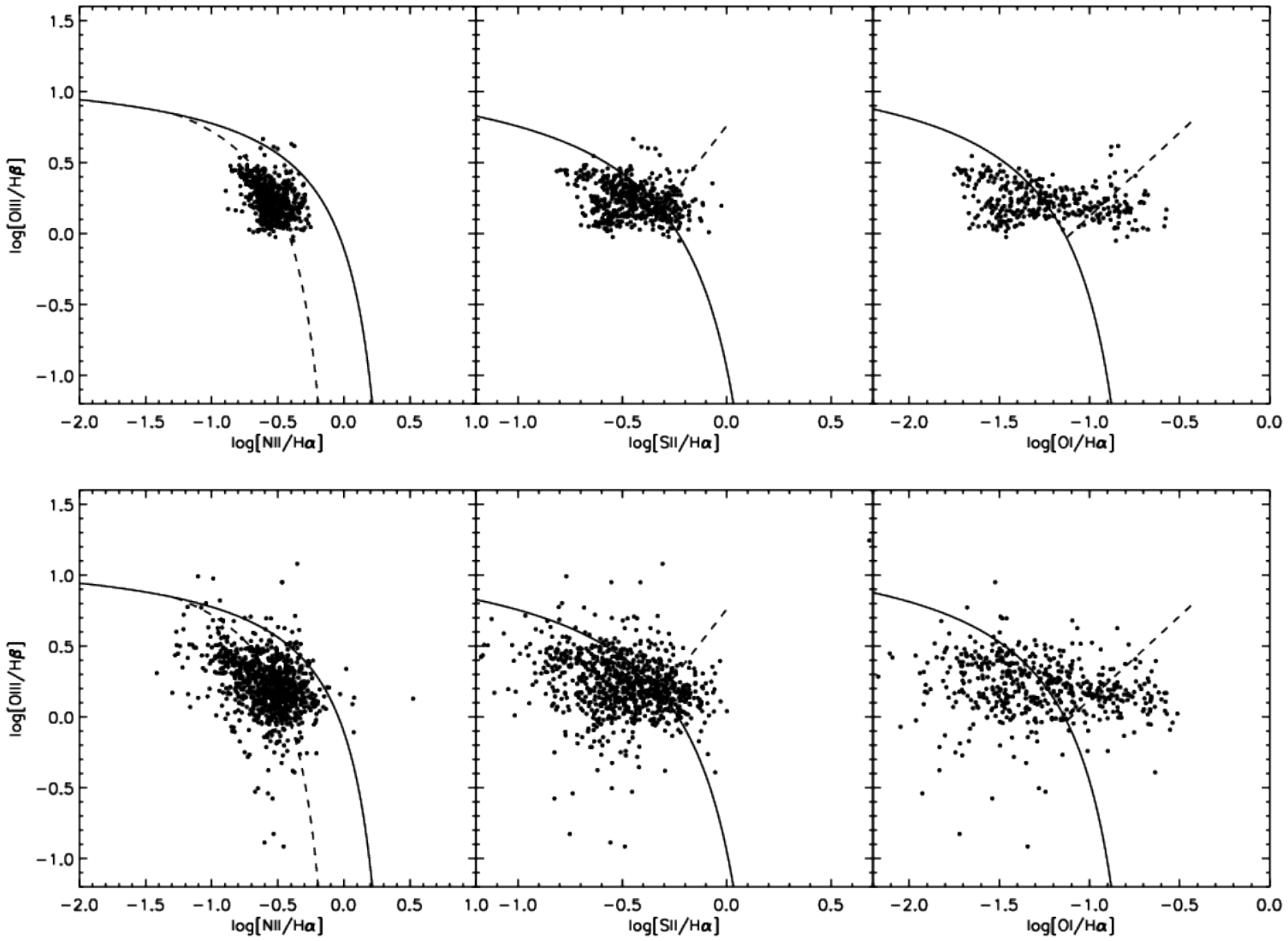

Figure A1. : The top left panel shows an *HST* I-band image of IRAS F01053-1746 aligned with the total WiFeS field of view with a 1-kpc bar. The top four panels to the right show emission line ratio maps for [NII]/Hα, [SII]/Hα, [OI]/Hα and [OIII]/Hβ with Hα contours measured from our data overlaid. The six bottom panels are standard diagnostic diagrams (Kewley et al. 2006). Points in the top three correspond to the total flux ratios in a single spaxel. Points in the bottom three correspond to line ratios from the individual components above S/N of 3 in each line. The same diagrams for the remaining portion of the sample are in Appendix 1.

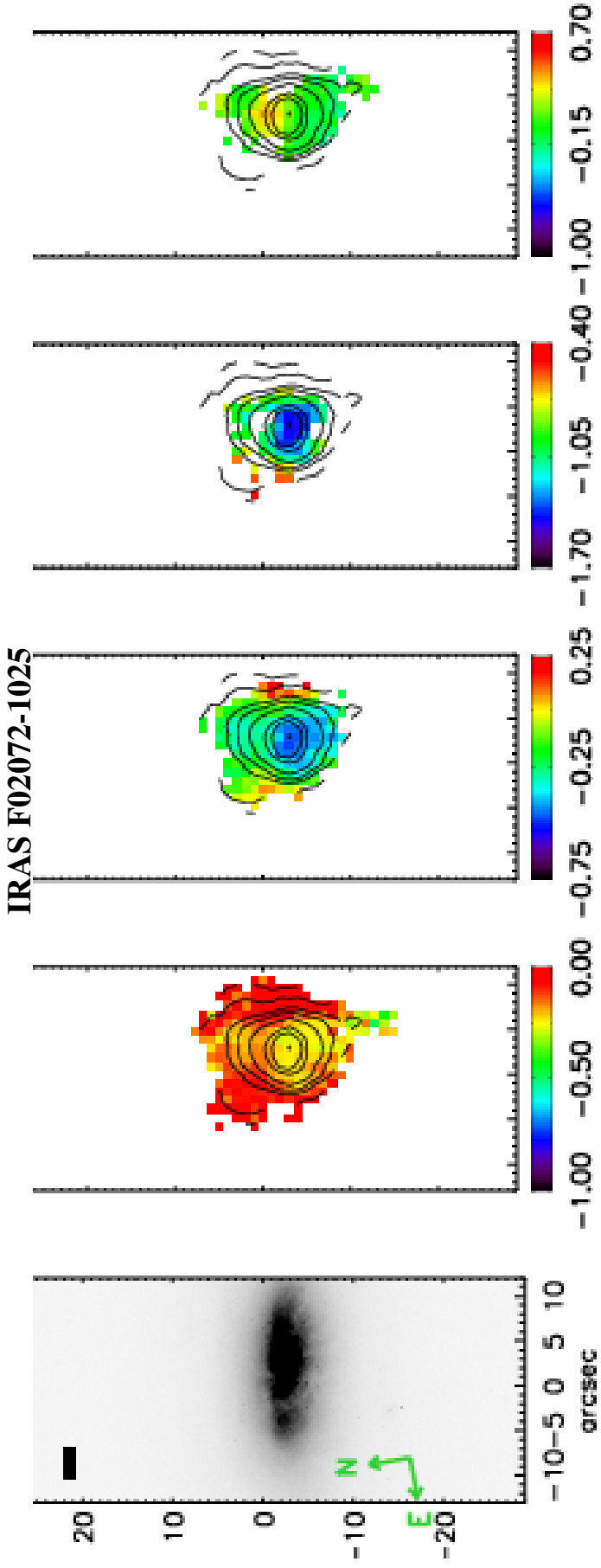
IRAS F02072-1025
−1.00 −0.50 0.00
−1.00 −0.75 −0.25 0.25
−1.70 −1.05 −0.40
−1.00 −0.15 0.70
−10 −5 0 5 10
arcsec
20
10
0
−10
−20
N
E

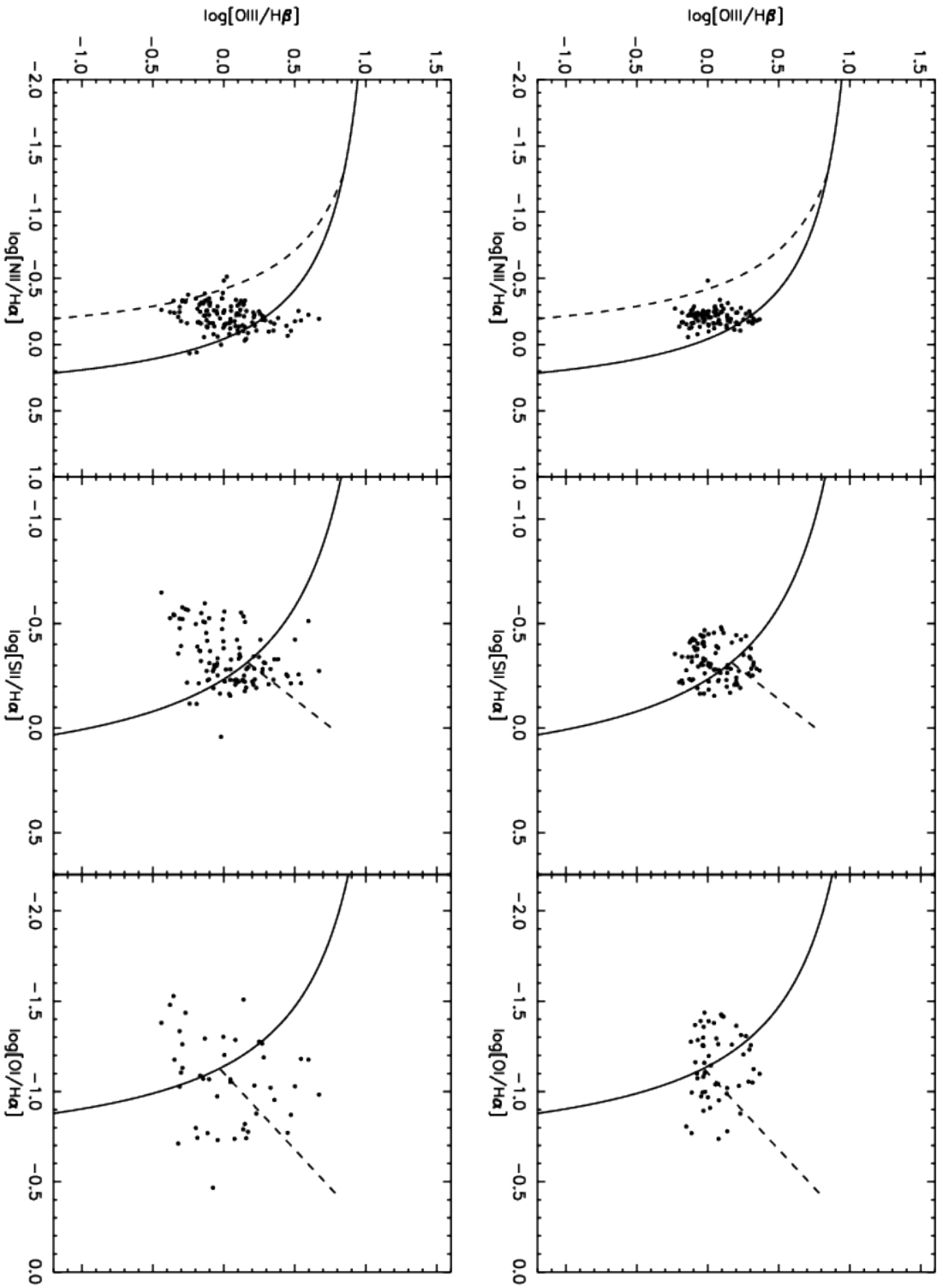

Figure A1. : Same as figure A1, but for IRAS F02072-1025.

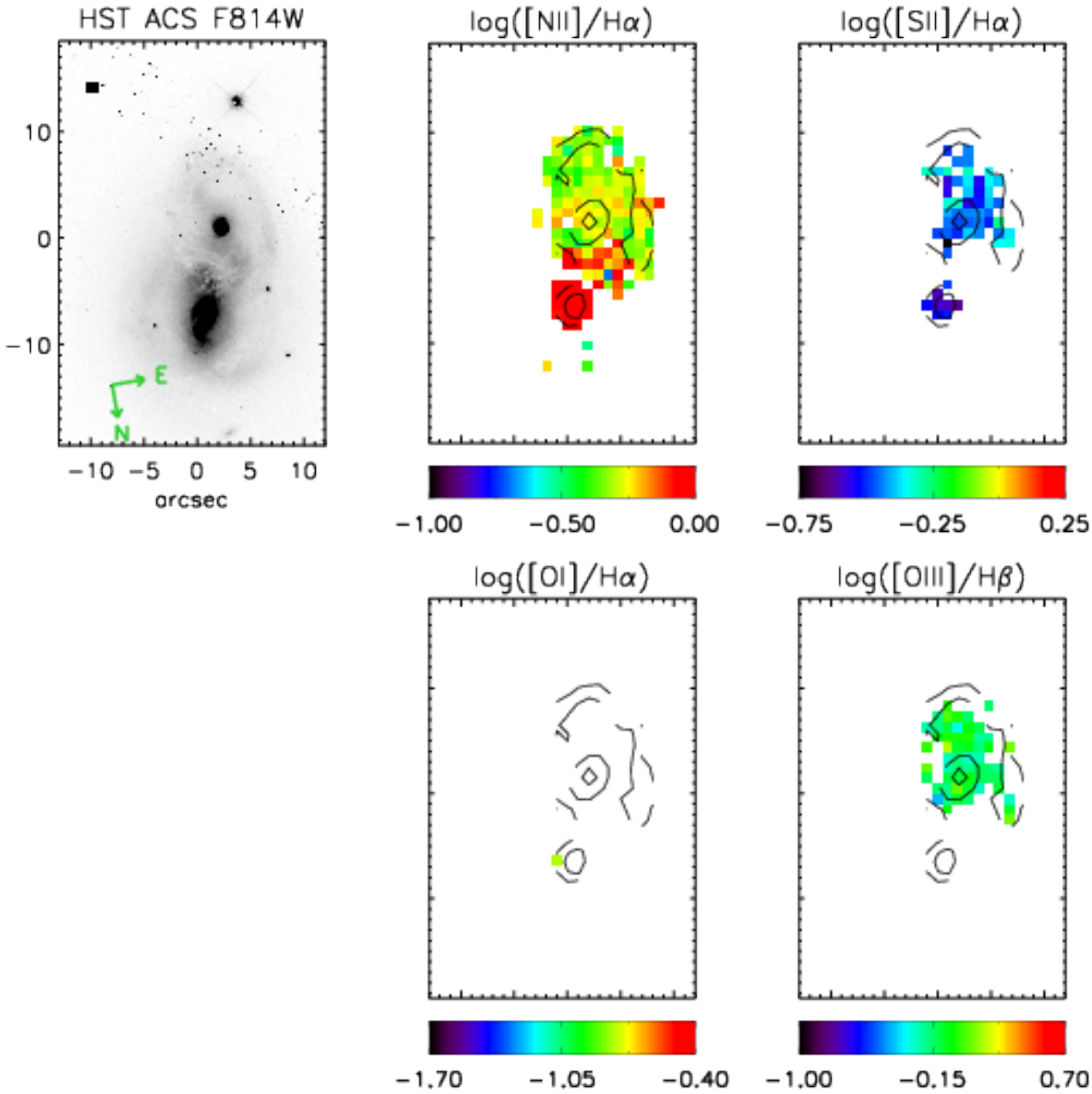

IRAS F06076-2139

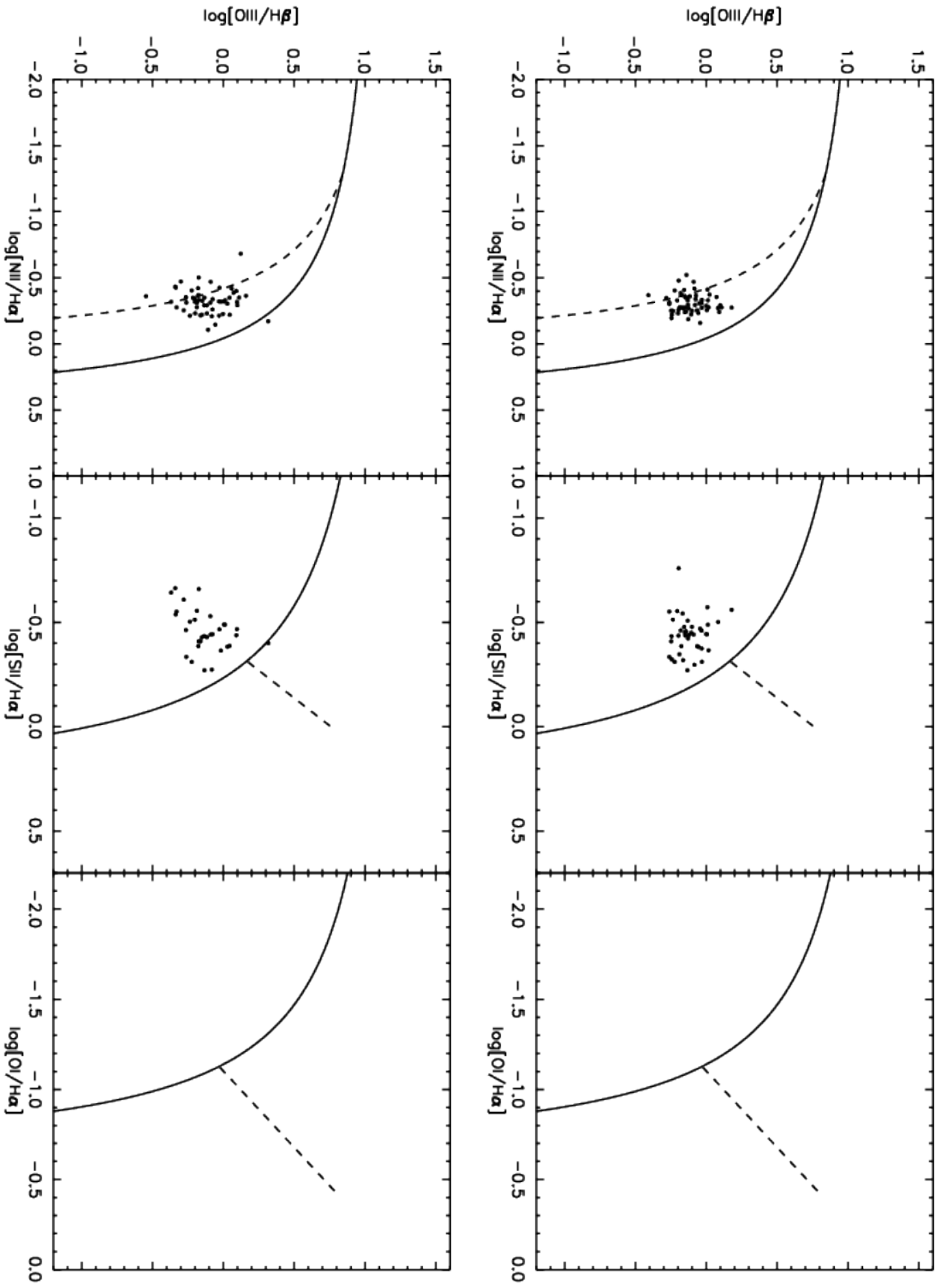

Figure A1. : Same as figure A1, but for IRAS F06076-2139.

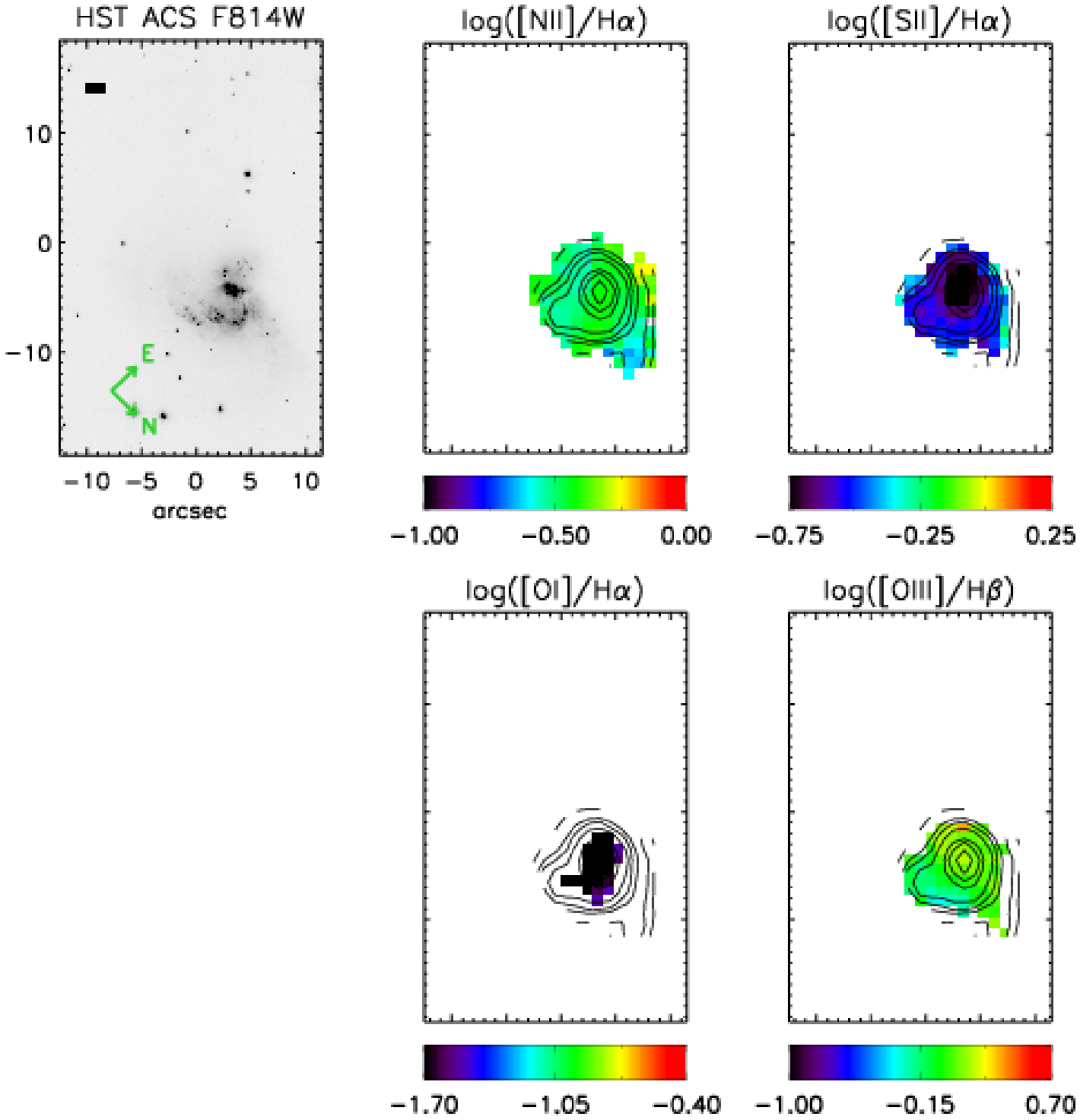

IRAS F08355-4944

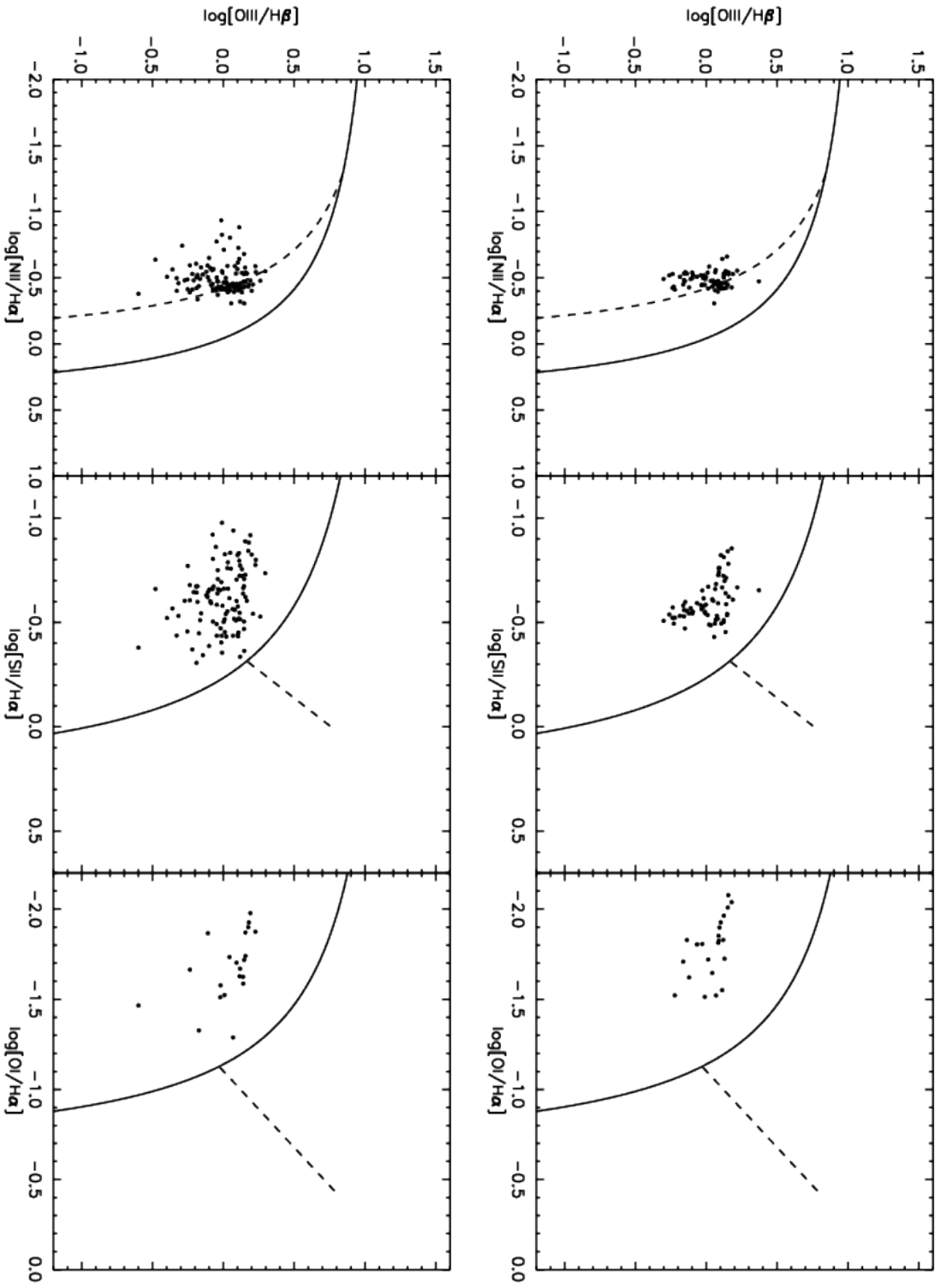

Figure A1. : Same as figure A1, but for IRAS 08355-4944.

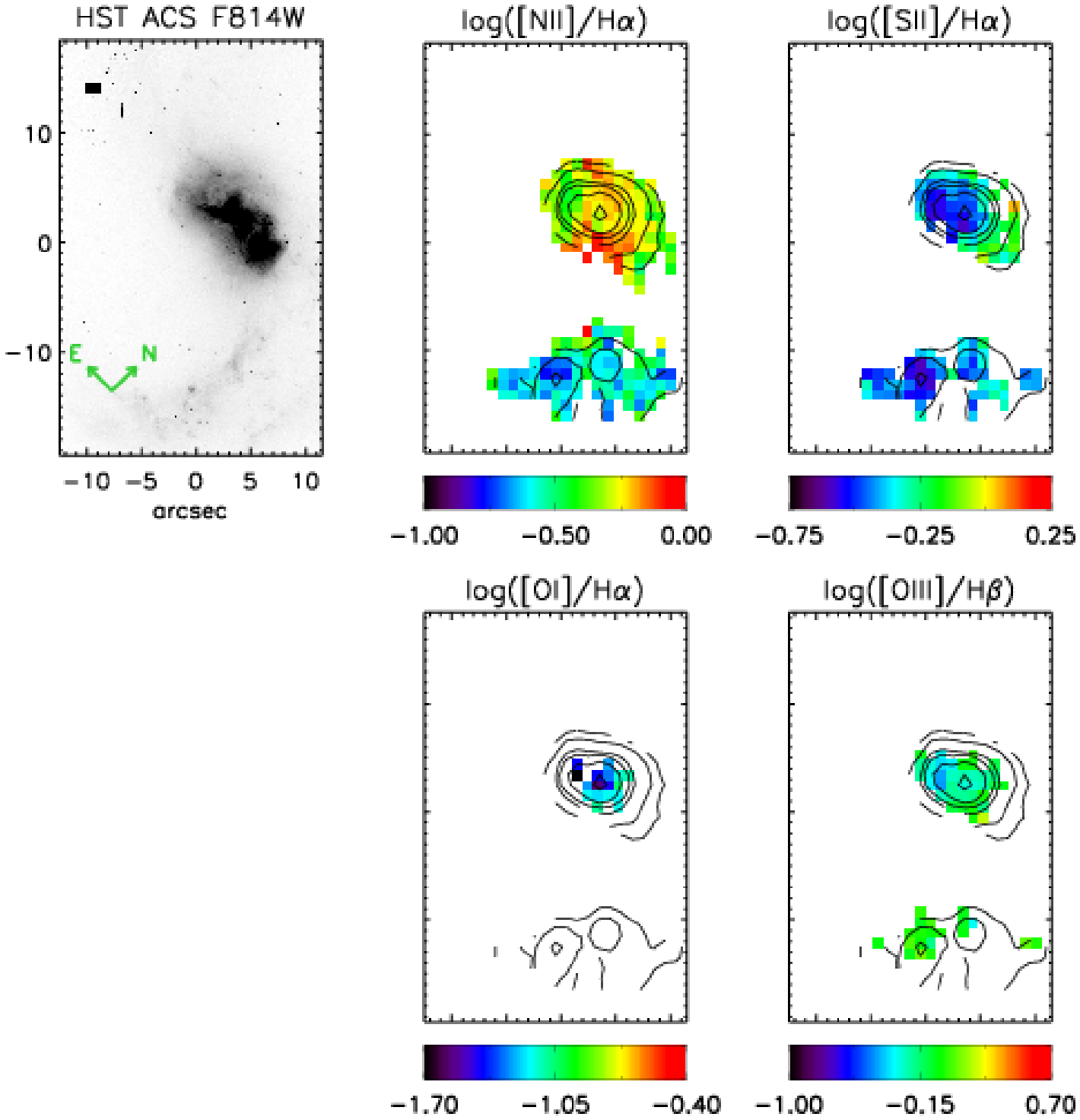

IRAS F10038-3338

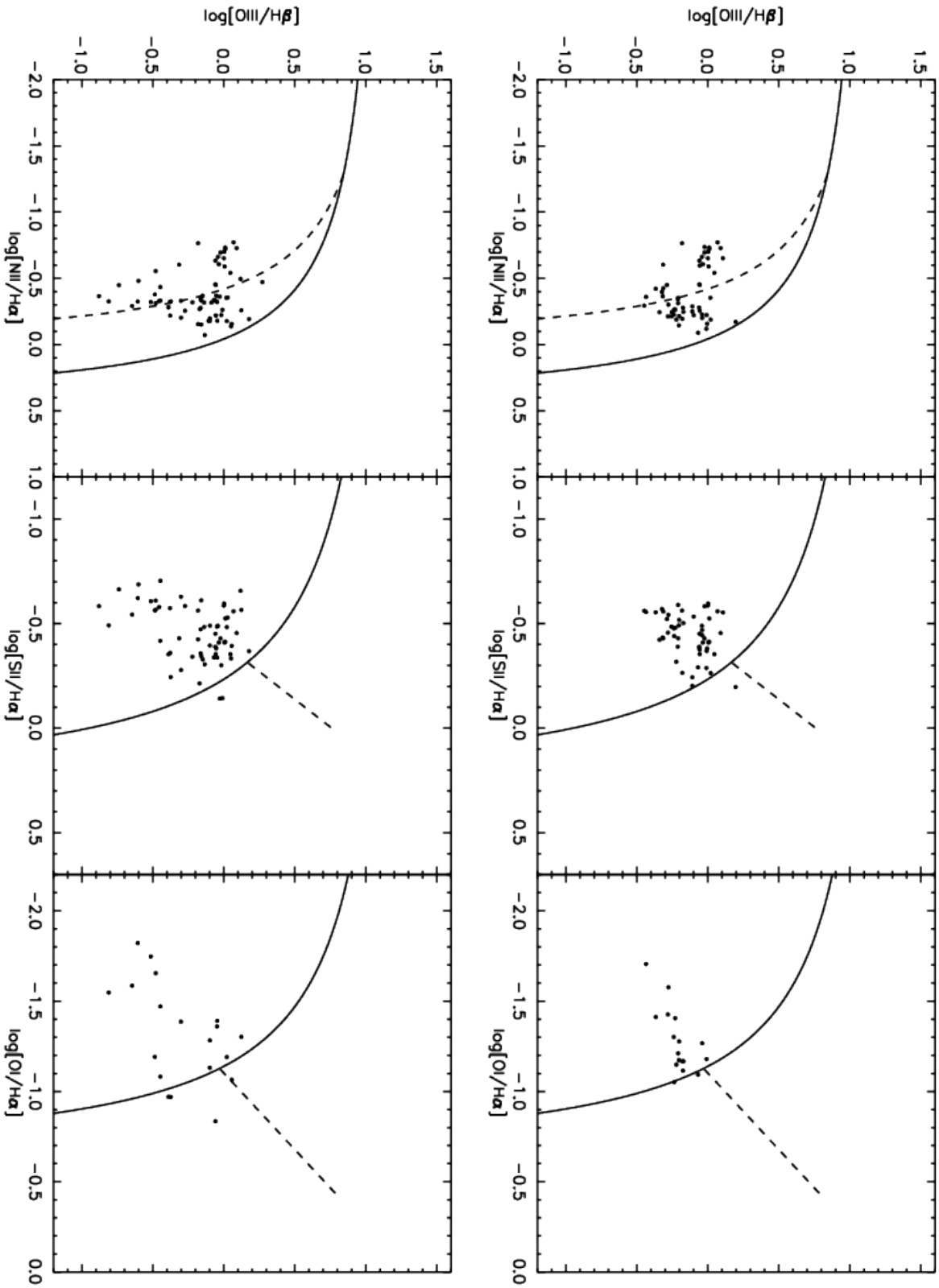

Figure A1. : Same as figure A1, but for IRAS F10038-3338.

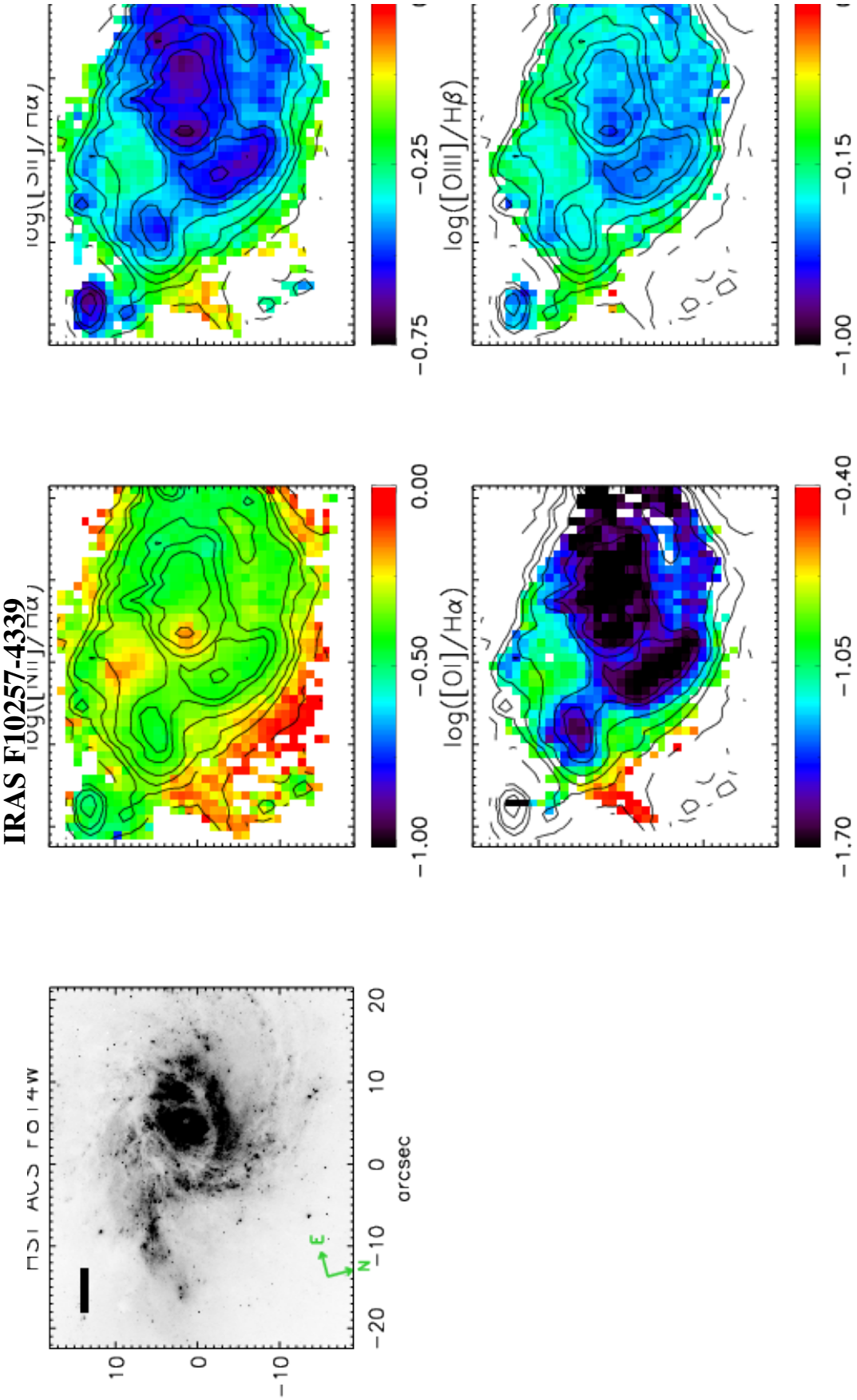
IRAS F10257-4339
log([NII]/Hα)
log([OIII]/Hβ)
log([OI]/Hα)
−1.00
−0.50
0.00
−0.75
−0.25
−1.70
−1.05
−0.40
−1.00
−0.15
HST ACS F814W
E
N
arcsec
20
10
0
−10
−20

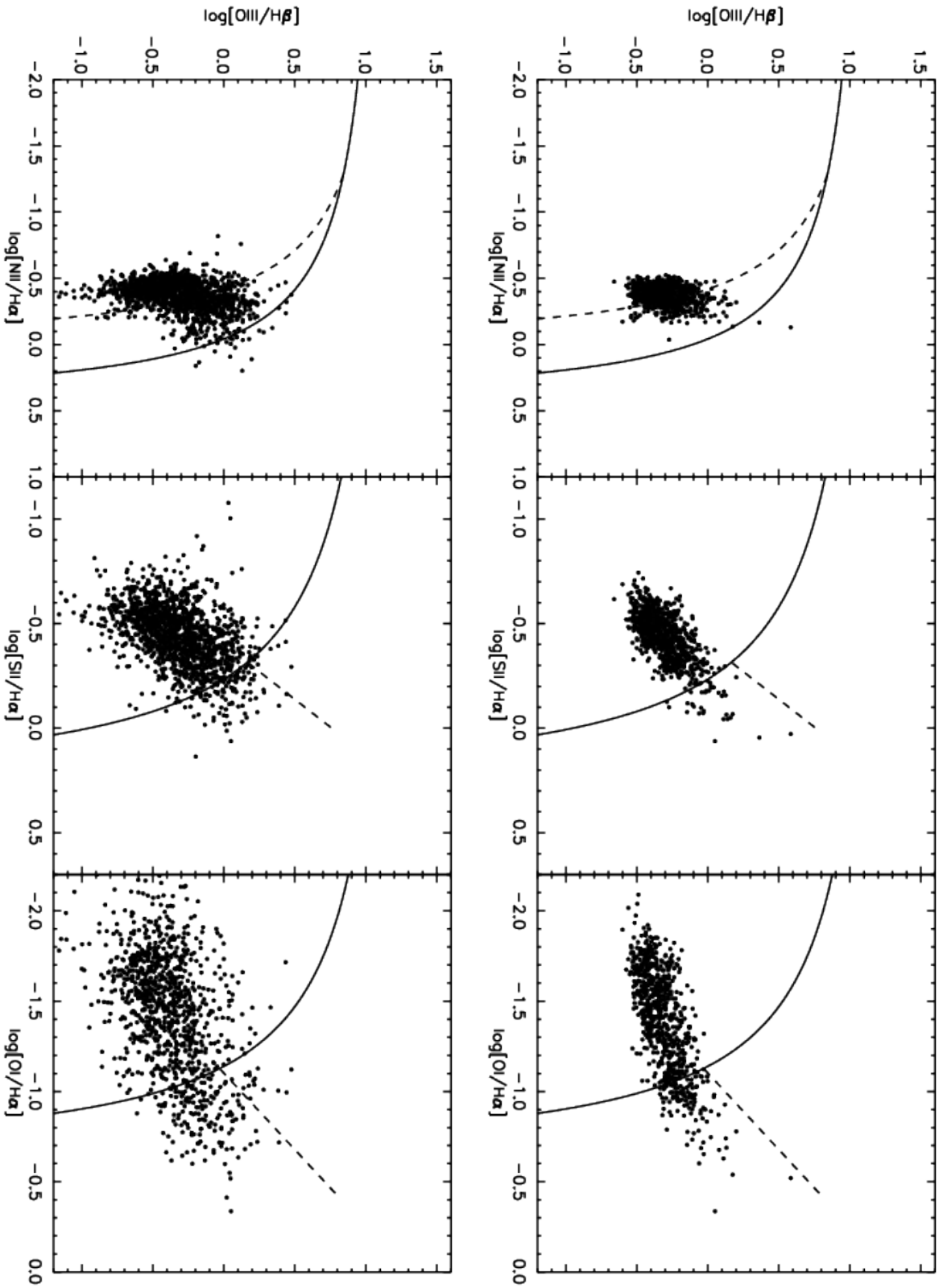

Figure A1. : Same as figure A1, but for IRAS F10257-4339.

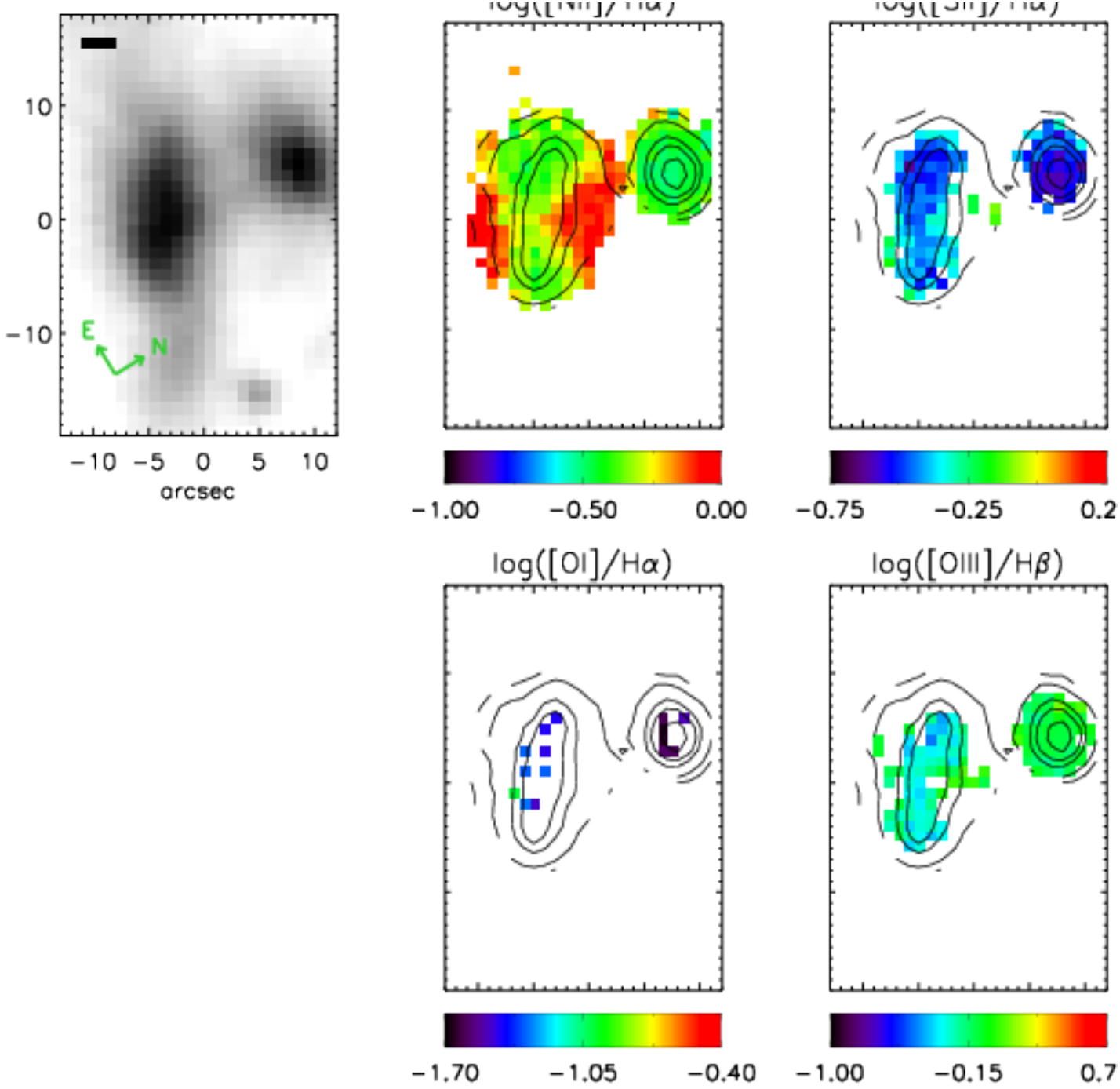

IRAS F12043-3140

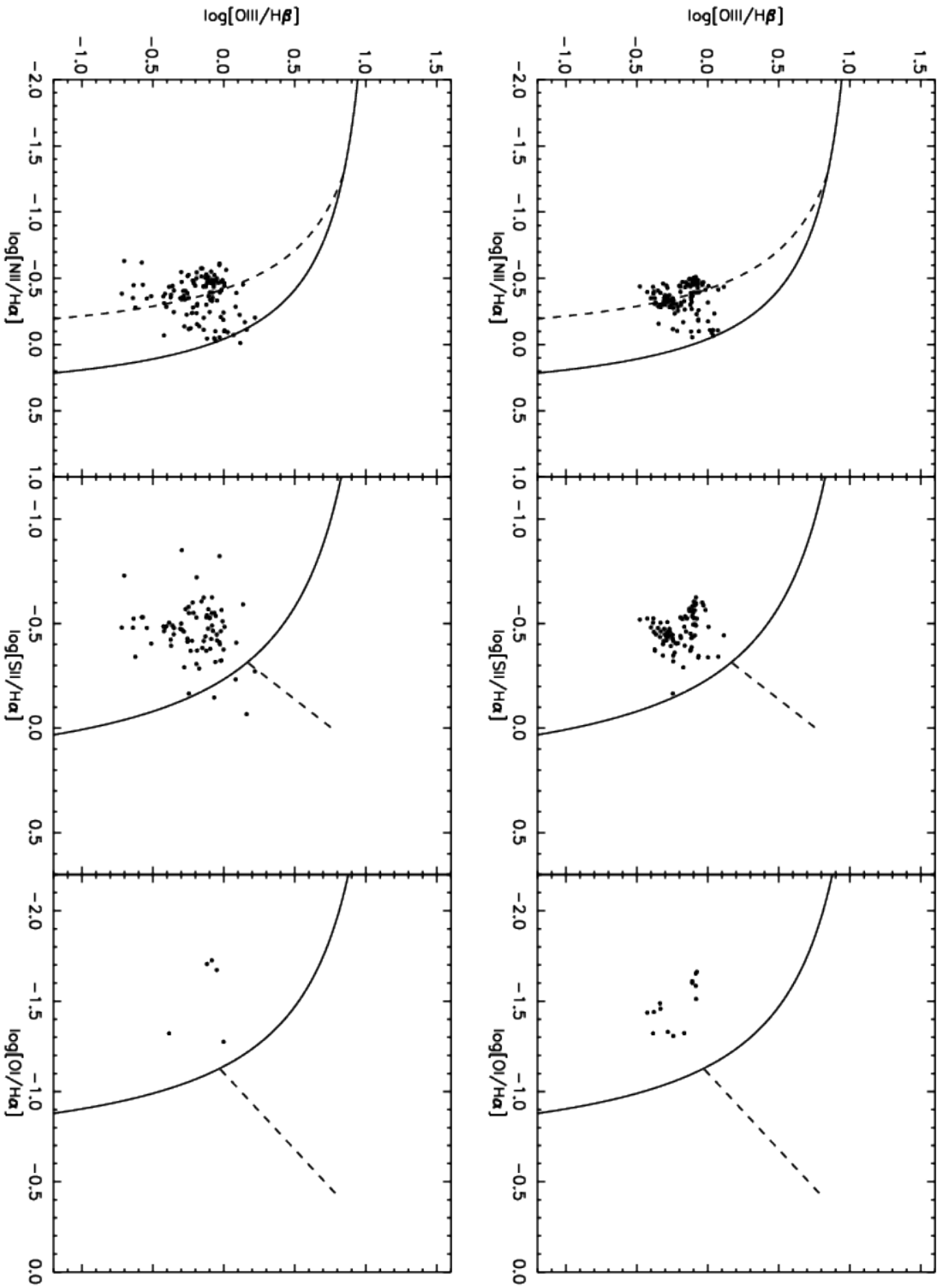

Figure A1. : Same as figure A1, but for IRAS F12043-3140 and a DSS R-band image.

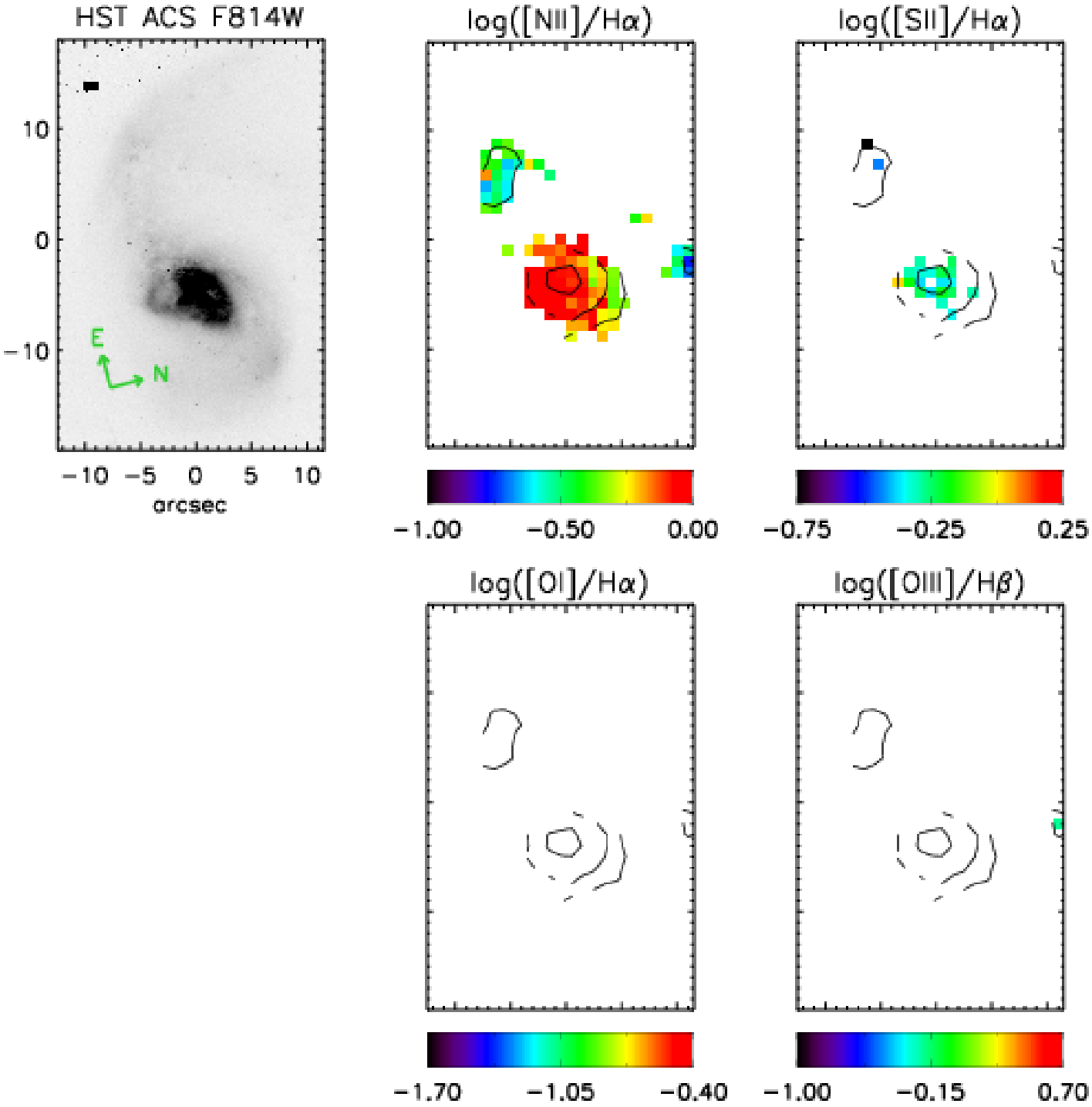

IRAS F12592+0436

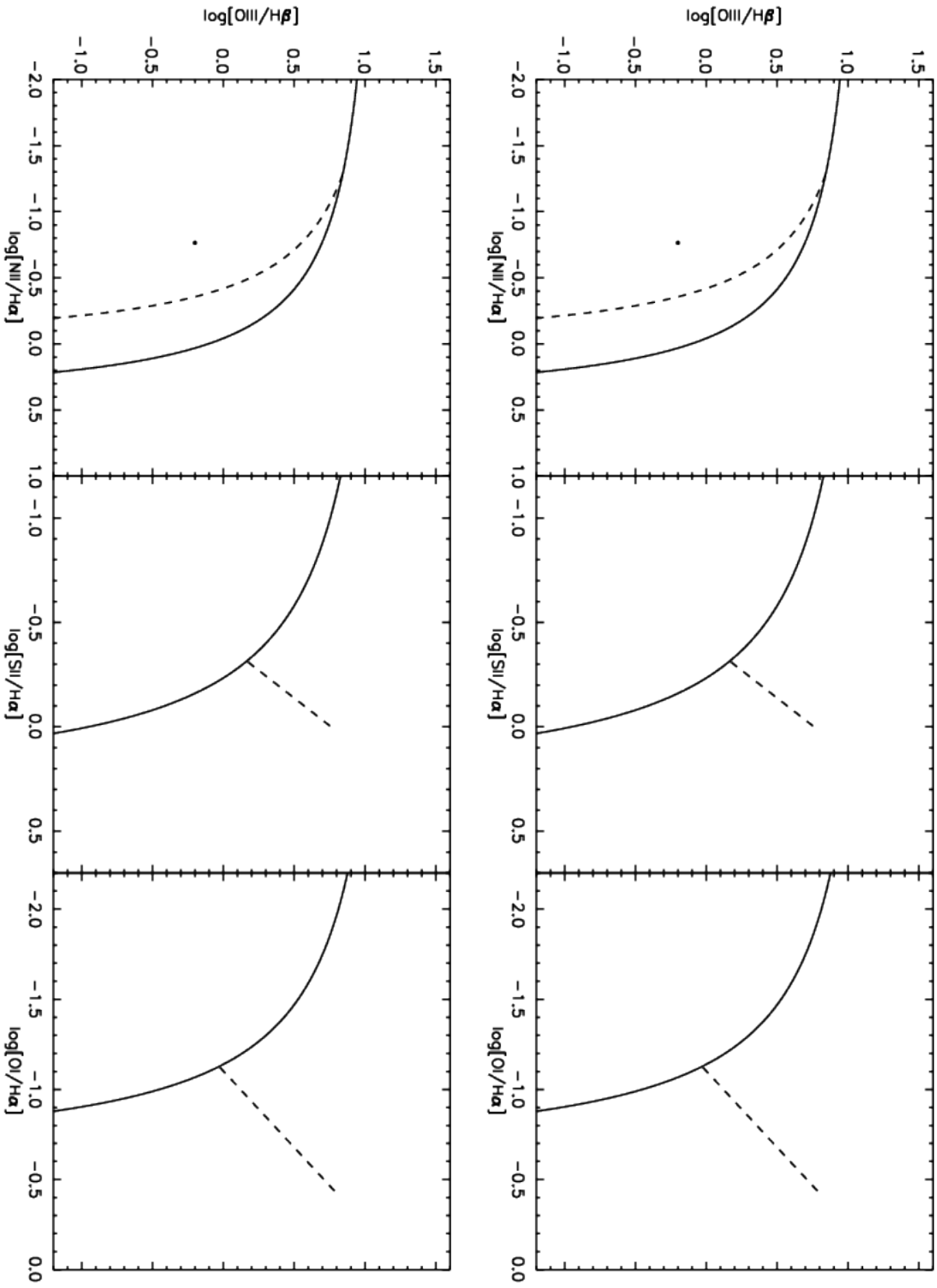

Figure A1. : Same as figure A1, but for IRAS F12592+0436.

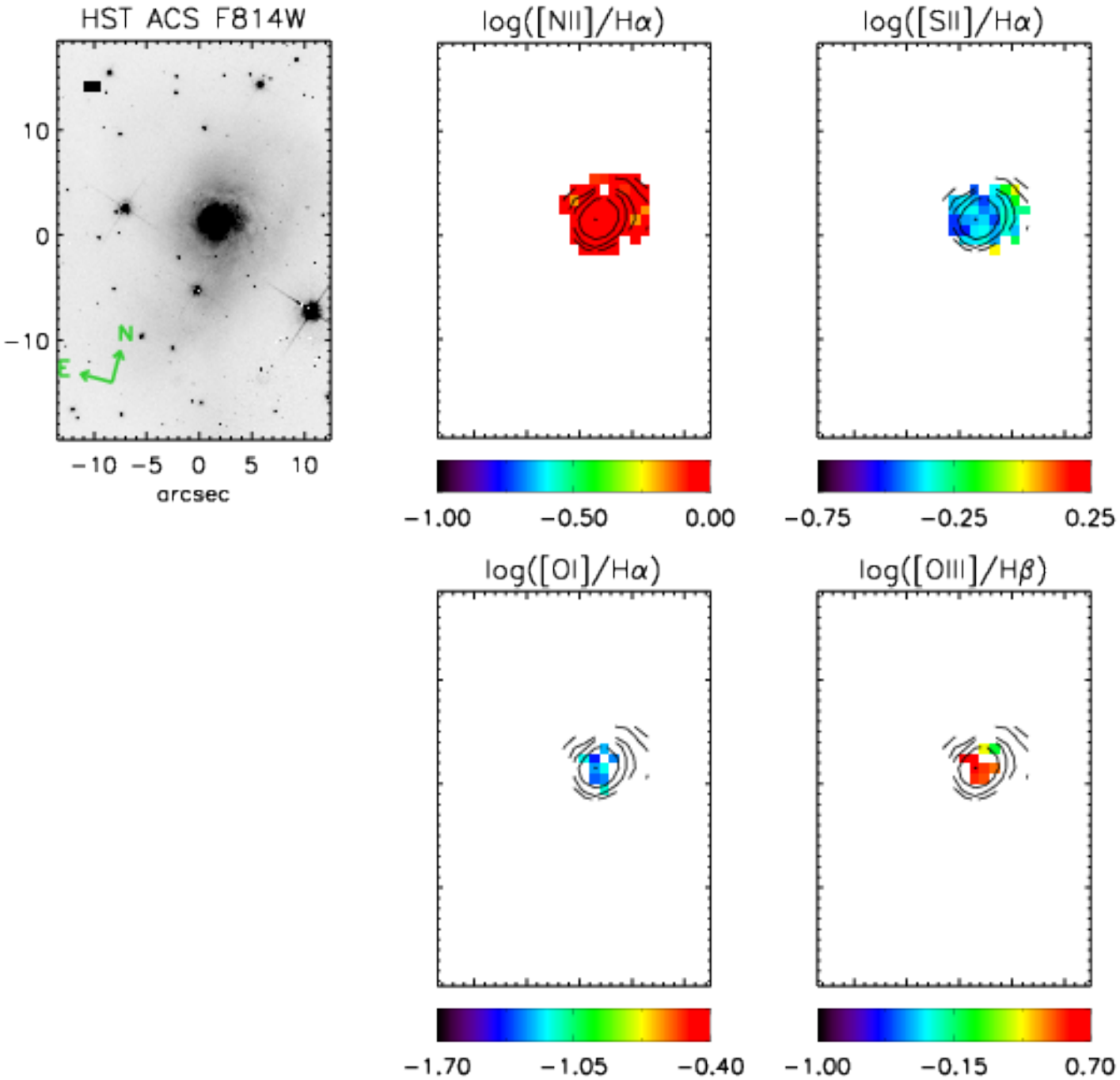

IRAS 13120-5453

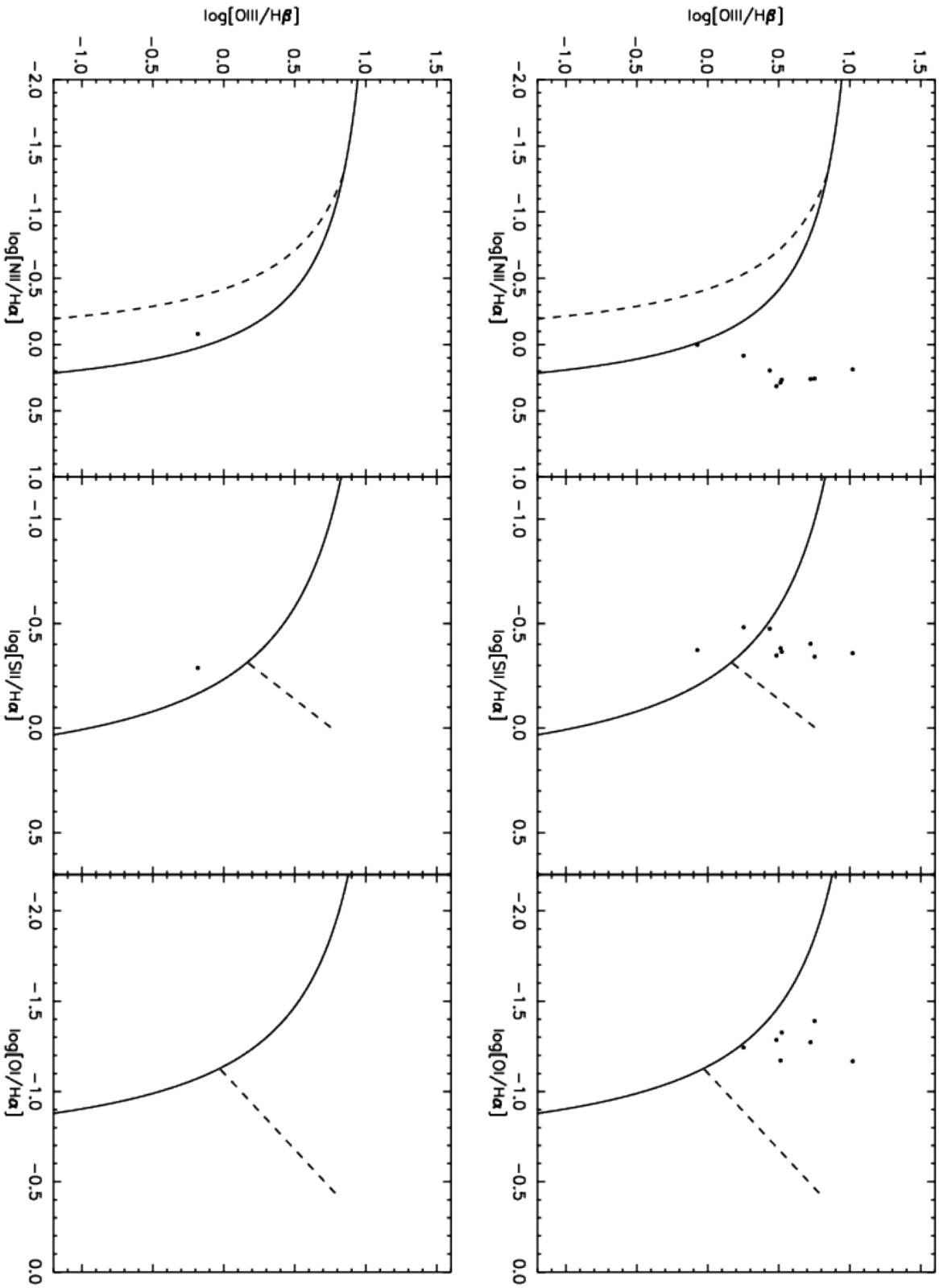

Figure A1. : Same as figure A1, but for IRAS 13120-5453.

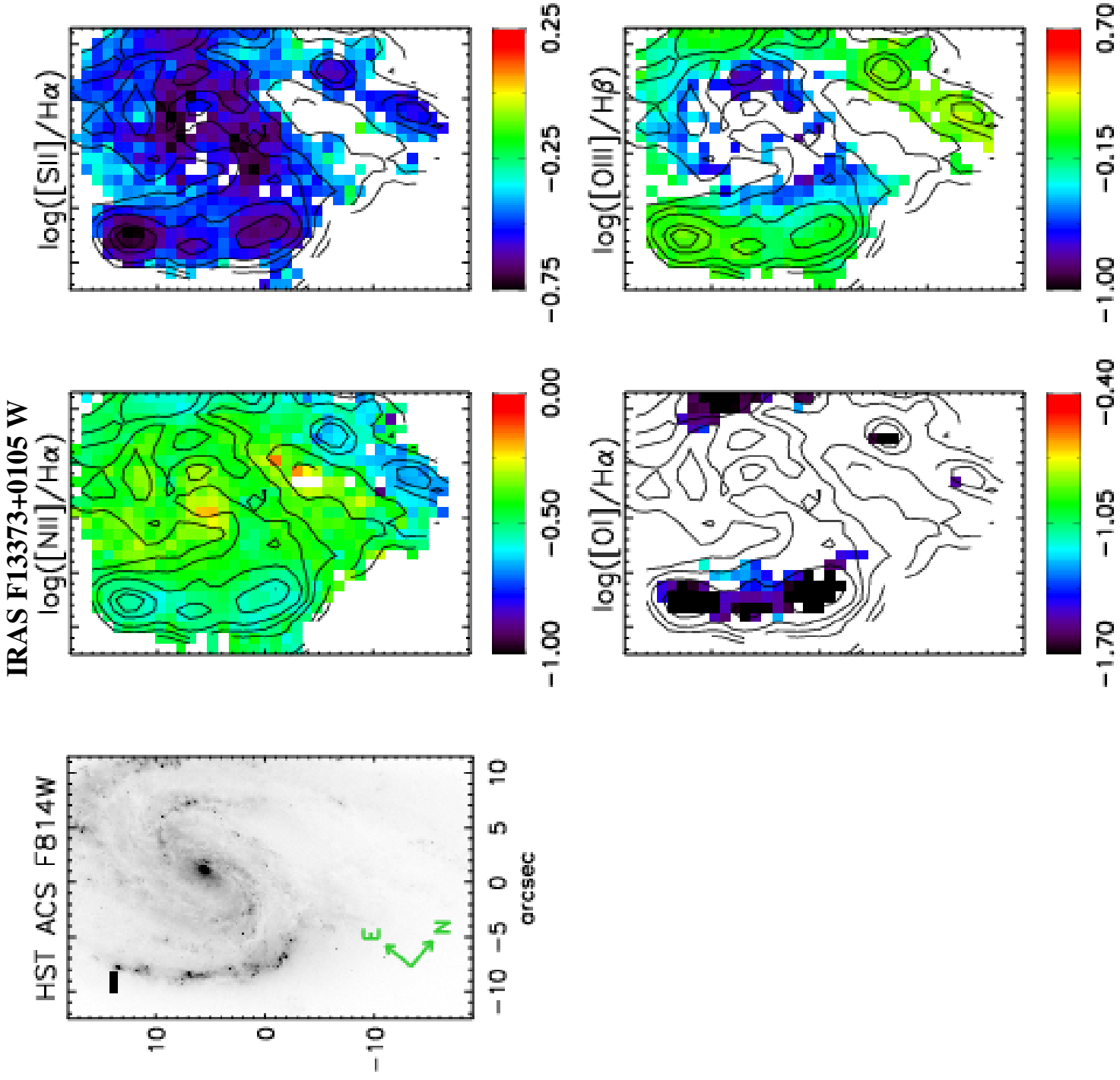
IRAS F13373+0105 W
HST ACS F814W
log([NII]/Hα)
log([SII]/Hα)
log([OI]/Hα)
log([OIII]/Hβ)
arcsec
E
N
10
0
−10
−5
5
−1.00
−0.50
0.00
−0.75
−0.25
0.25
−1.70
−1.05
−0.40
−1.00
−0.15
0.70

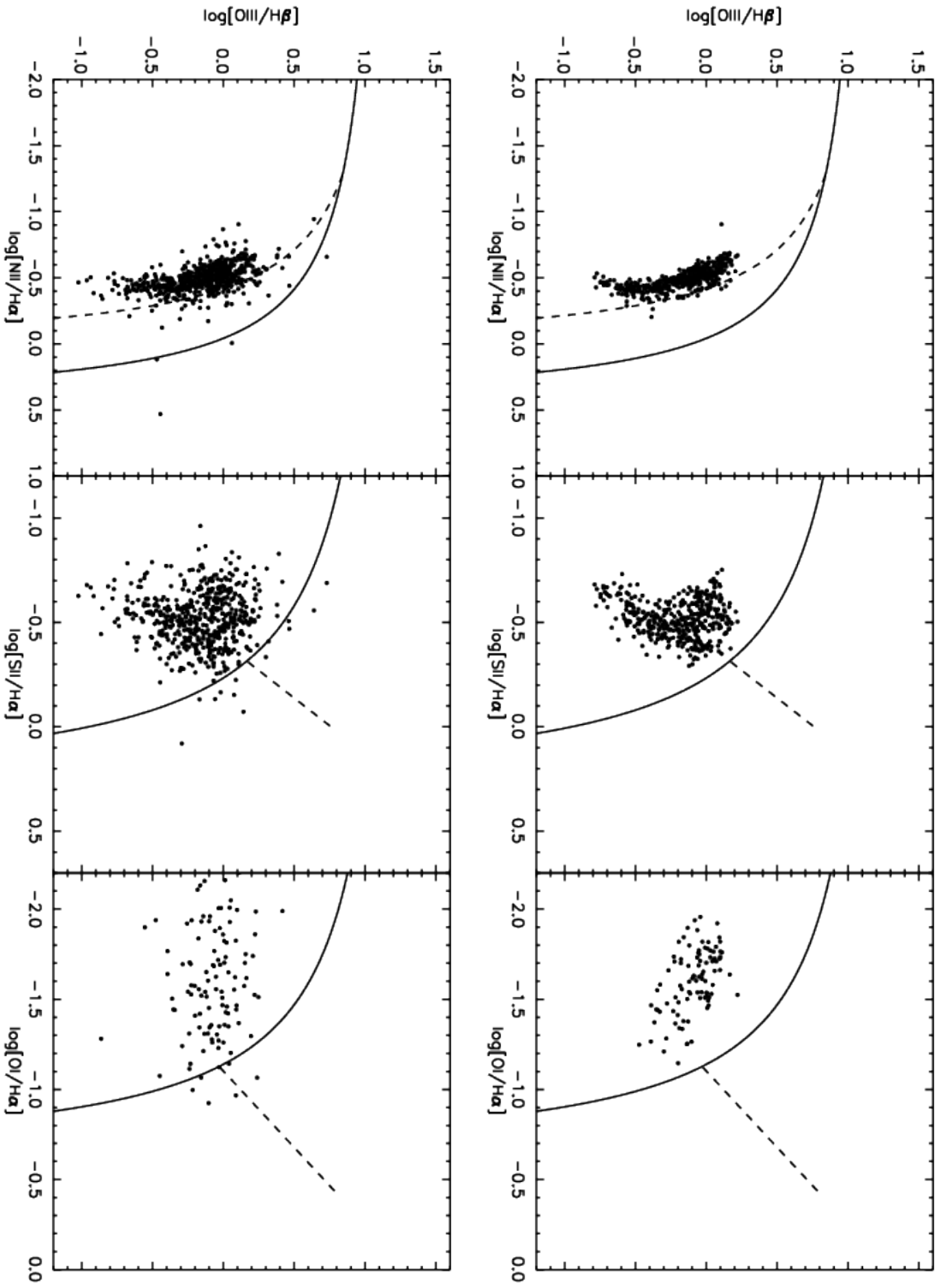

Figure A1. : Same as figure A1, but for IRAS F13373+0105 W.

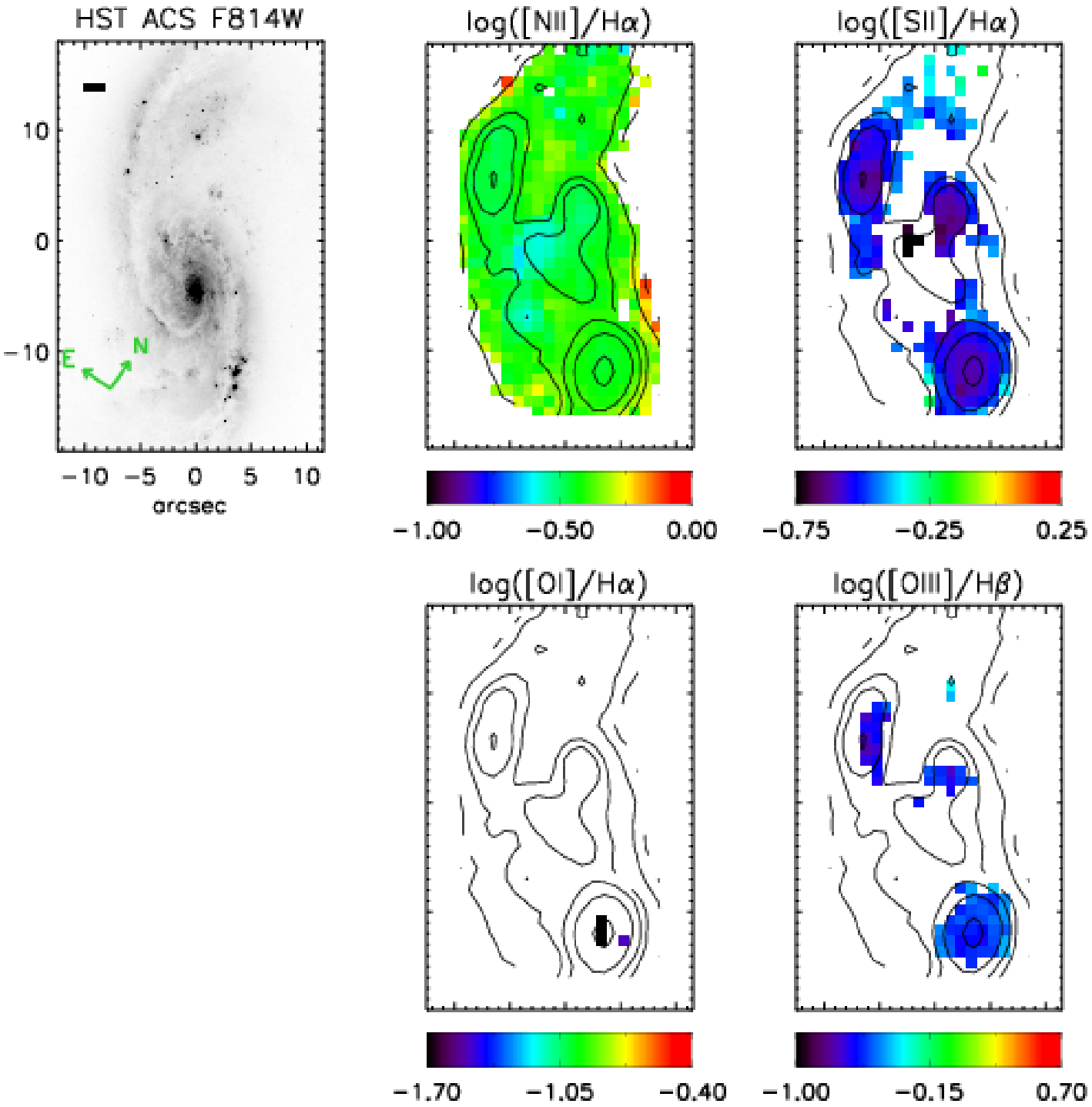

IRAS F13373+0105 E

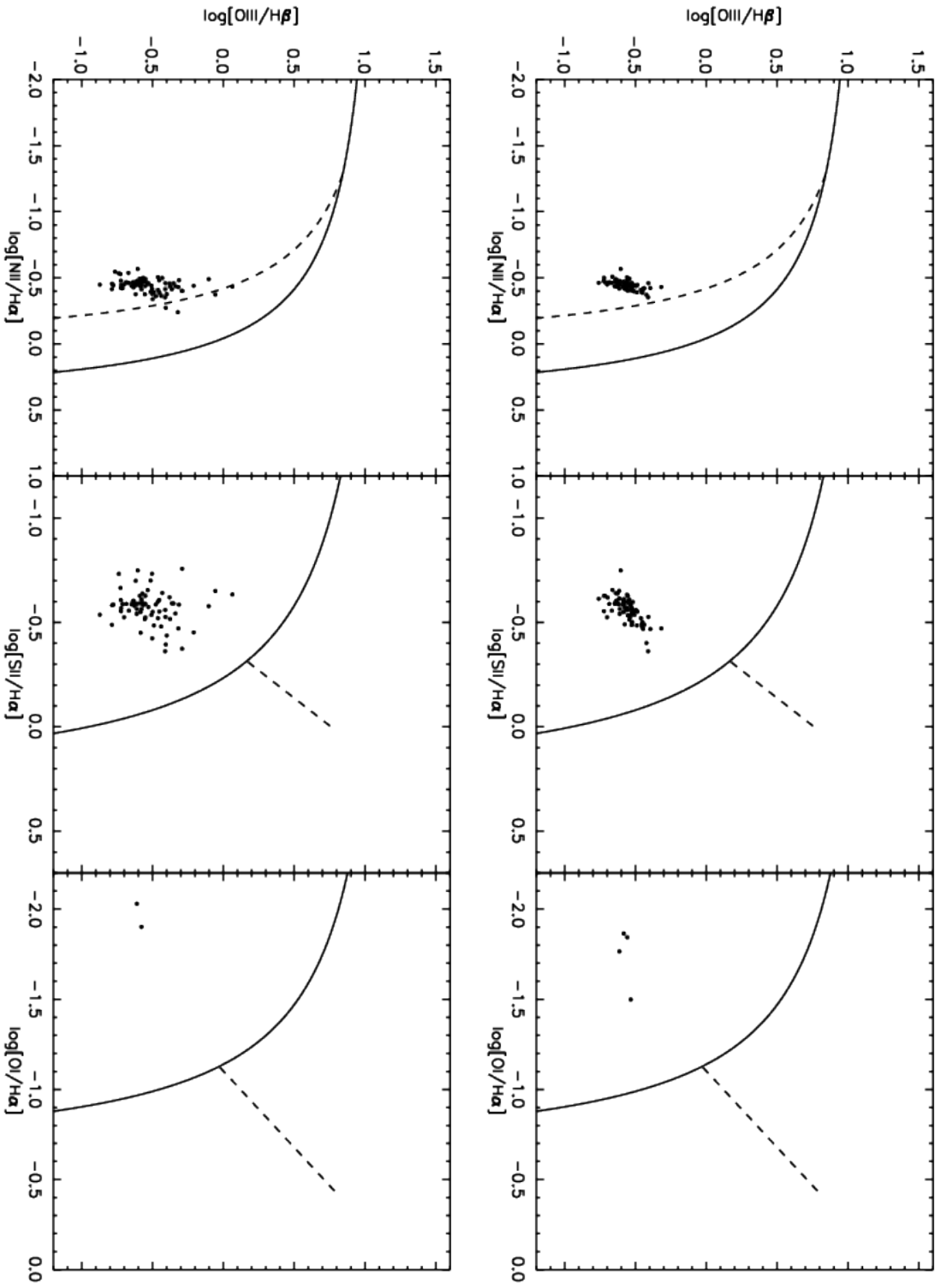

Figure A1. : Same as figure A1, but for IRAS F13373+0105 E.

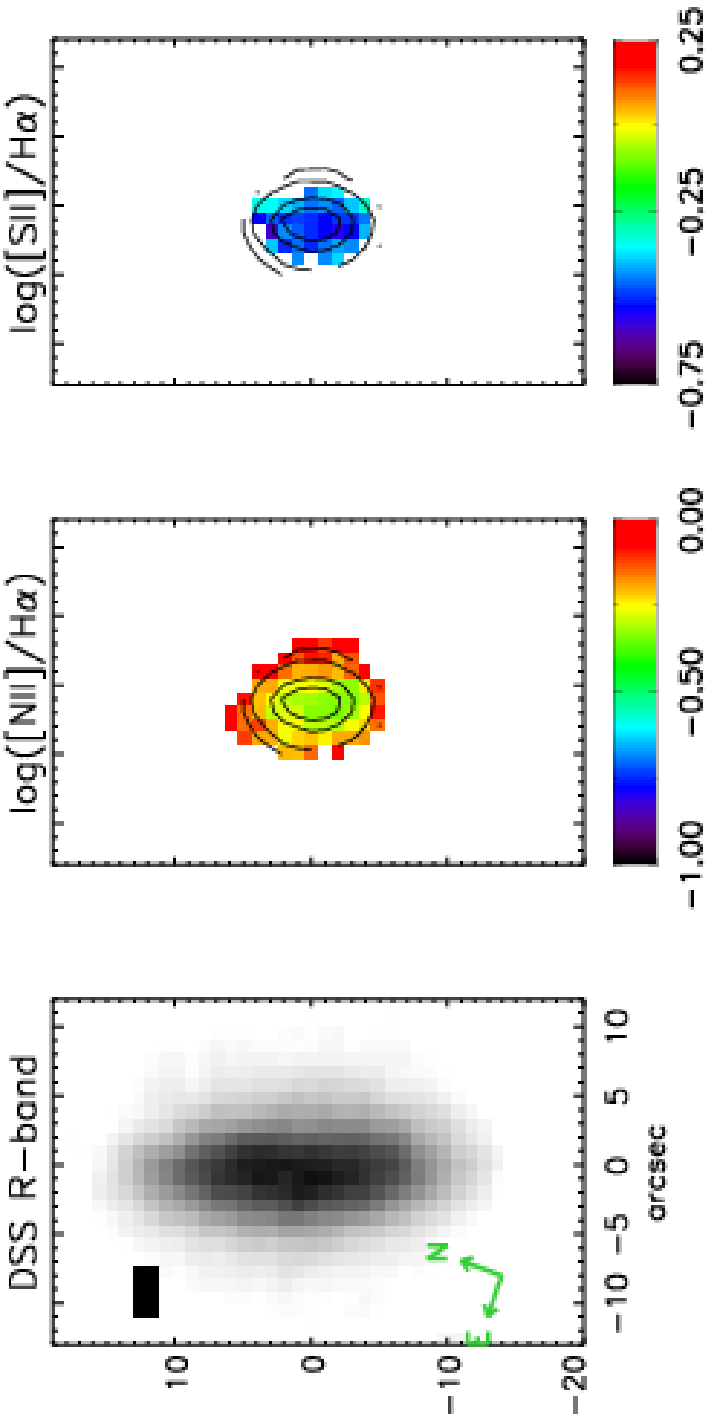

IRAS F15107+0724

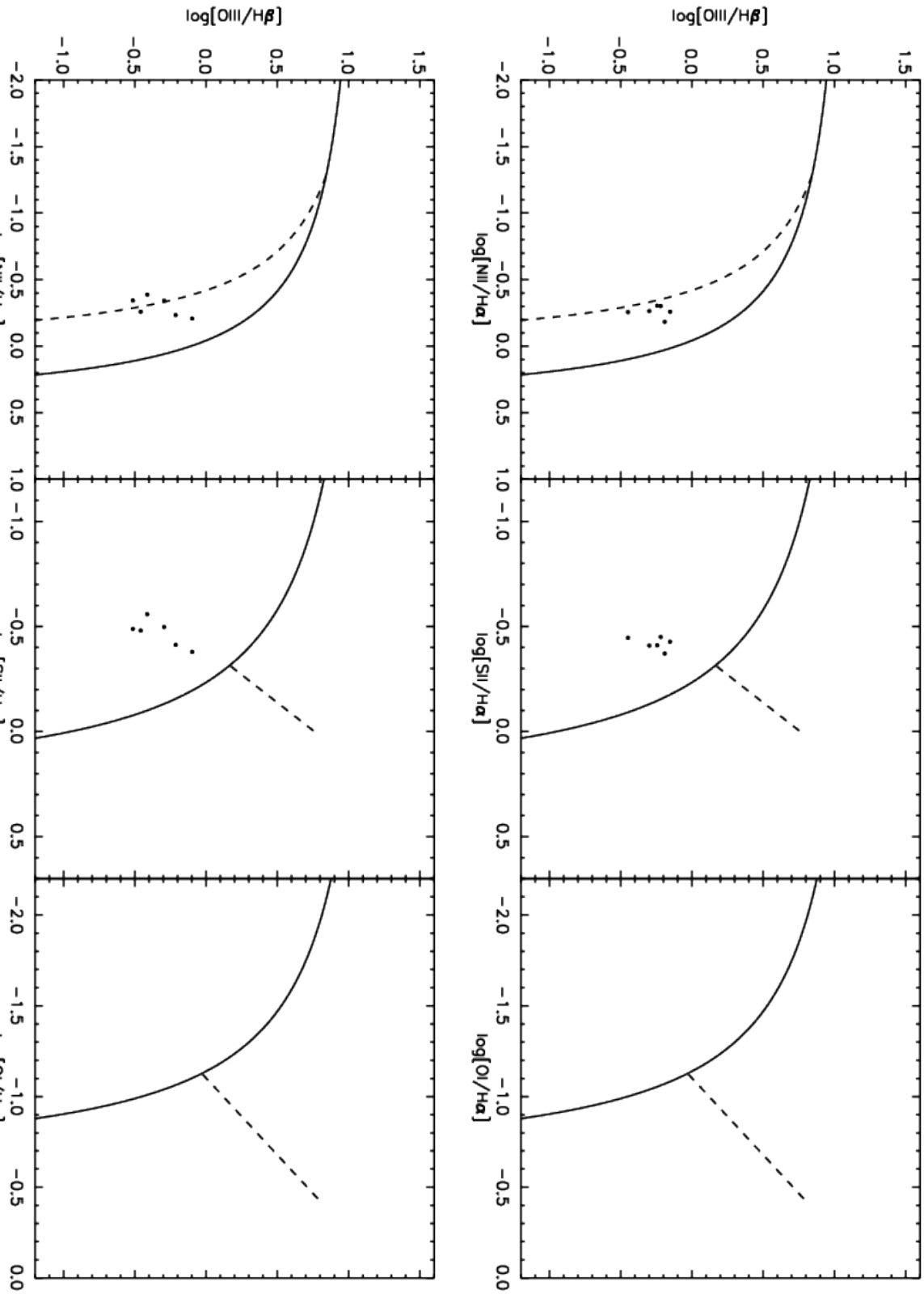

Figure A1. : Same as figure A1, but for IRAS F15107+0724 and a DSS R-band image.

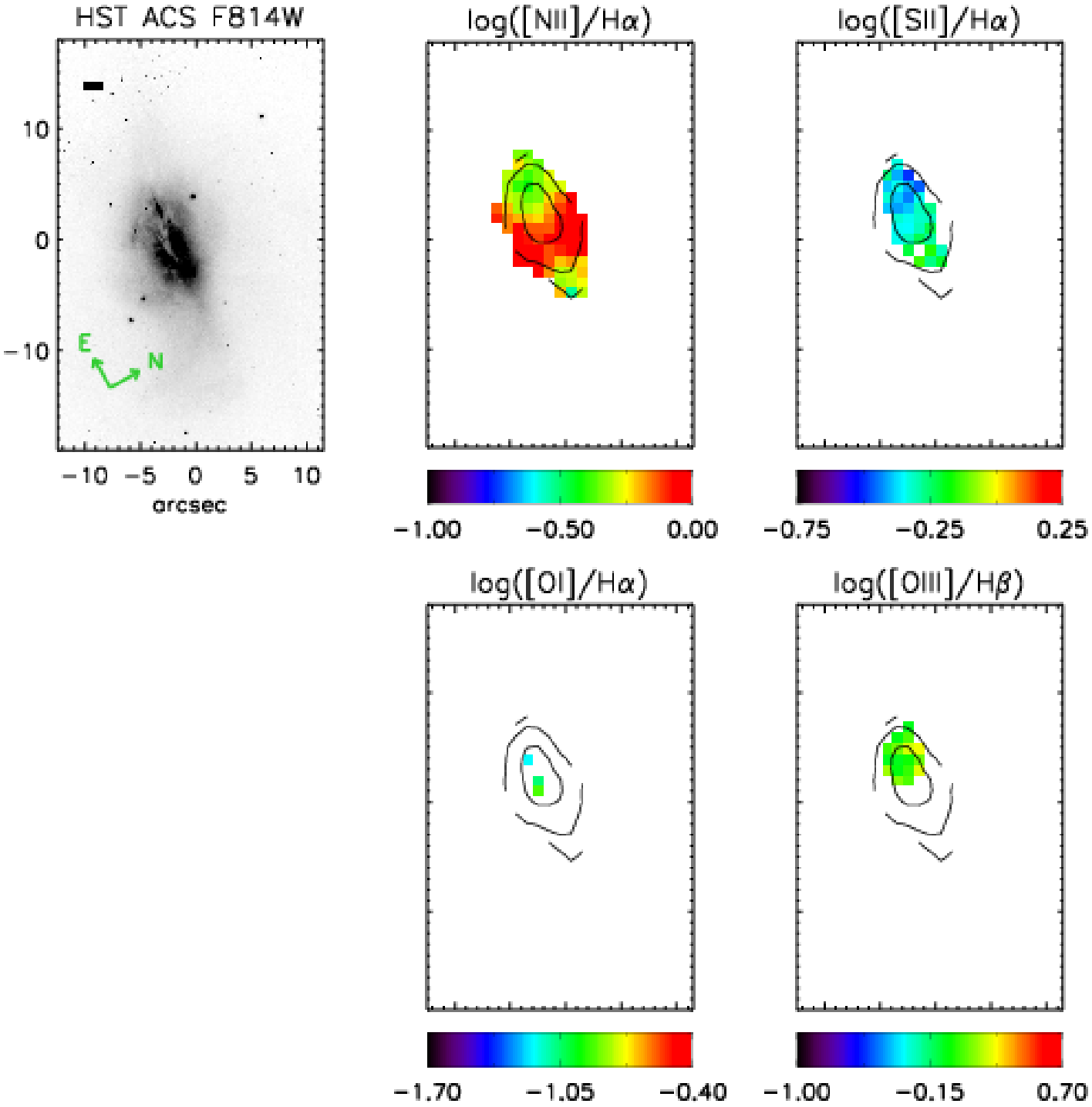

IRAS F16164-0746

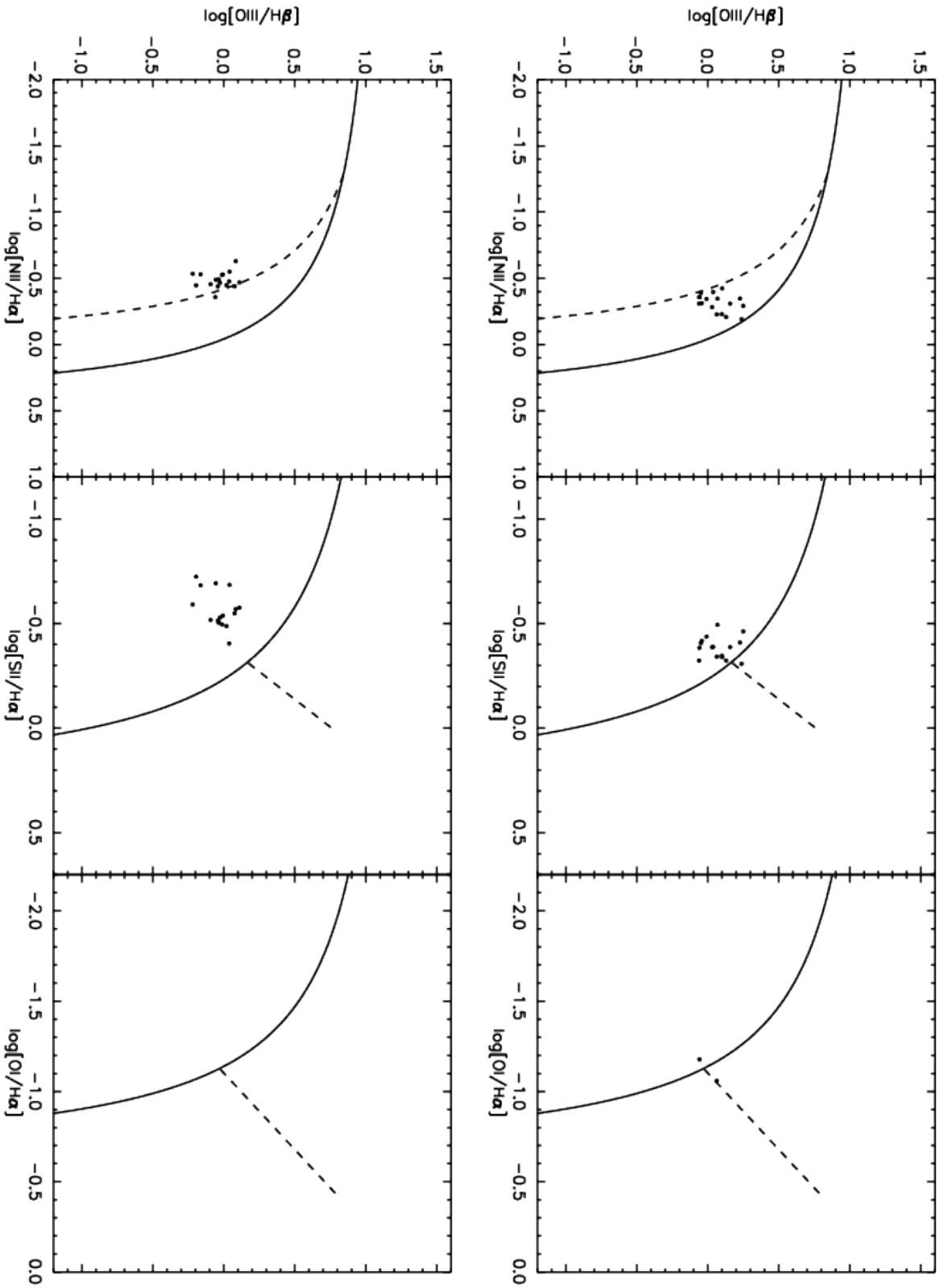

Figure A1. : Same as figure A1, but for IRAS F16164-0746.

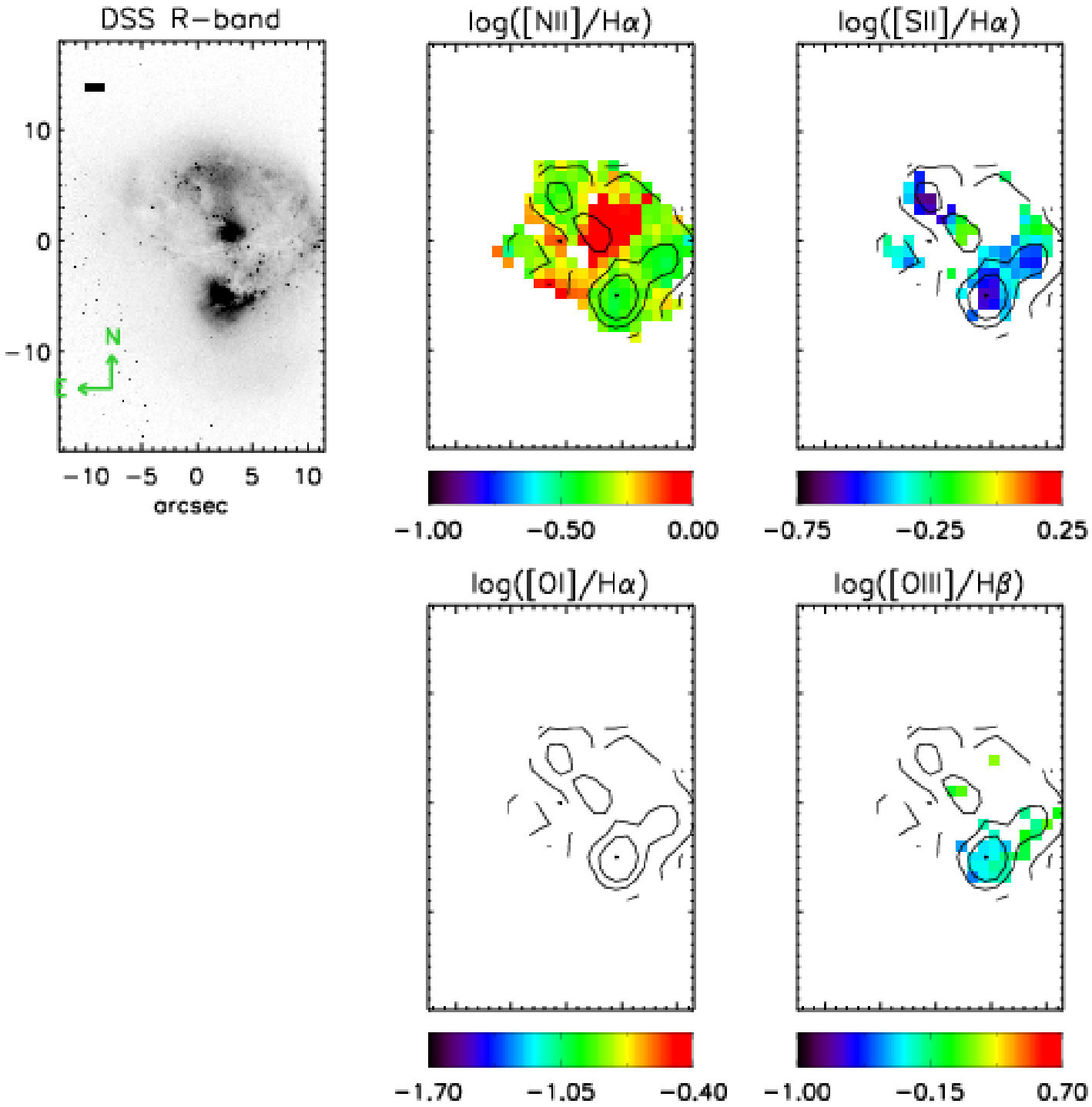

IRAS F16399-0937

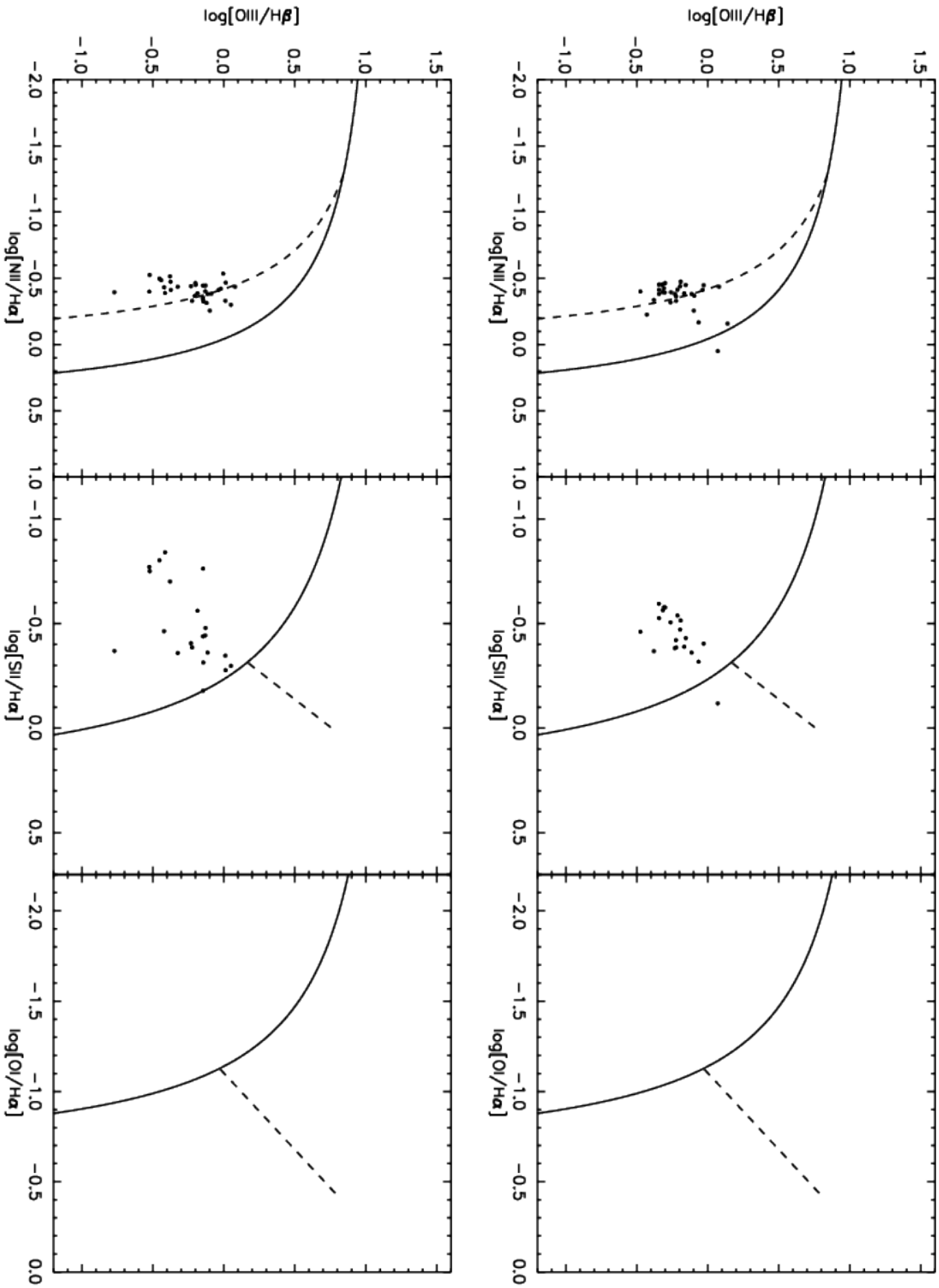

Figure A1. : Same as figure A1, but for IRAS F16399-0937.

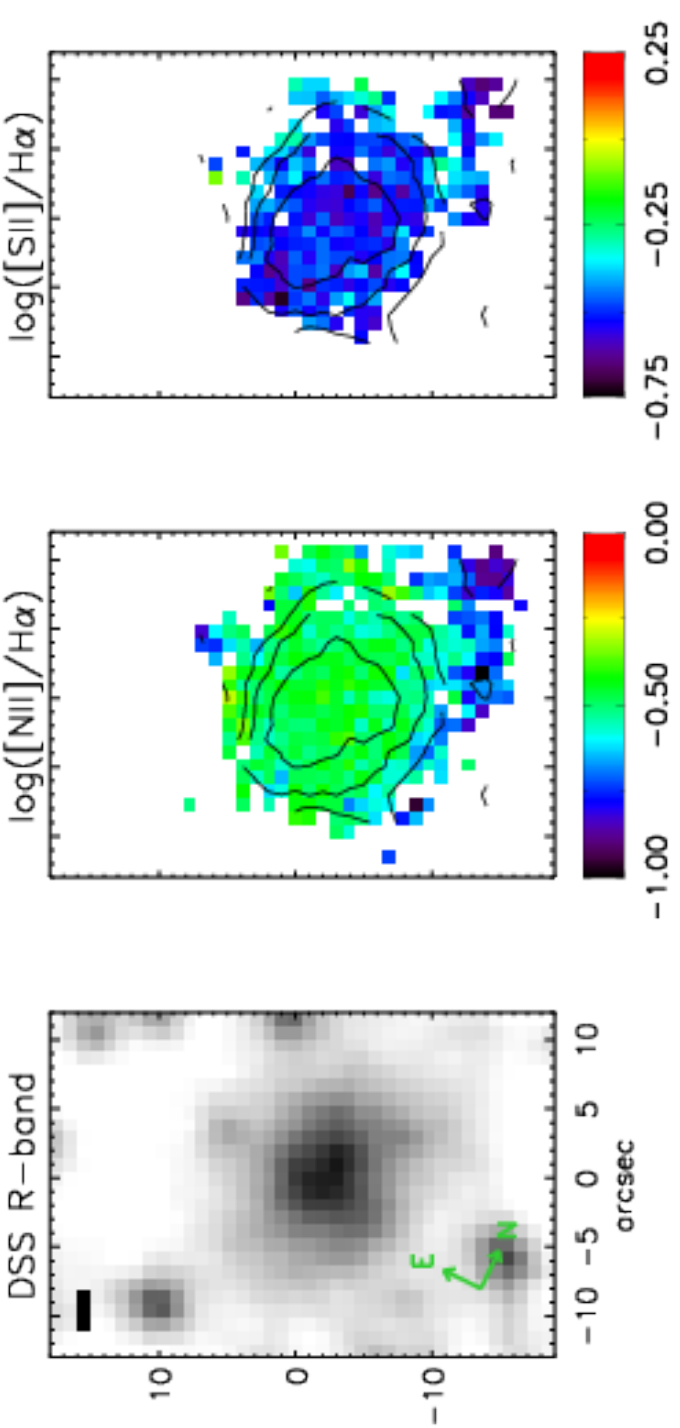

IRAS F16443-2915 N

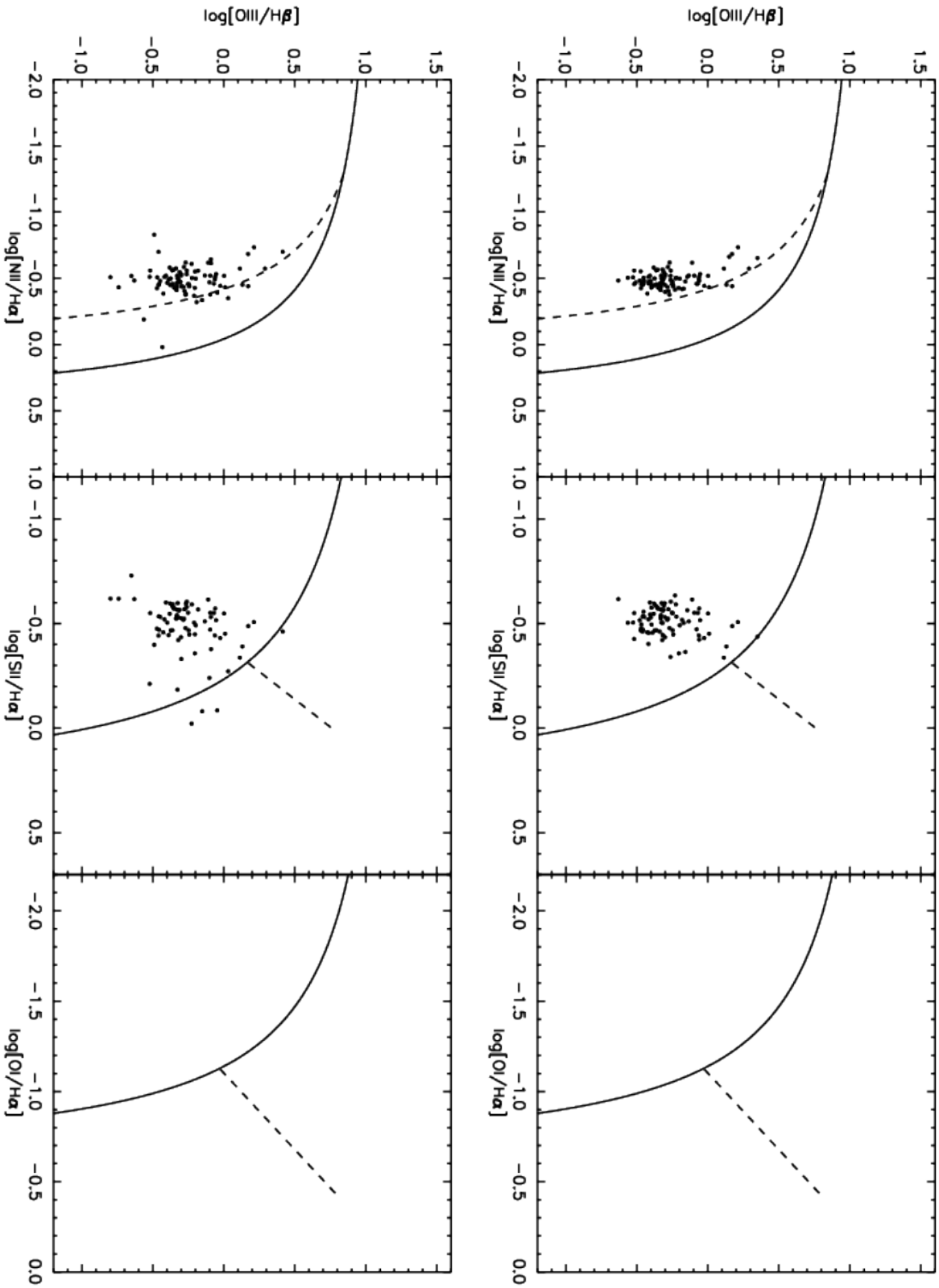

Figure A1. : Same as figure A1, but for IRAS F16443-2915 N and a DSS R-band image.

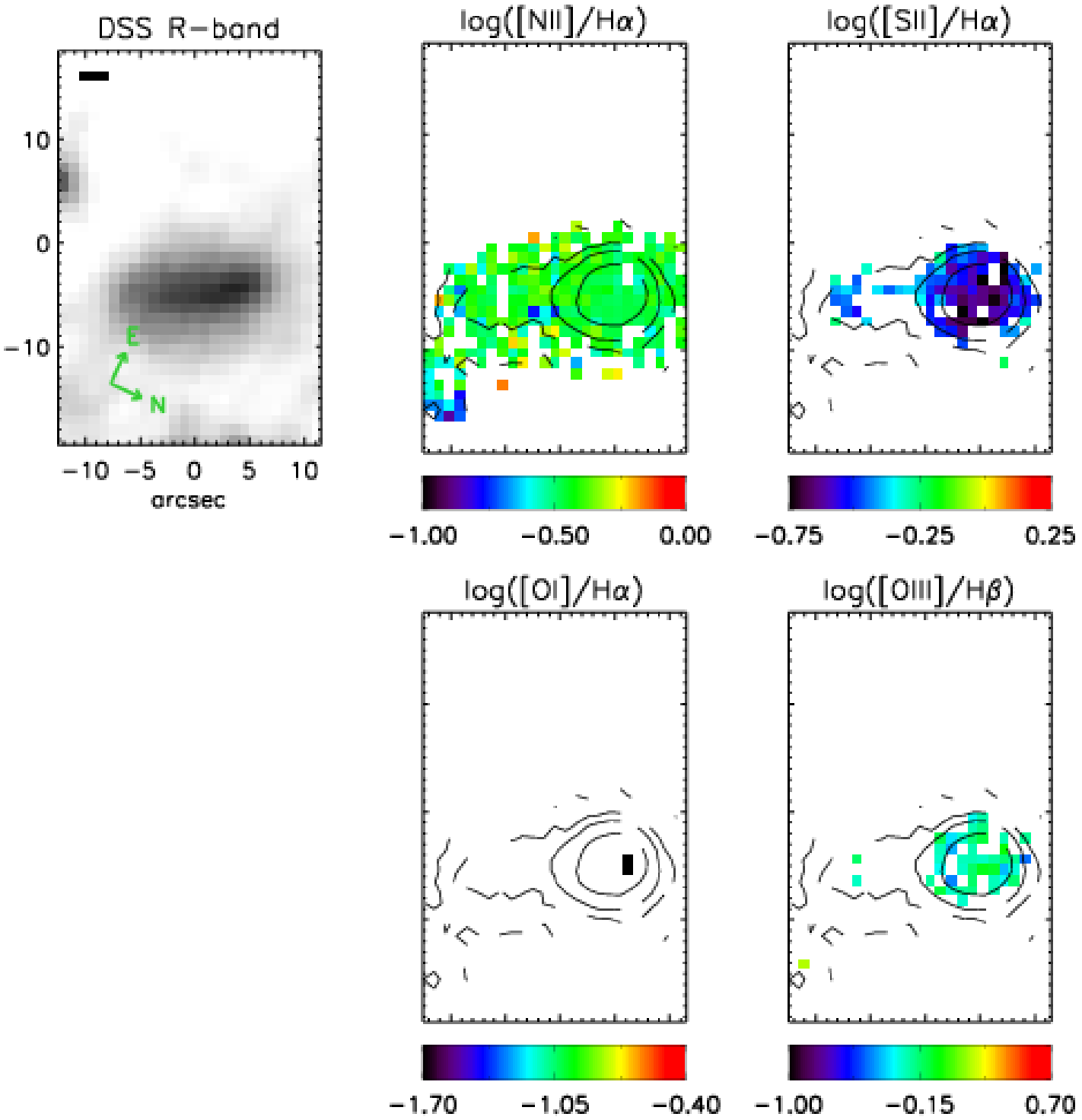

IRAS F16443-2915 S

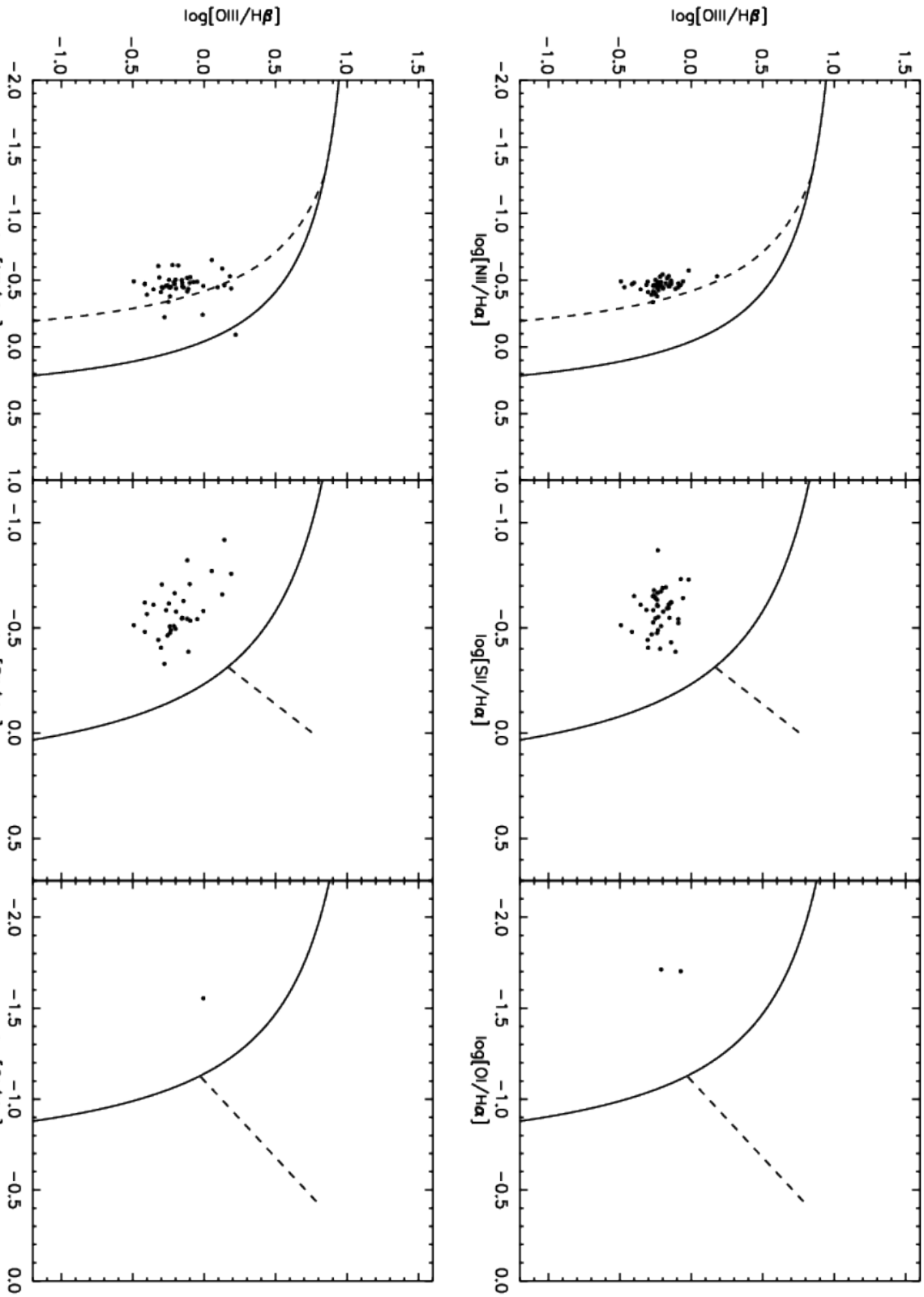

Figure A1. : Same as figure A1, but for IRAS F16443-2915 S and a DSS R-band image.

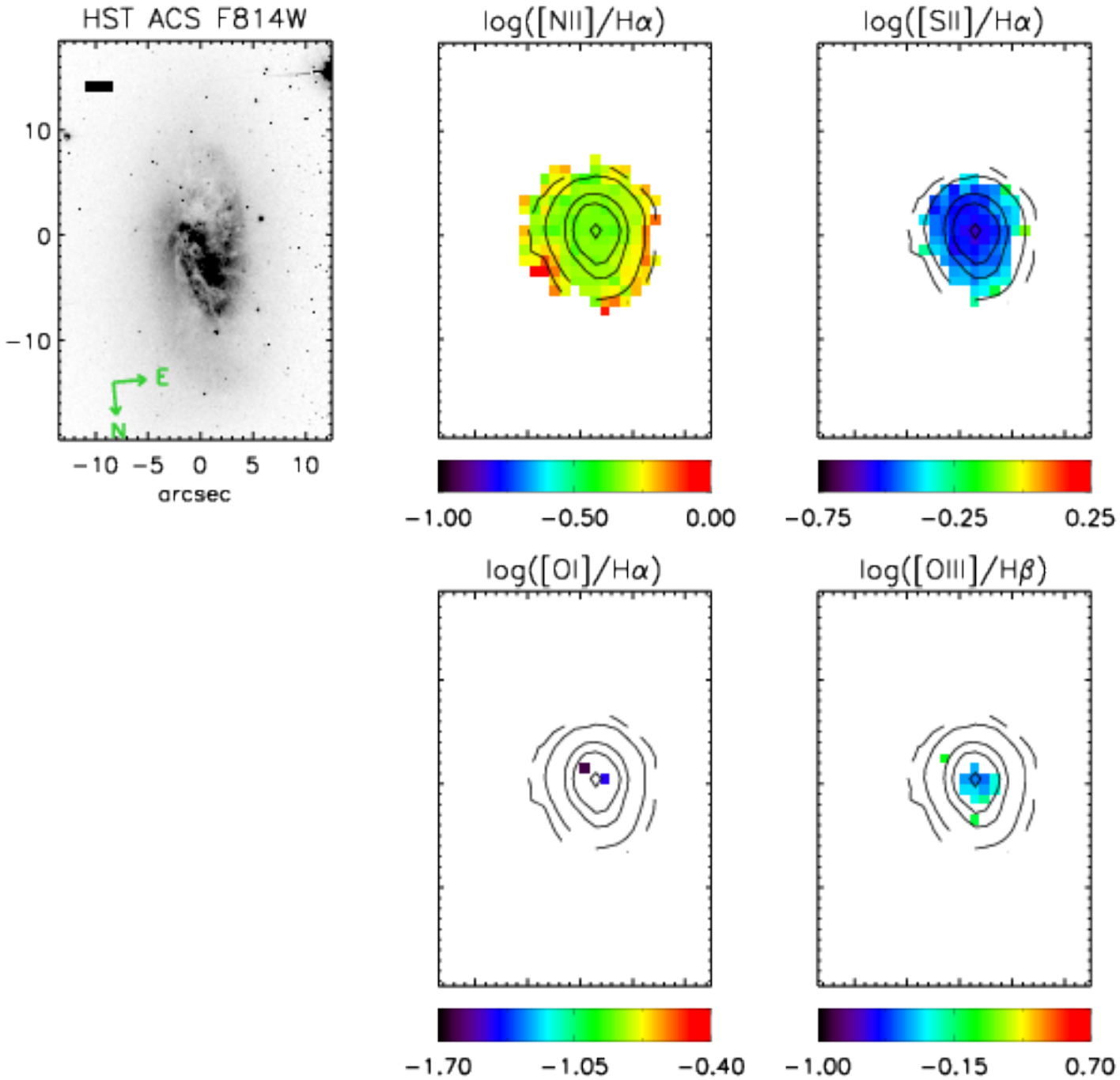

IRAS F17138-1017

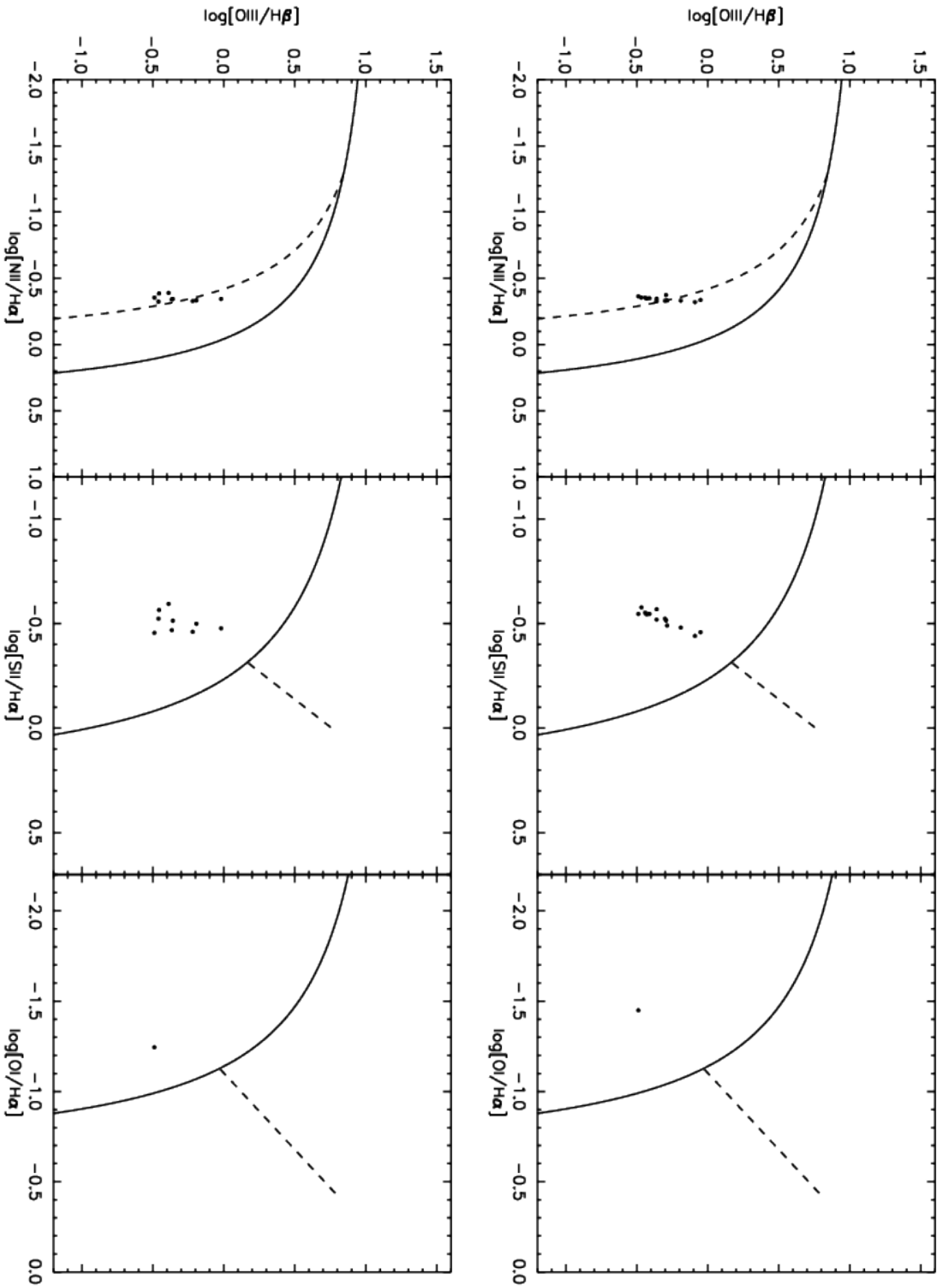

Figure A1. : Same as figure A1, but for IRAS F17138-1017.

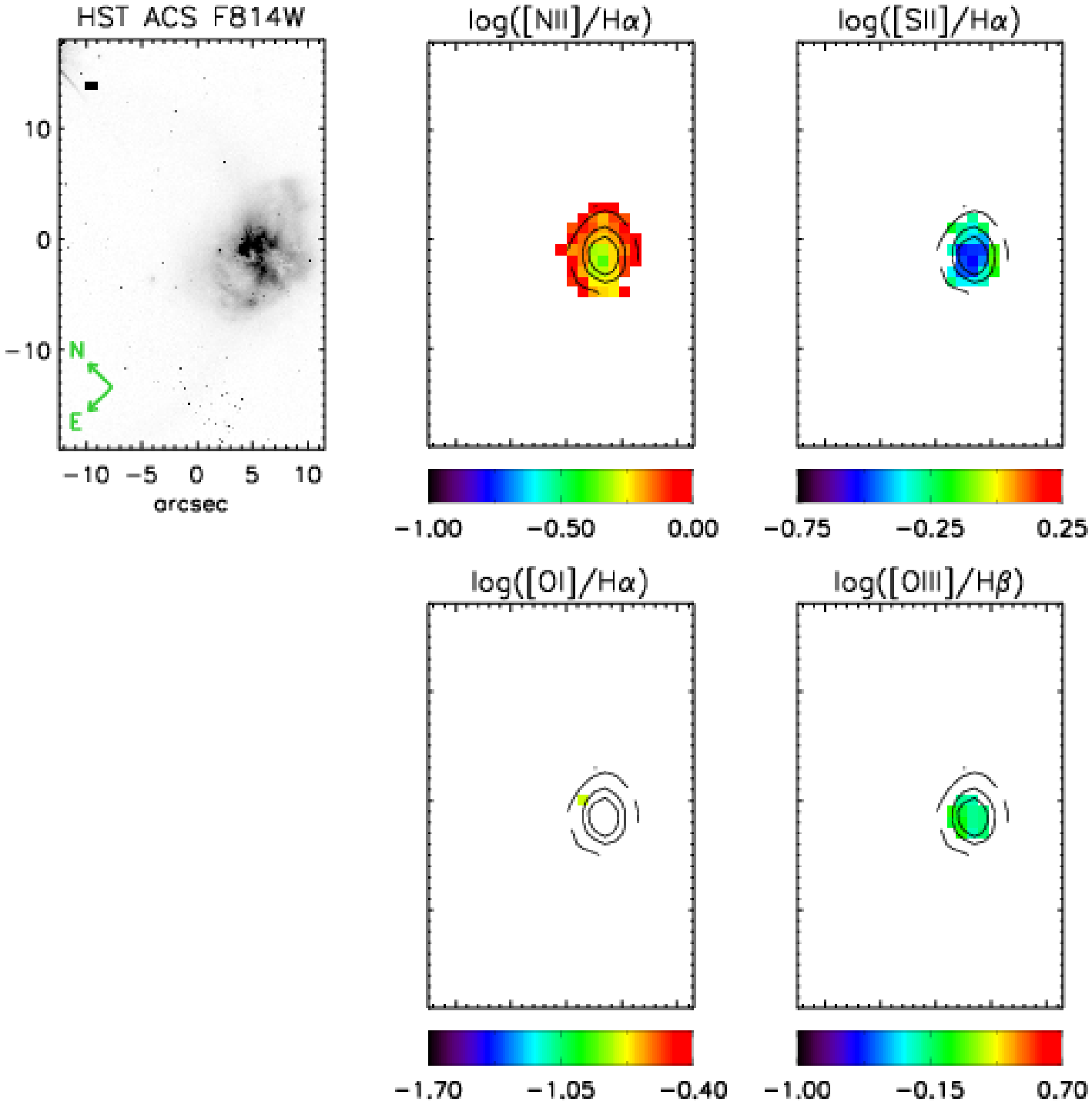

IRAS F17207-0014

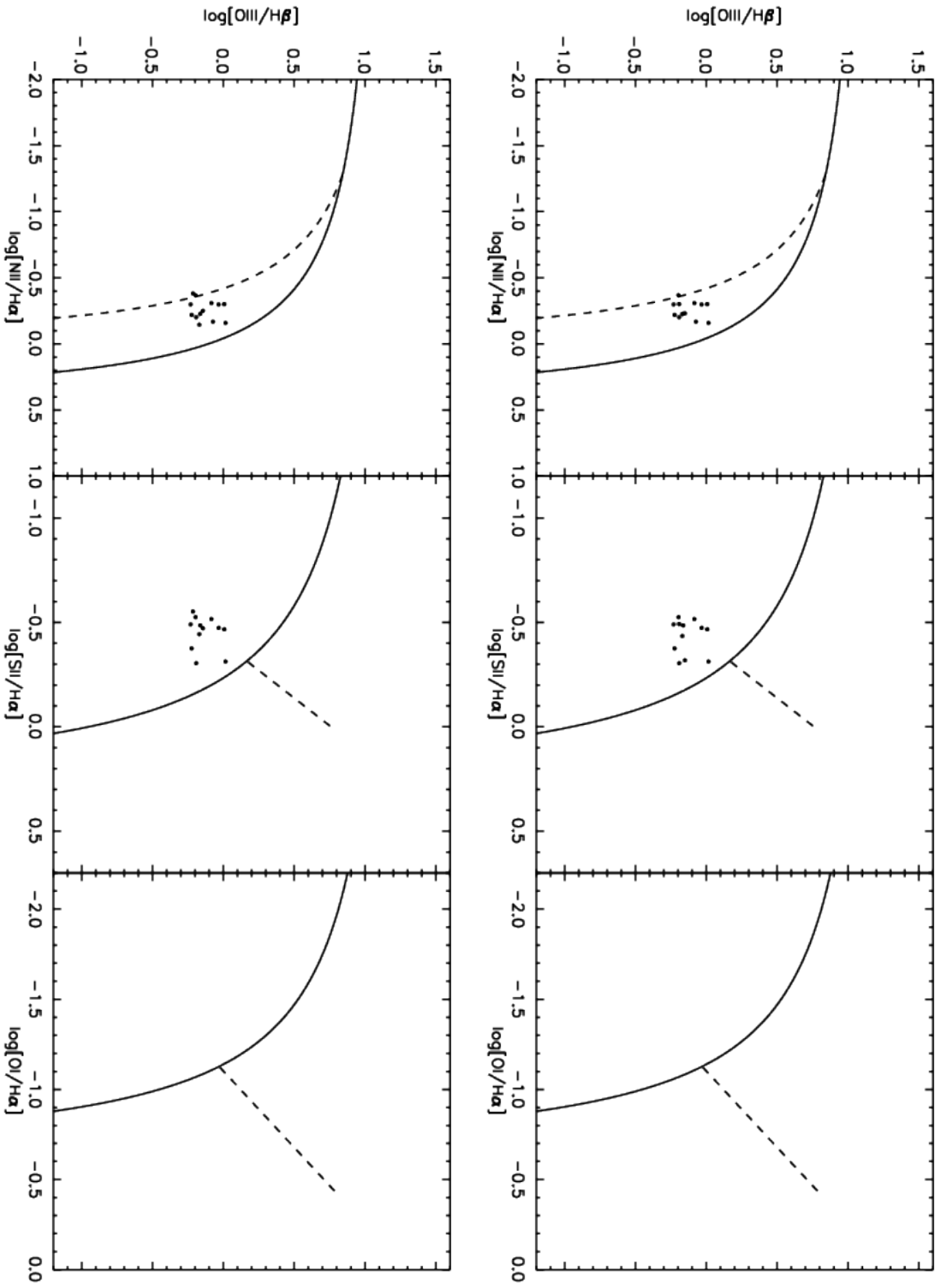

Figure A1. : Same as figure A1, but for IRAS F17207-0014.

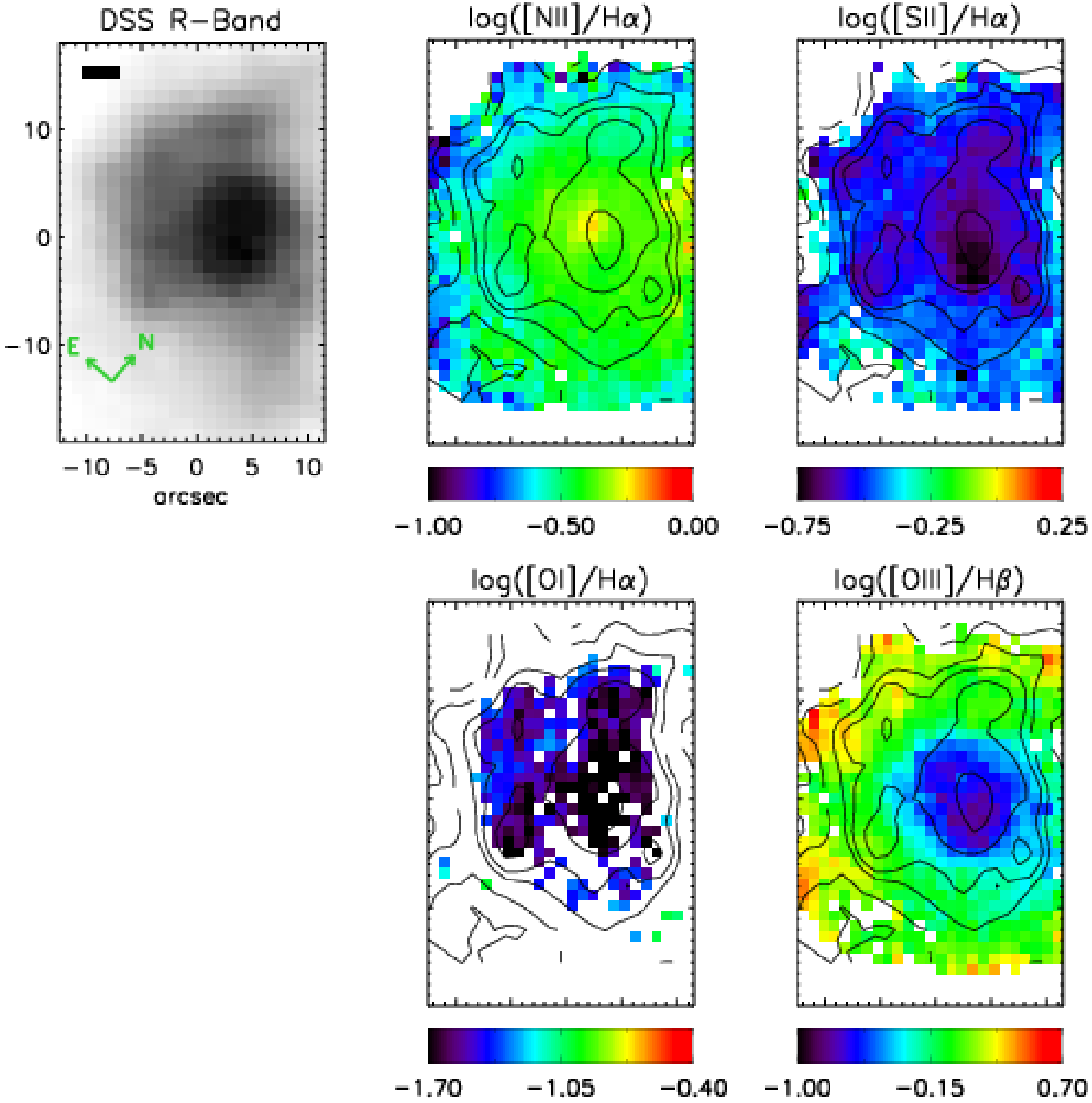

IRAS F17222-5953

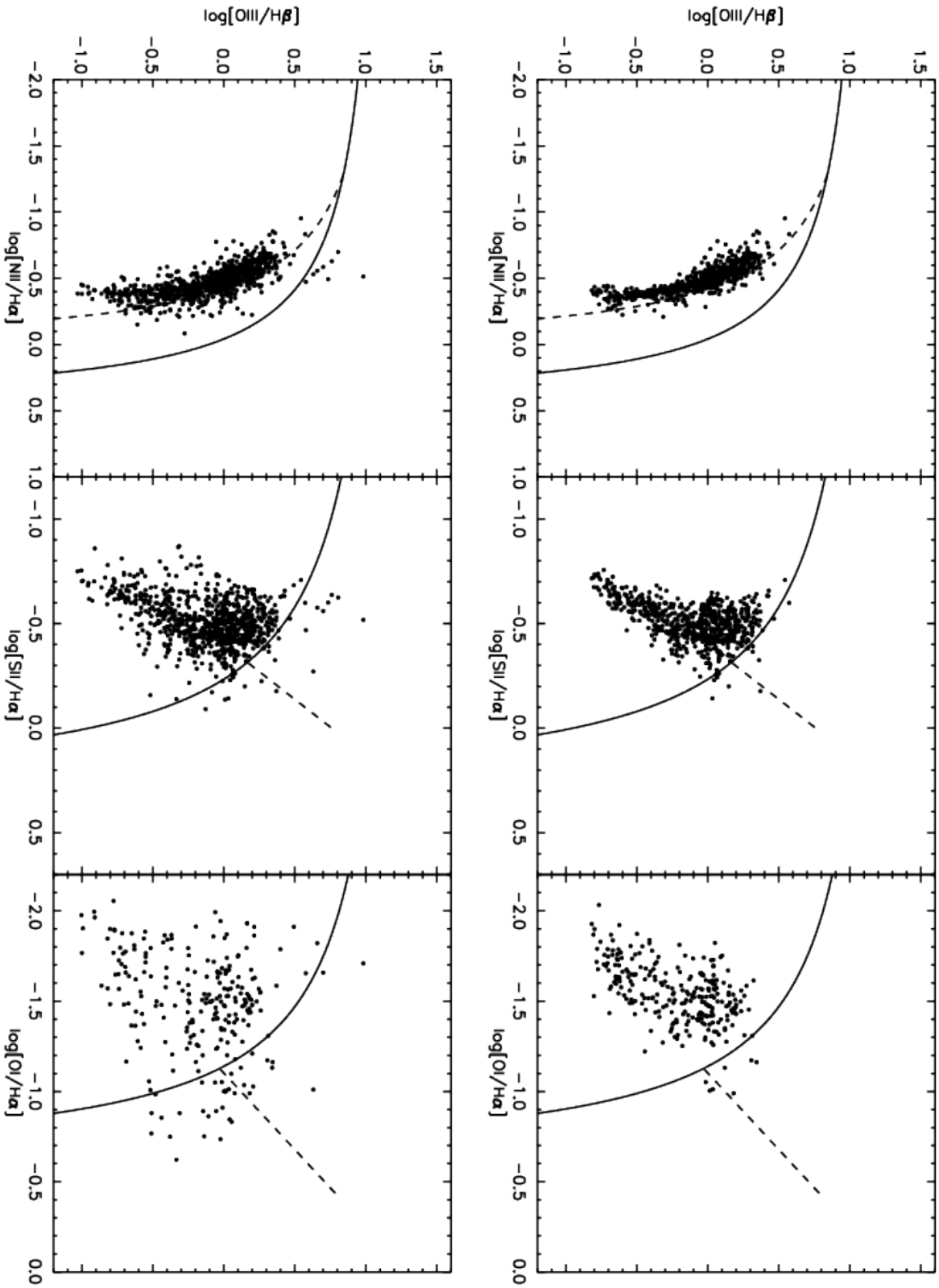

Figure A1. : Same as figure A1, but for IRAS F17222-5953 and a DSS R-band image.

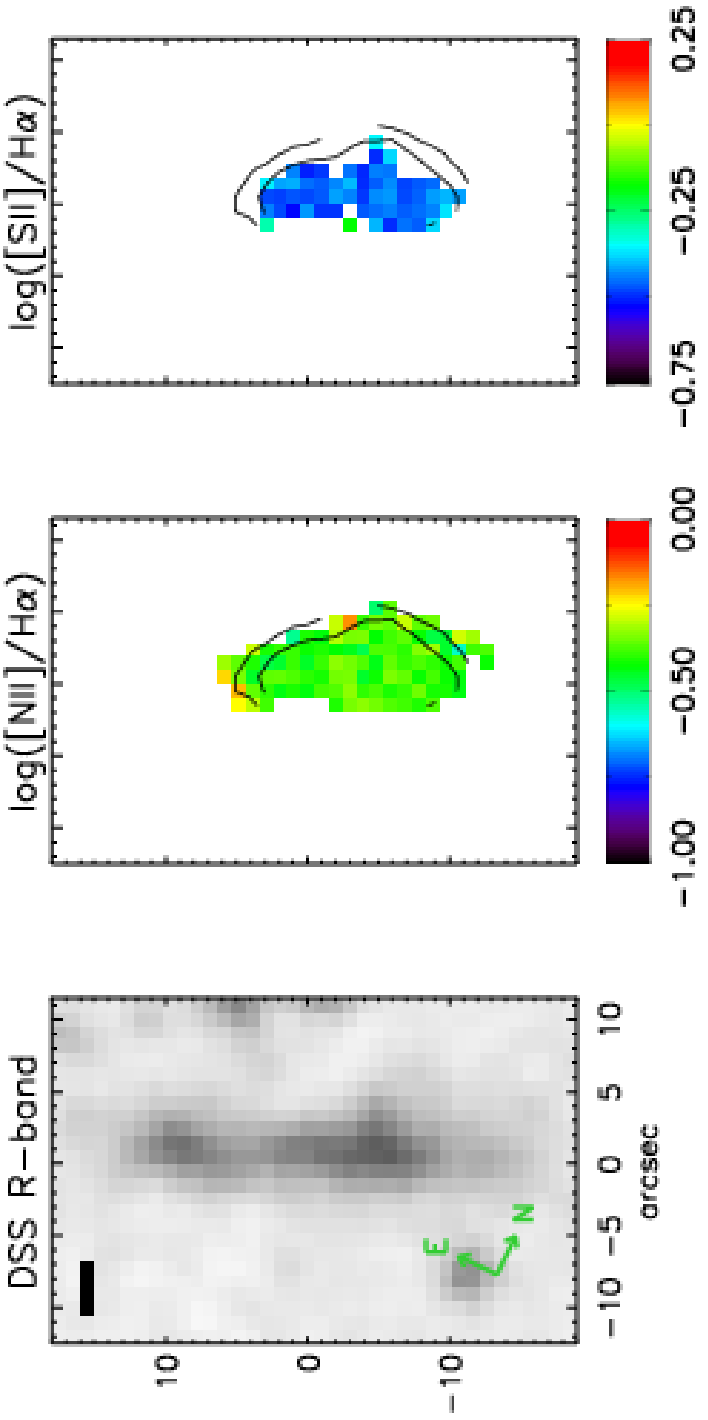

IRAS 17578-0400

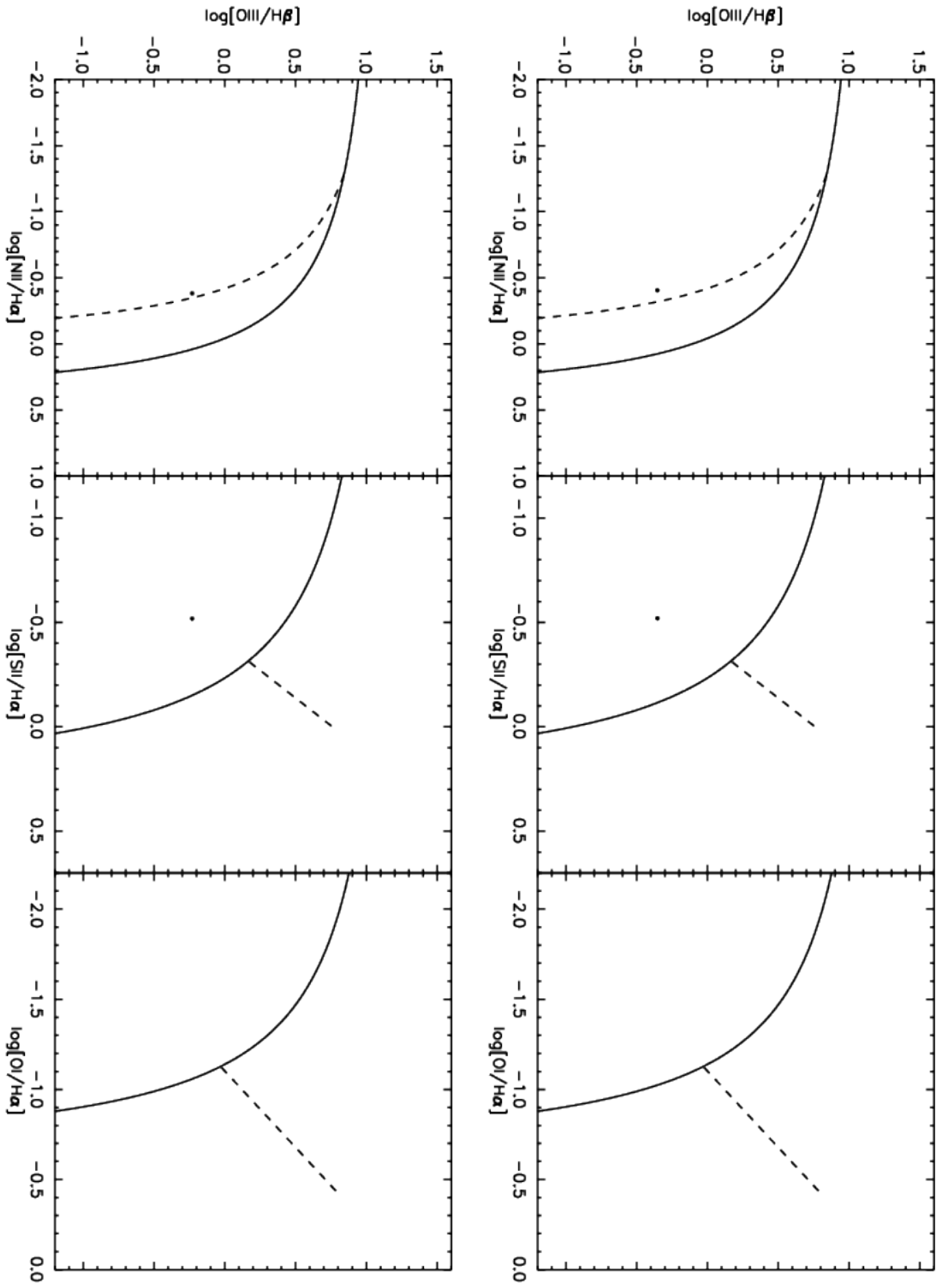

Figure A1. : Same as figure A1, but for IRAS 17578-0400 and a DSS R-band image.

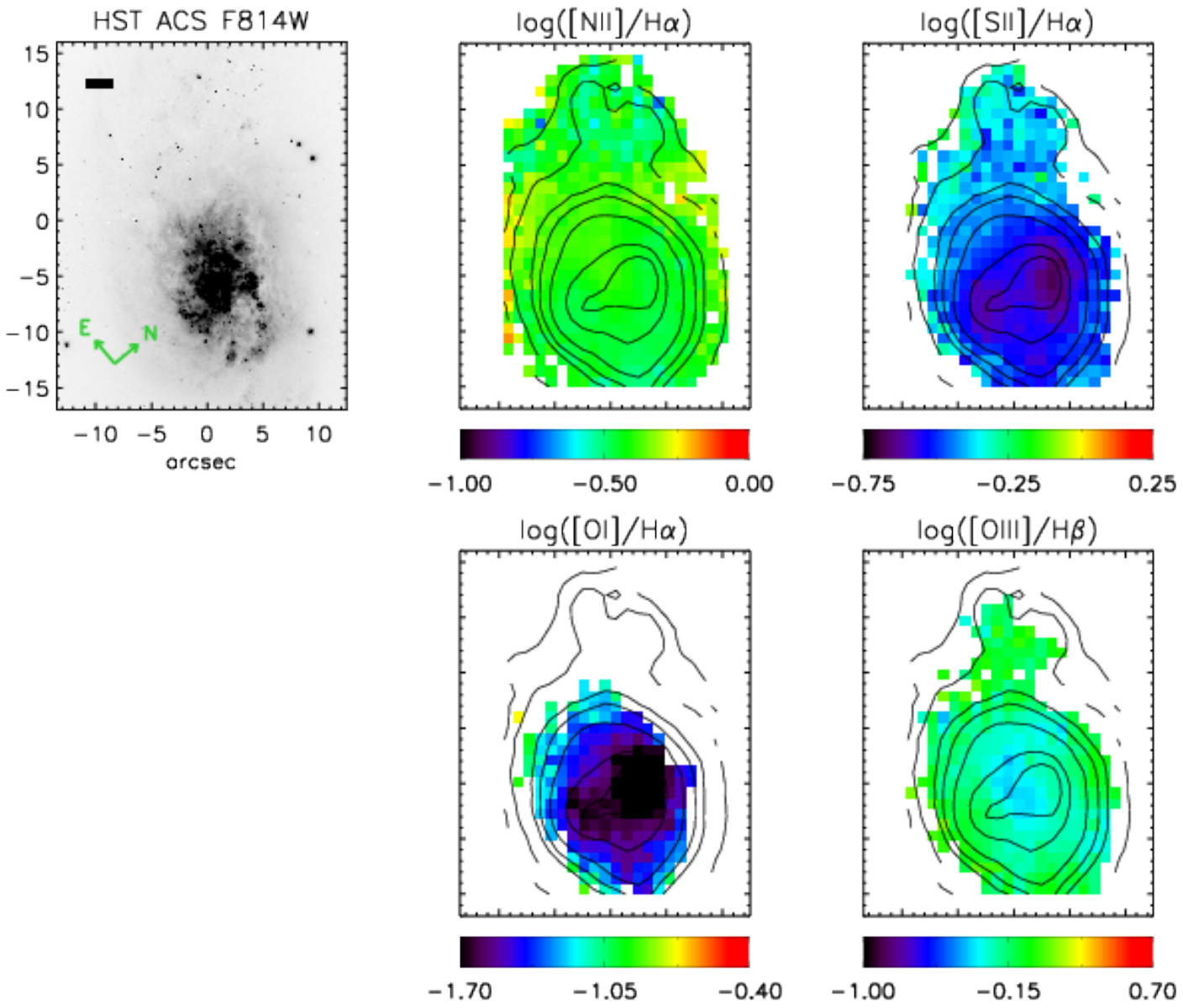

IRAS F18093-5744 N

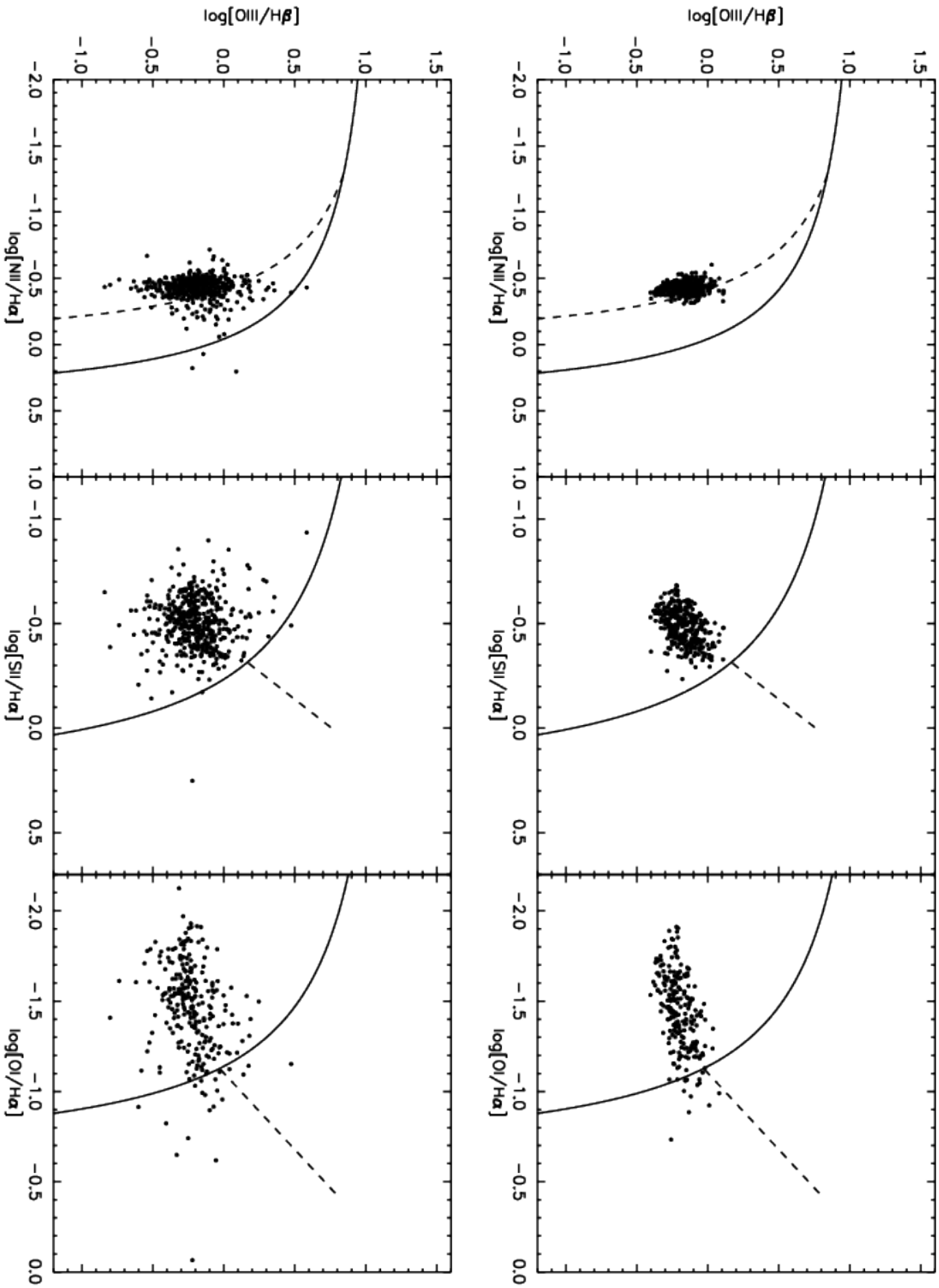

Figure A1. : Same as figure A1, but for IRAS F18093-5744 N.

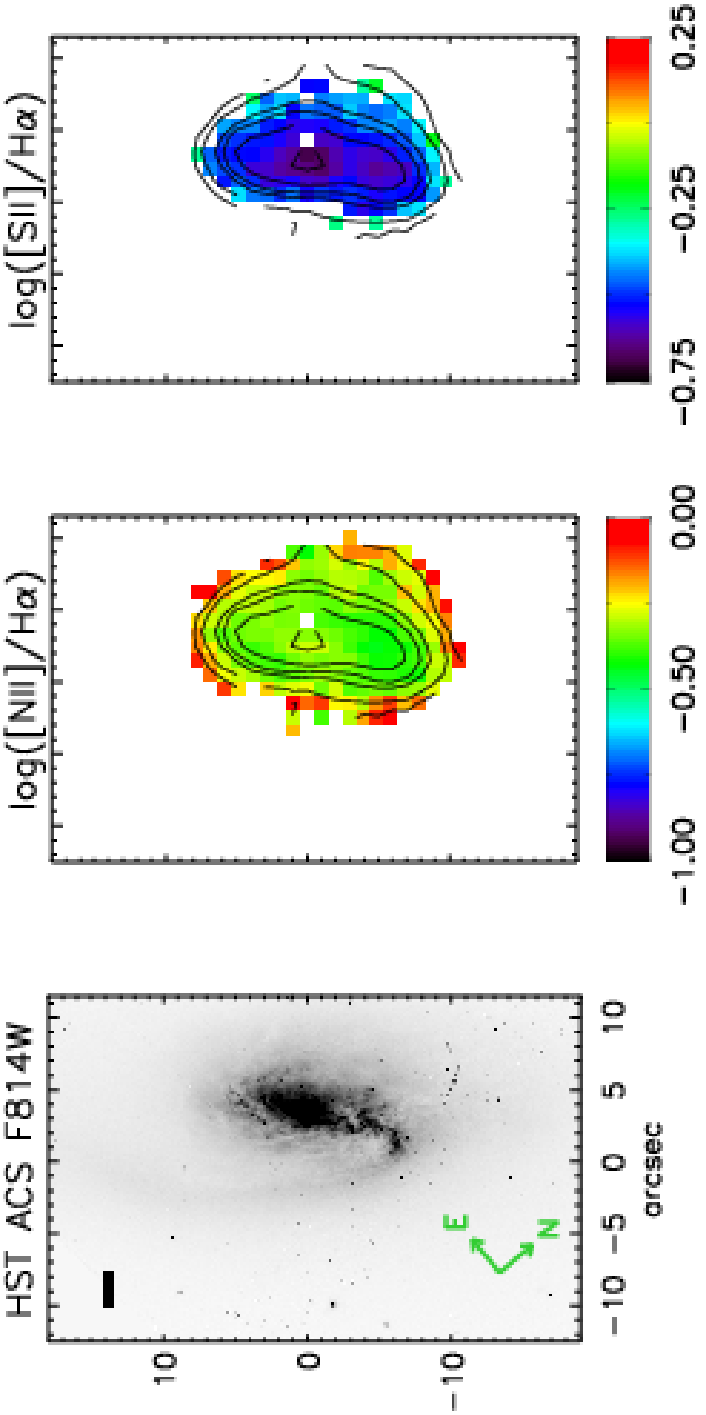

IRAS F18093-5744 S

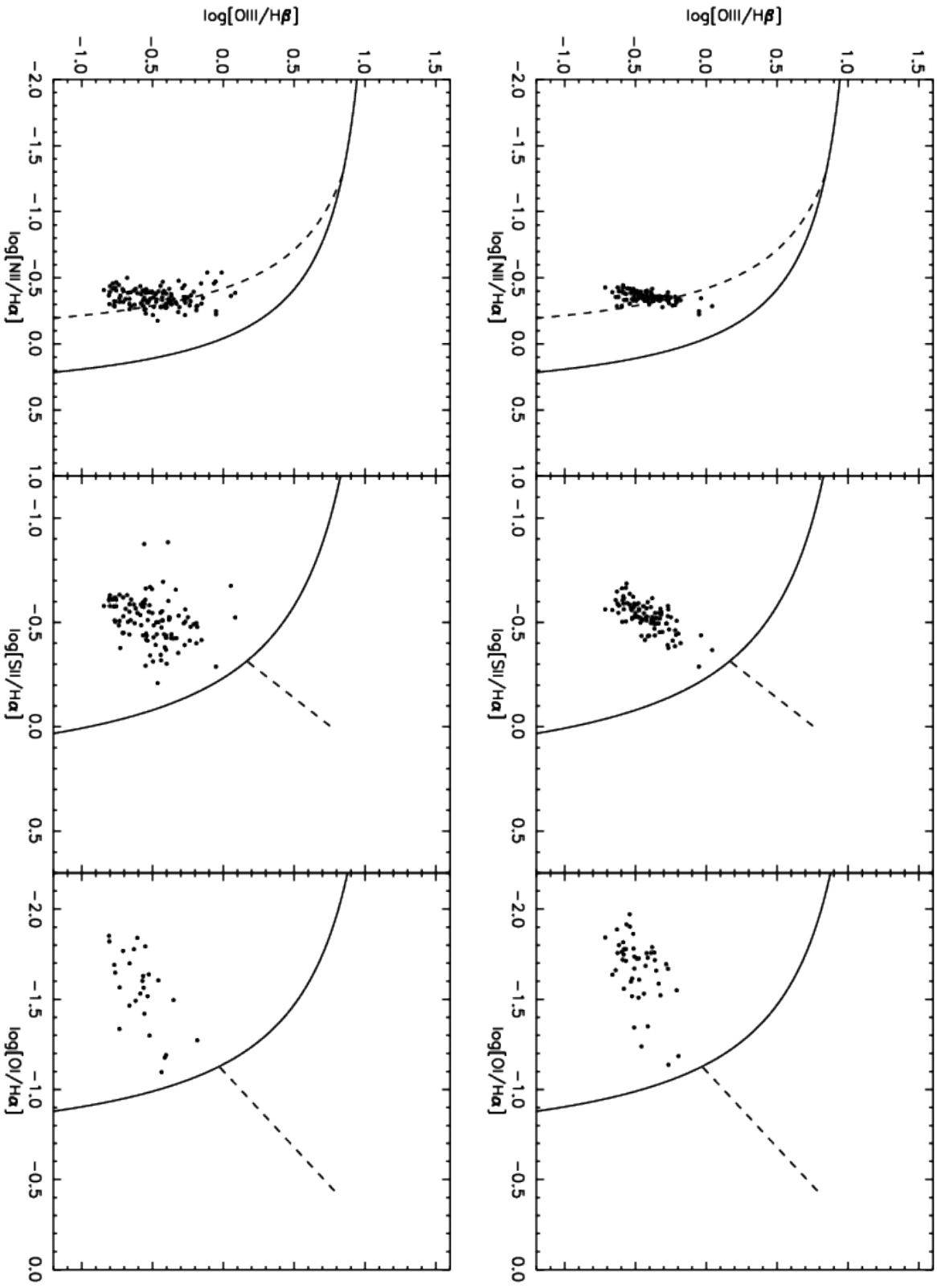

Figure A1. : Same as figure A1, but for IRAS F18093-5744 S.

IRAS F18093-5744 C

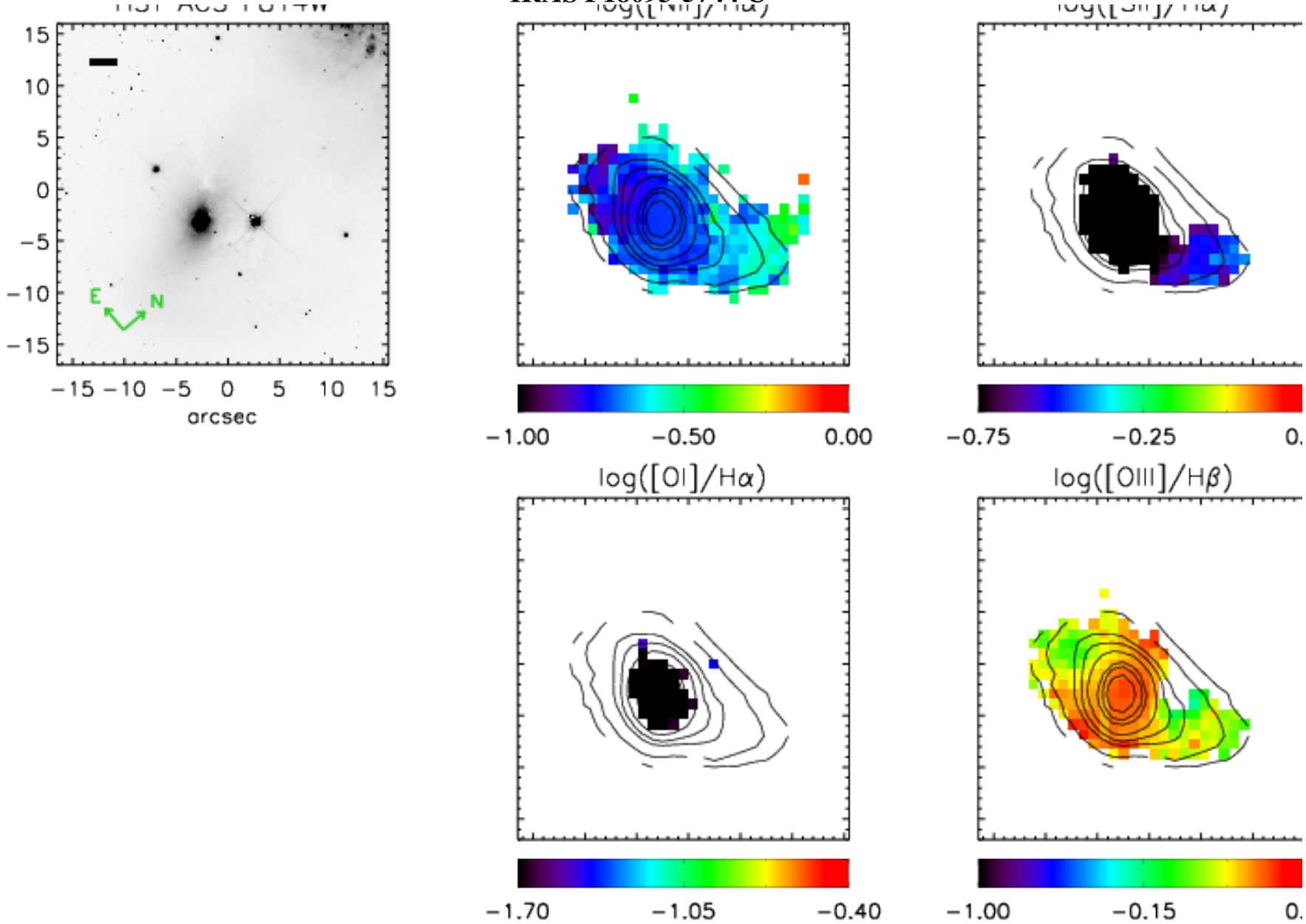

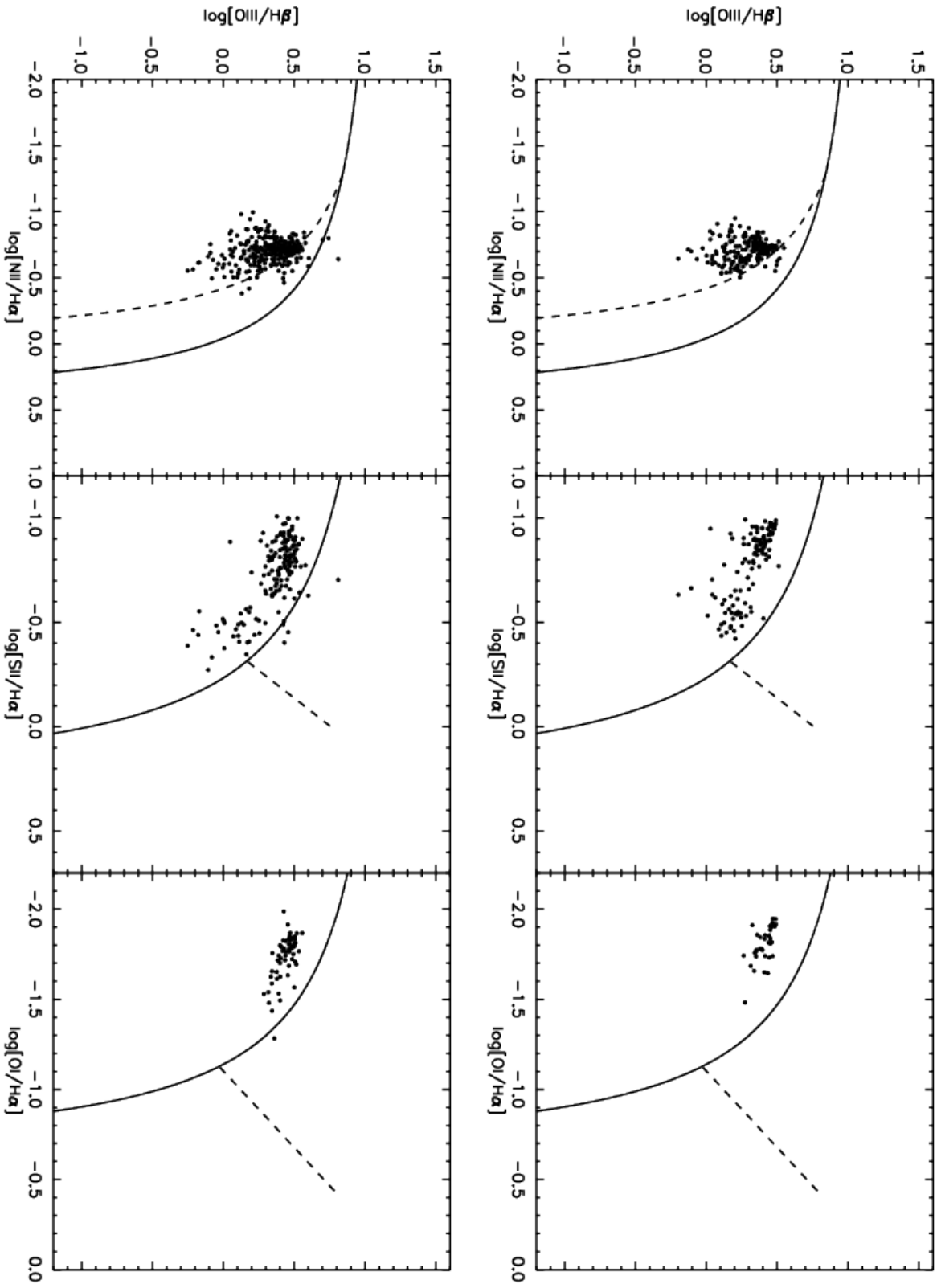

Figure A1. : Same as figure A1, but for IRAS F18093-5744 C.

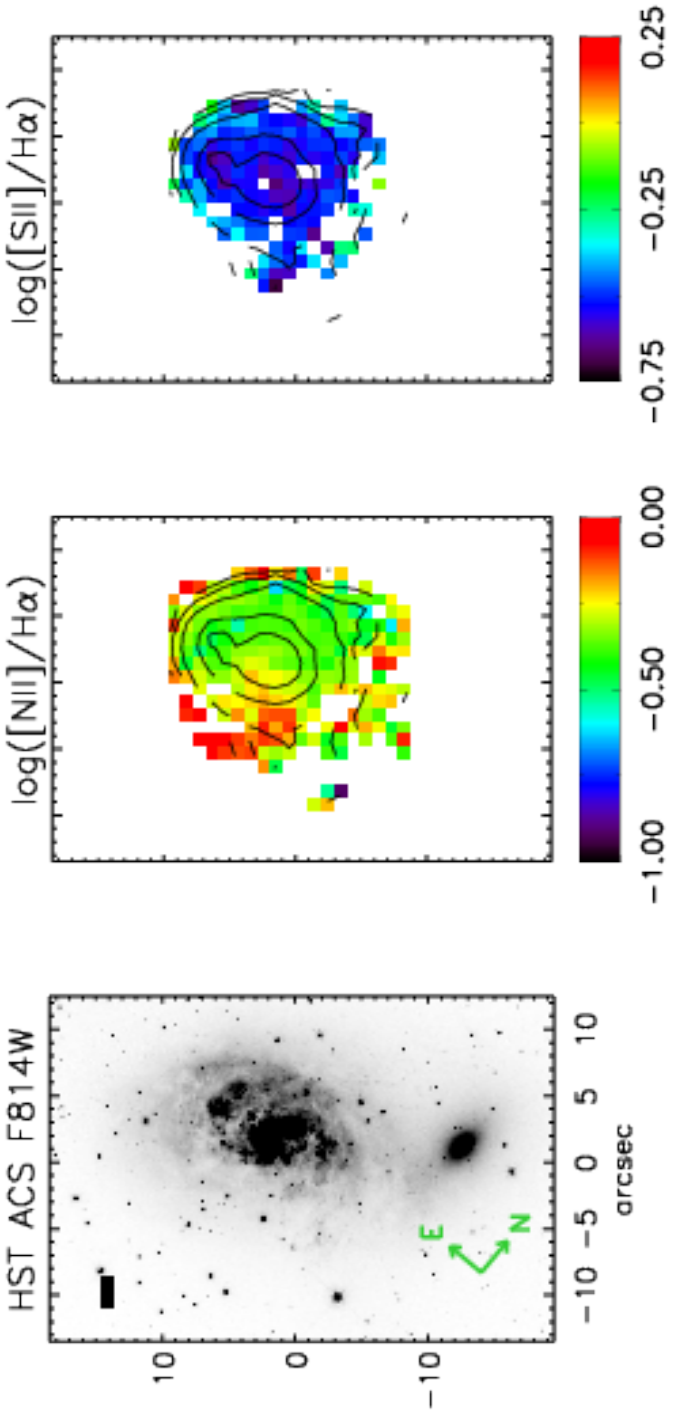

IRAS F18293-3413

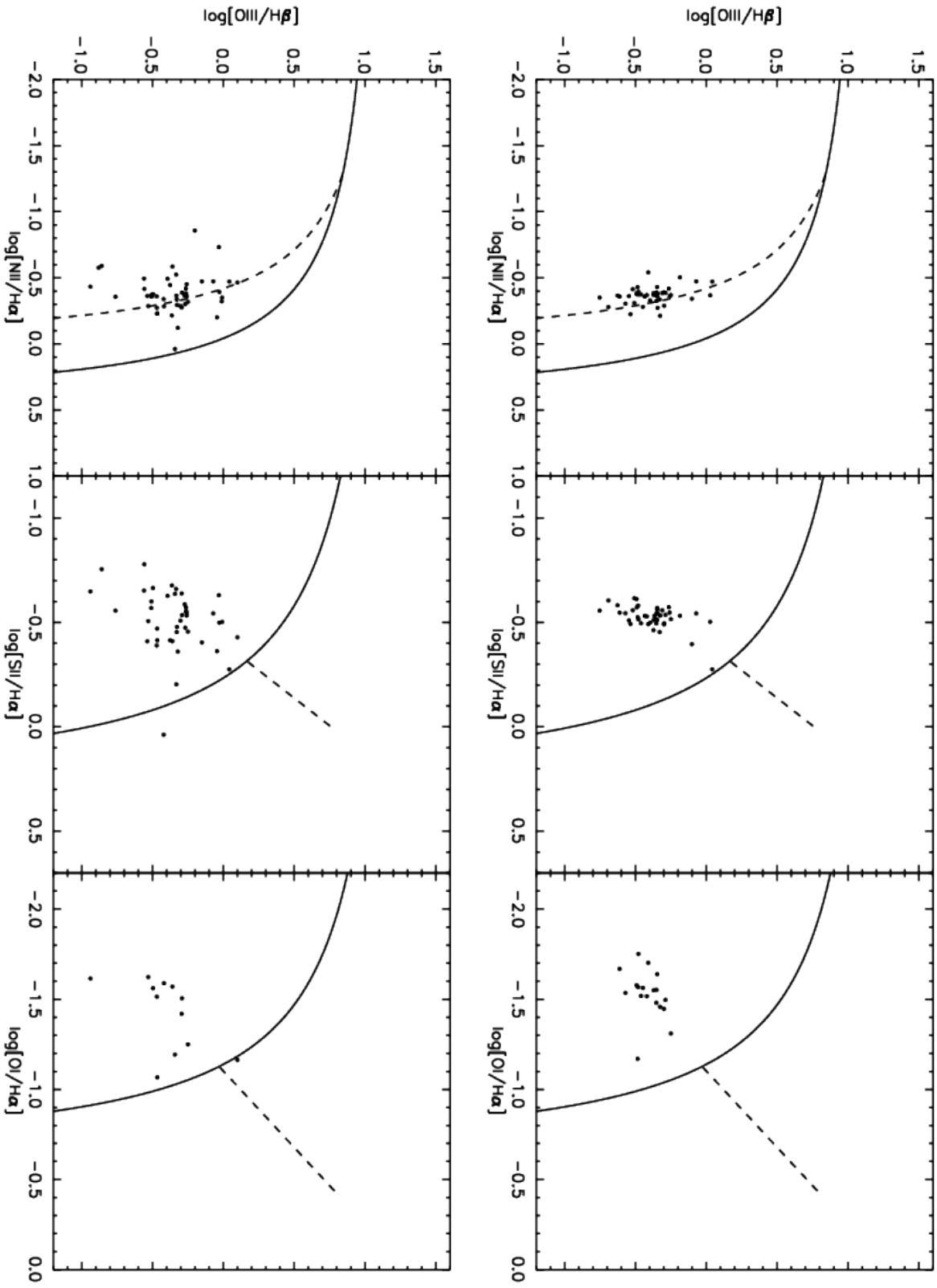

Figure A1. : Same as figure A1, but for IRAS F18293-3413.

IRAS F18341-5732

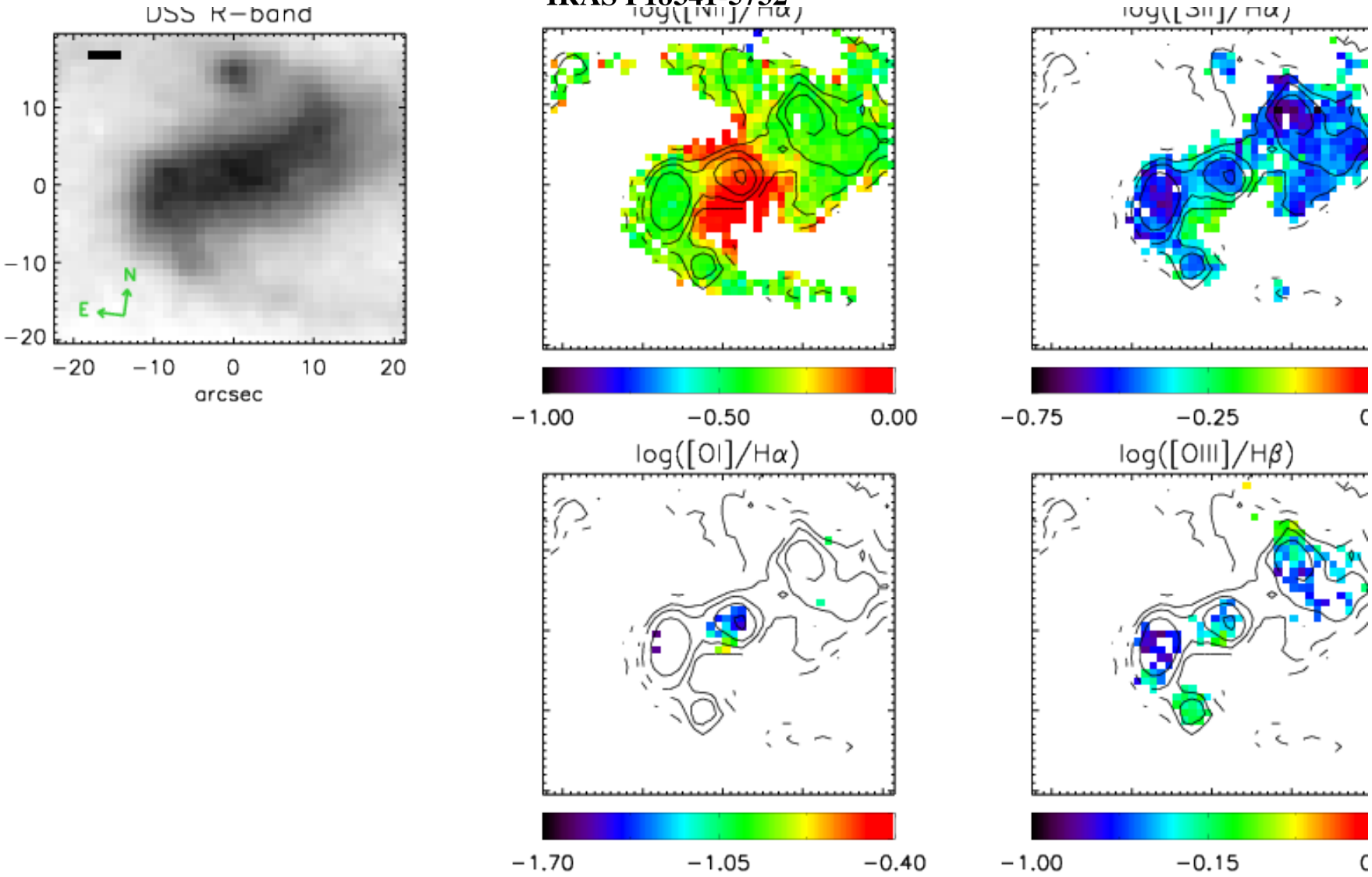

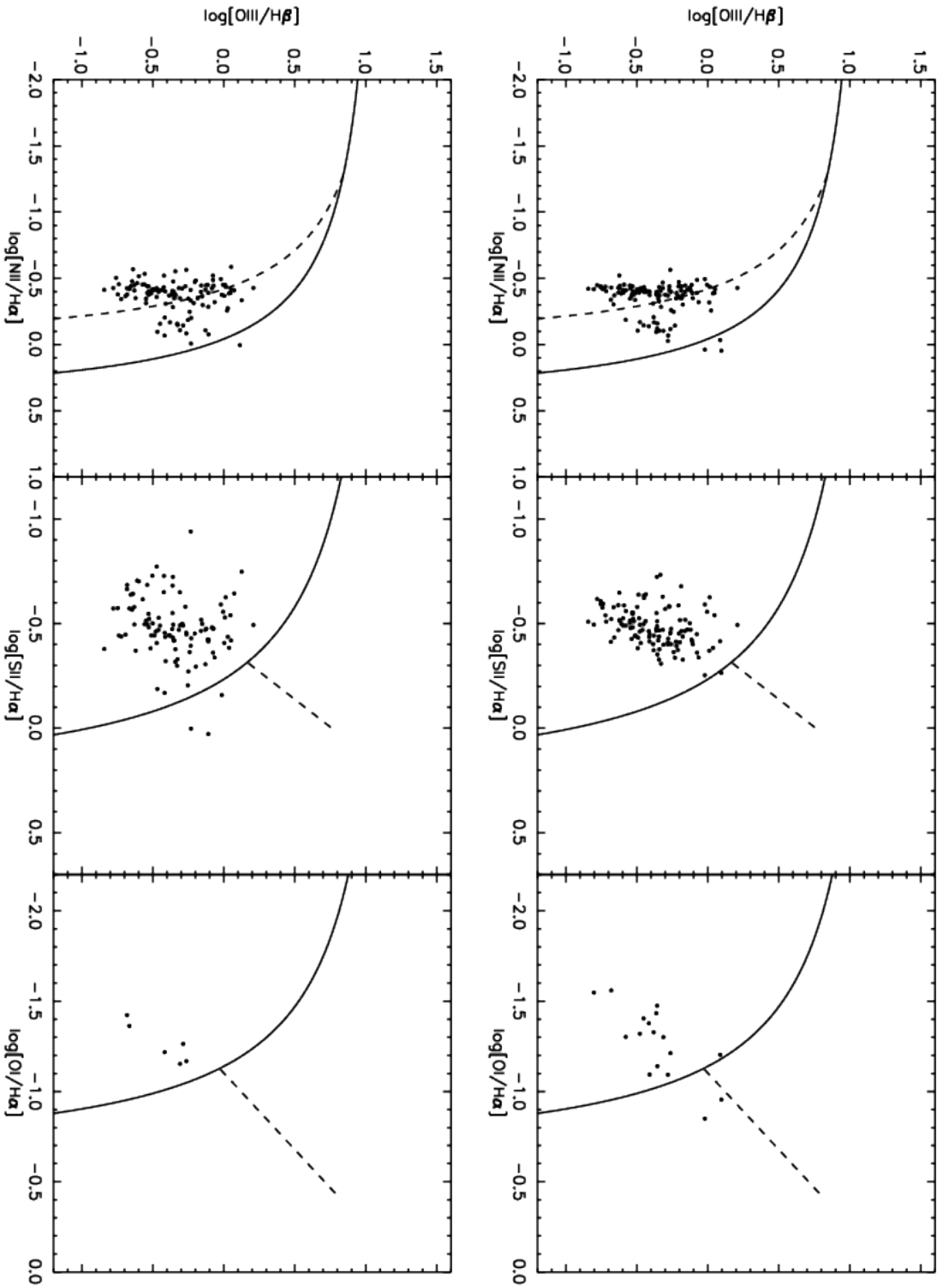

Figure A1. : Same as figure A1, but for IRAS F18341-5732 and a DSS R-band image.

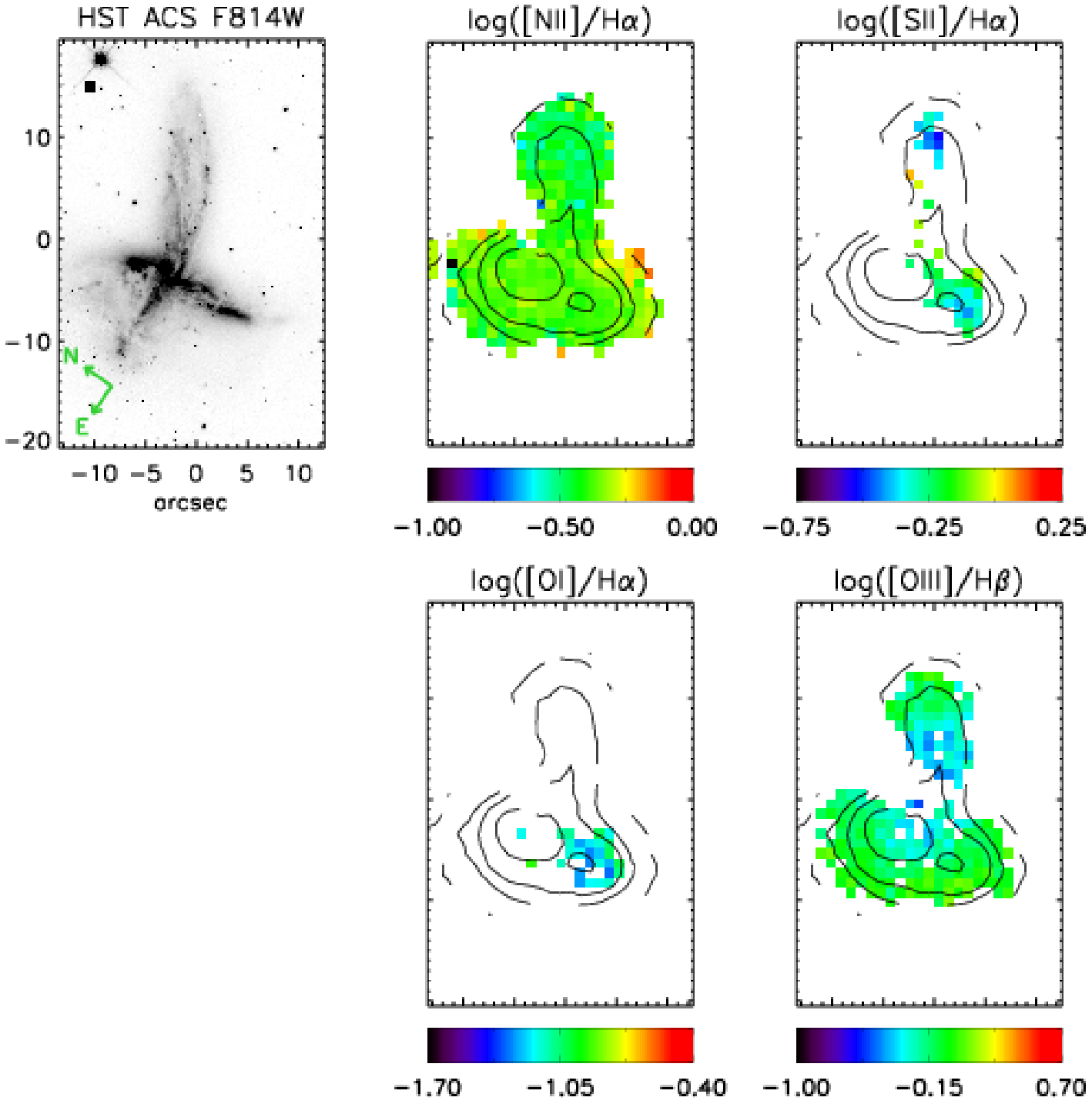

IRAS F19115-2124

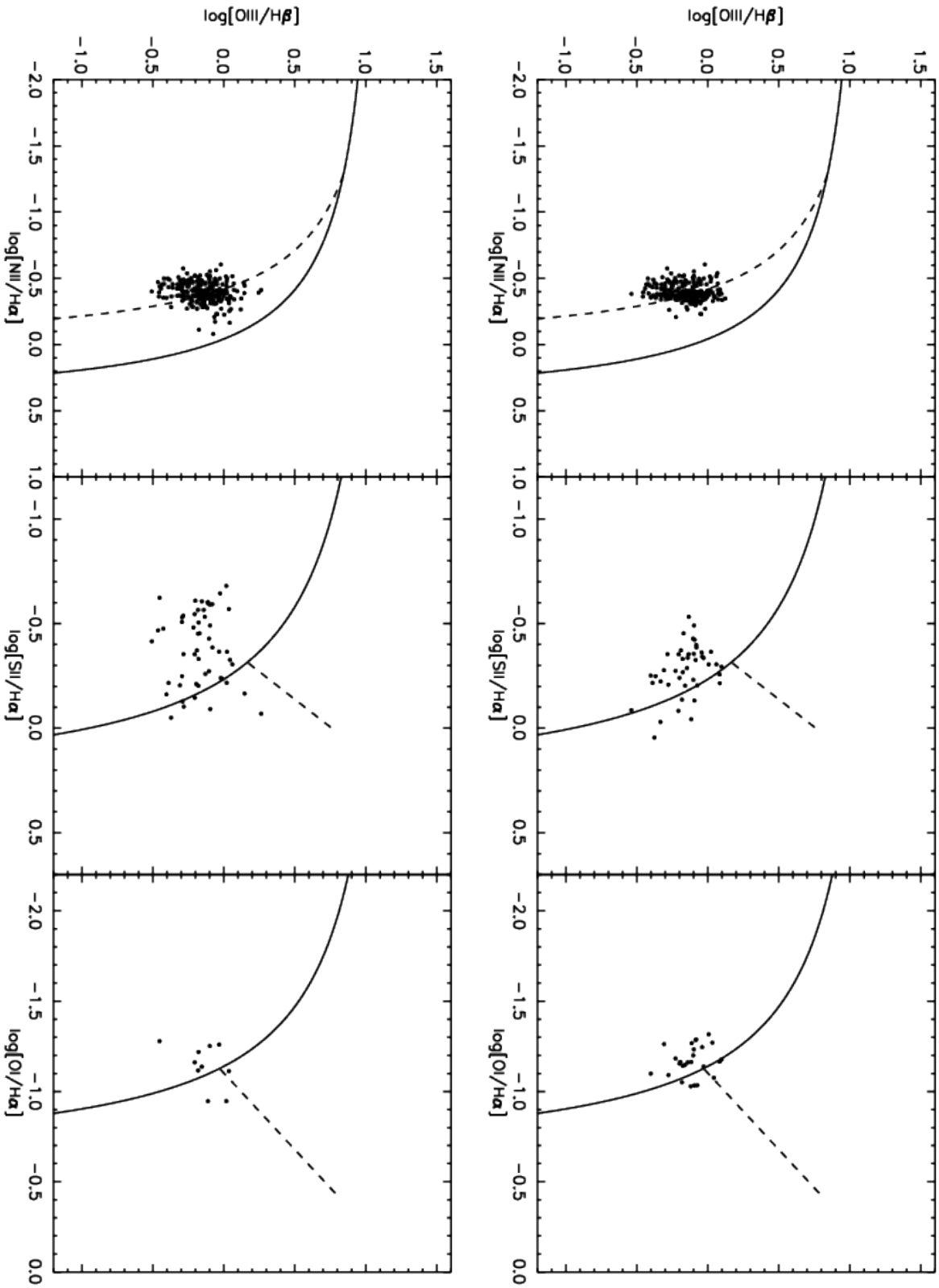

Figure A1. : Same as figure A1, but for IRAS F19115-2124.

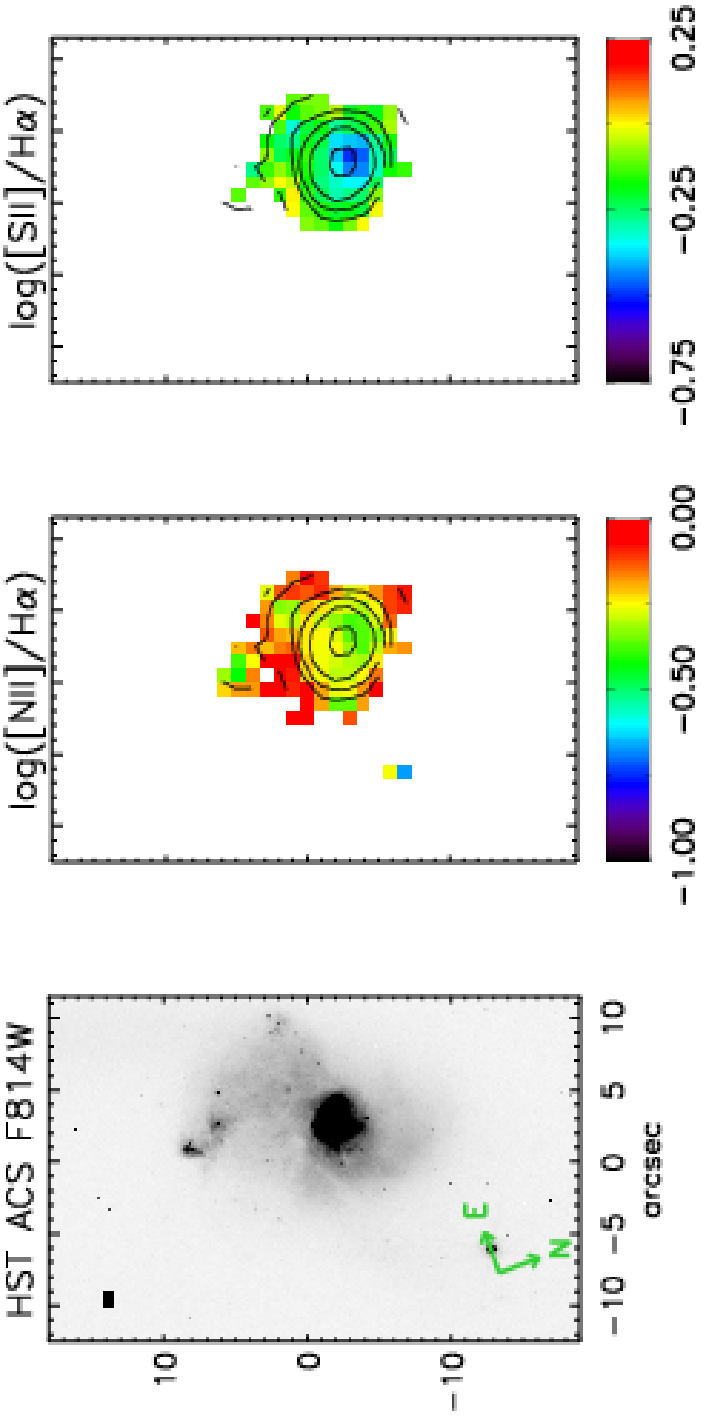

IRAS F20551-4250

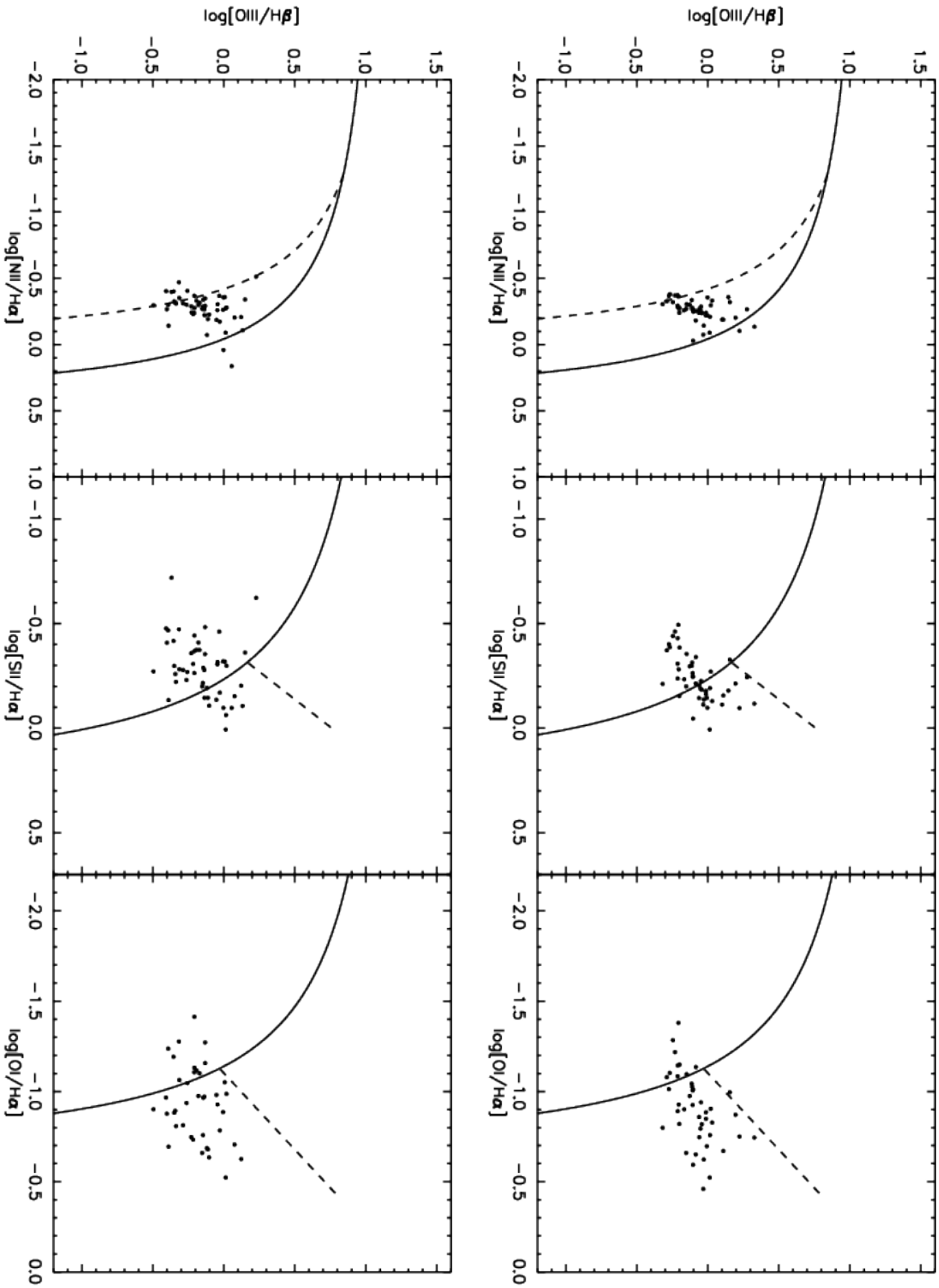

Figure A1. : Same as figure A1, but for IRAS F20551-4250.

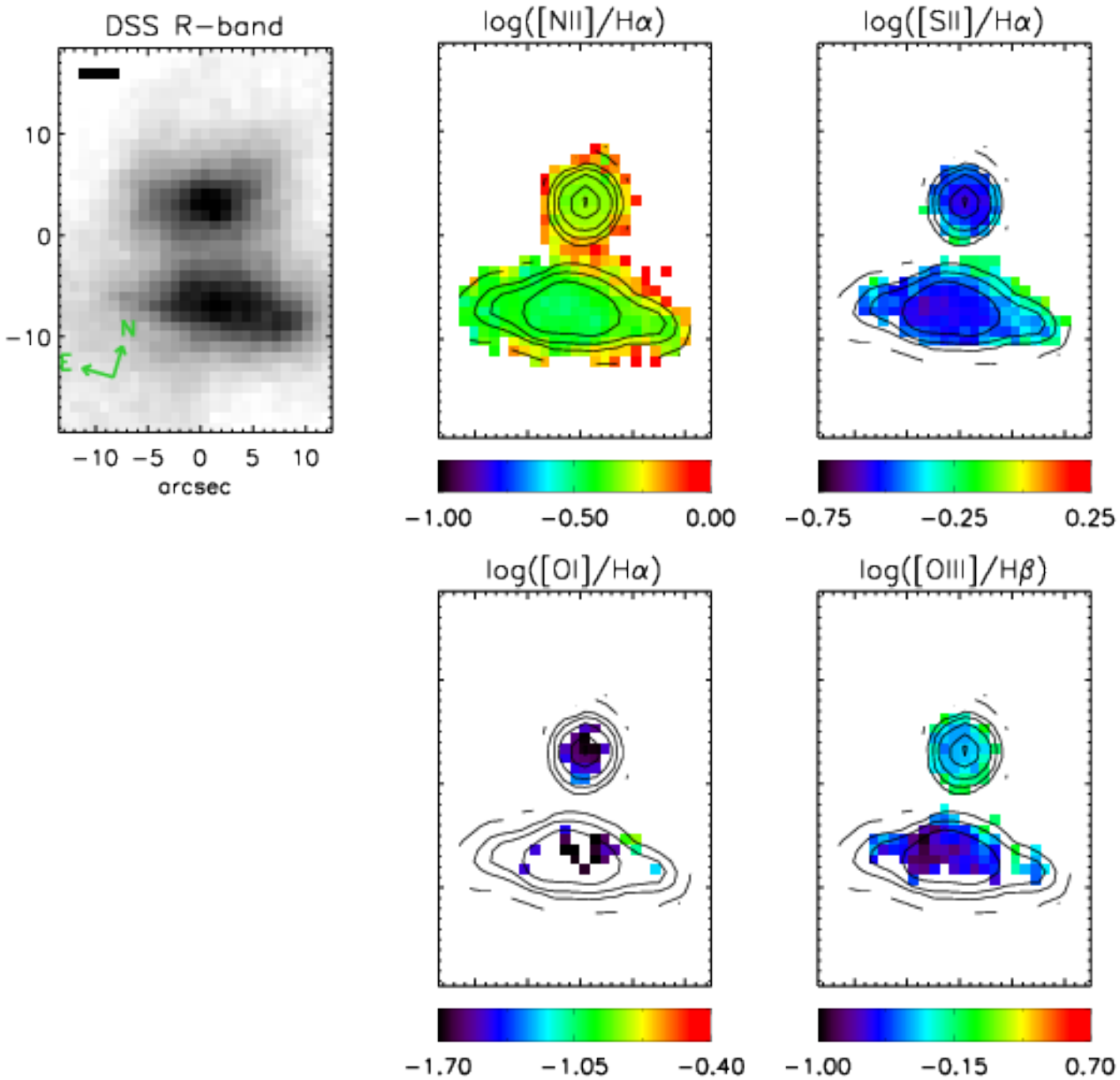

IRAS F21330-3846

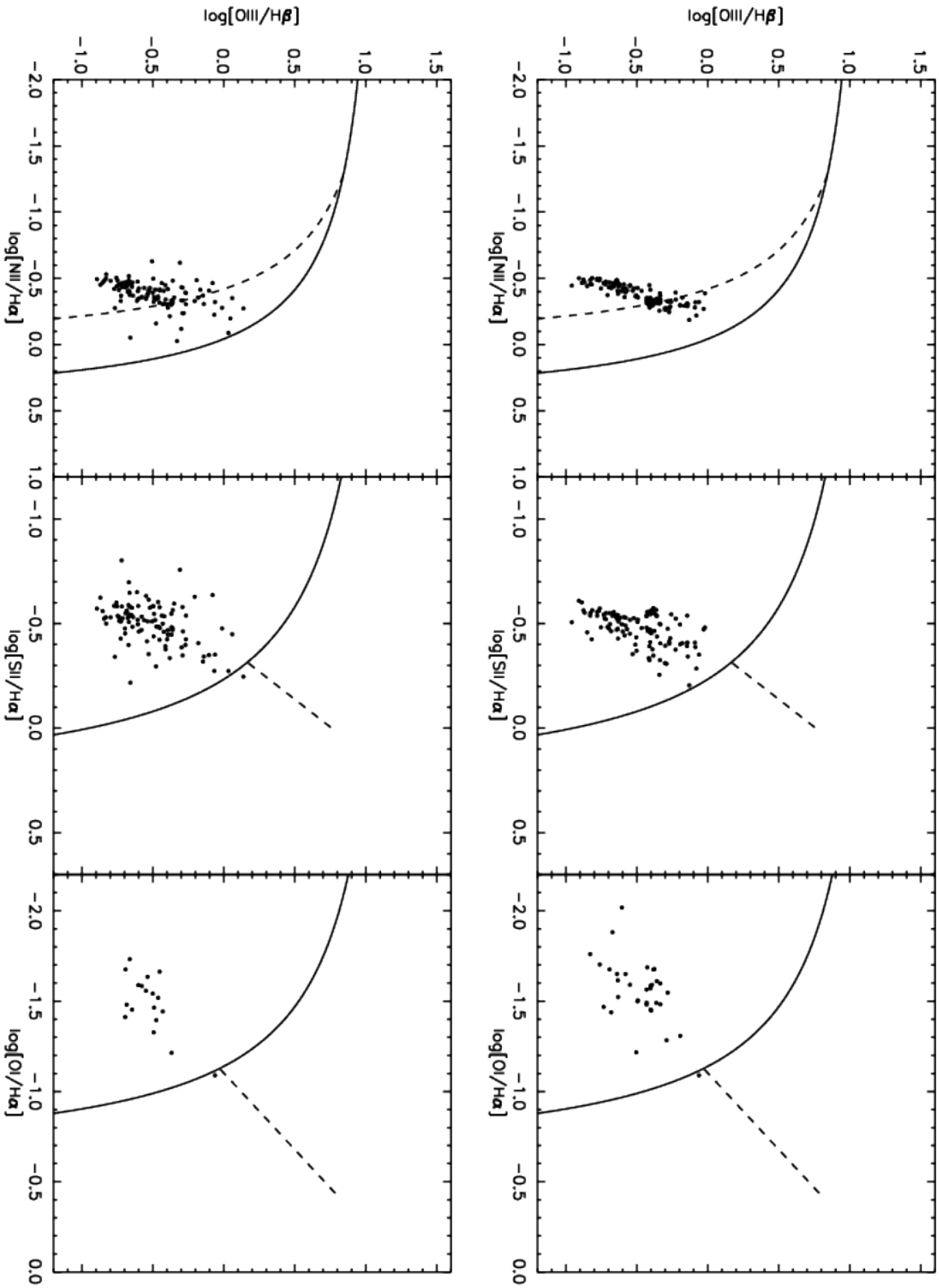

Figure A1. : Same as figure A1, but for IRAS F21330-3846 and a DSS R-band image.

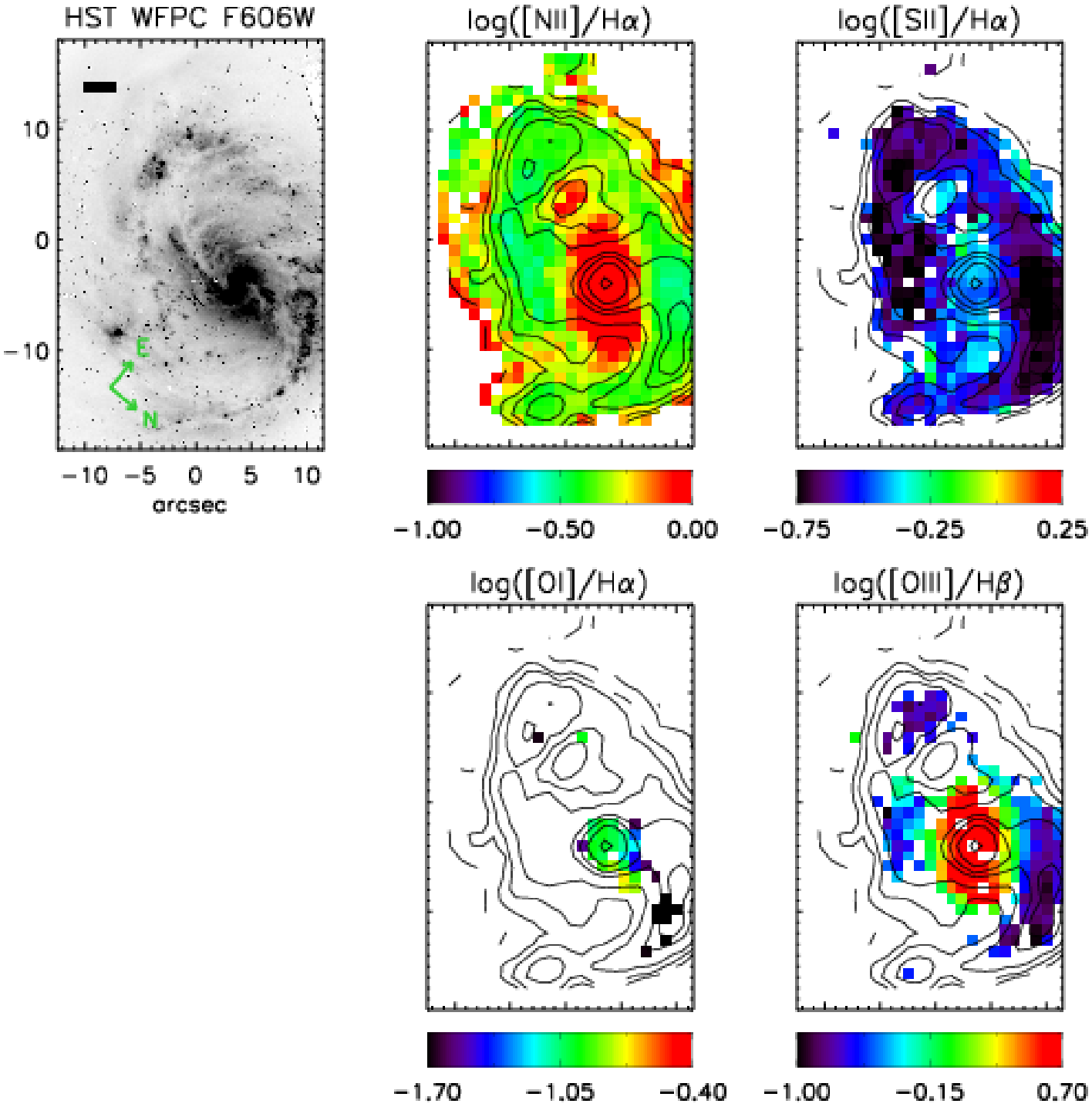

IRAS F21453-3511

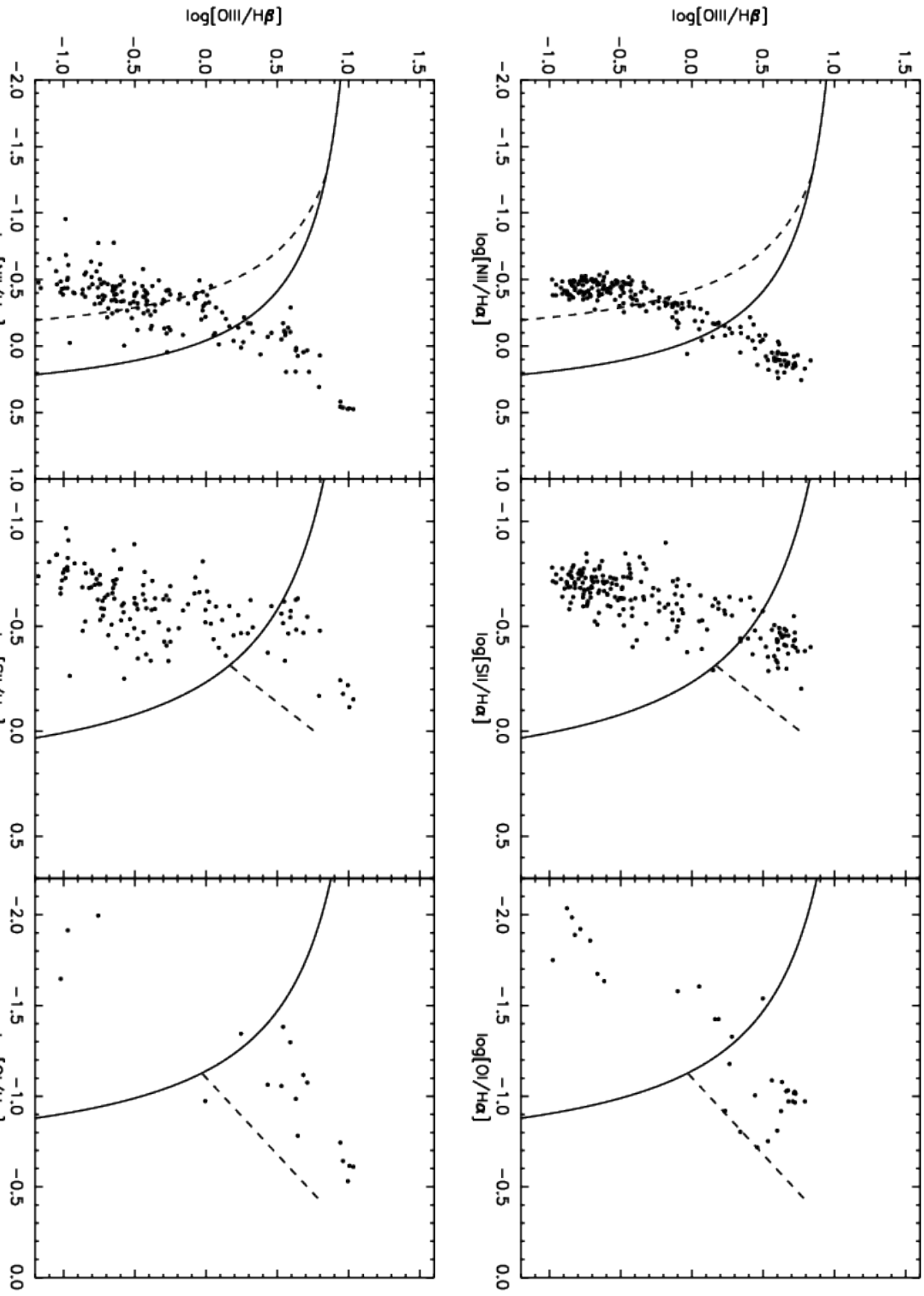

Figure A1. : Same as figure A1, but for IRAS F21453-3511 and an *HST* G-band image.

IRAS F22467-4906

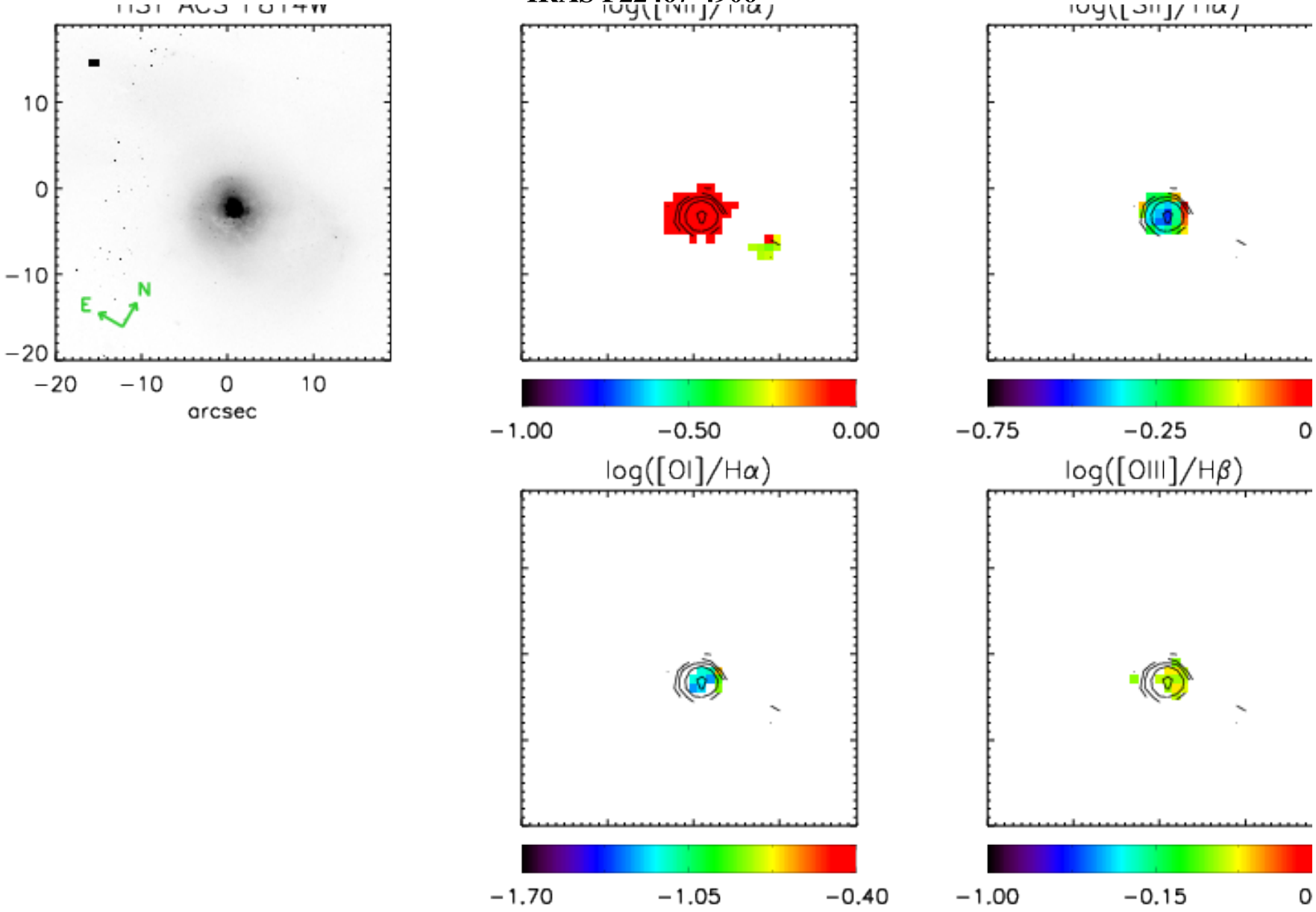

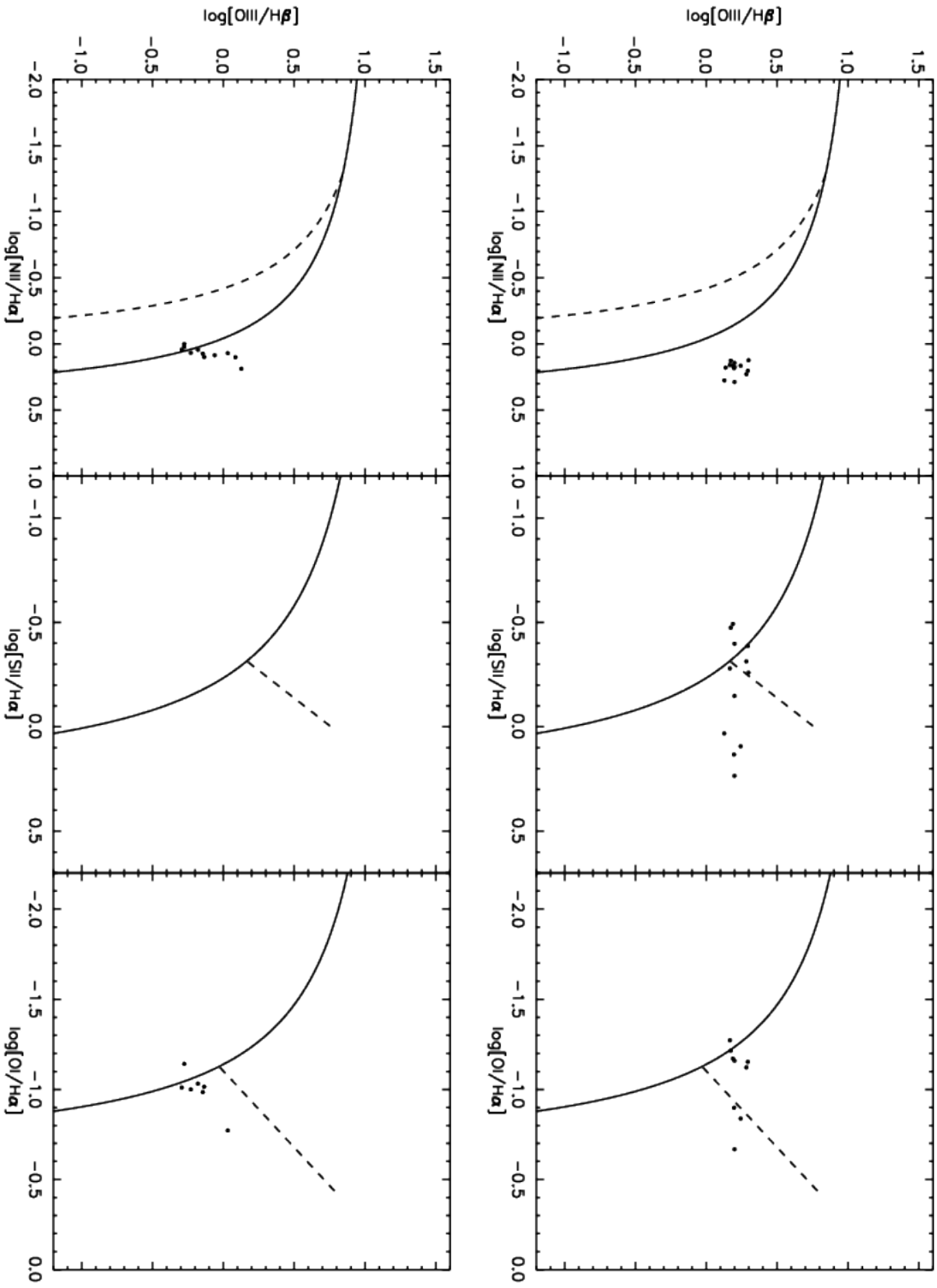

Figure A1. : Same as figure A1, but for IRAS F22467-4906.

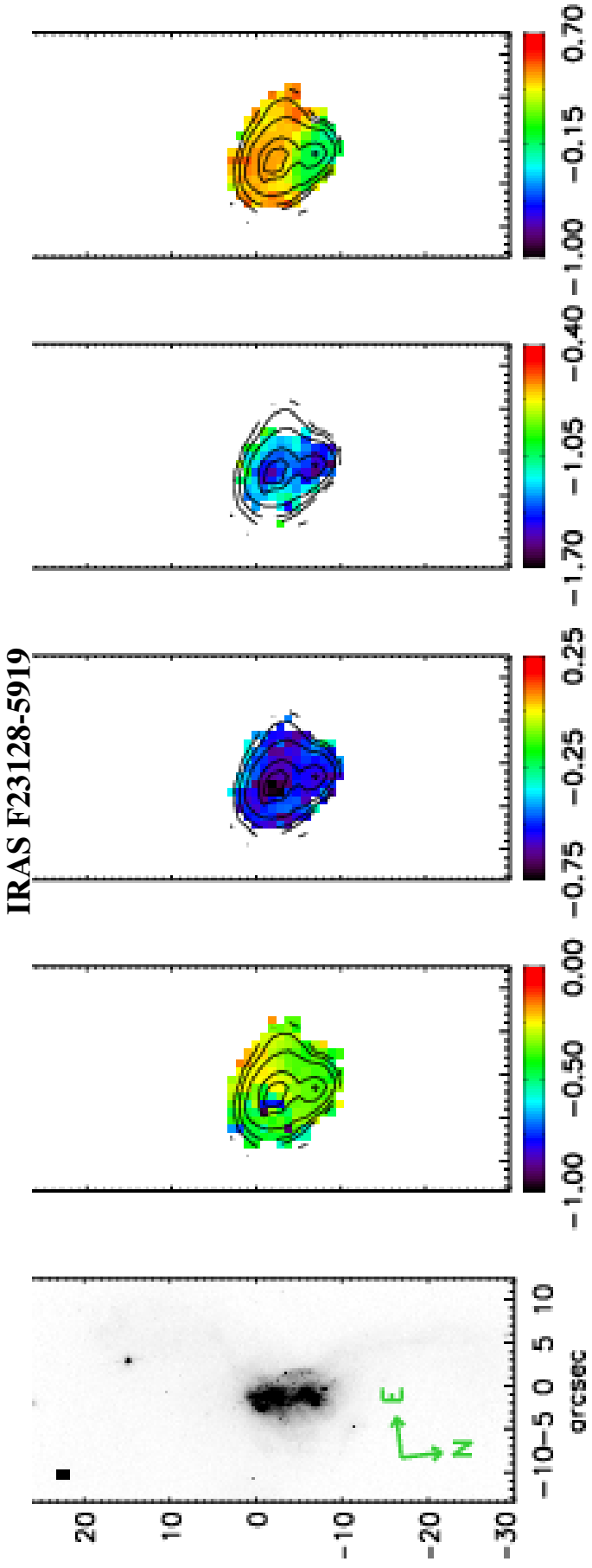
IRAS F23128-5919
20
10
0
-10
-20
-30
-10 -5 0 5 10
arcsec
E
N
-1.00 -0.50 0.00
-1.00 -0.75 -0.25 0.25
-1.70 -1.05 -0.40
-1.00 -0.15 0.70

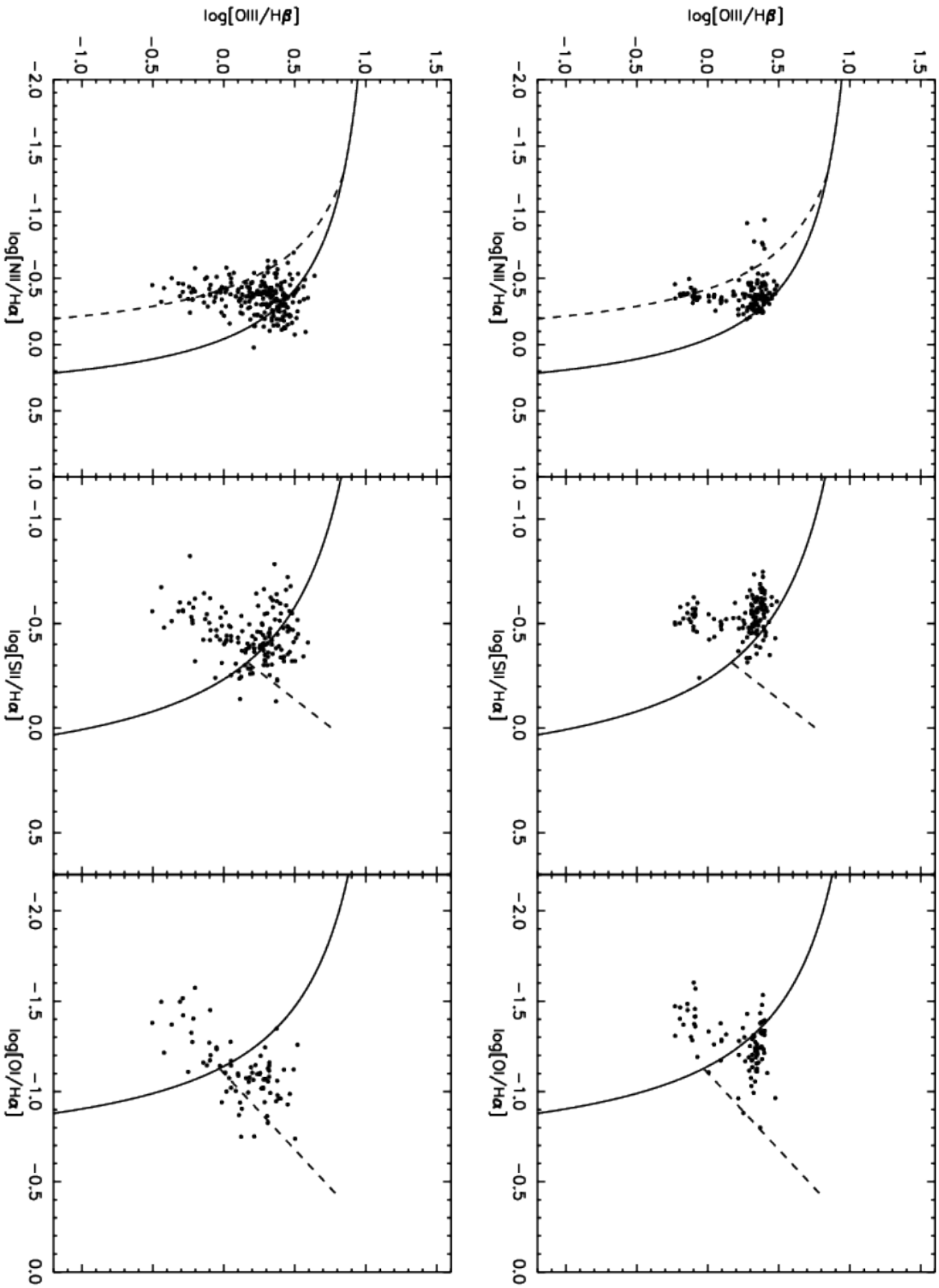

Figure A1. : Same as figure A1, but for IRAS F23128-5919.

B. VELOCITY DISPERSION DISTRIBUTIONS

This section contains the velocity dispersion distributions and comparison to line ratios for the entire WiFeS GOALS sample, generated as described in section 5.

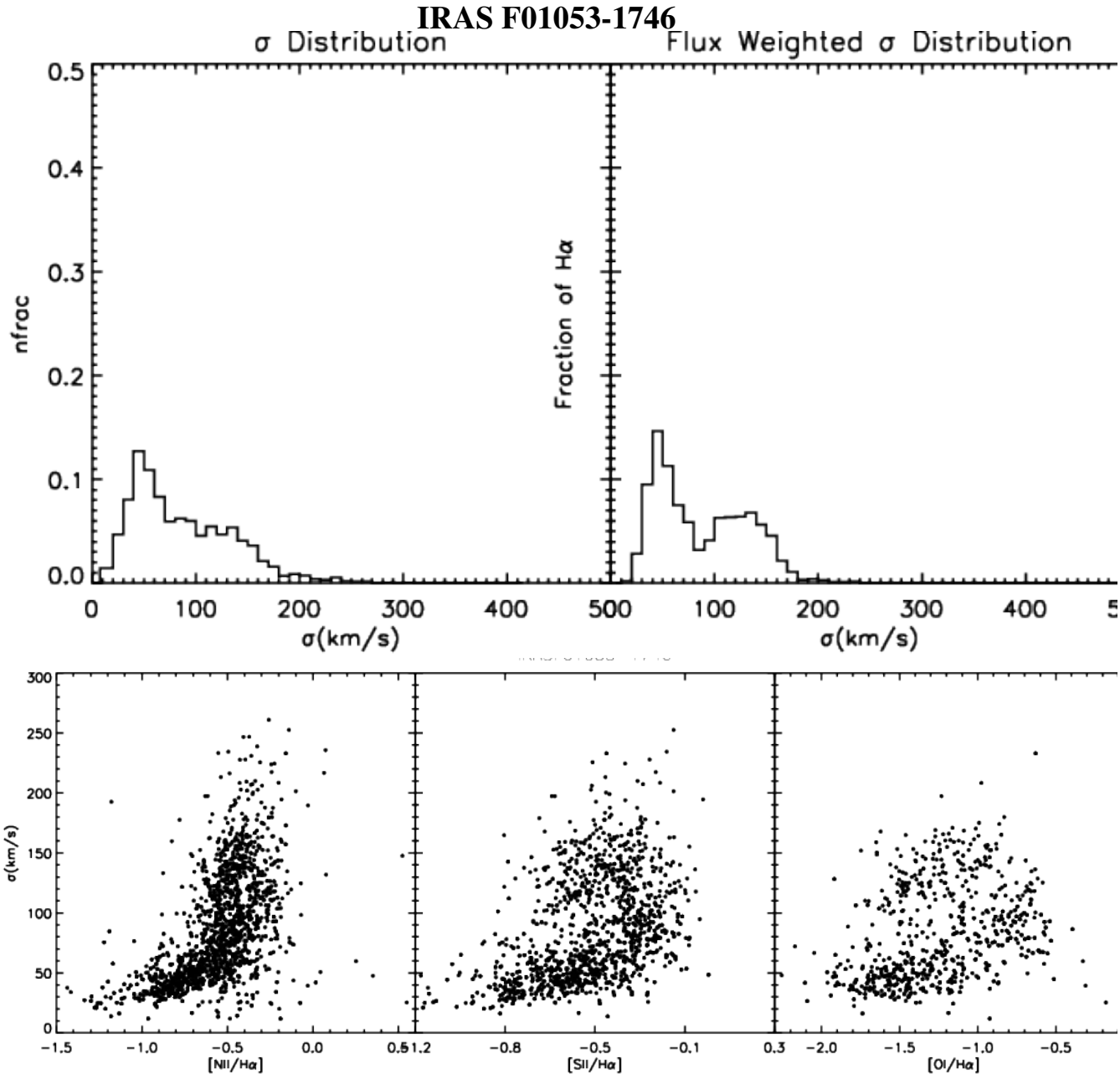

Figure B1. : Velocity dispersion distribution and comparison with line ratios. The top left panel shows the histogram for the fraction of the total number of components for a given velocity dispersion The top right panel shows a similar histogram, but with the fraction of the total Hα flux for a given velocity dispersion. Systems with a stronger contribution from shocks show a larger fraction above $\sigma > 90km\ s^{-1}$. The bottom three panels show various diagnostic emission line ratios vs. velocity dispersion. Lower emission line ratios are, on average, dominated by lower-σ star forming regions.

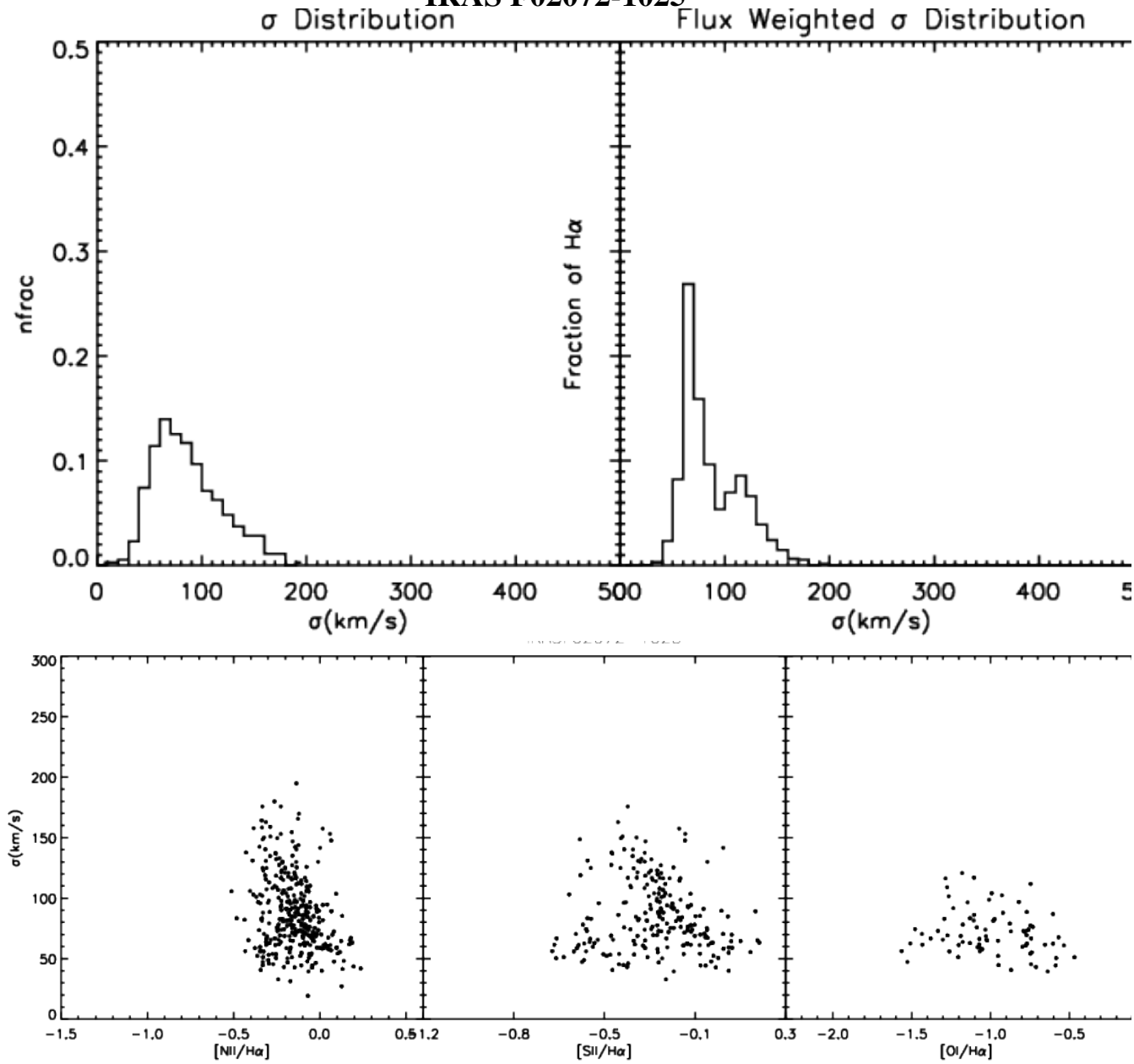

Figure B2. : Same as Figure B1, but for IRAS F02072-1025.

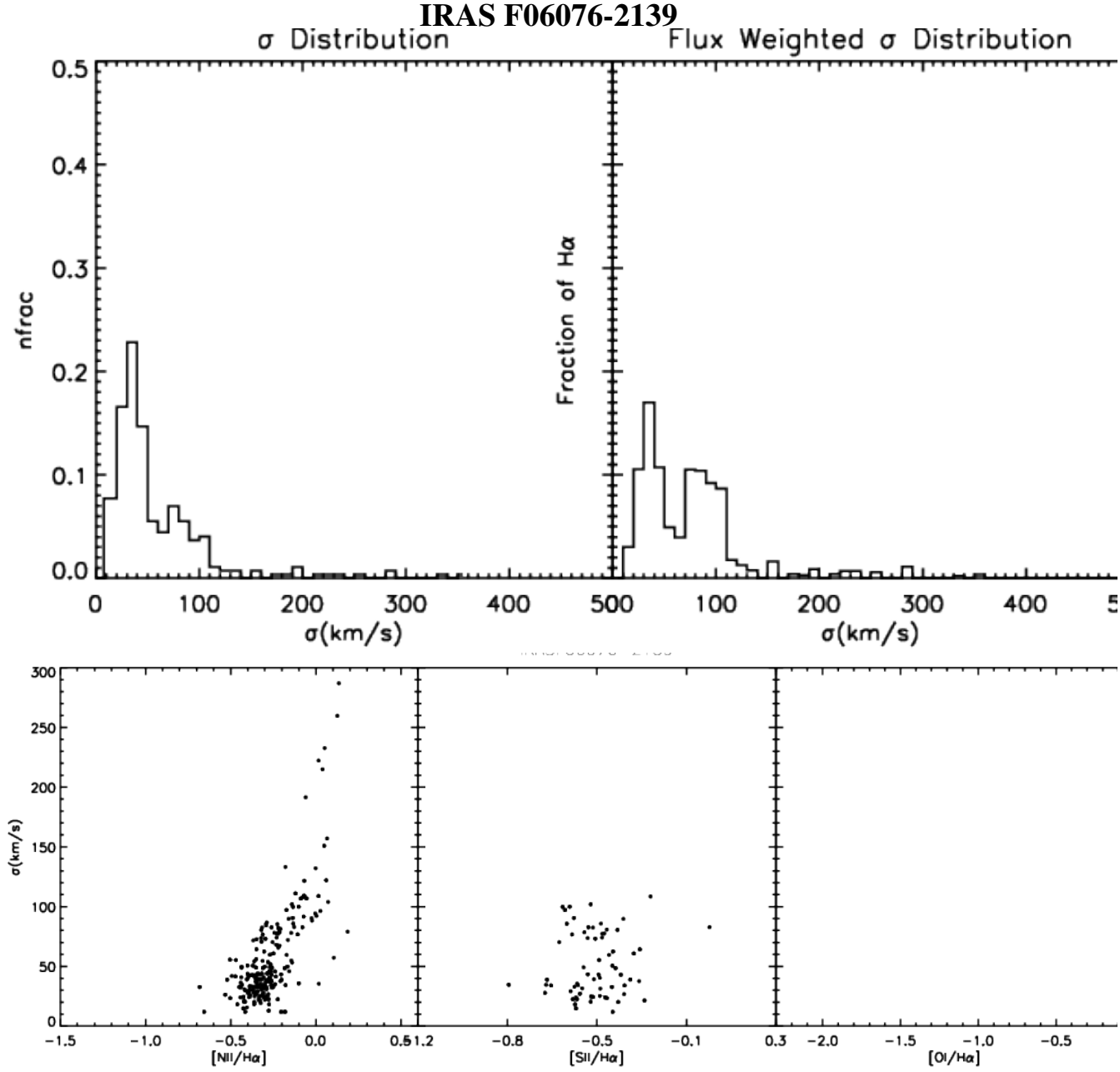

Figure B3. : Same as Figure B1, but for IRAS F06076-2139.

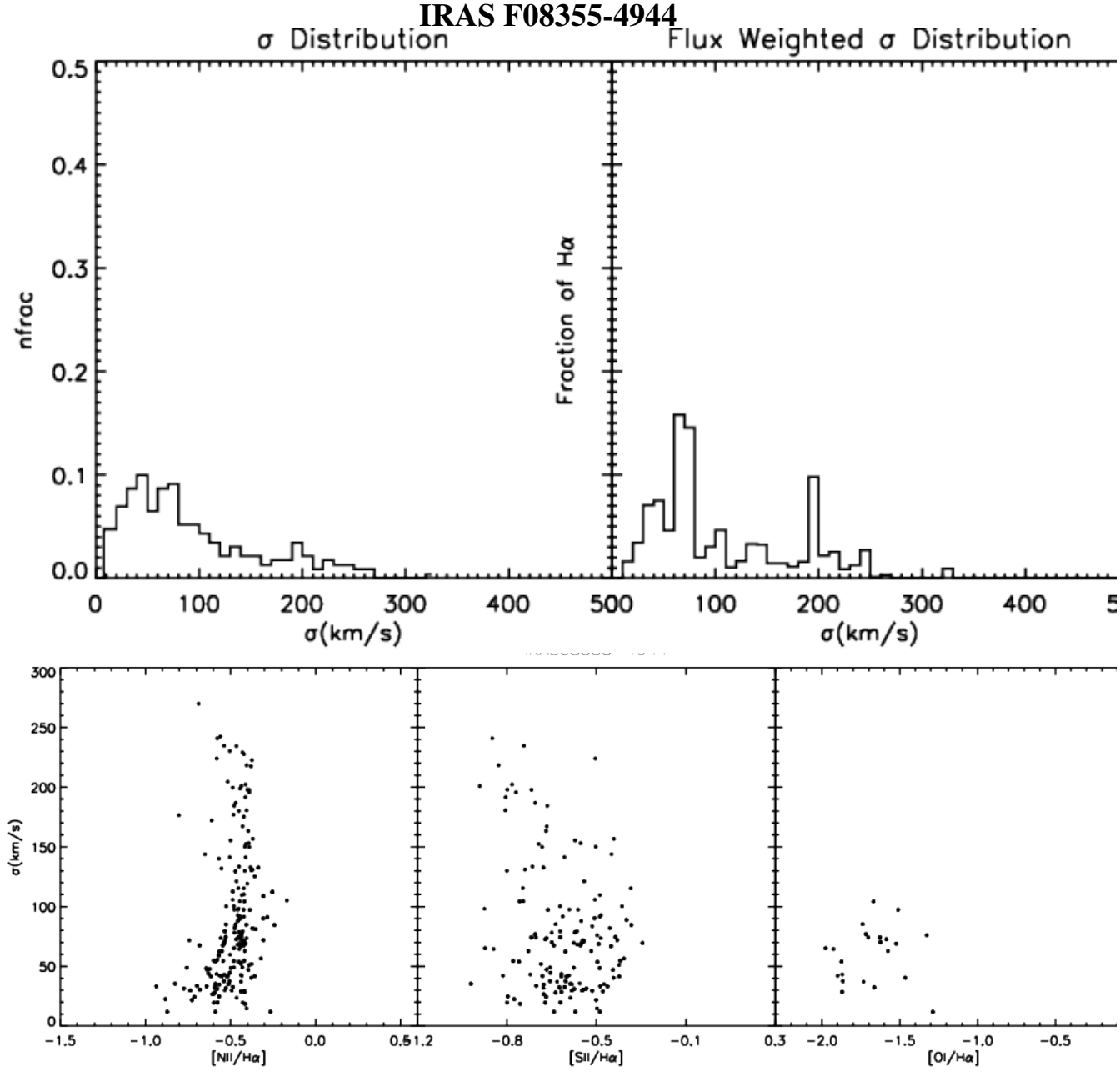

Figure B4. : Same as Figure B1, but for IRAS 08355-4944.

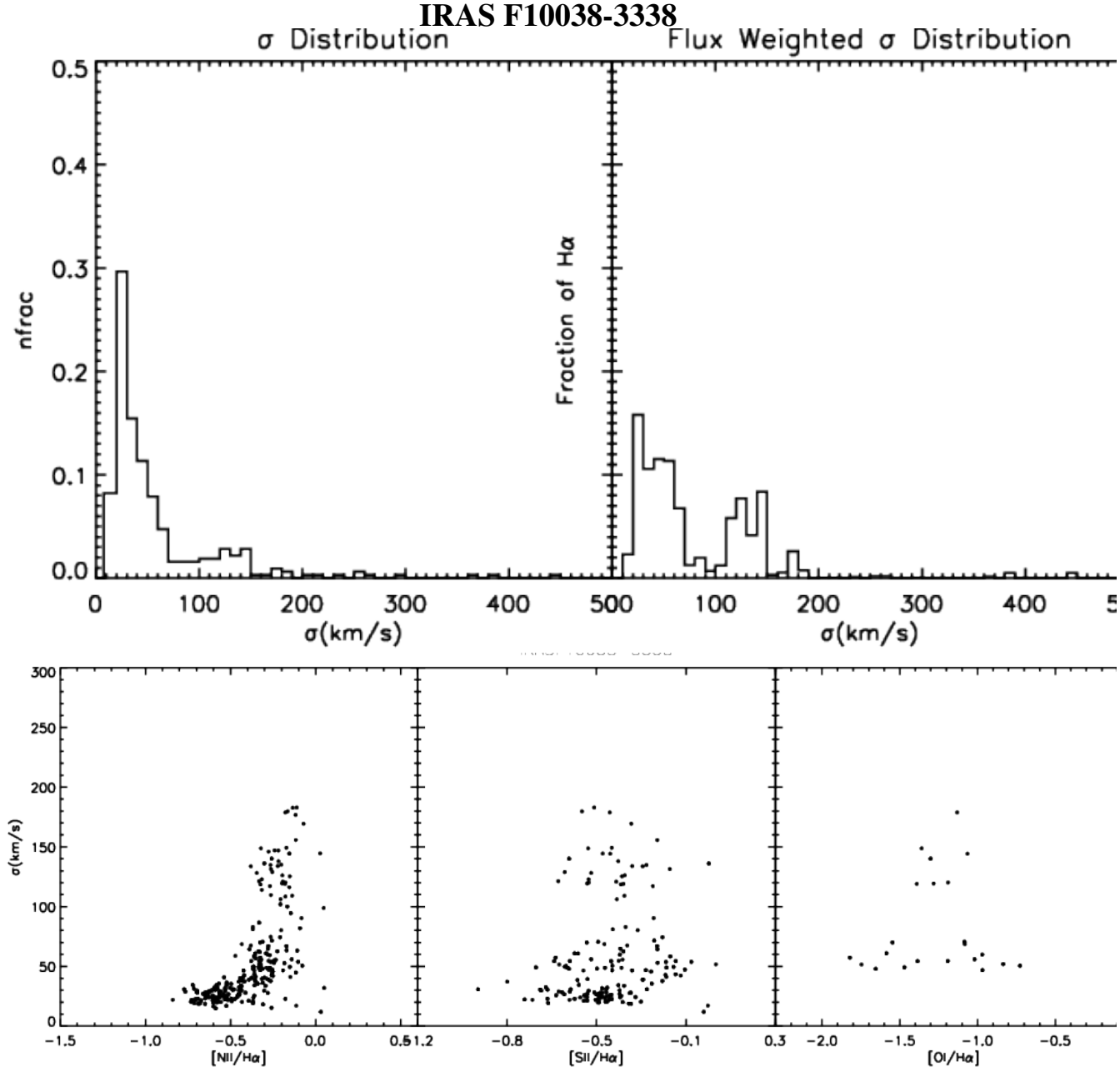

Figure B5. : Same as Figure B1, but for IRAS F10038-3338.

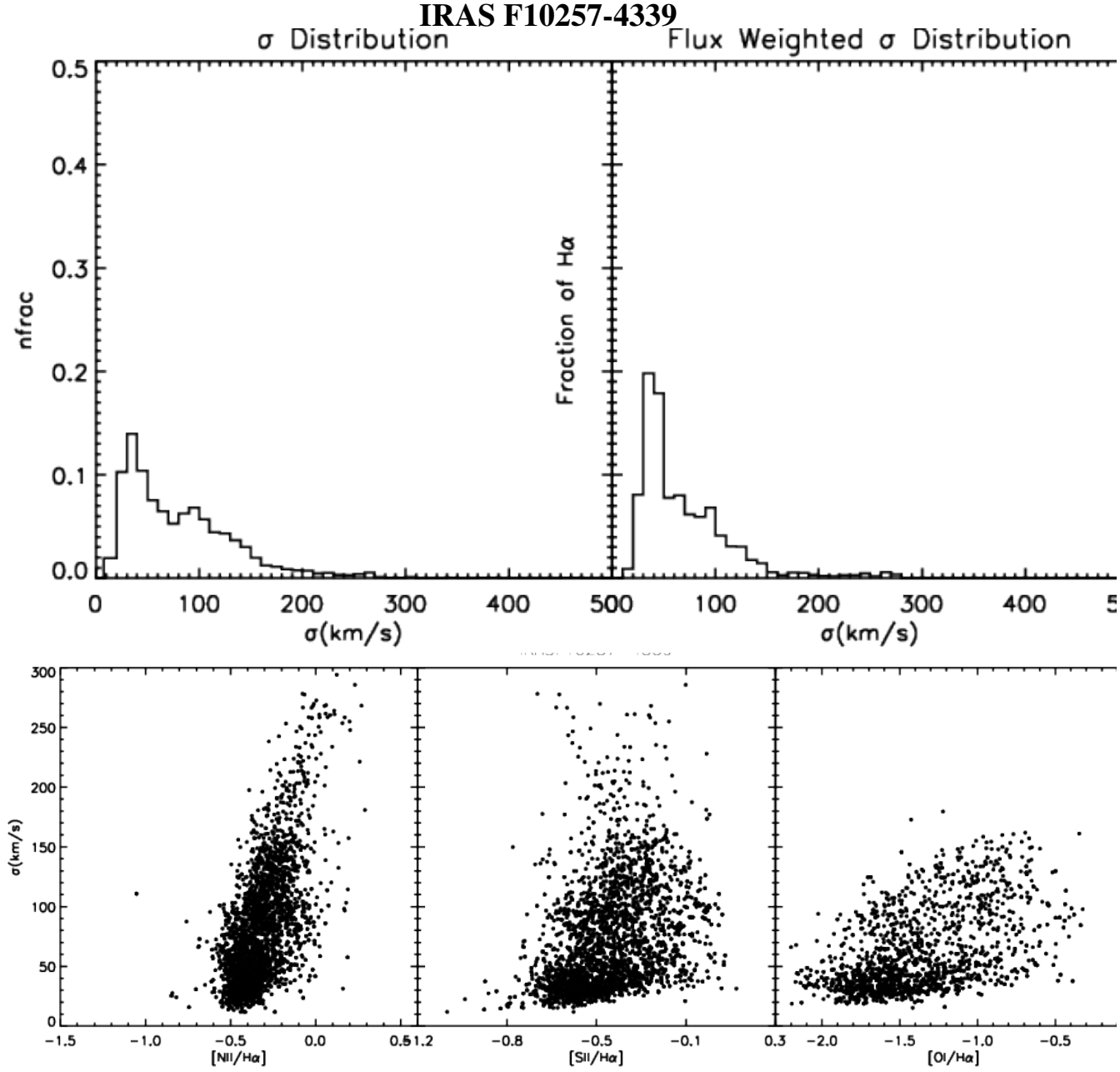

Figure B6. : Same as Figure B1, but for IRAS F10257-4339.

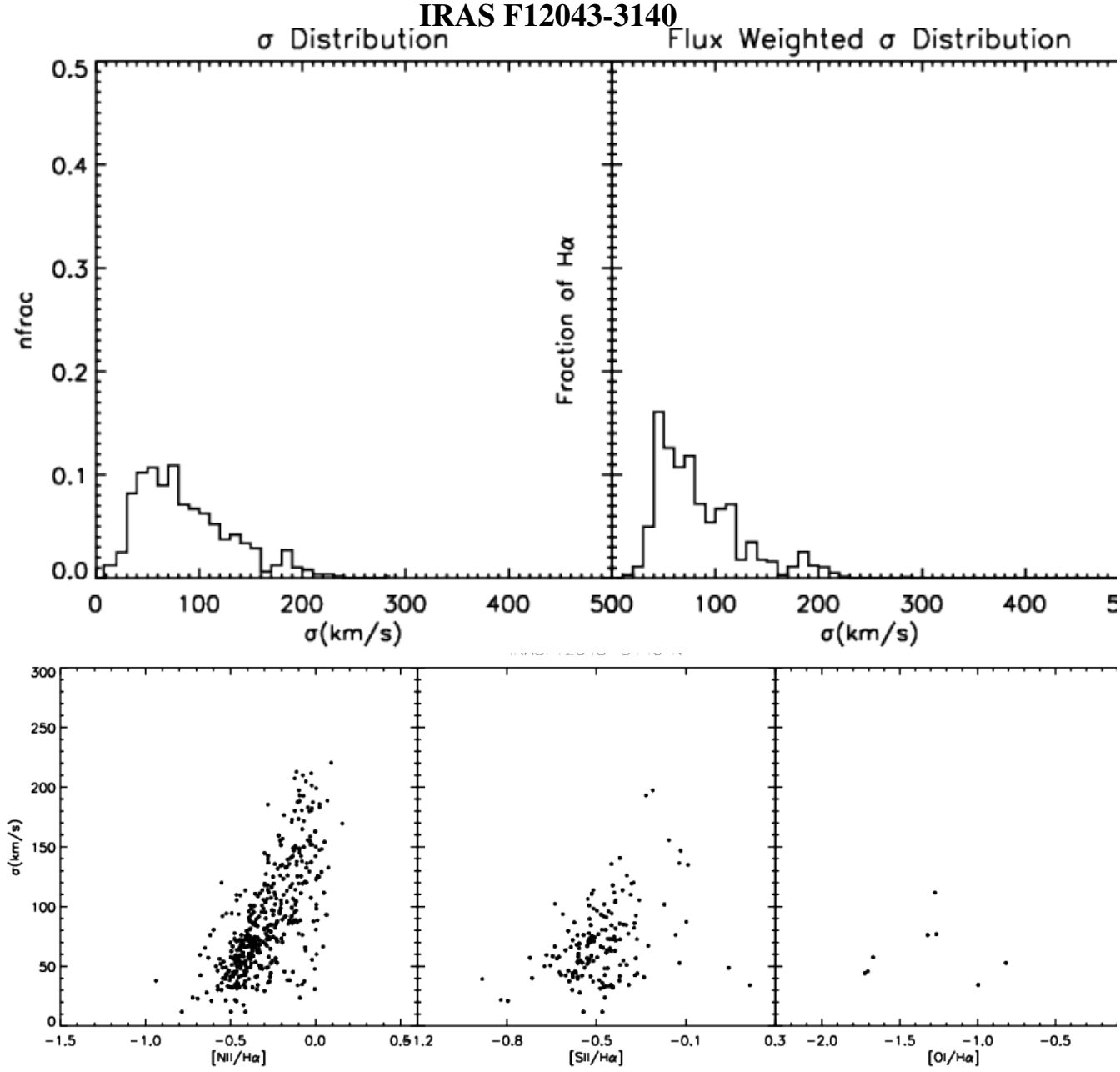

Figure B7. : Same as Figure B1, but for IRAS F12043-3140.

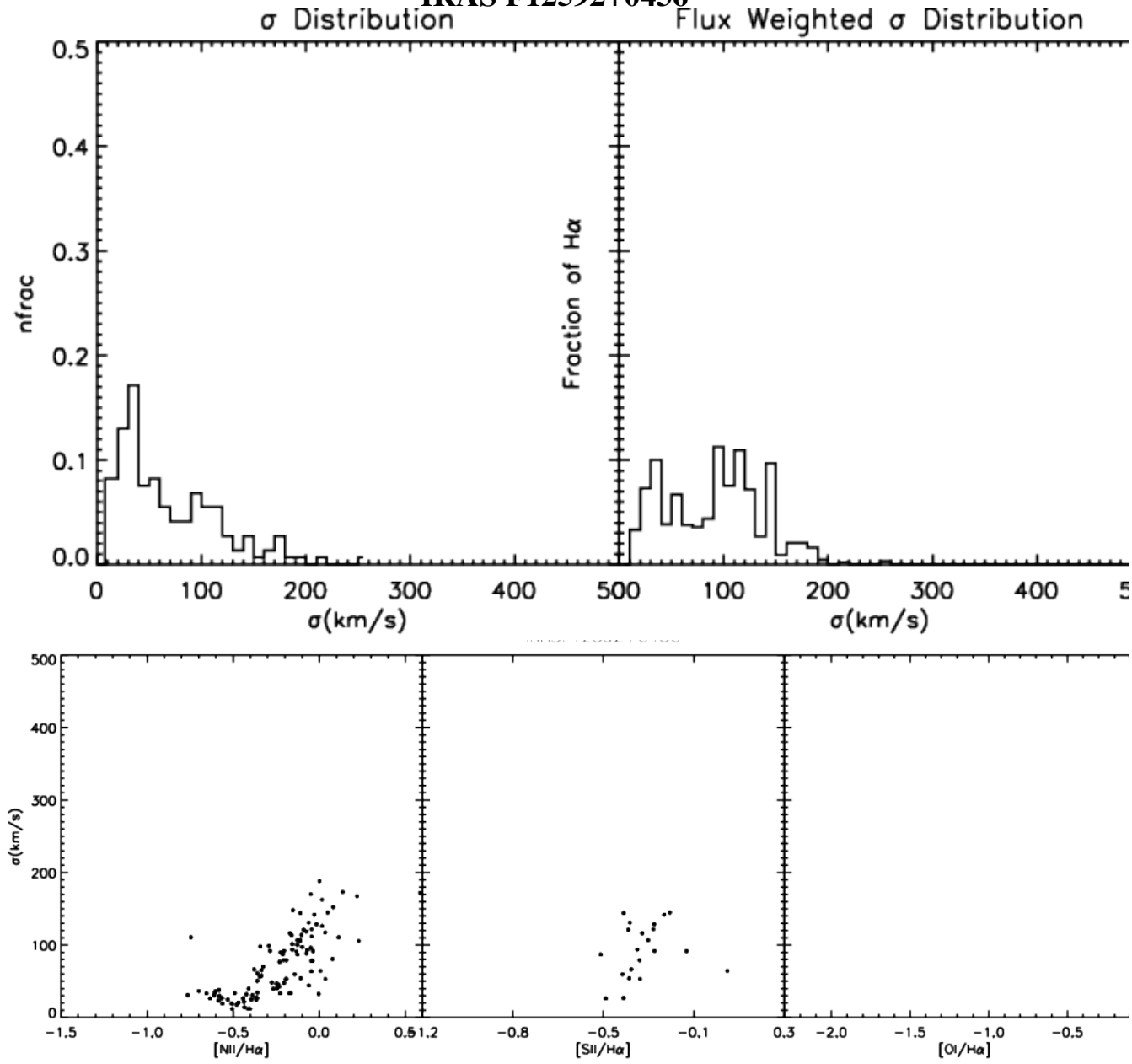

Figure B8. : Same as Figure B1, but for IRAS F12592+0436.

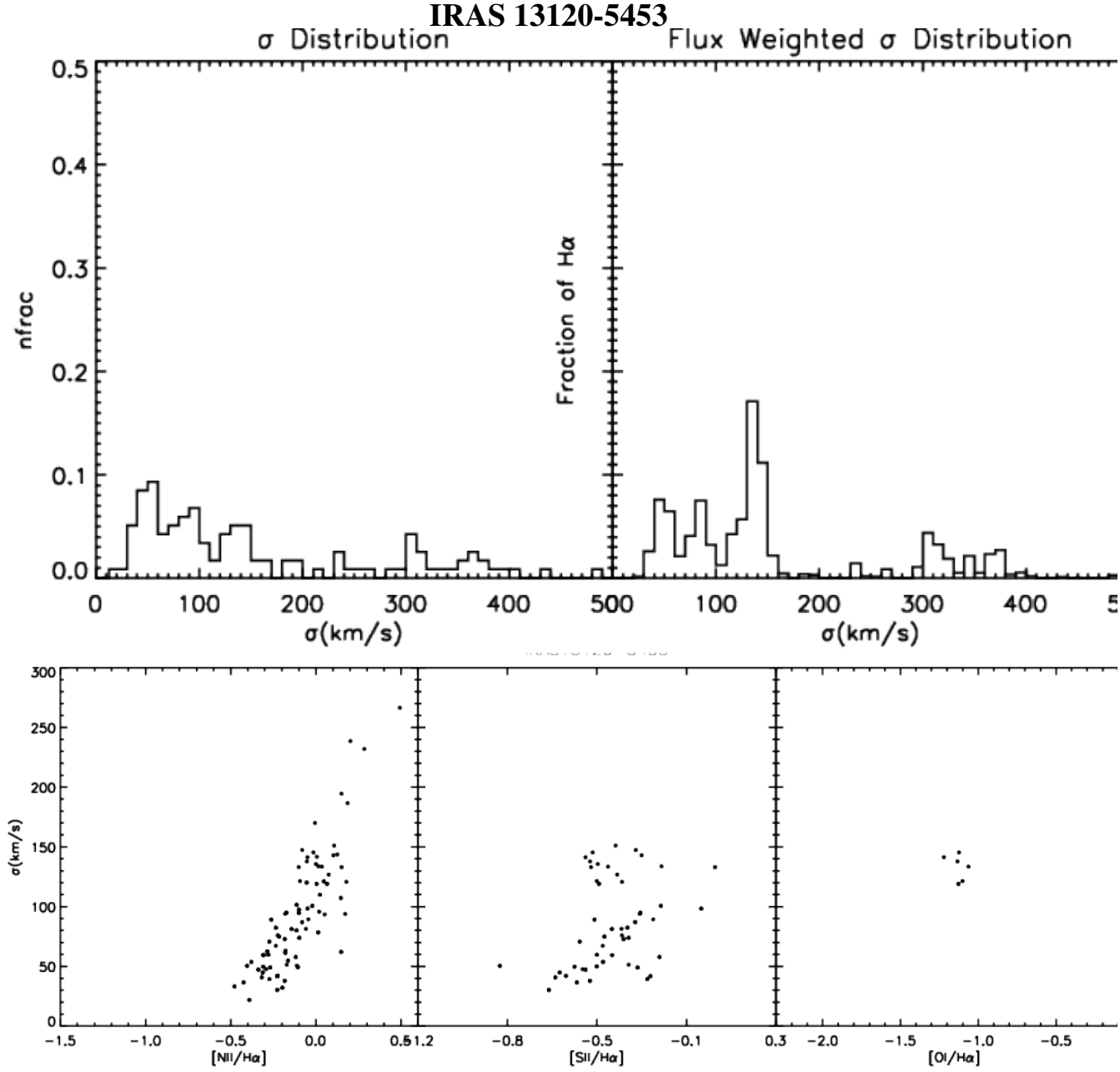

Figure B9. : Same as Figure B1, but for IRAS 13120-5453.

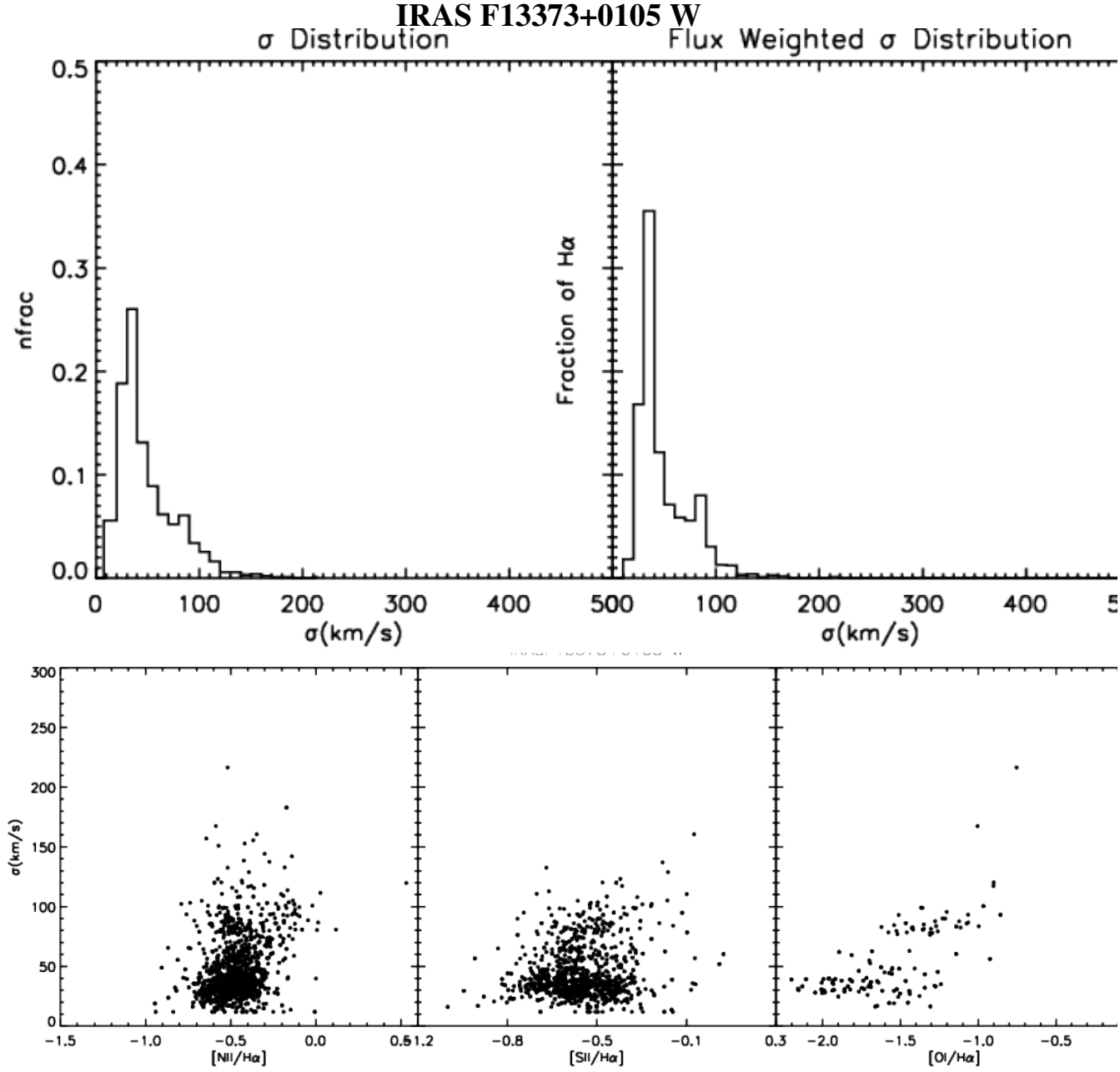

Figure B10. : Same as Figure B1, but for IRAS F13373+0105 W.

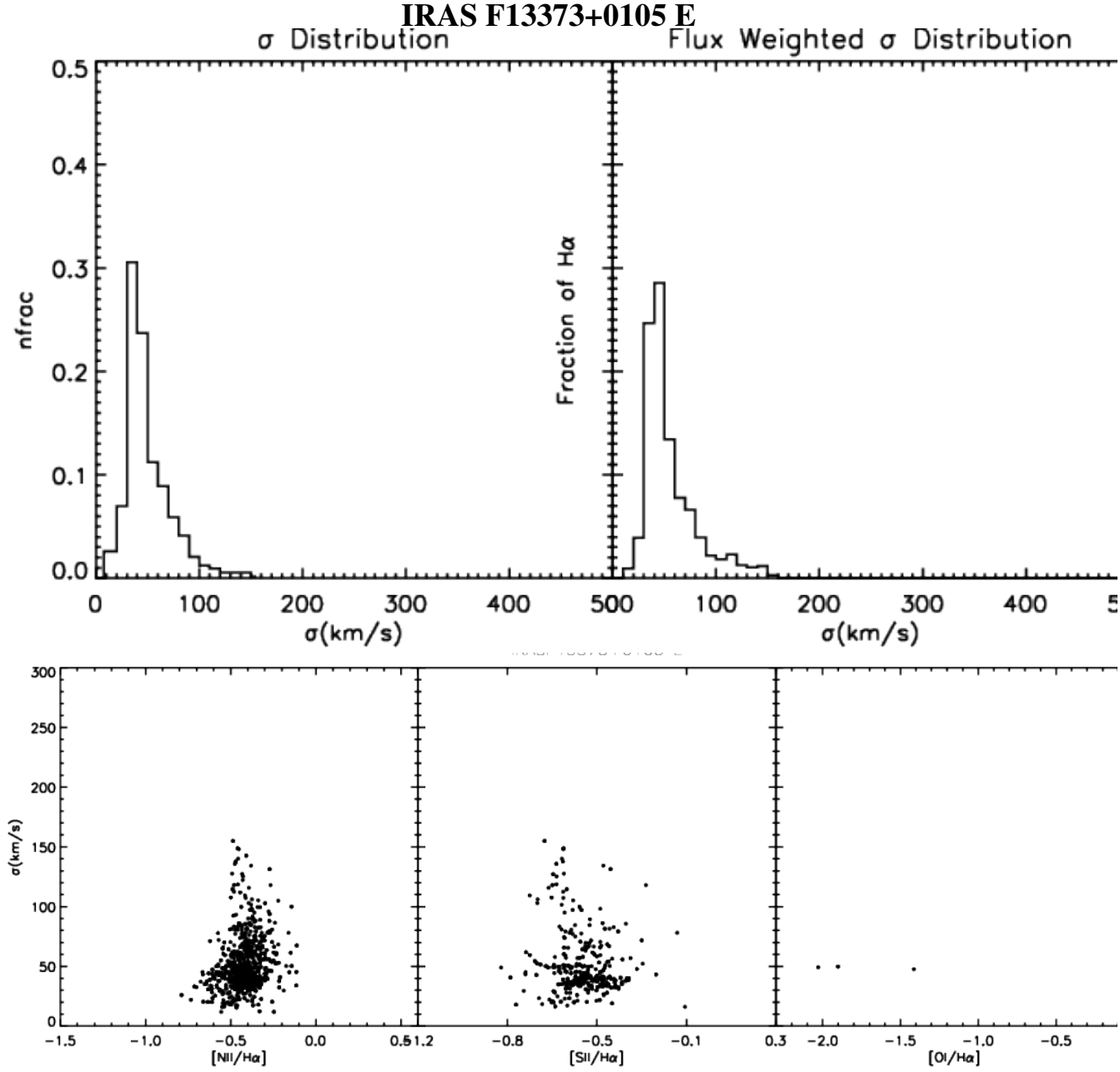

Figure B11. : Same as Figure B1, but for IRAS F13373+0105 E.

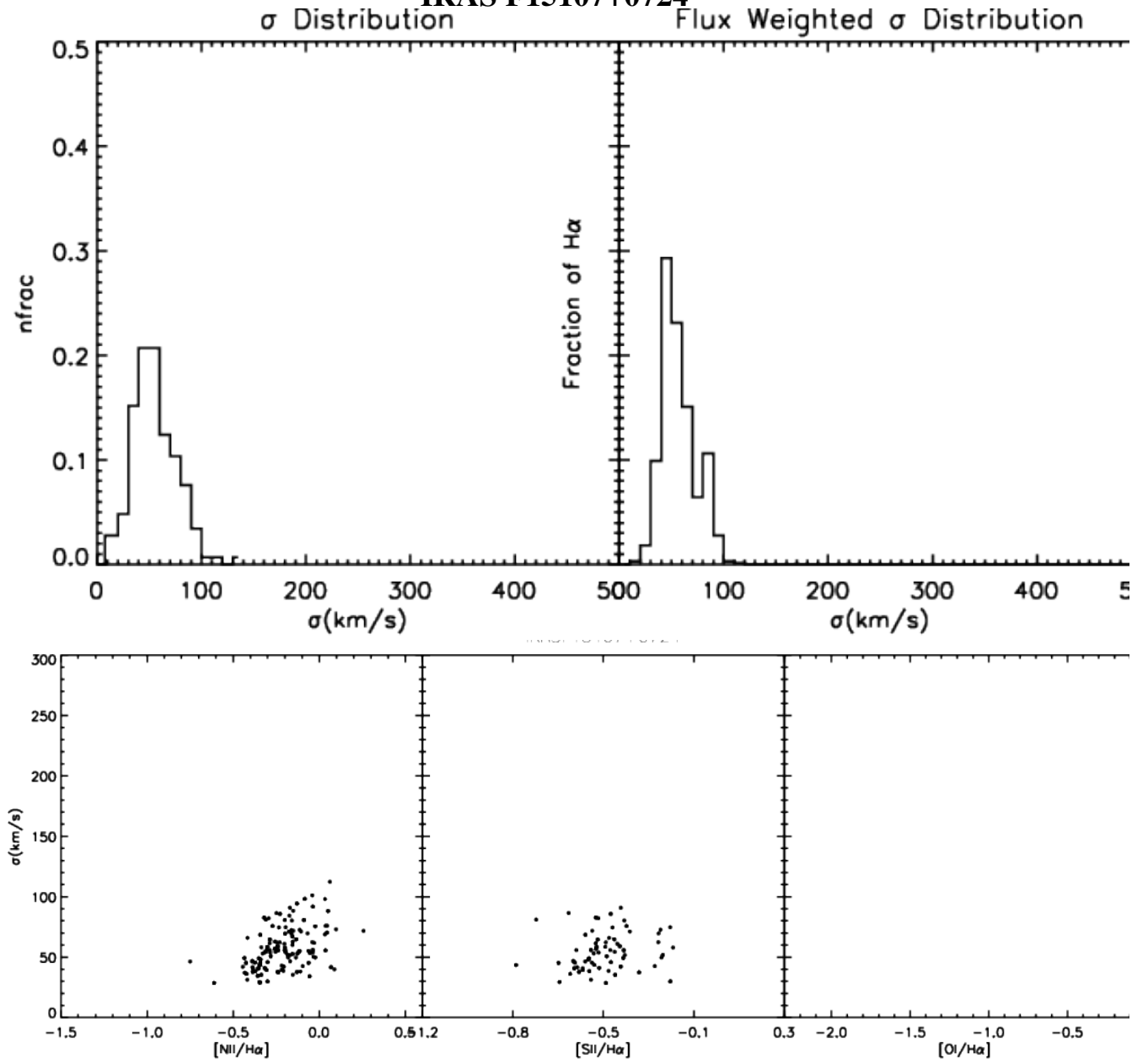

Figure B12. : Same as Figure B1, but for IRAS F15107+0724.

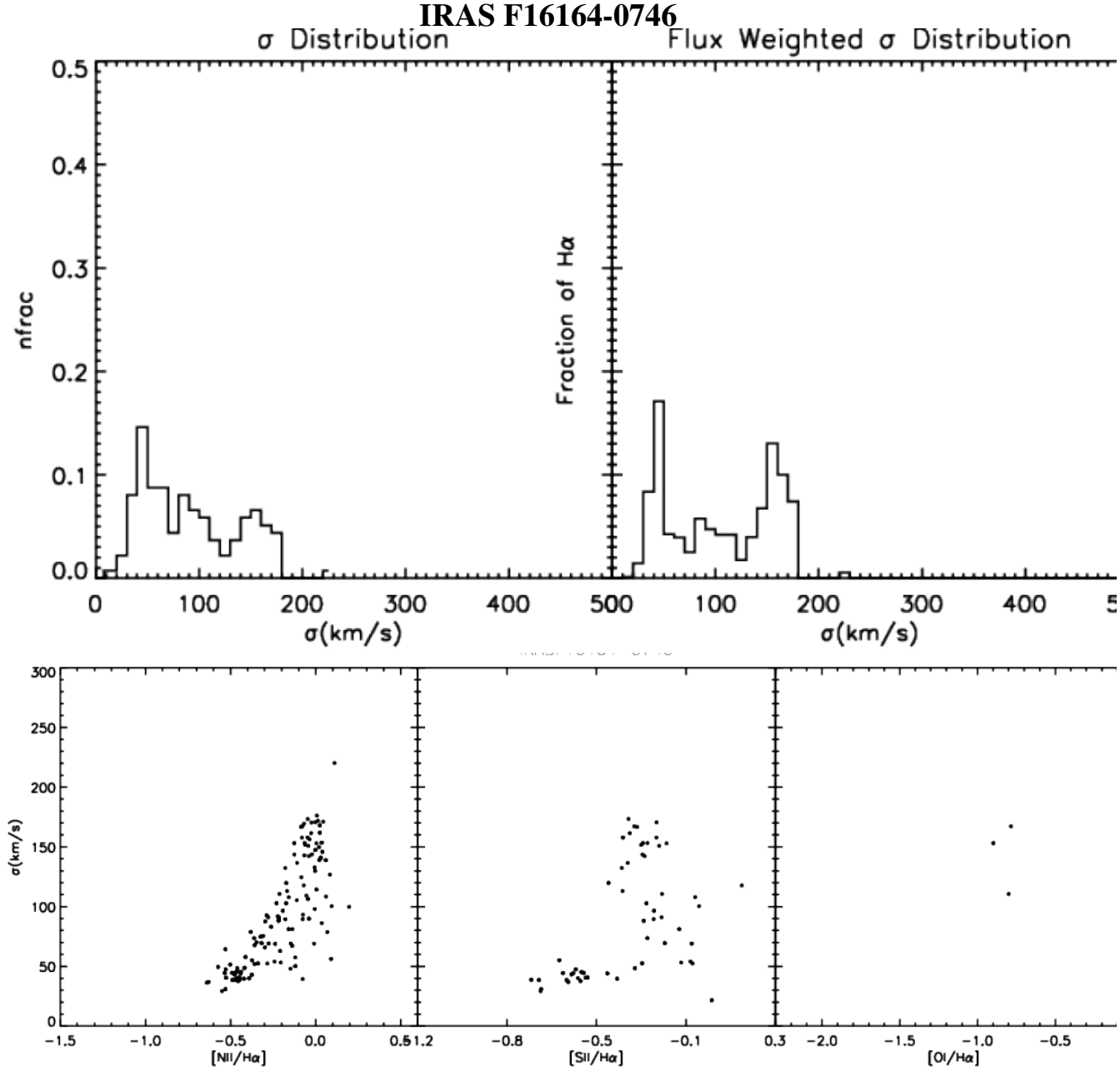

Figure B13. : Same as Figure B1, but for IRAS F16164-0746.

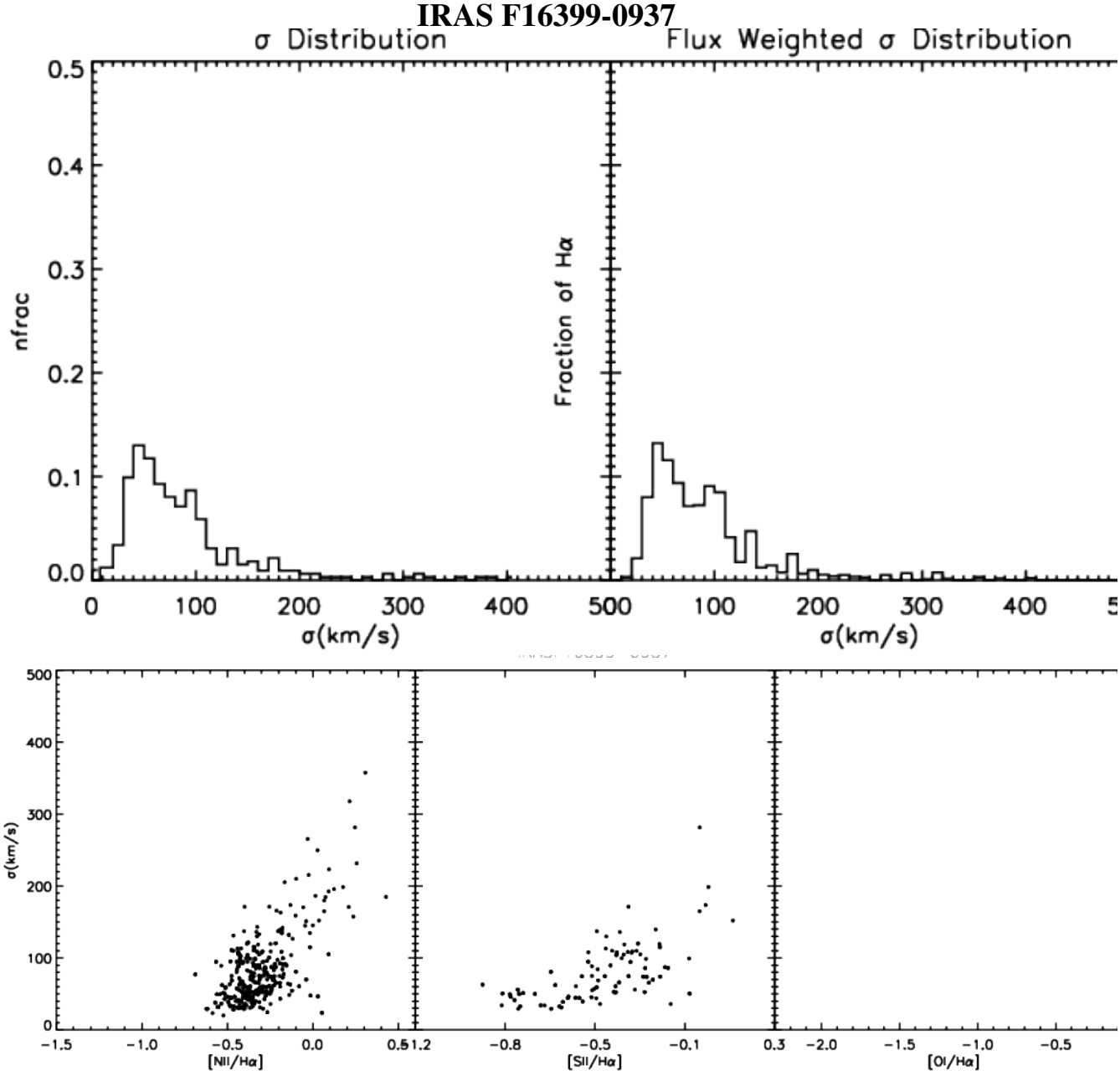

Figure B14. : Same as Figure B1, but for IRAS F16399-0937.

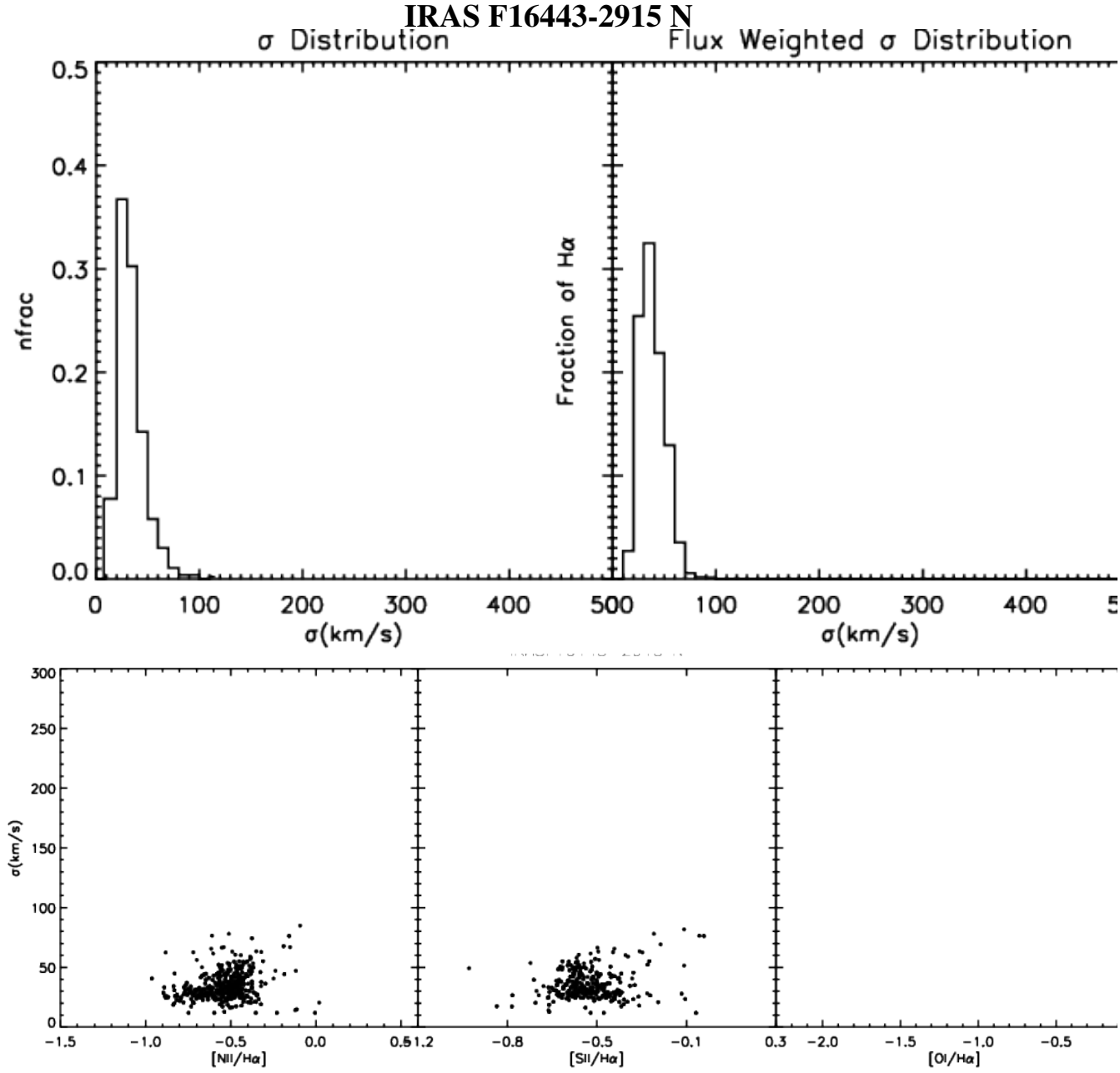

Figure B15. : Same as Figure B1, but for IRAS F16443-2915 N.

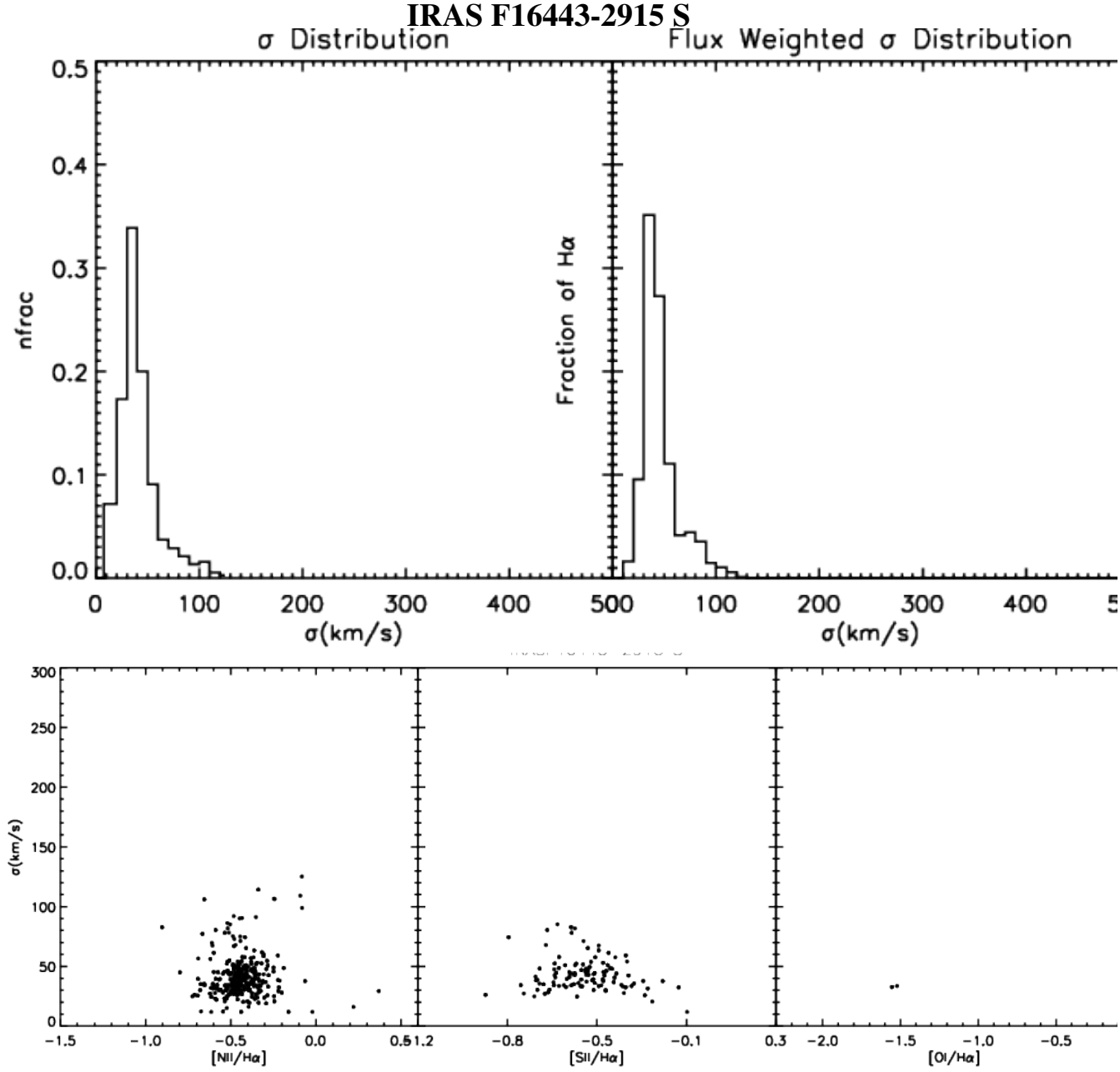

Figure B16. : Same as Figure B1, but for IRAS F16443-2915 S.

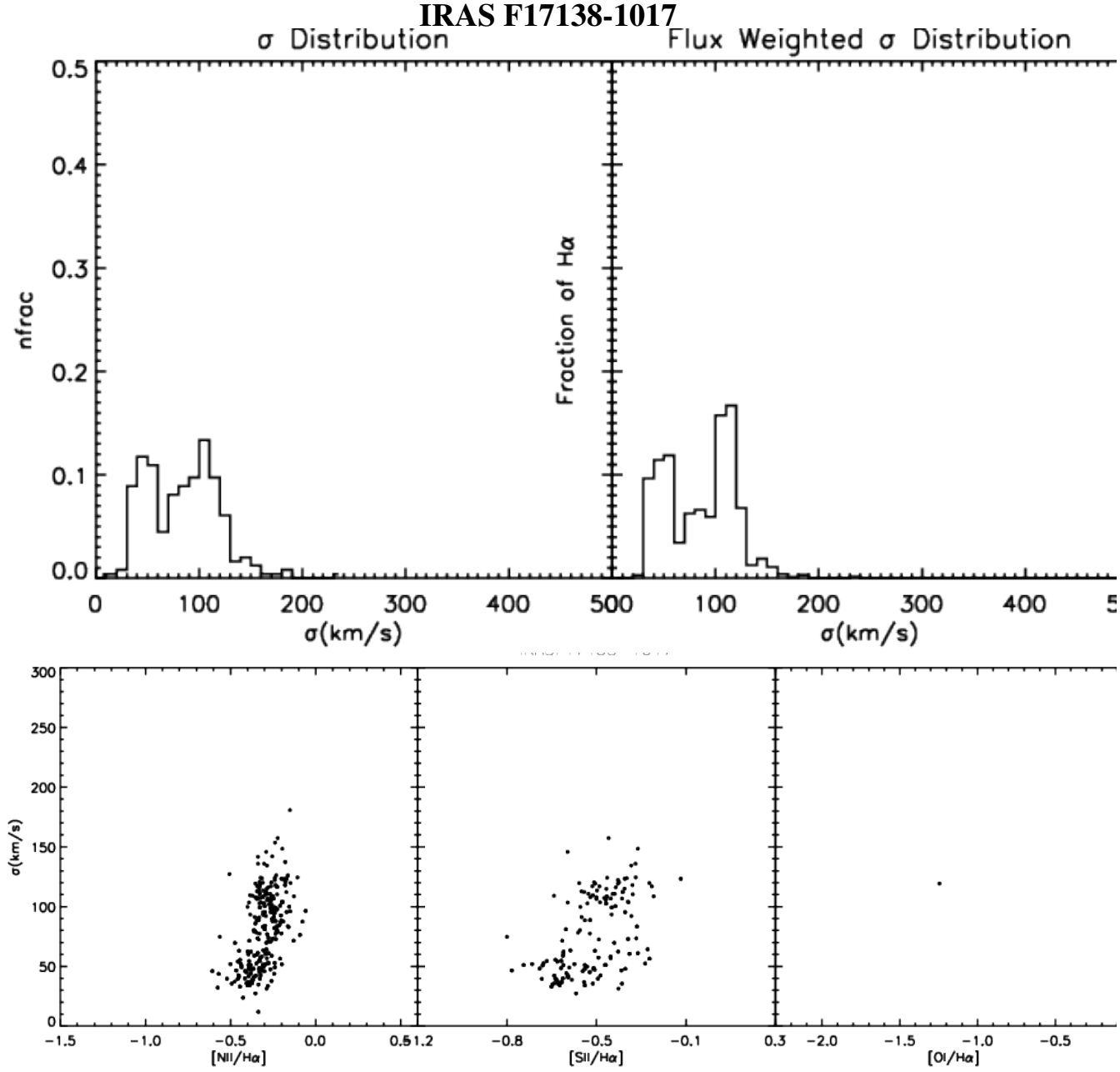

Figure B17. : Same as Figure B1, but for IRAS F17138-1017.

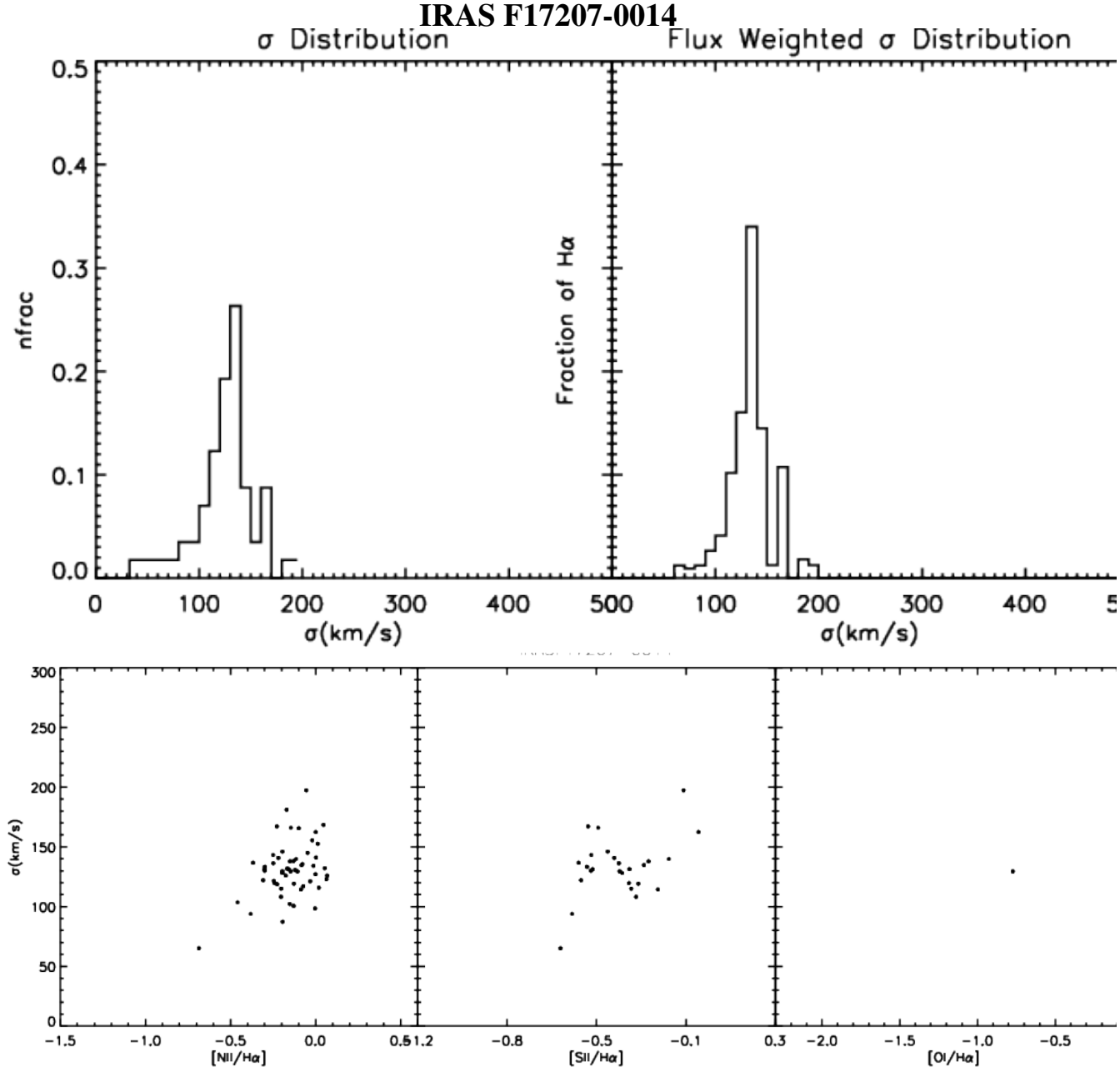

Figure B18. : Same as Figure B1, but for IRAS F17207-0014.

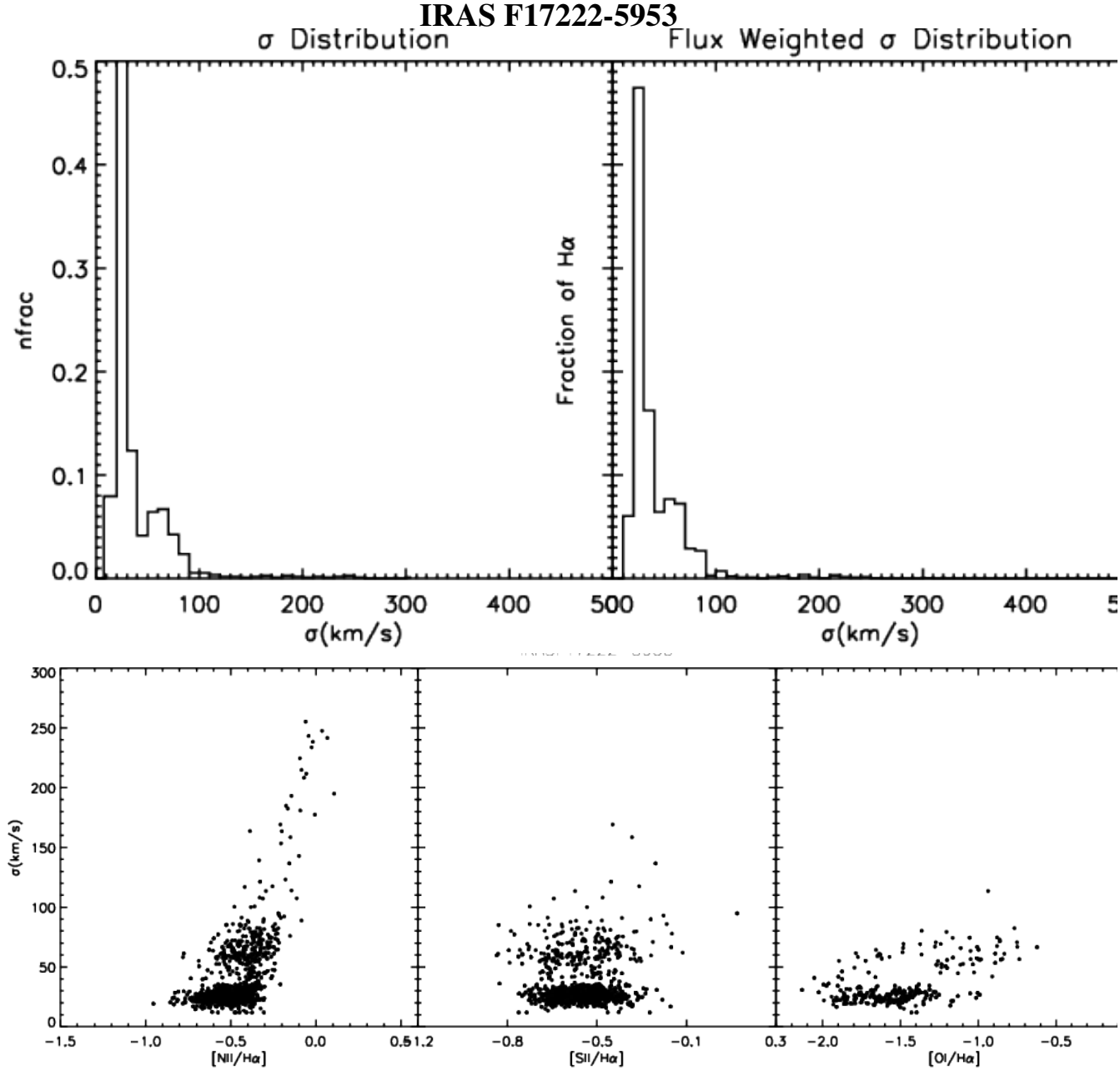

Figure B19. : Same as Figure B1, but for IRAS F17222-5953.

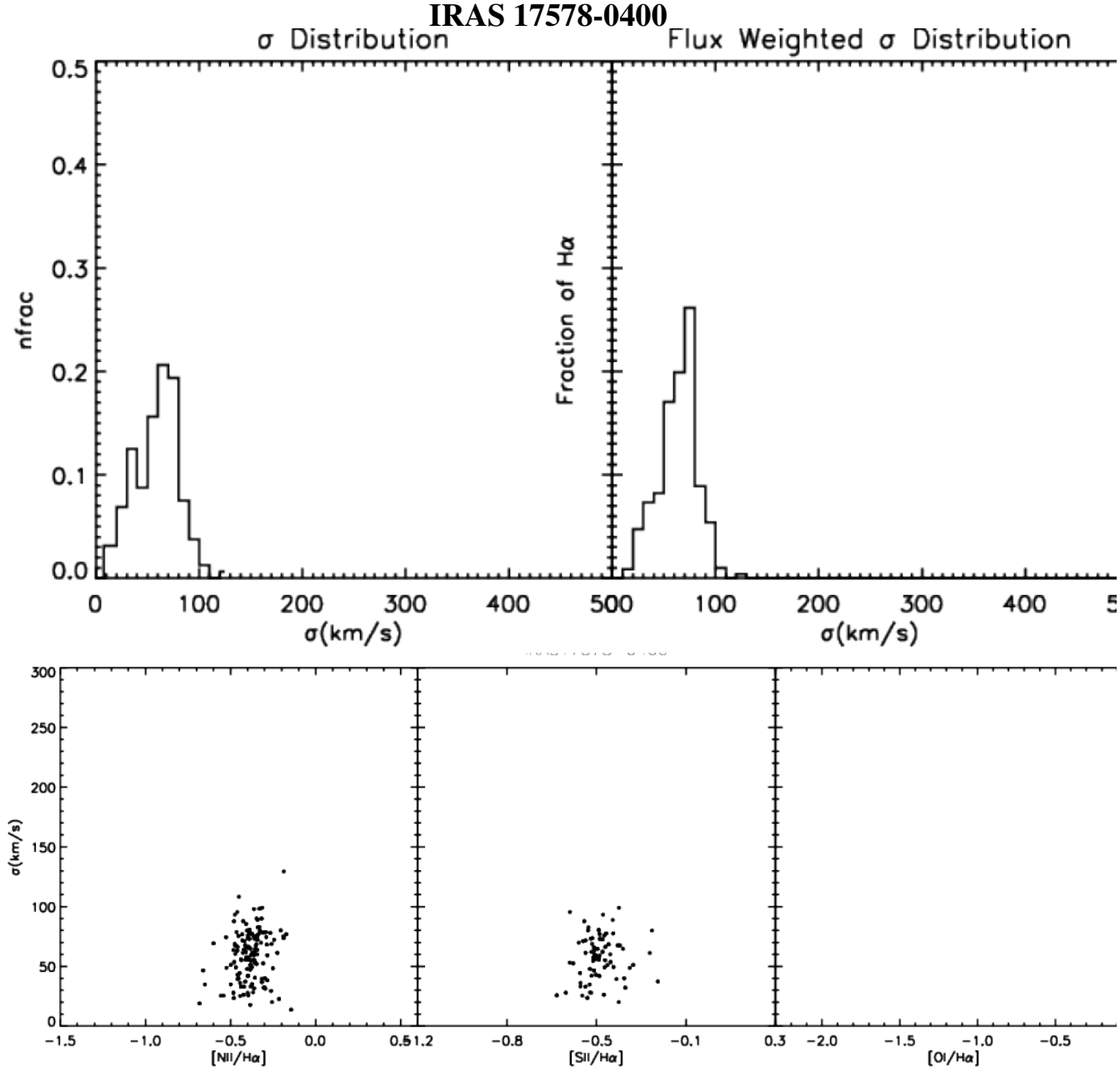

Figure B20. : Same as Figure B1, but for IRAS 17578-0400.

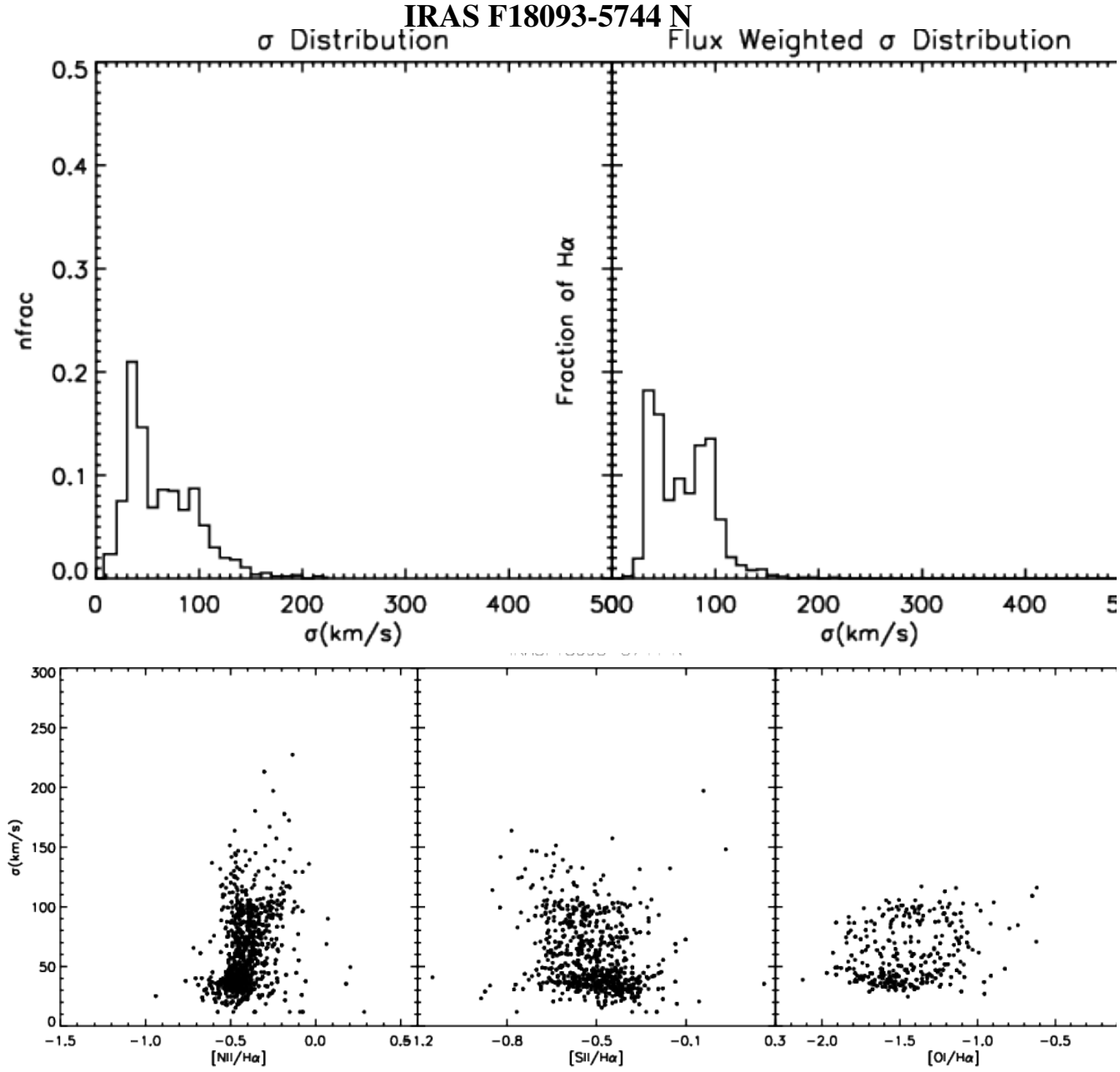

Figure B21. : Same as Figure B1, but for IRAS F18093-5744 N.

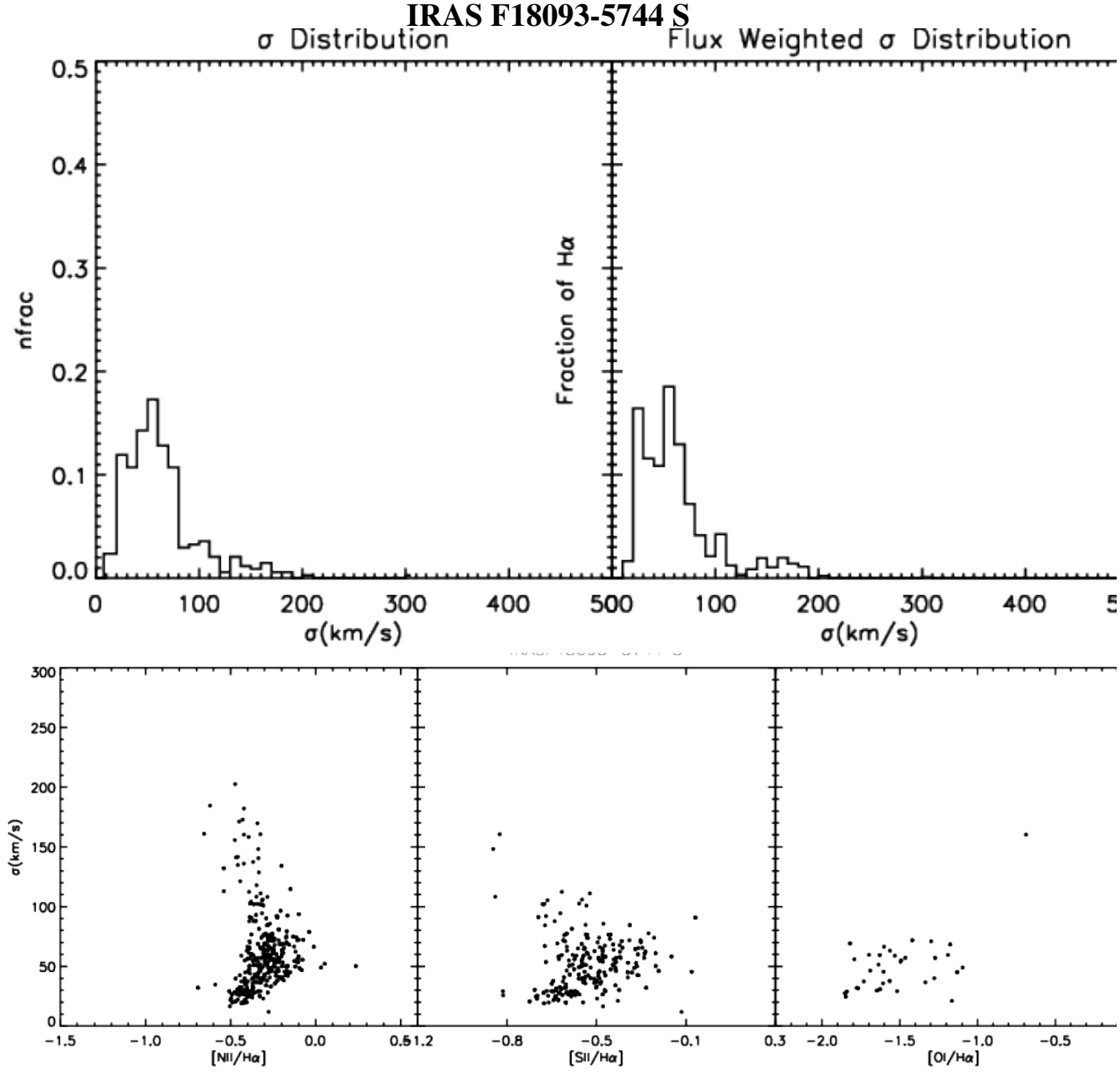

Figure B22. : Same as Figure B1, but for IRAS F18093-5744 S.

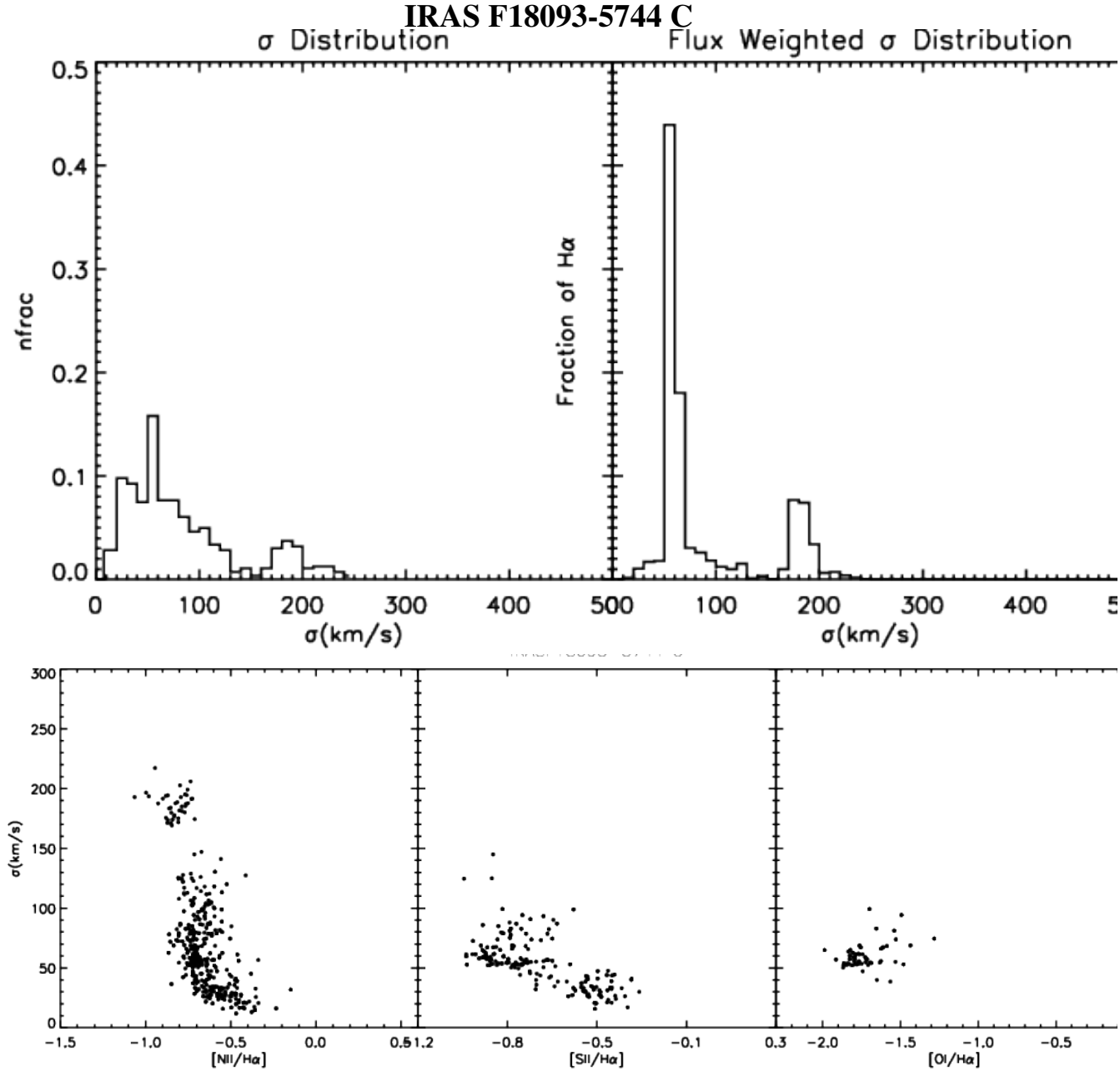

Figure B23. : Same as Figure B1, but for IRAS F18093-5744 C.

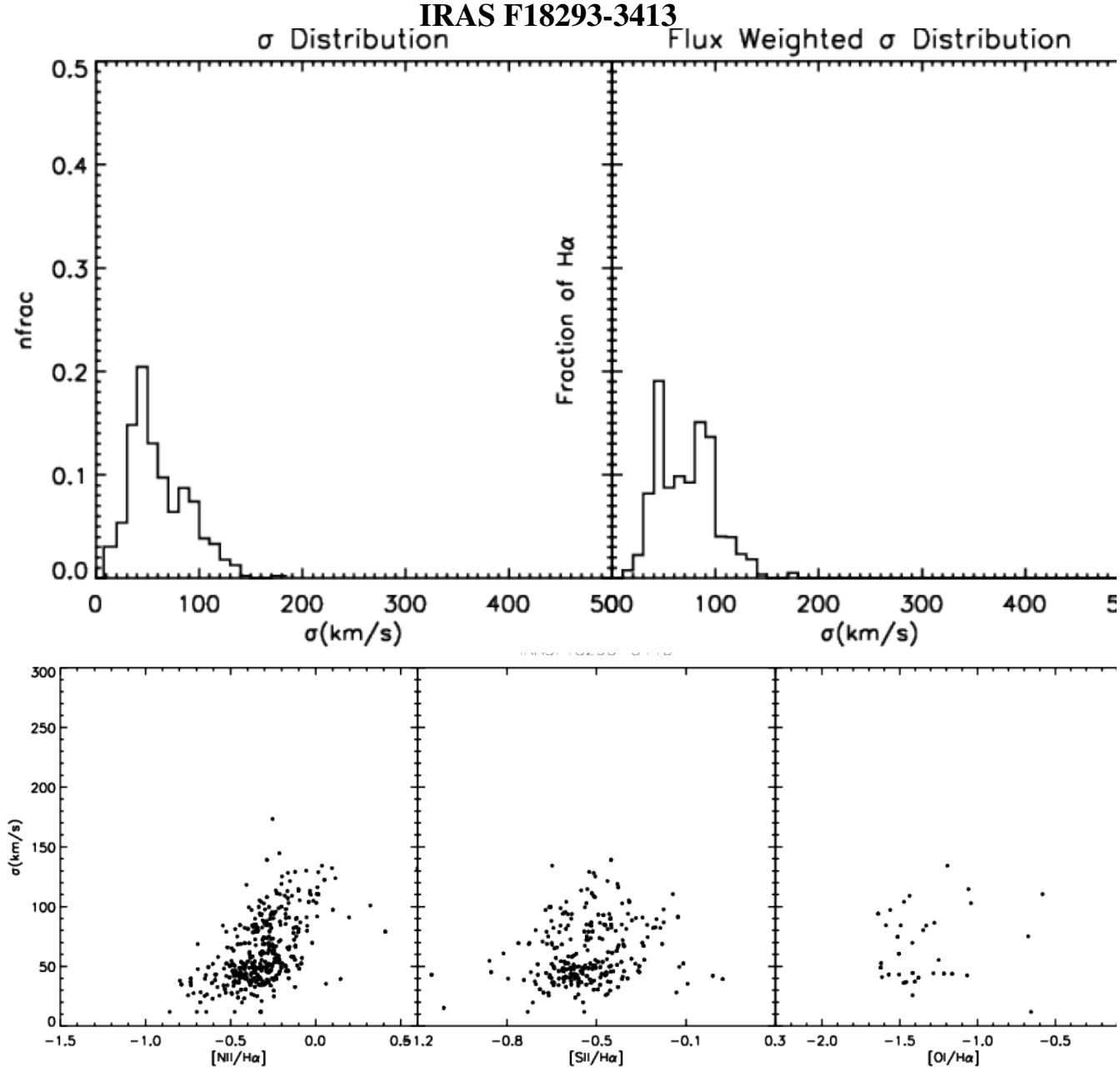

Figure B24. : Same as Figure B1, but for IRAS F18293-3413.

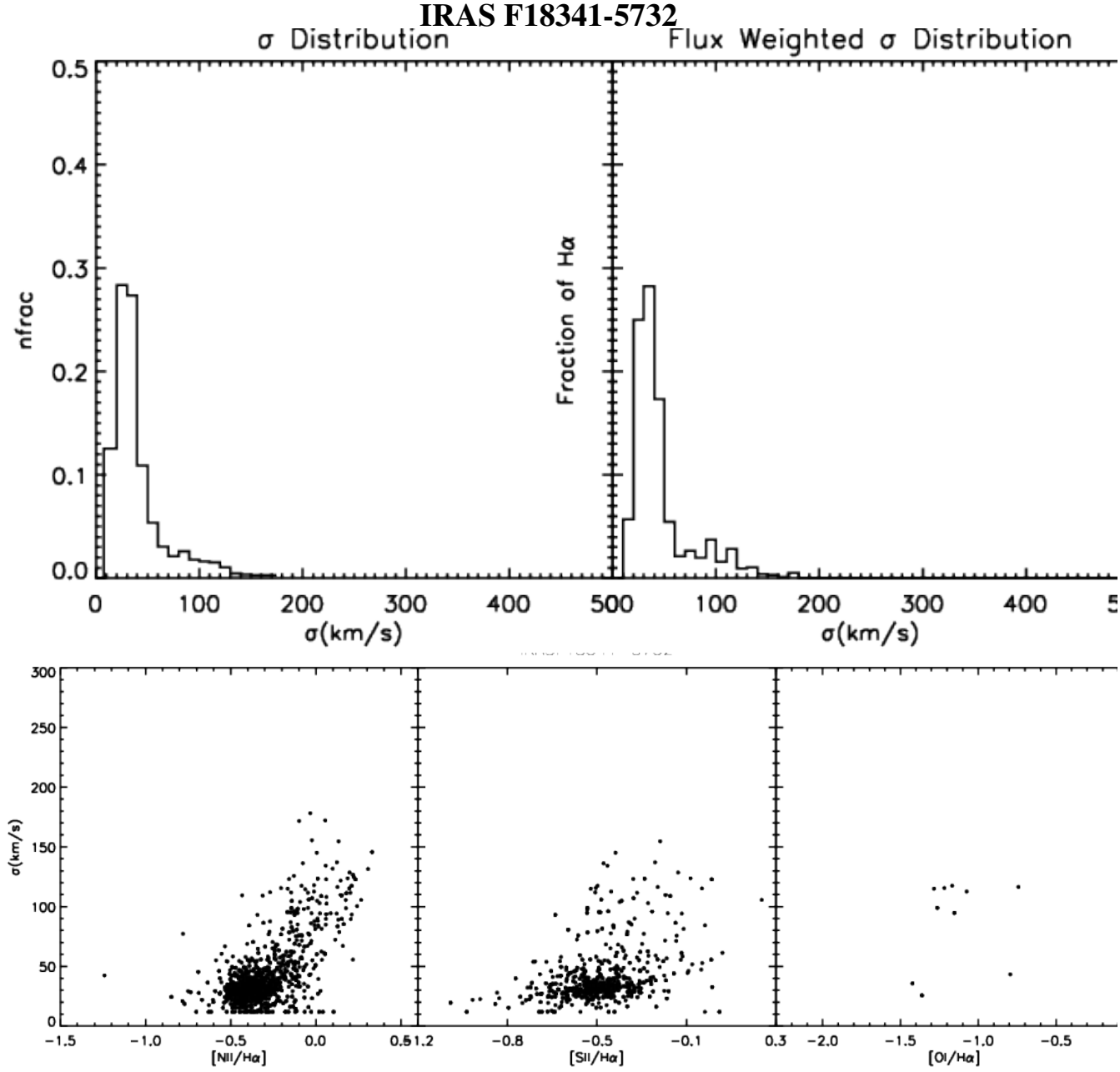

Figure B25. : Same as Figure B1, but for IRAS F18341-5732.

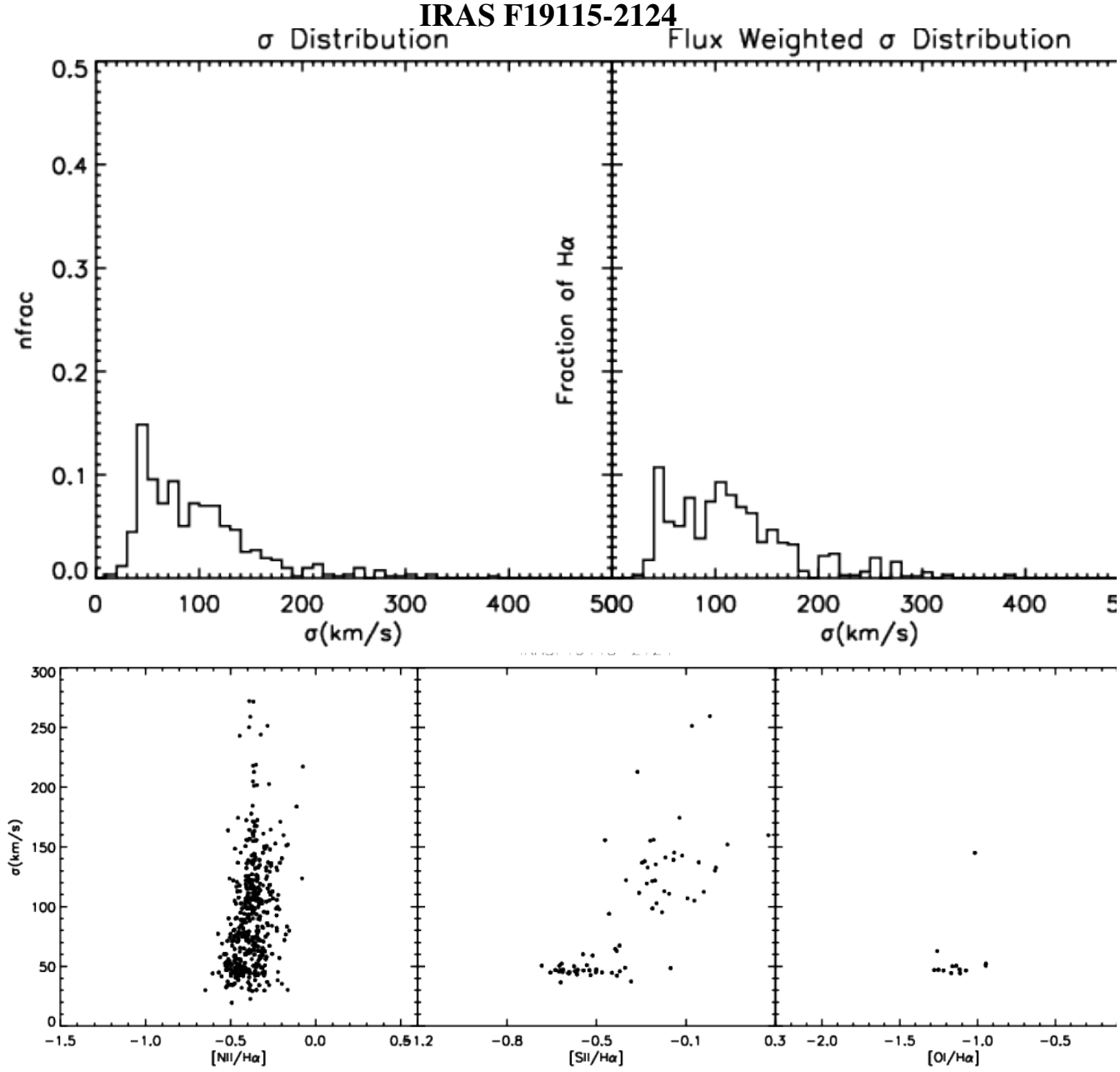

Figure B26. : Same as Figure B1, but for IRAS F19115-2124.

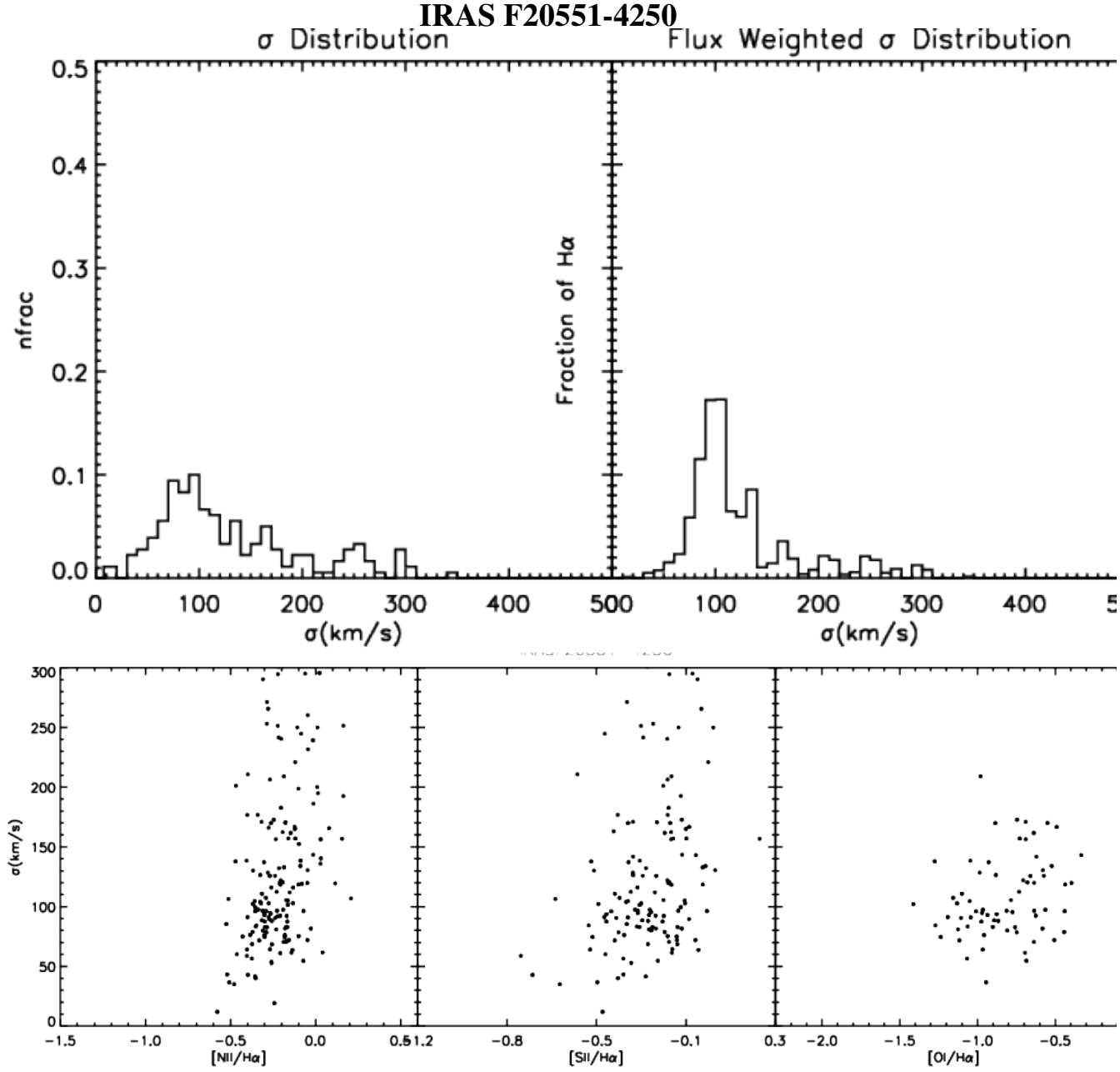

Figure B27. : Same as Figure B1, but for IRAS F20551-4250.

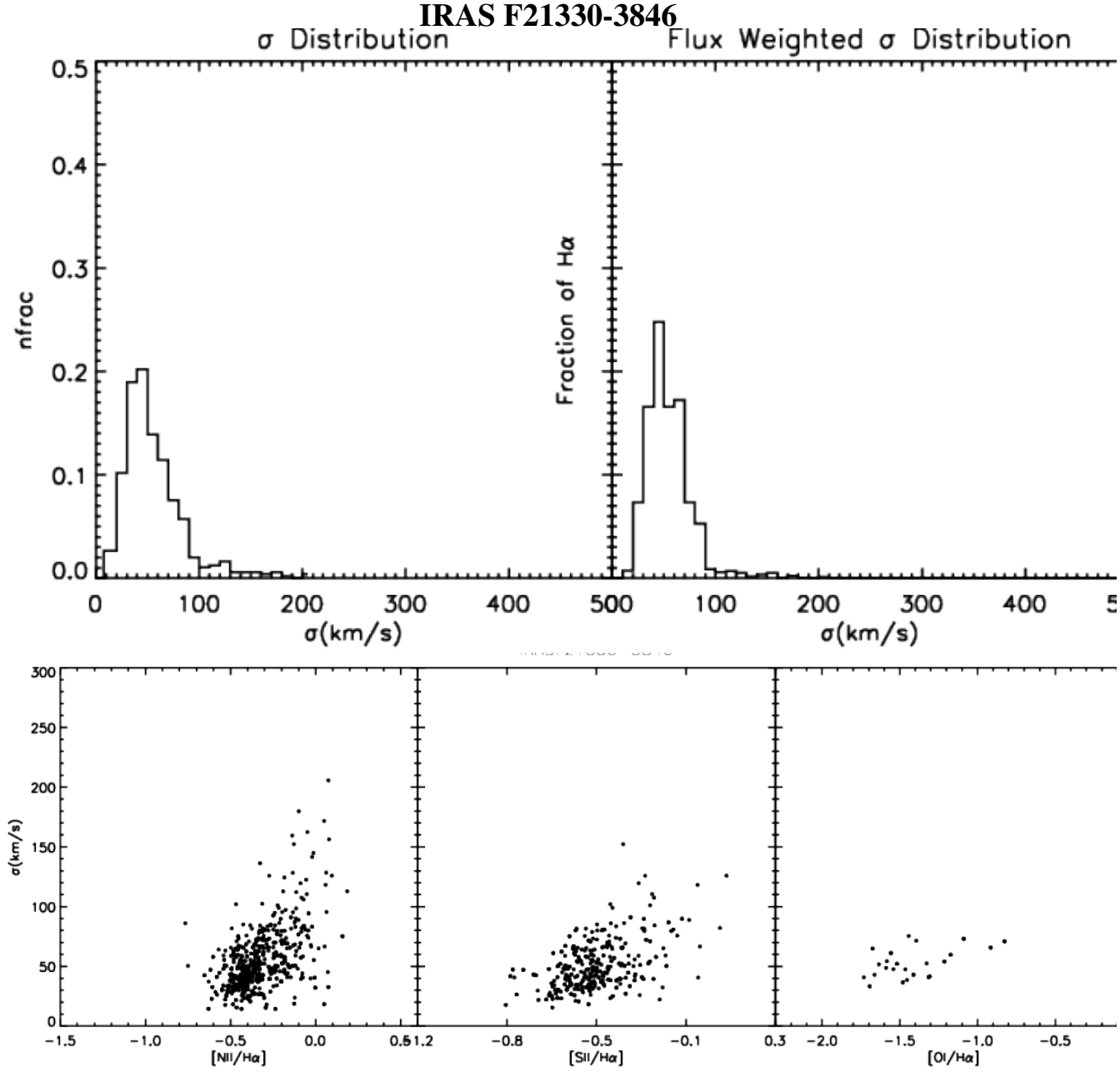

Figure B28. : Same as Figure B1, but for IRAS F21330-3846

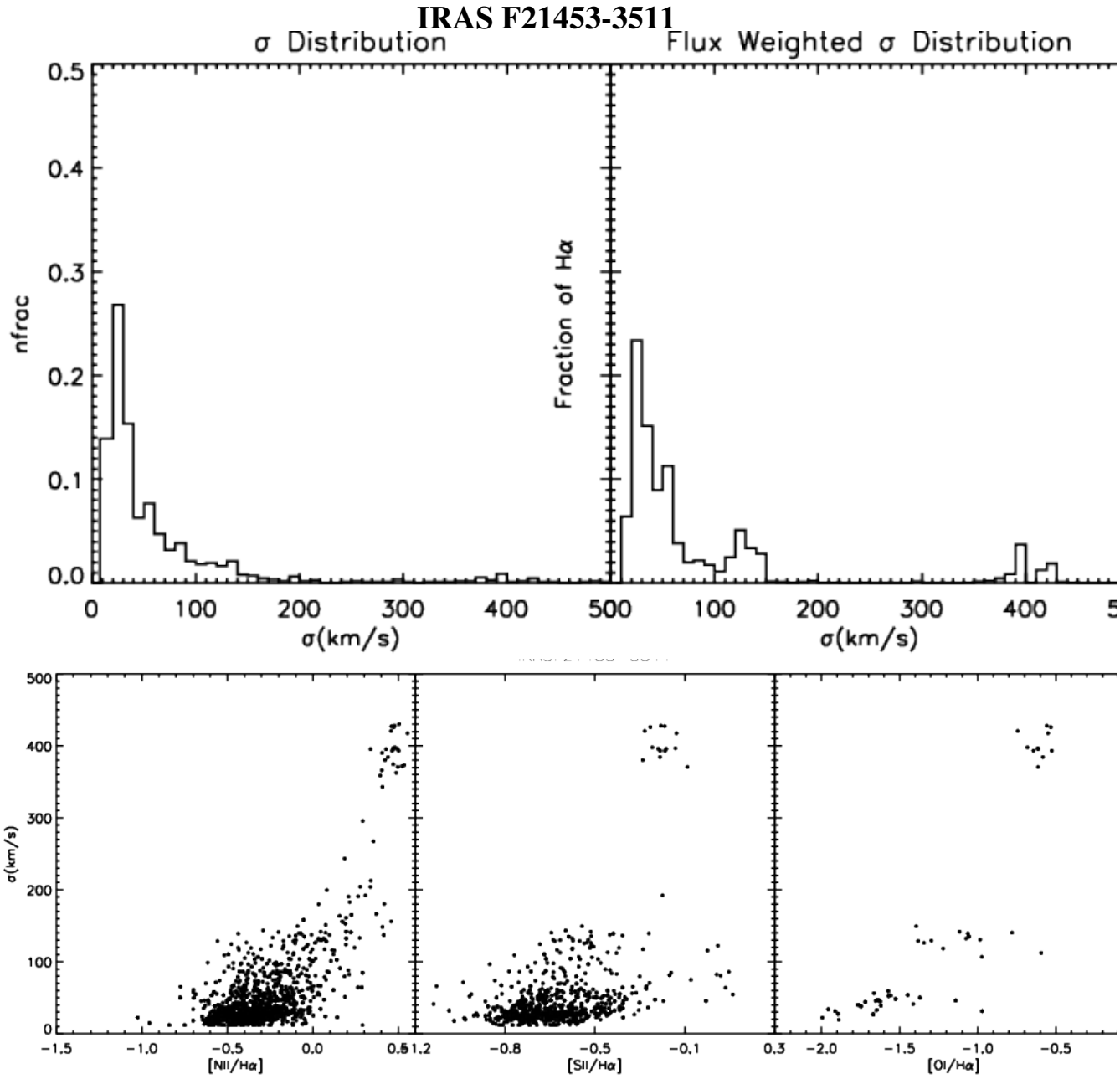

Figure B29. : Same as Figure B1, but for IRAS F21453-3511

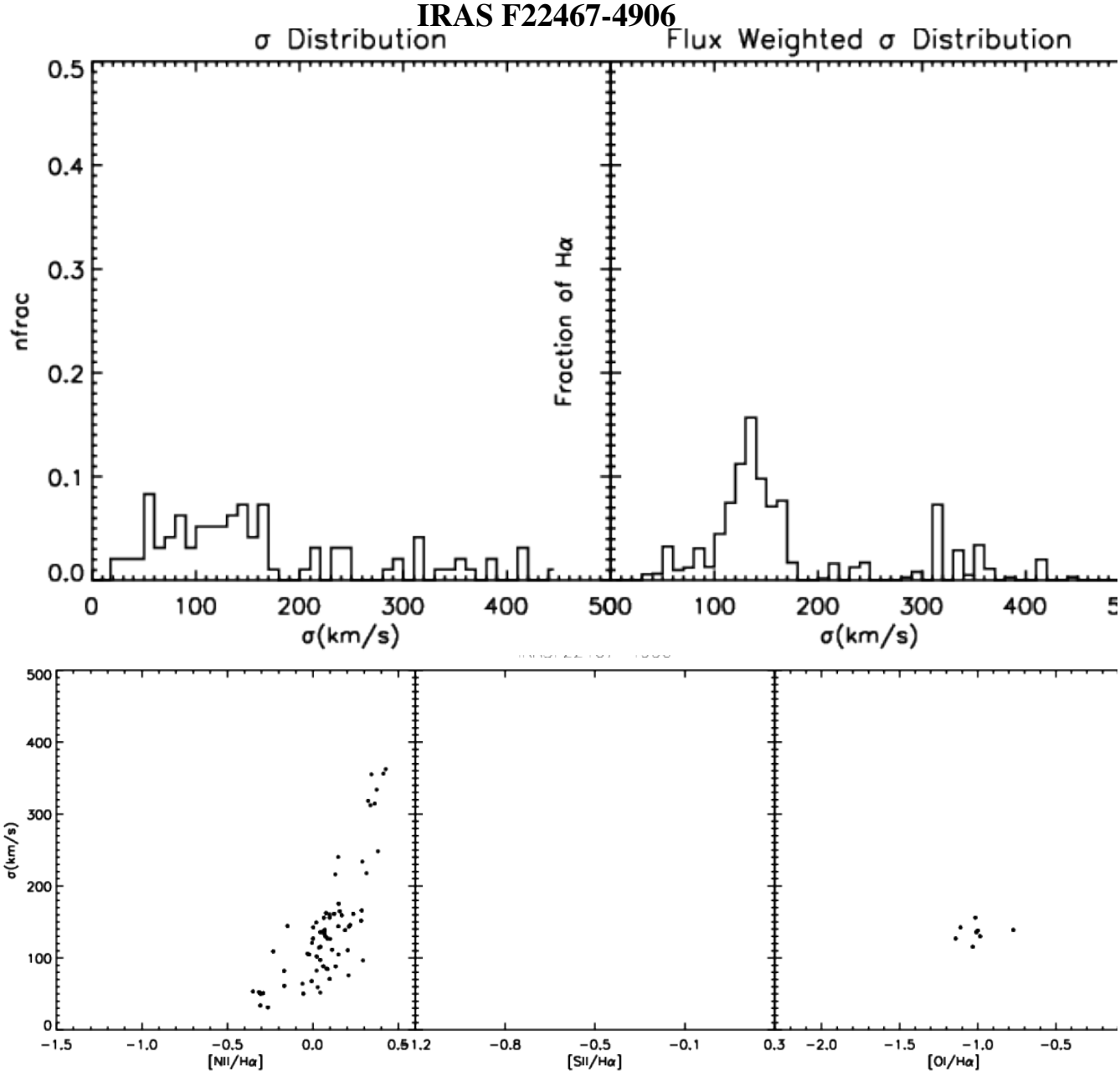

Figure B30. : Same as Figure B1, but for IRAS F22467-4906.

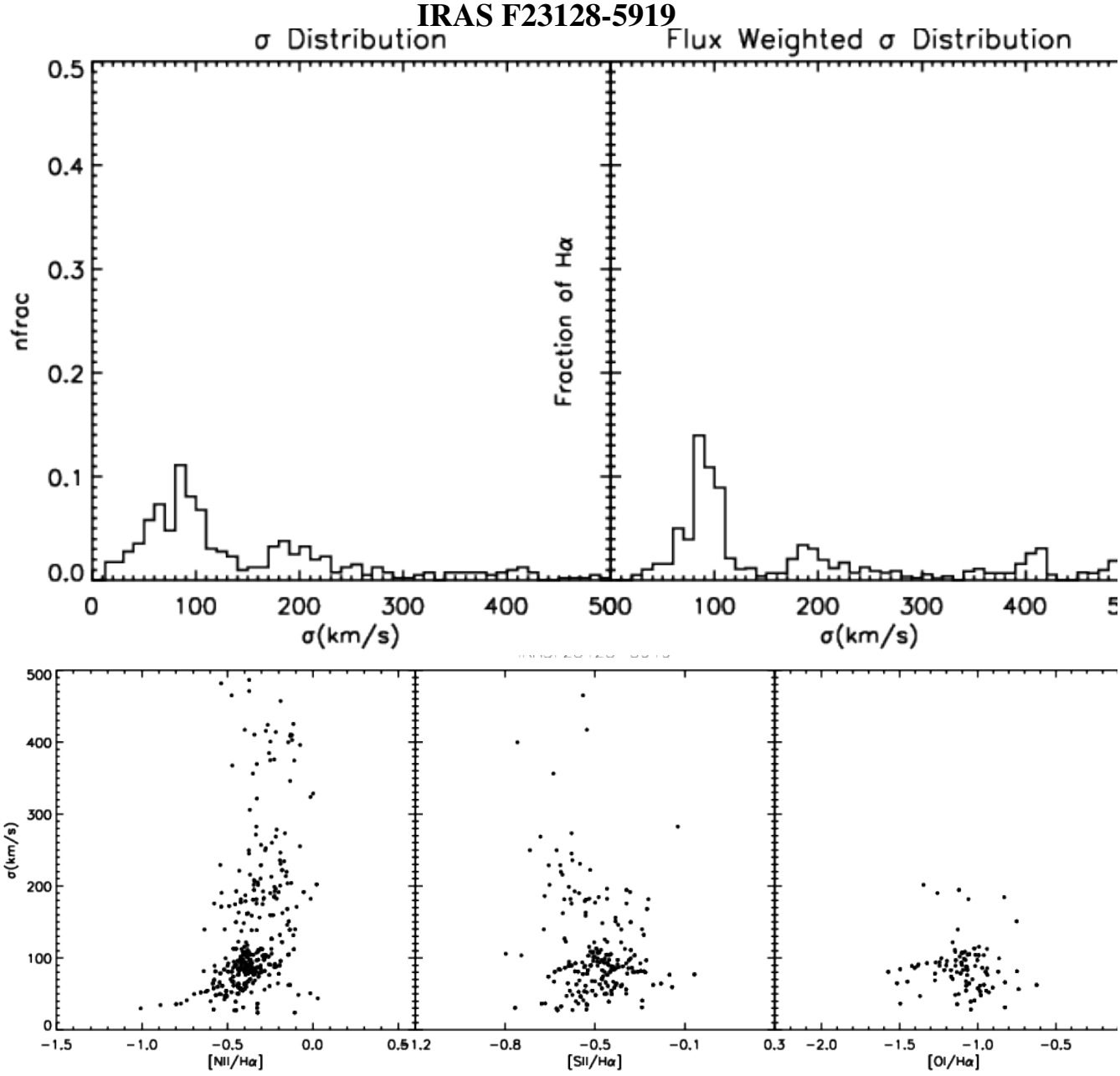

Figure B31. : Same as Figure B1, but for IRAS F23128-5919.

C. VELOCITY DISPERSION CLASSIFICATION MAPS

This section contains maps of the distribution of low, moderate and high σ for each velocity component fit. Isolated galaxies like IRAS F17222-5953 and widely separated pairs like IRAS F13373+0105 show primarily low and moderate (blue and green) velocity dispersion distributions, consistent with their emission being dominated primarily by star formation while the middle and late stage mergers show widespread high-σ emission in at least one velocity component, consistent with a strong contribution from shocks. These maps provide a spatially resolved complement to the interpretation of Figs 5, 6, 8, 9 and 10 as discussed in Section 7.

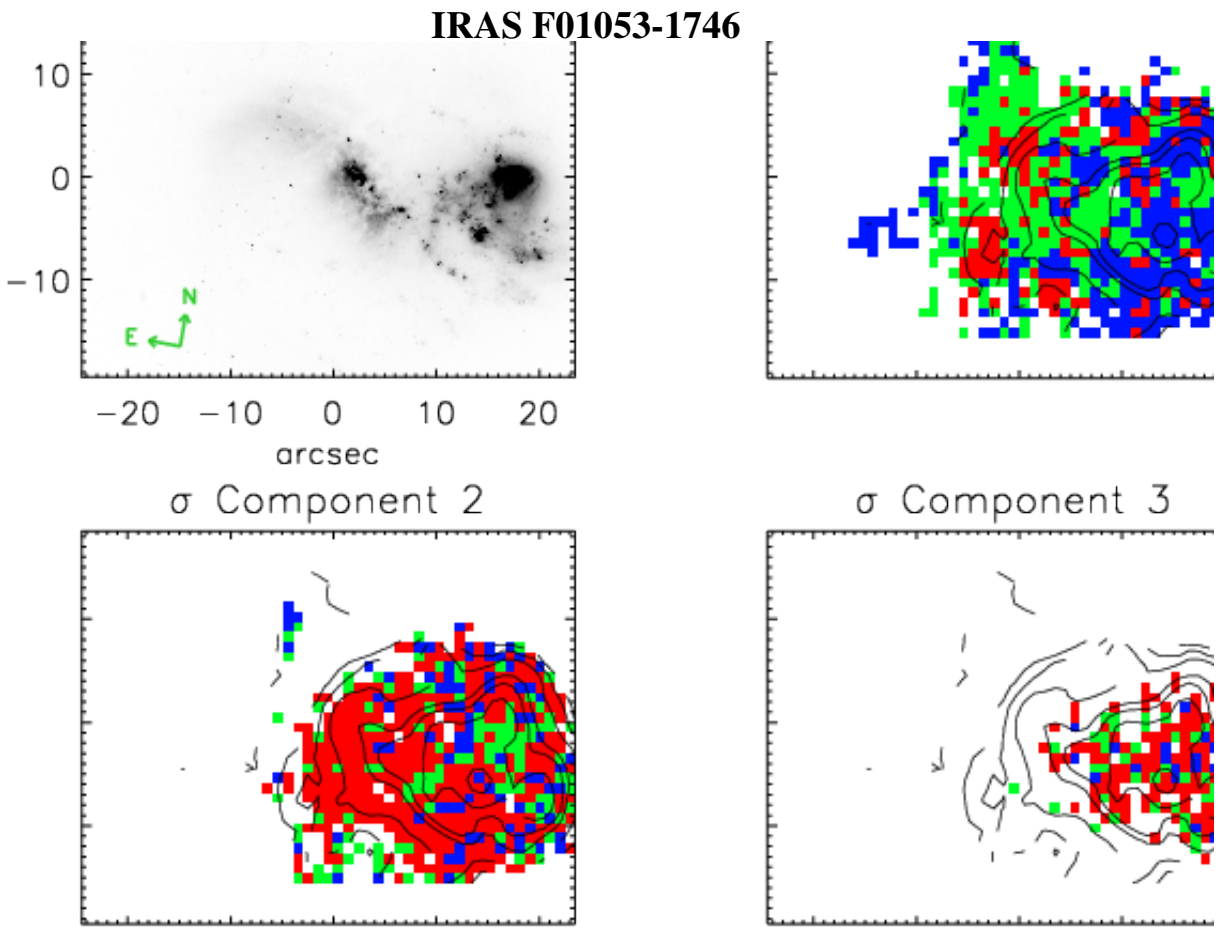

Figure C1. : Maps of each velocity component color coded by velocity dispersion classification with cutoffs as shown in Figs. 5 & 6 and discussed in Section 7: blue, low-σ ($\sigma < 50km\ s^{-1}$), green mid-$\sigma(50km\ s^{-1} < \sigma < 90km\ s^{-1})$ and high-$\sigma(\sigma > 90km\ s^{-1})$ velocity dispersion classification. IRAS F01053-1746 shows a strong combination of HII-region and turbulent star formation, seen as blue and green components as well as a widespread high-σ component from shocks. Many of the mid to late stage mergers show a similar pattern. The upper left panel shows the galaxy image for comparison and the maps are shown with Hα contours overlaid, as with the figures in Appendix A.

IRAS F02072-1025

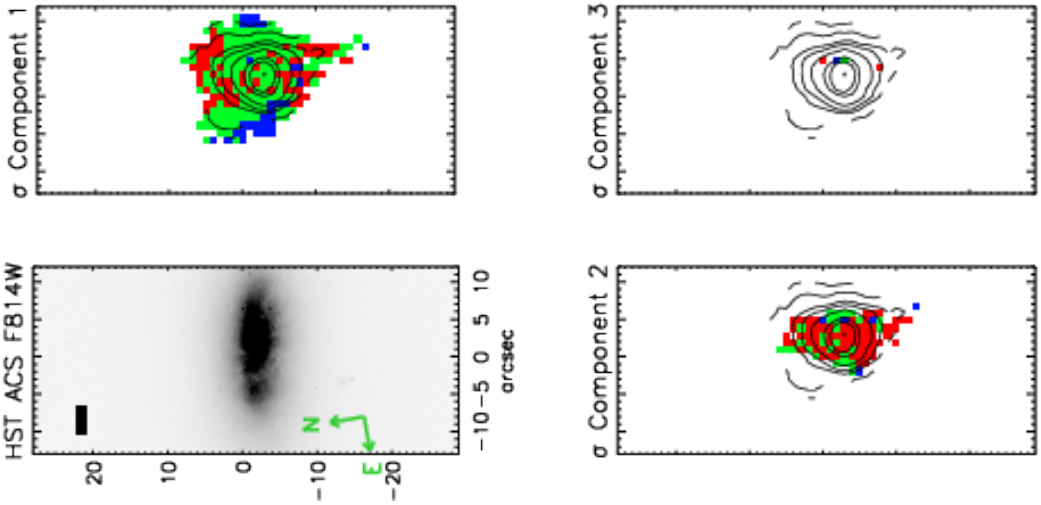

Figure C2. : Same as Figure C1, but for IRAS F02072-1025.

IRAS F06076-2139

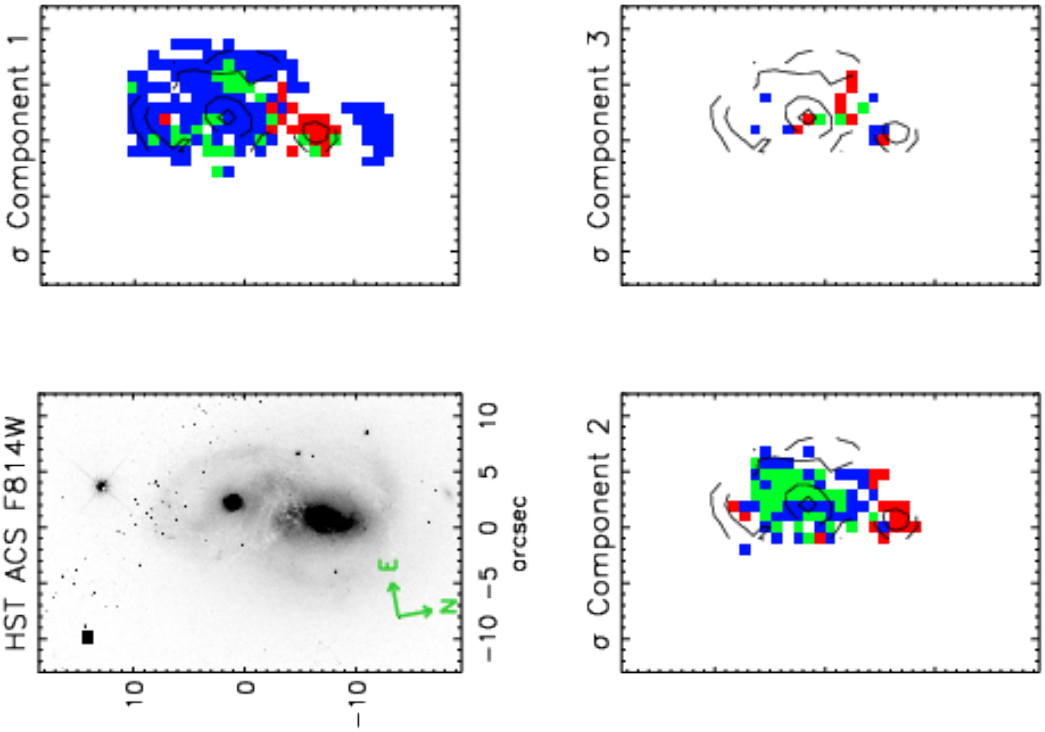

Figure C3. : Same as Figure C1, but for IRAS F06076-2139.

IRAS F08355-4944

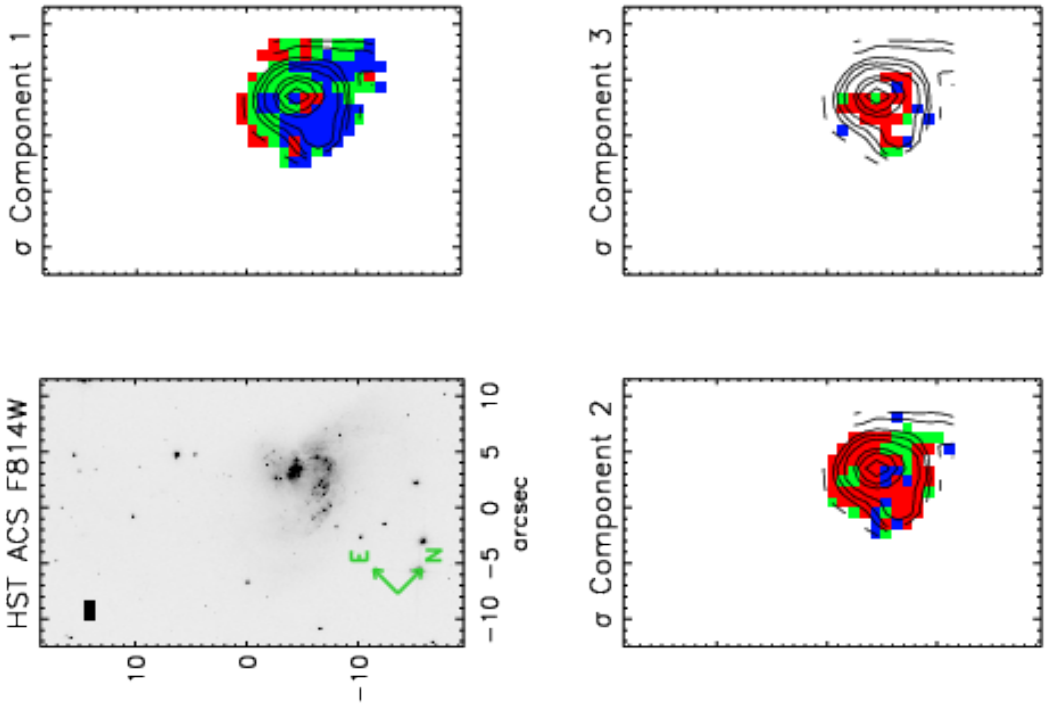

Figure C4. : Same as Figure C1, but for IRAS 08355-4944.

IRAS F10038-3338

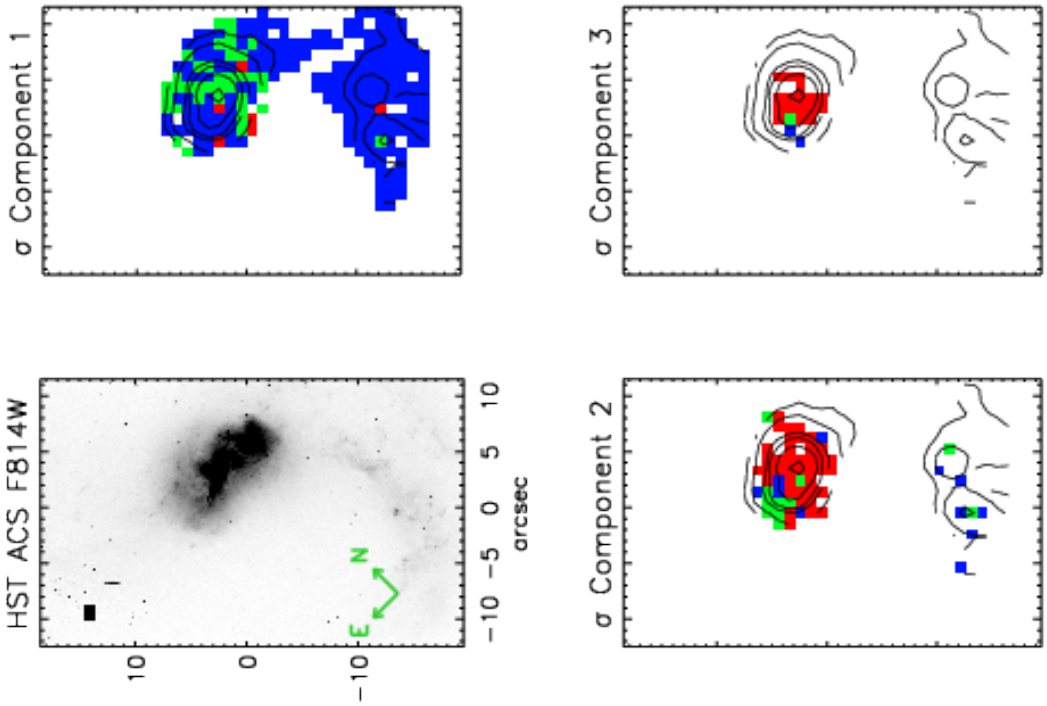

Figure C5. : Same as Figure C1, but for IRAS F10038-3338.

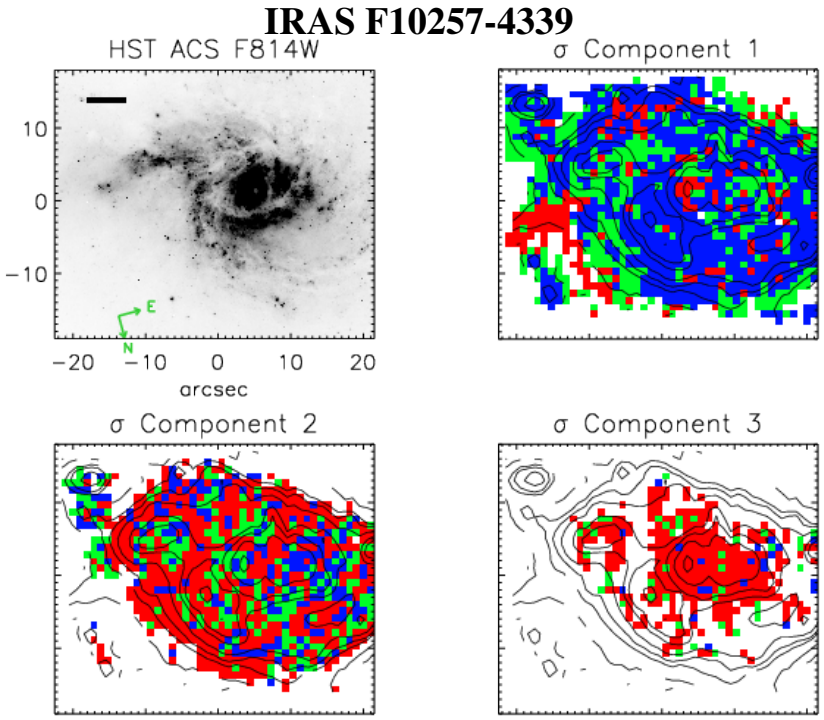

Figure C6. : Same as Figure C1, but for IRAS F10257-4339.

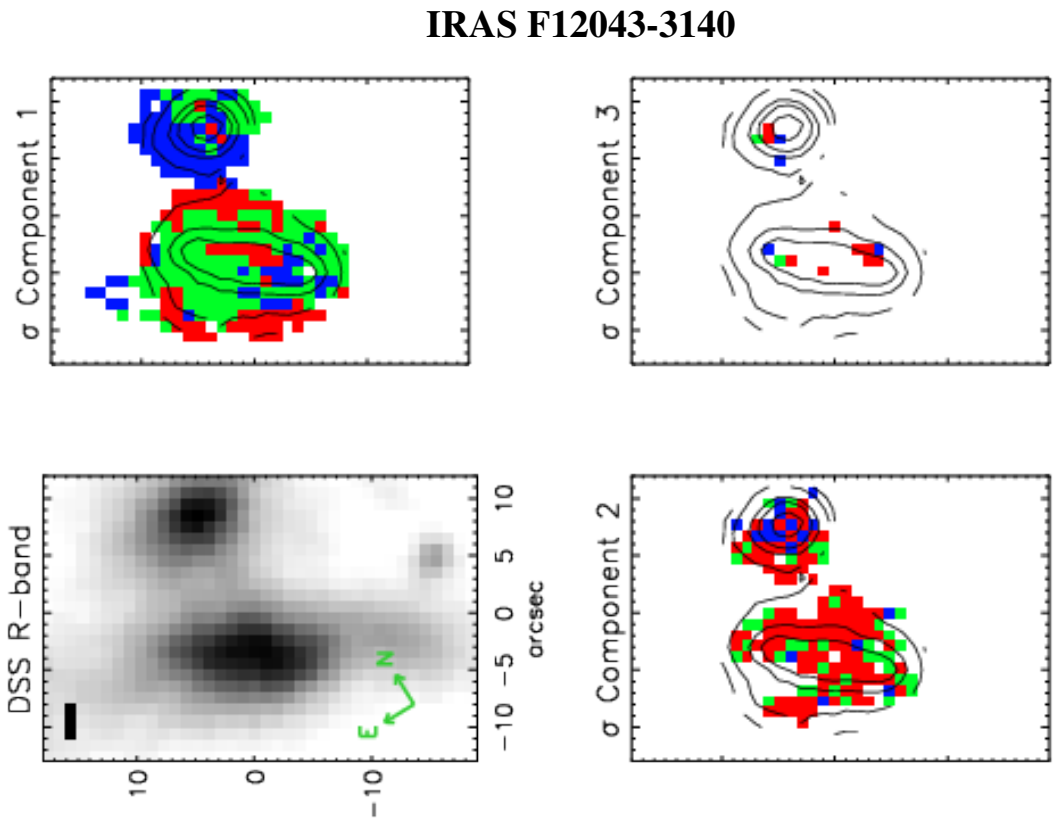

Figure C7. : Same as Figure C1, but for IRAS F12043-3140.

IRAS F12592+0436

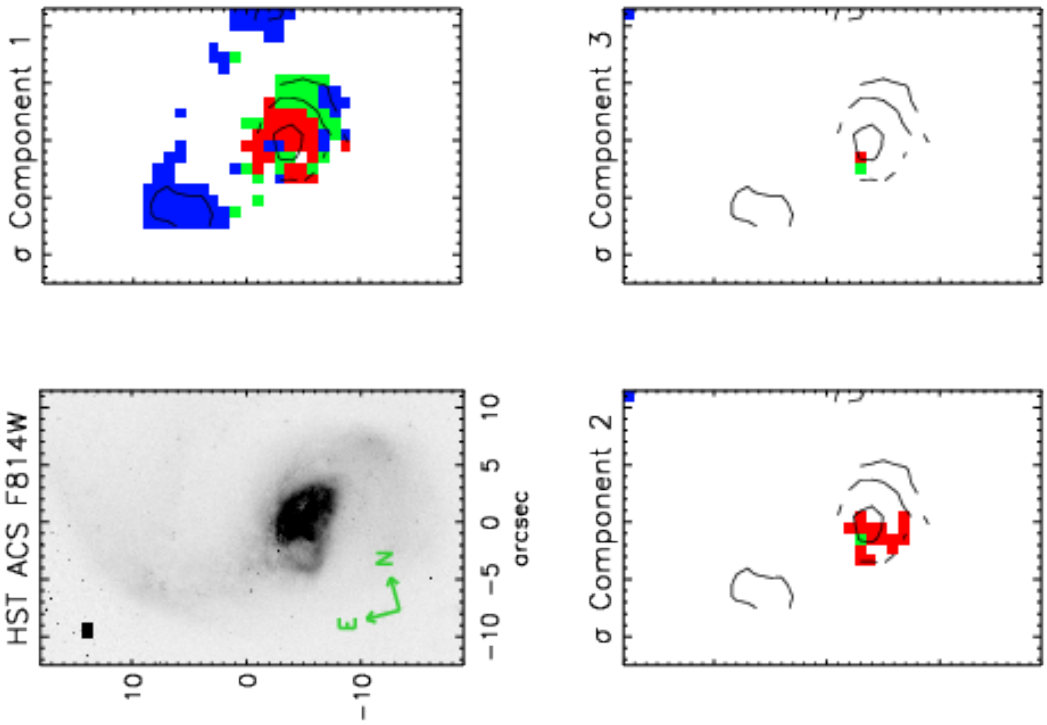

Figure C8. : Same as Figure C1, but for IRAS F12592+0436.

IRAS 13120-5453

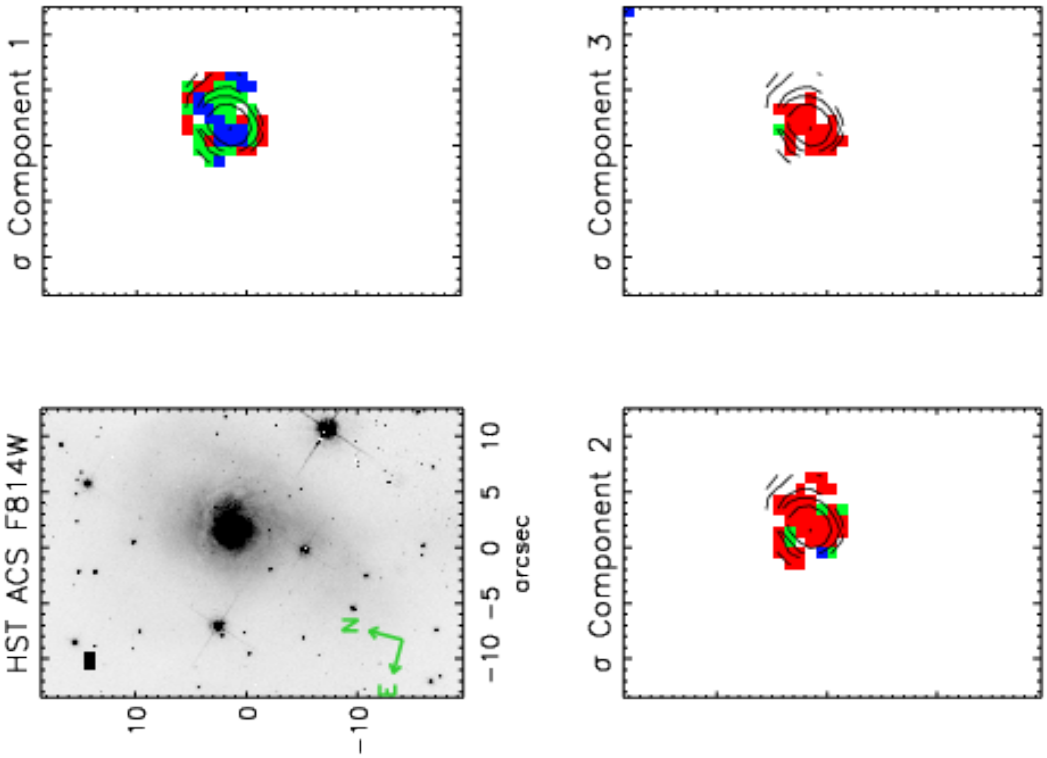

Figure C9. : Same as Figure C1, but for IRAS 13120-5453.

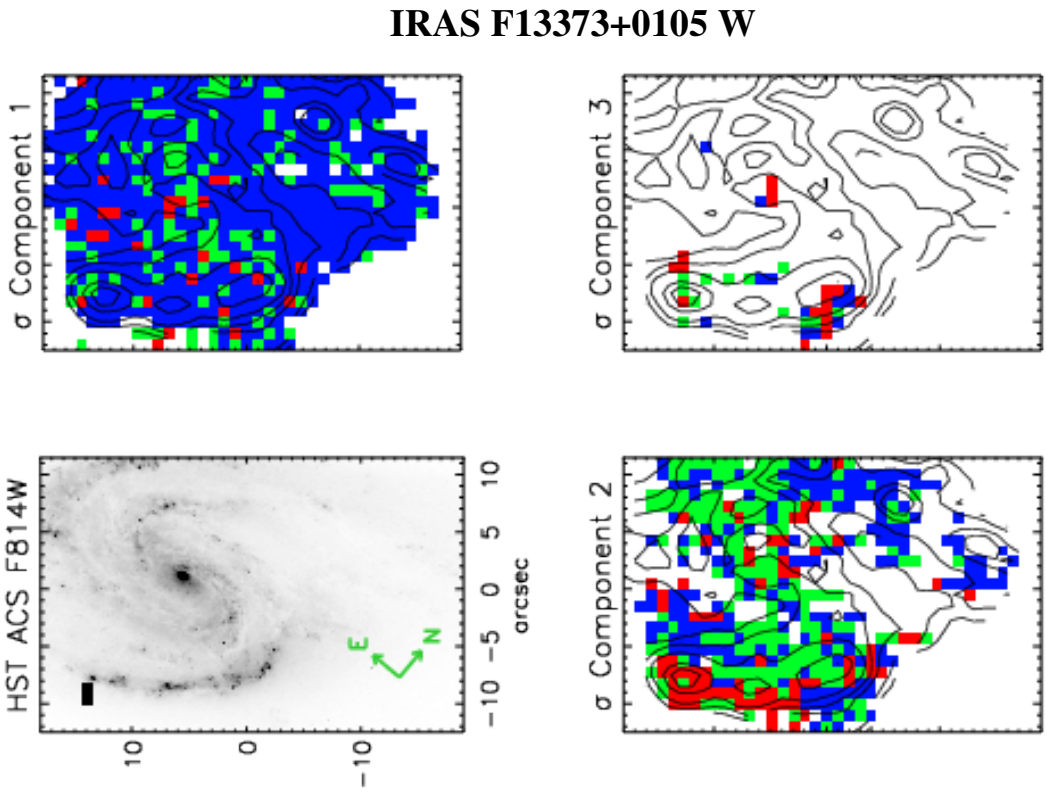

Figure C10. : Same as Figure C1, but for IRAS F13373+0105 W.

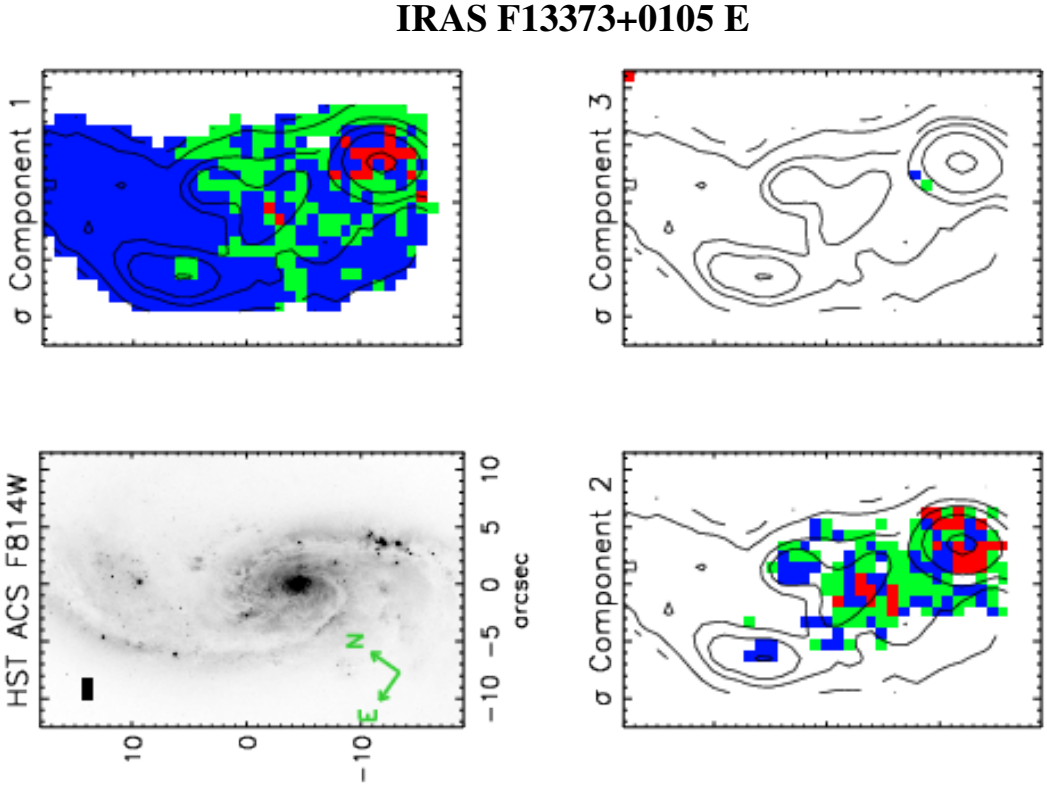

Figure C11. : Same as Figure C1, but for IRAS F13373+0105 E.

IRAS F15107+0724

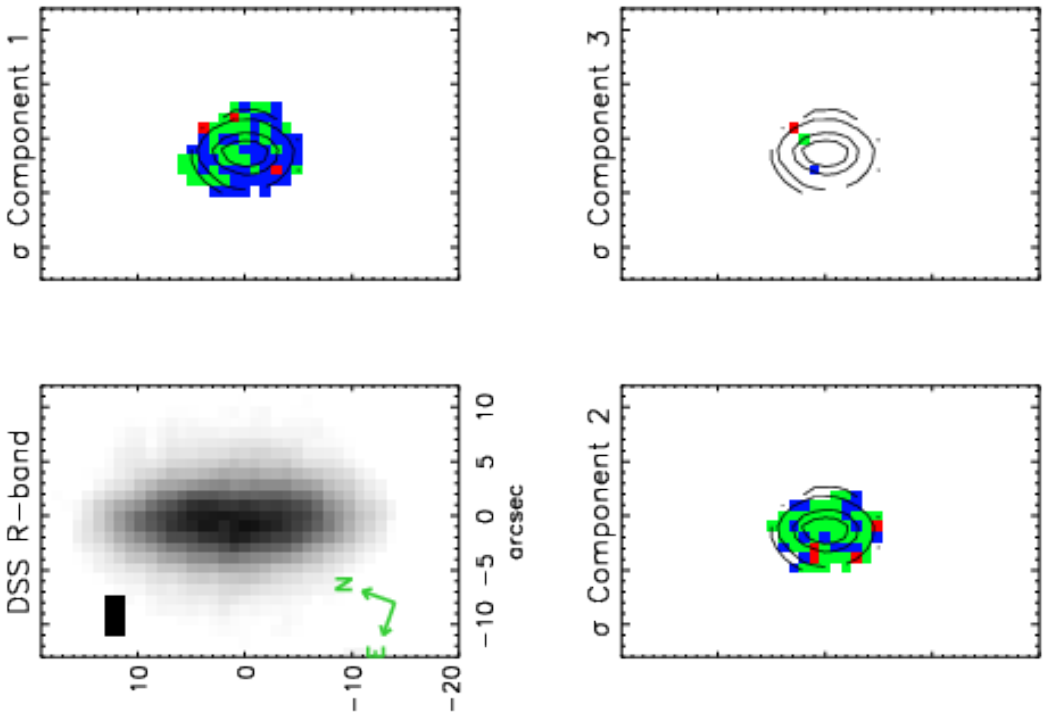

Figure C12. : Same as Figure C1, but for IRAS F15107+0724.

IRAS F16164-0746

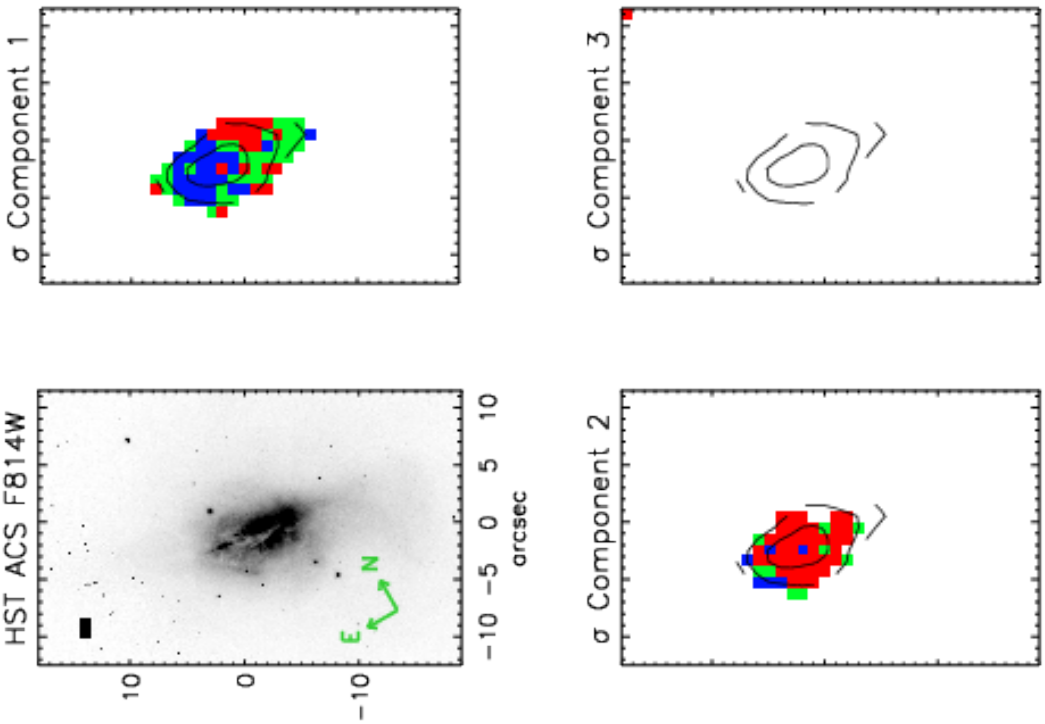

Figure C13. : Same as Figure C1, but for IRAS F16164-0746.

IRAS F16399-0937

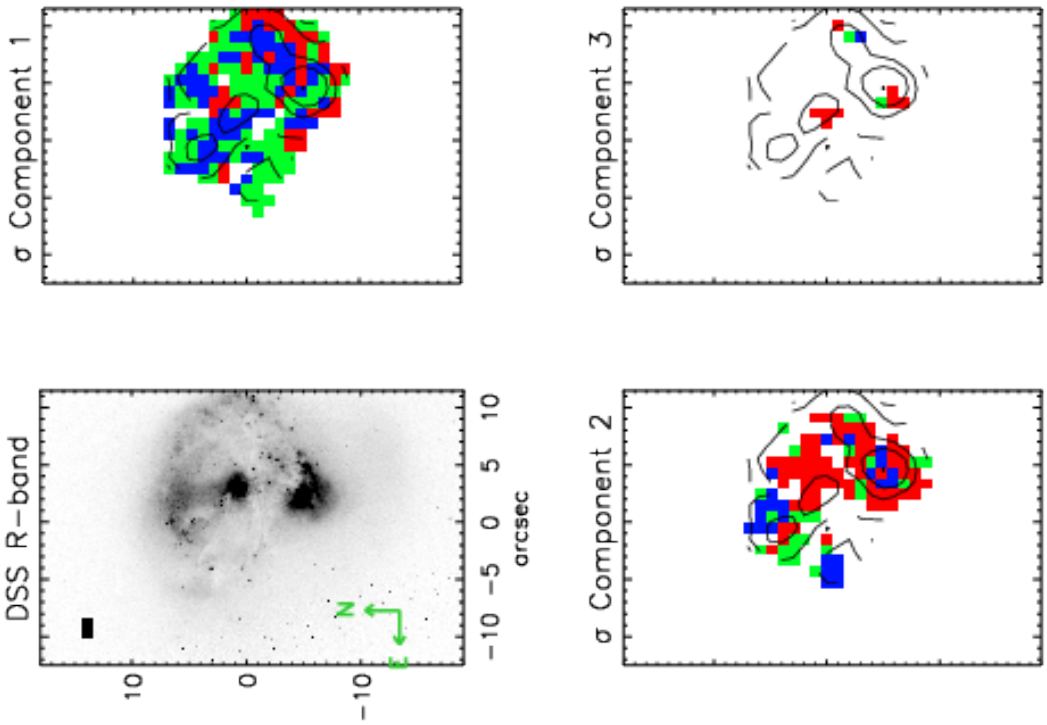

Figure C14. : Same as Figure C1, but for IRAS F16399-0937.

IRAS F16443-2915 N

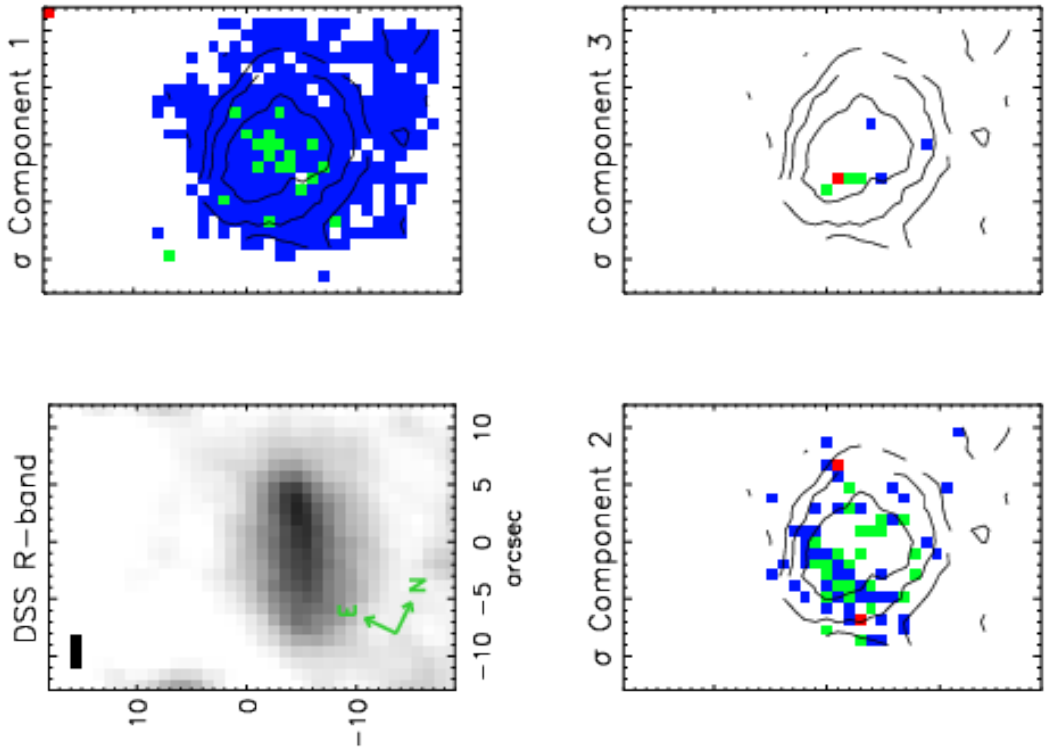

Figure C15. : Same as Figure C1, but for IRAS F16443-2915 N.

IRAS F16443-2915 S

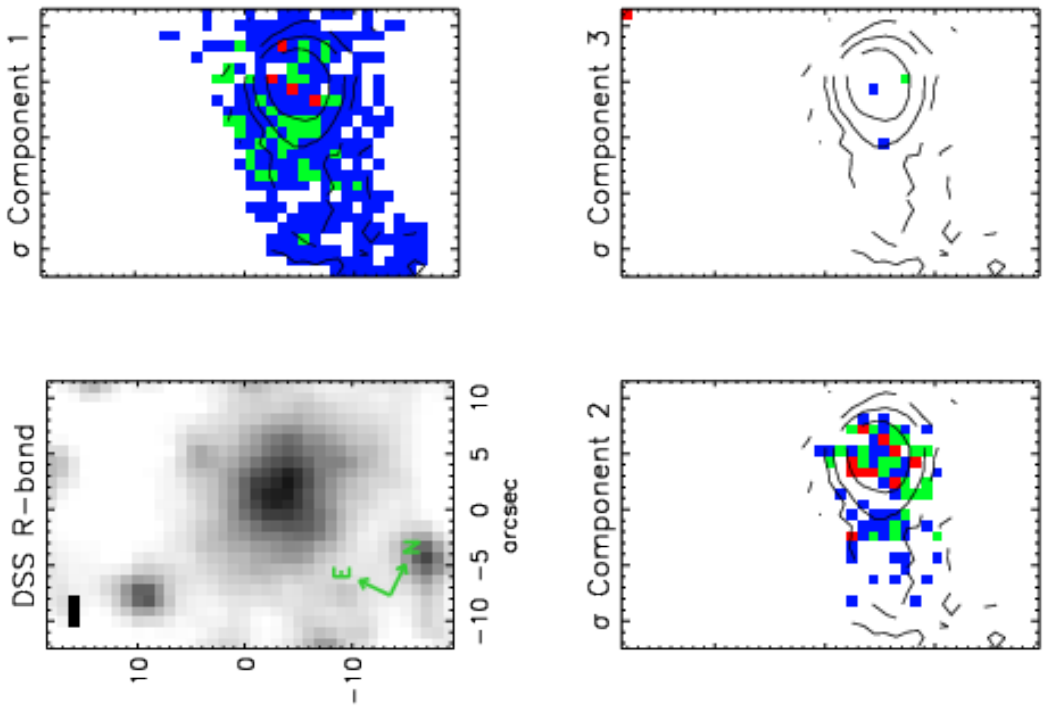

Figure C16. : Same as Figure C1, but for IRAS F16443-2915 S.

IRAS F17138-1017

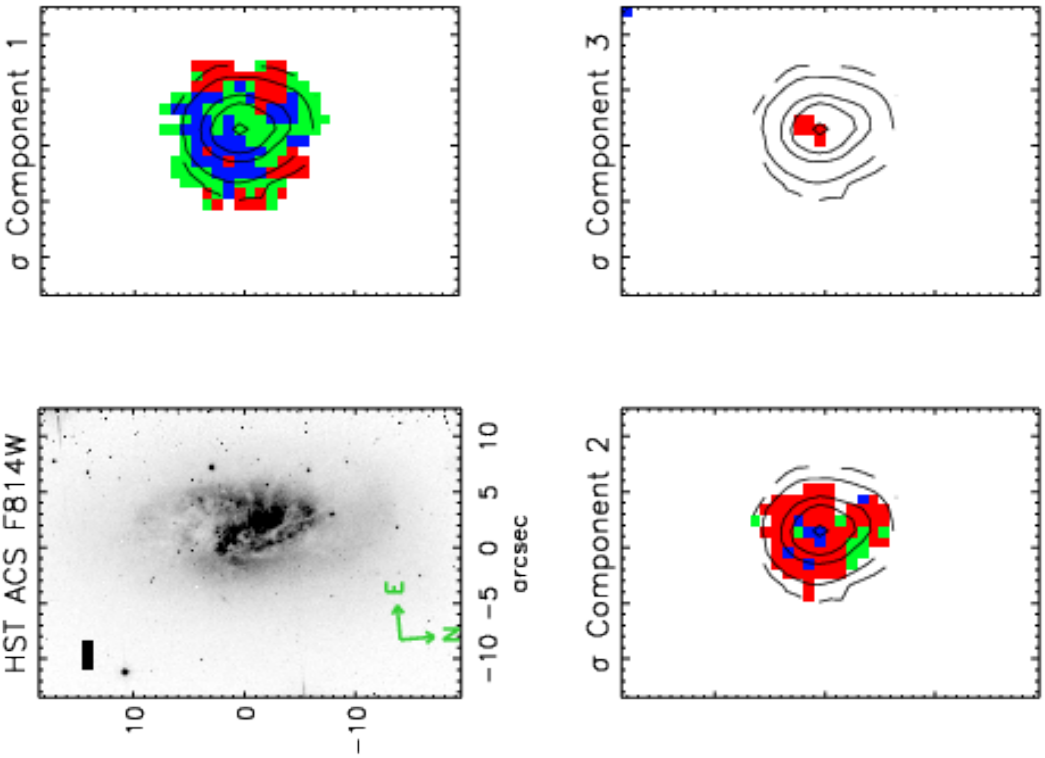

Figure C17. : Same as Figure C1, but for IRAS F17138-1017.

IRAS F17207-0014

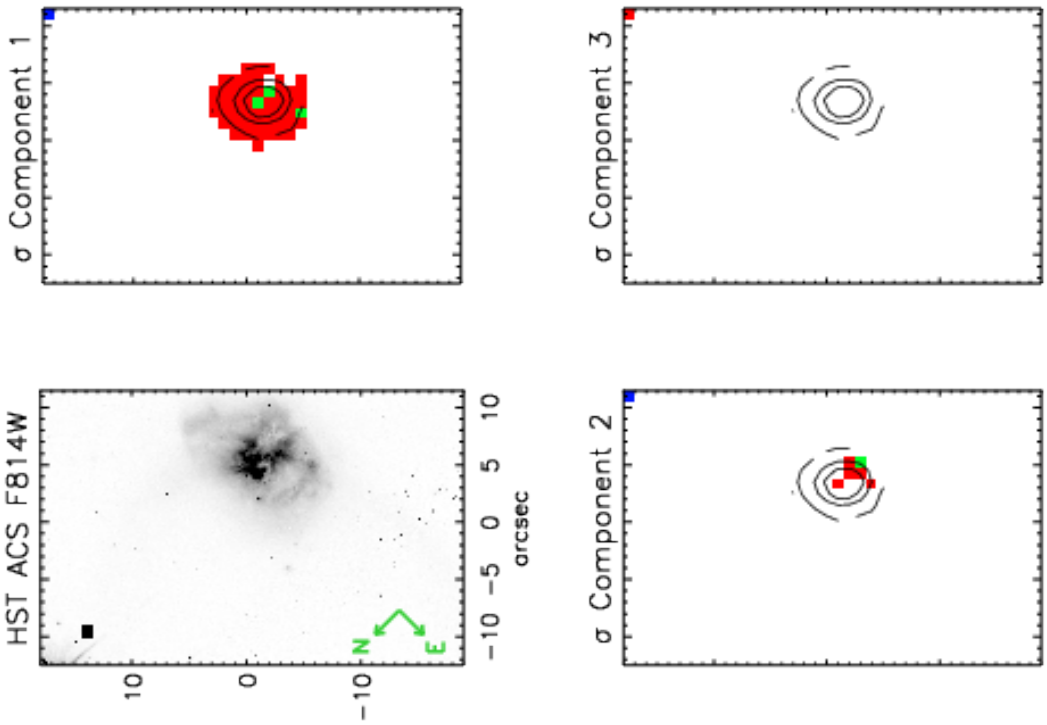

Figure C18. : Same as Figure C1, but for IRAS F17207-0014.

IRAS F17222-5953

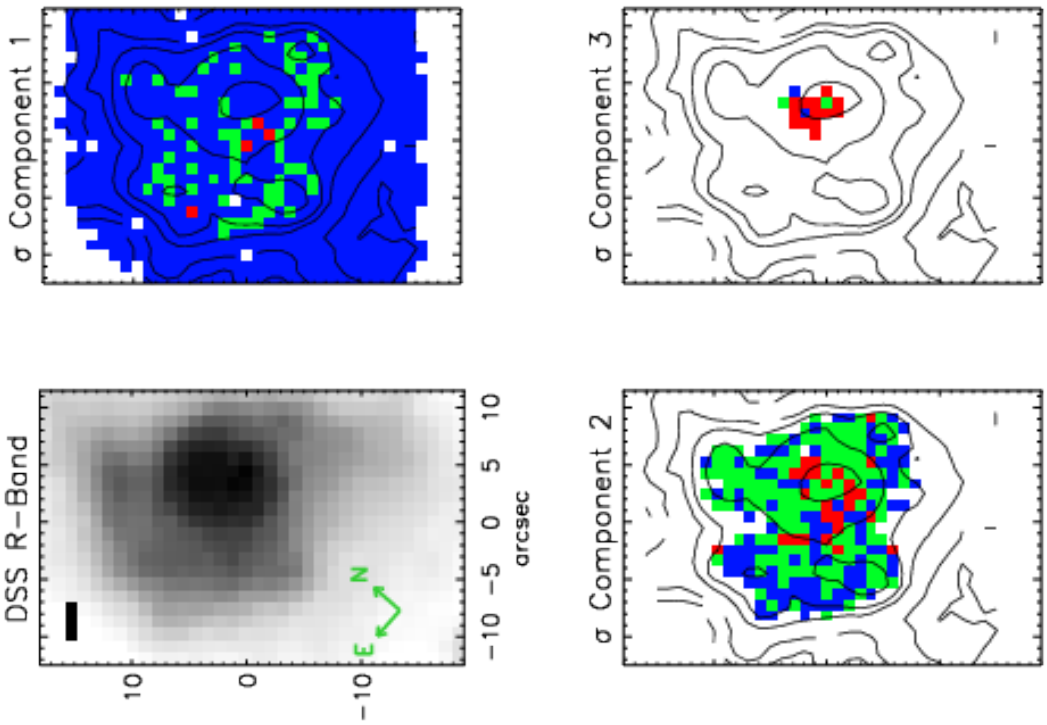

Figure C19. : Same as Figure C1, but for IRAS F17222-5953.

IRAS 17578-0400

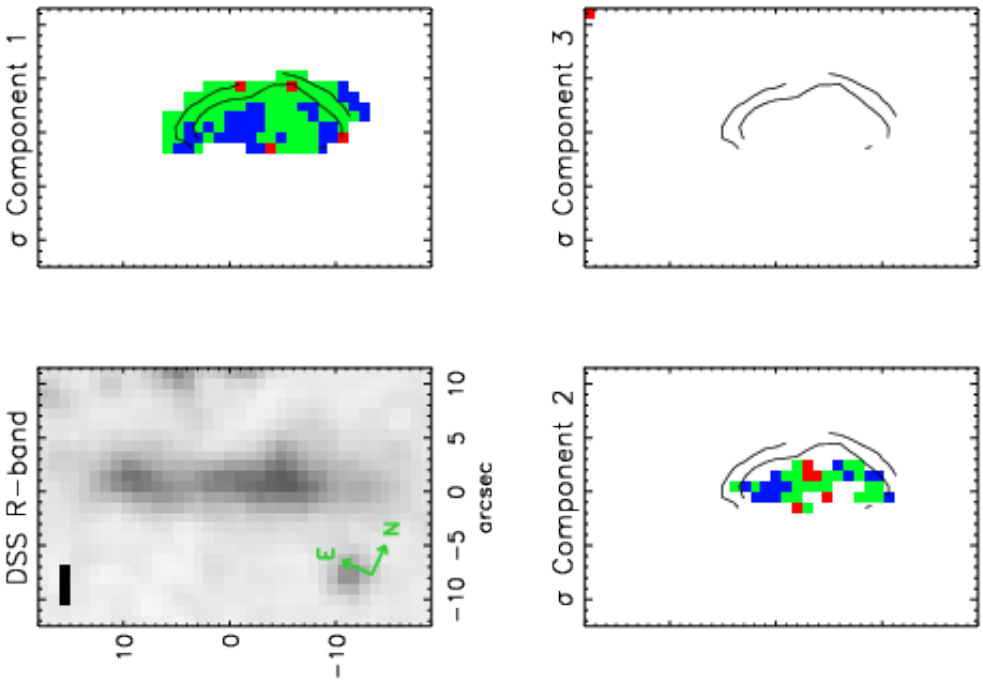

Figure C20. : Same as Figure C1, but for IRAS 17578-0400.

IRAS F18093-5744 N

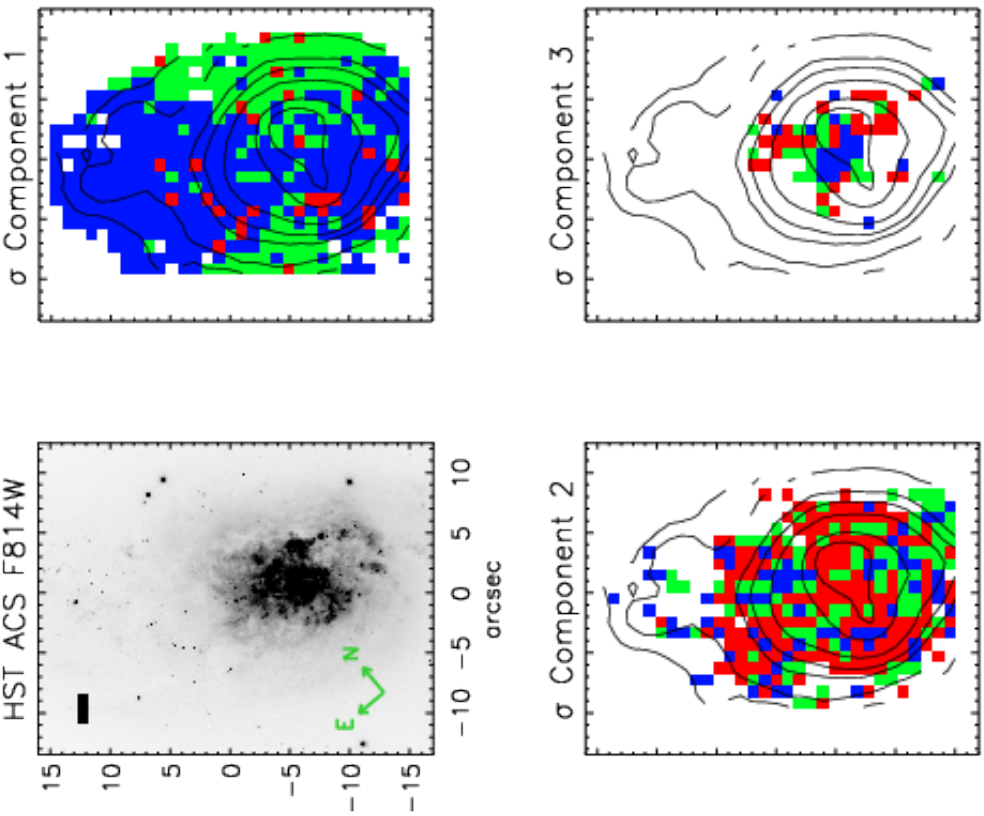

Figure C21. : Same as Figure C1, but for IRAS F18093-5744 N.

IRAS F18093-5744 S

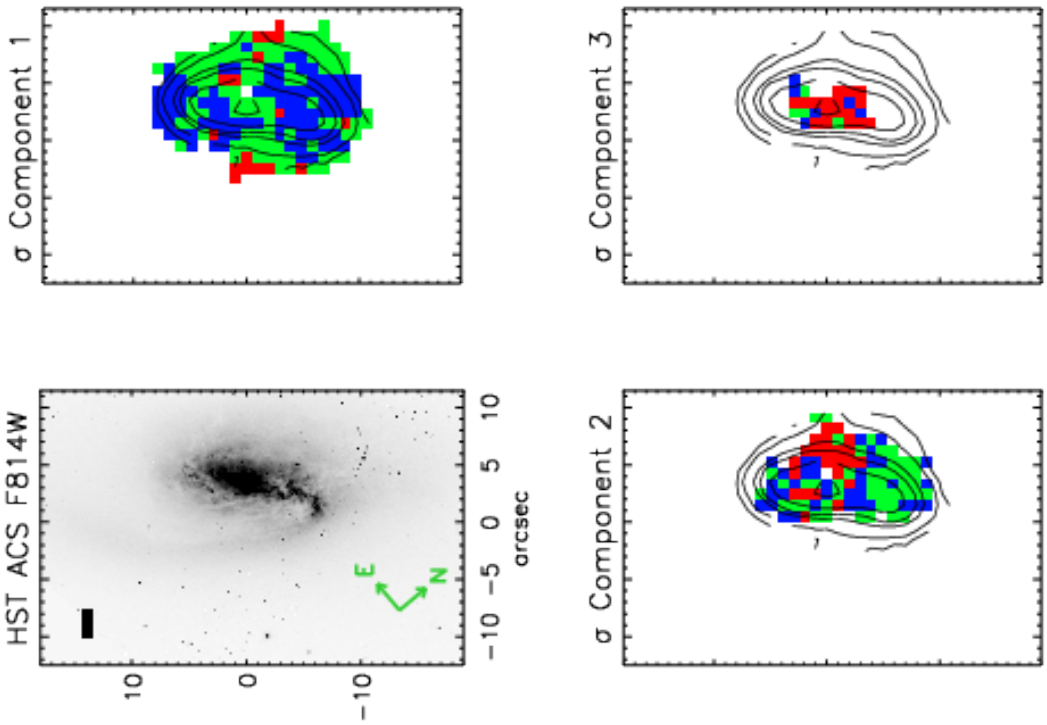

Figure C22. : Same as Figure C1, but for IRAS F18093-5744 S.

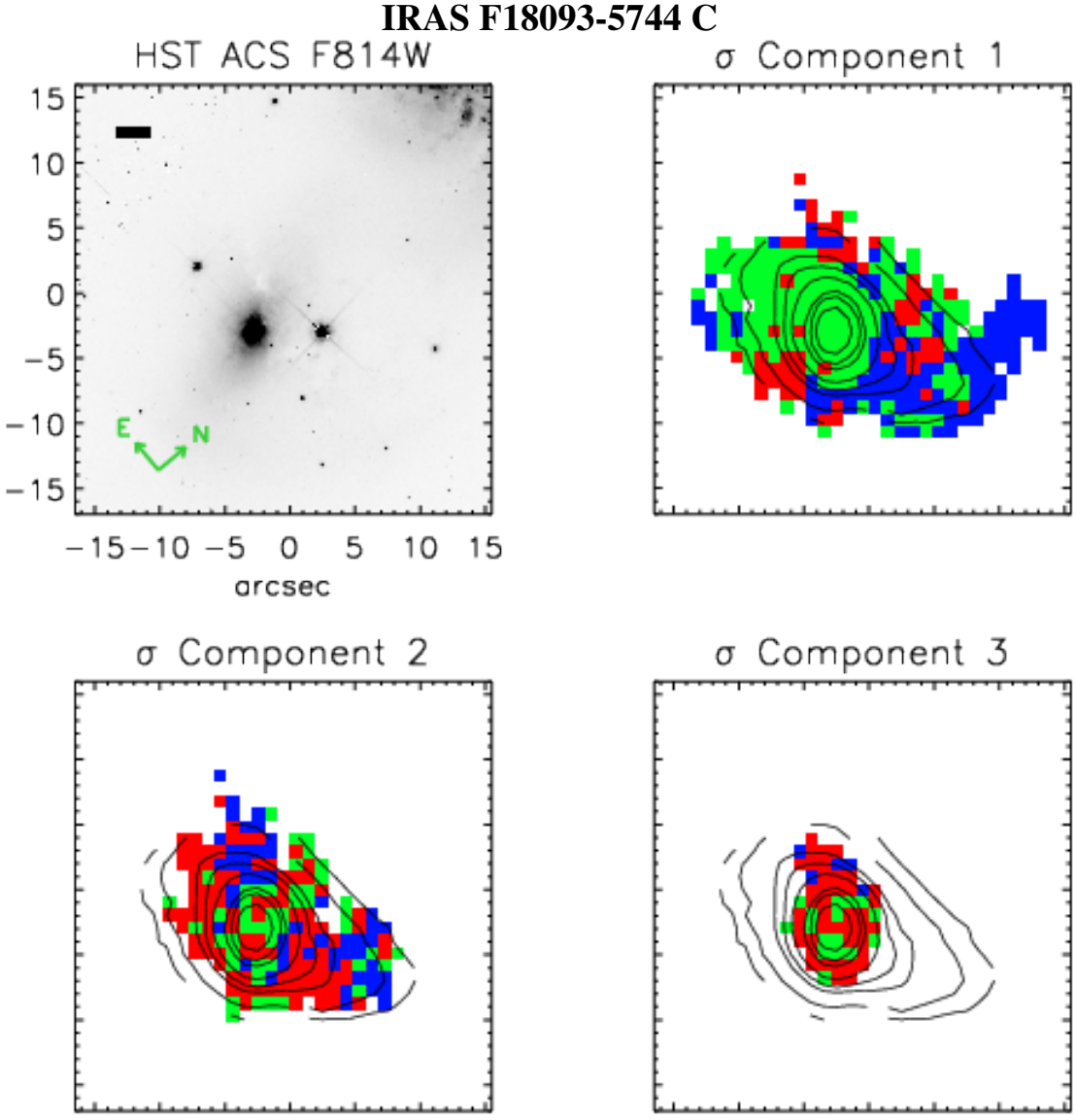

Figure C23. : Same as Figure C1, but for IRAS F18093-5744 C.

IRAS F18293-3413

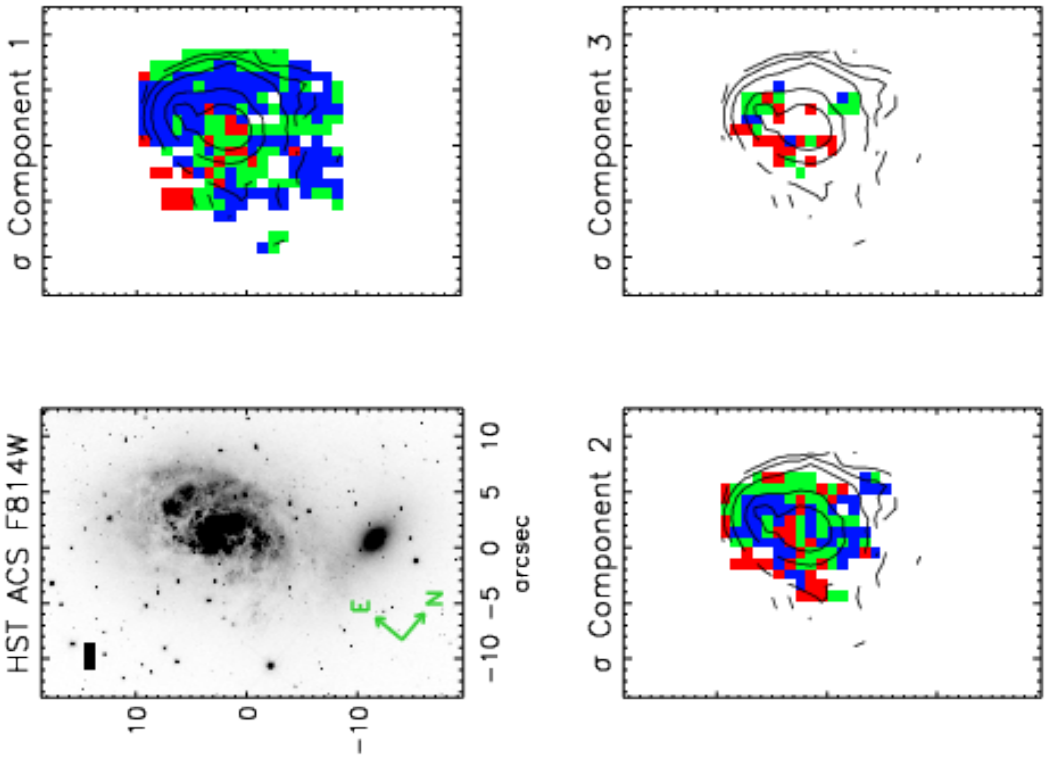

Figure C24. : Same as Figure C1, but for IRAS F18293-3413.

IRAS F18341-5732

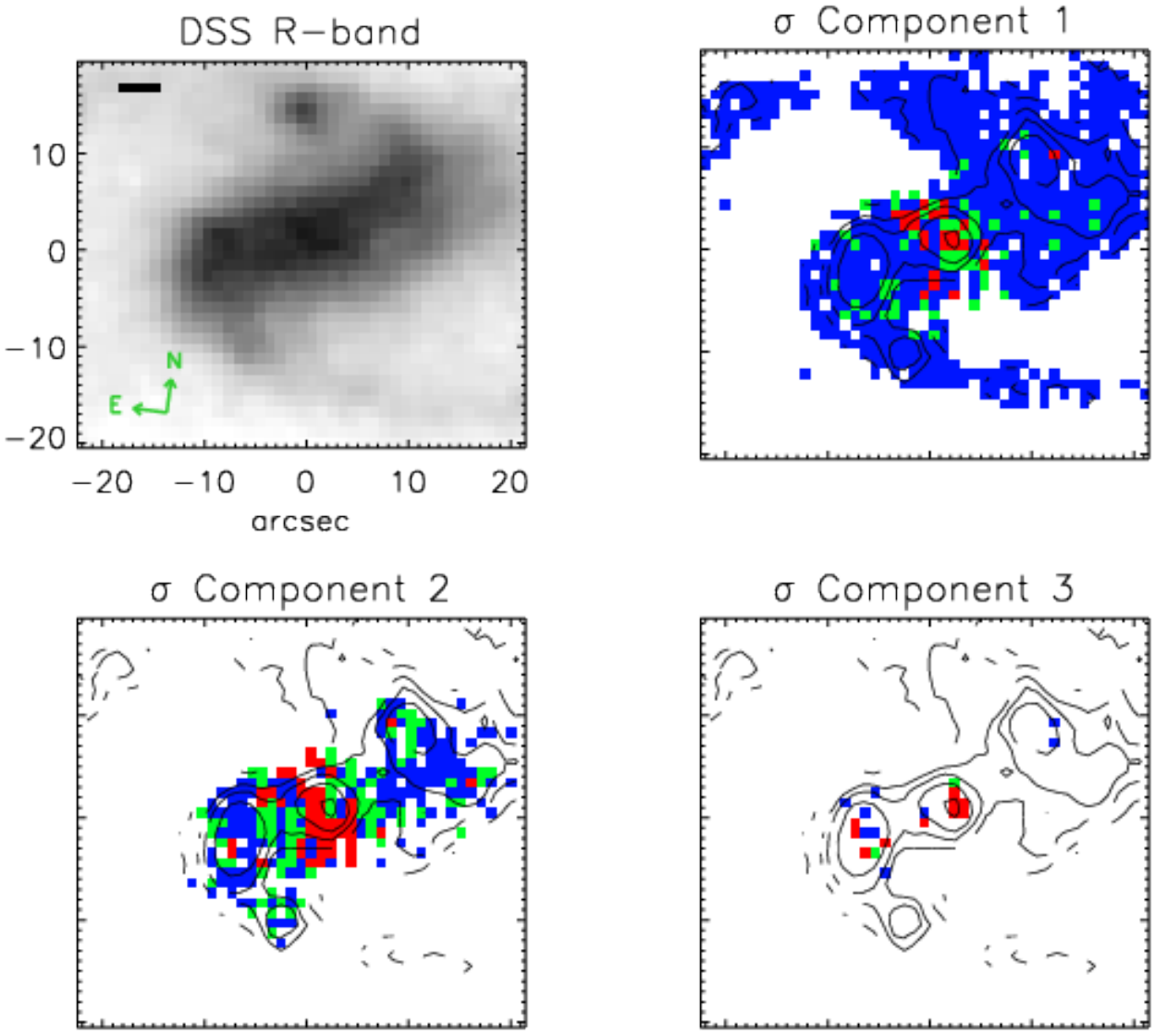

Figure C25. : Same as Figure C1, but for IRAS F18341-5732.

IRAS F19115-2124

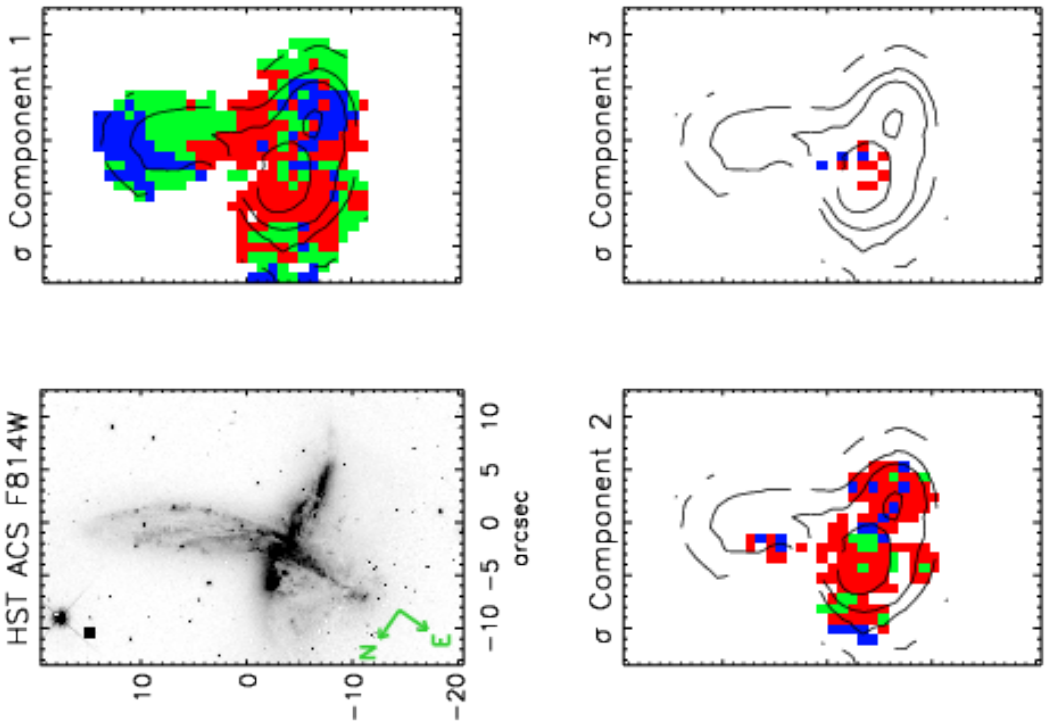

Figure C26. : Same as Figure C1, but for IRAS F19115-2124.

IRAS F20551-4250

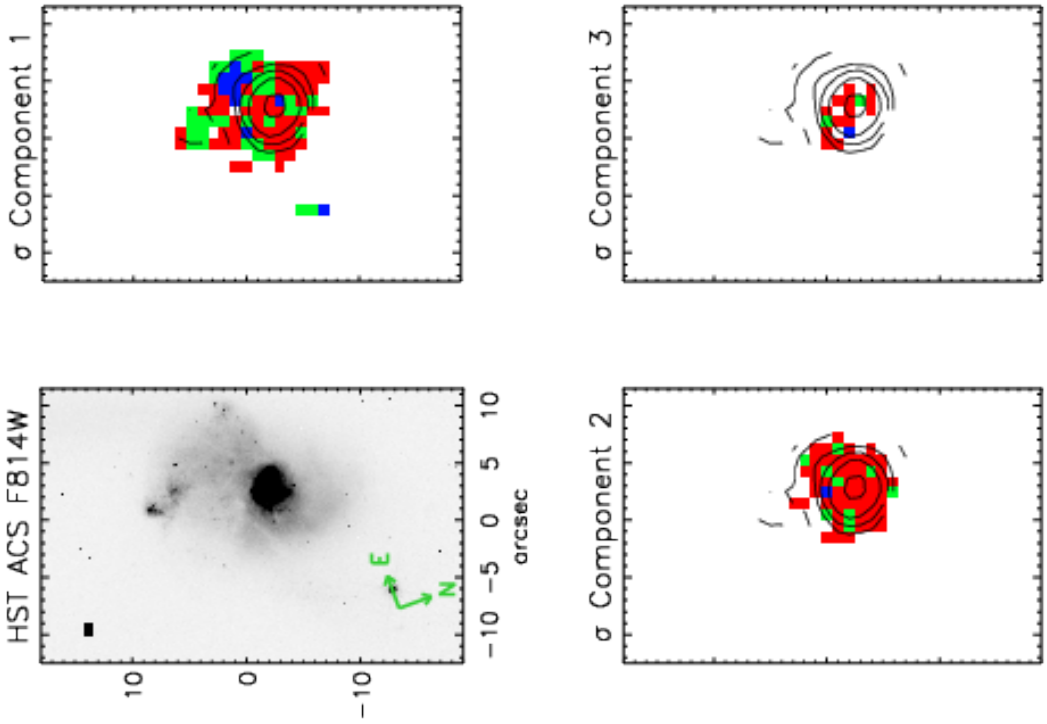

Figure C27. : Same as Figure C1, but for IRAS F20551-4250.

IRAS F21330-3846

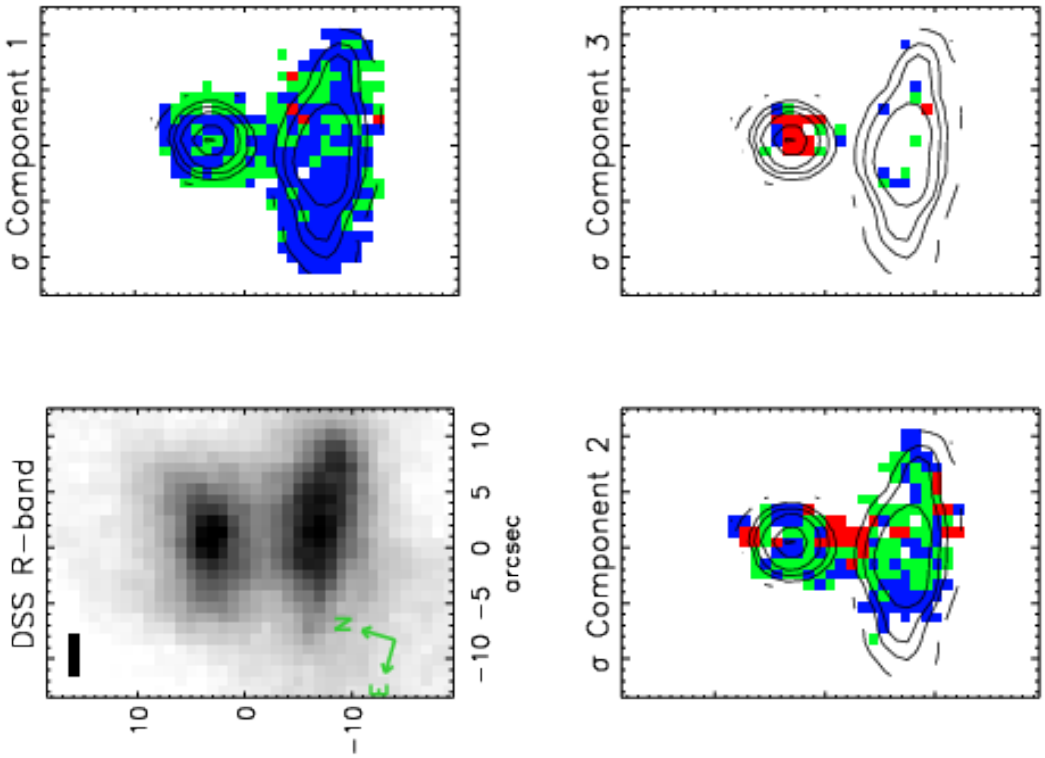

Figure C28. : Same as Figure C1, but for IRAS F21330-3846

IRAS F21453-3511

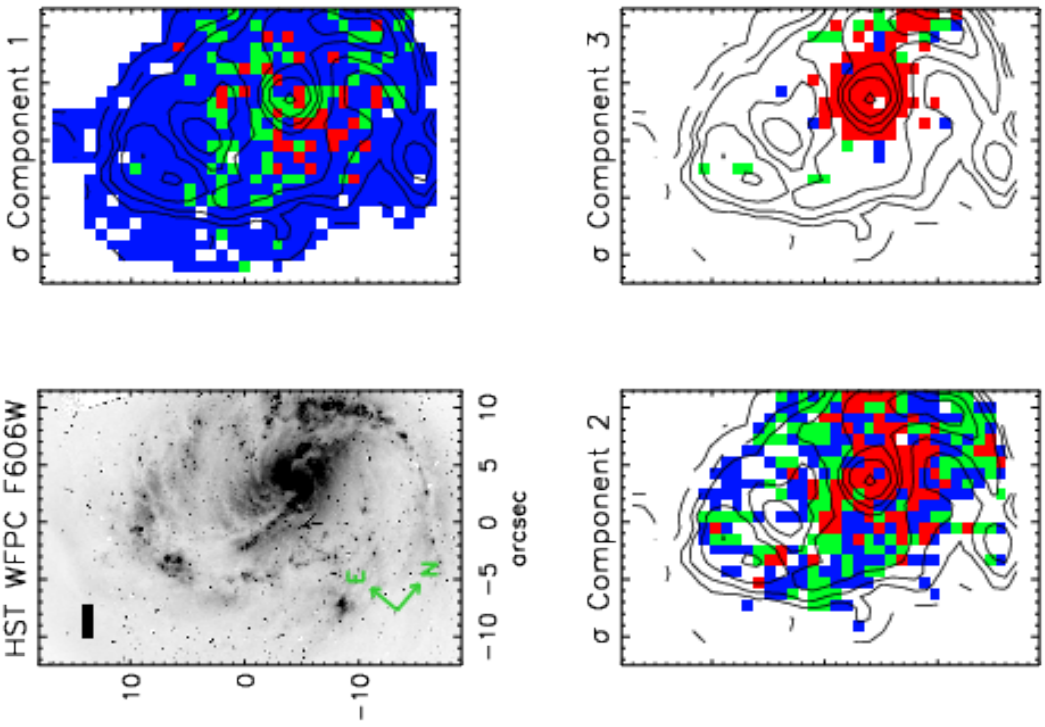

Figure C29. : Same as Figure C1, but for IRAS F21453-3511

IRAS F22467-4906

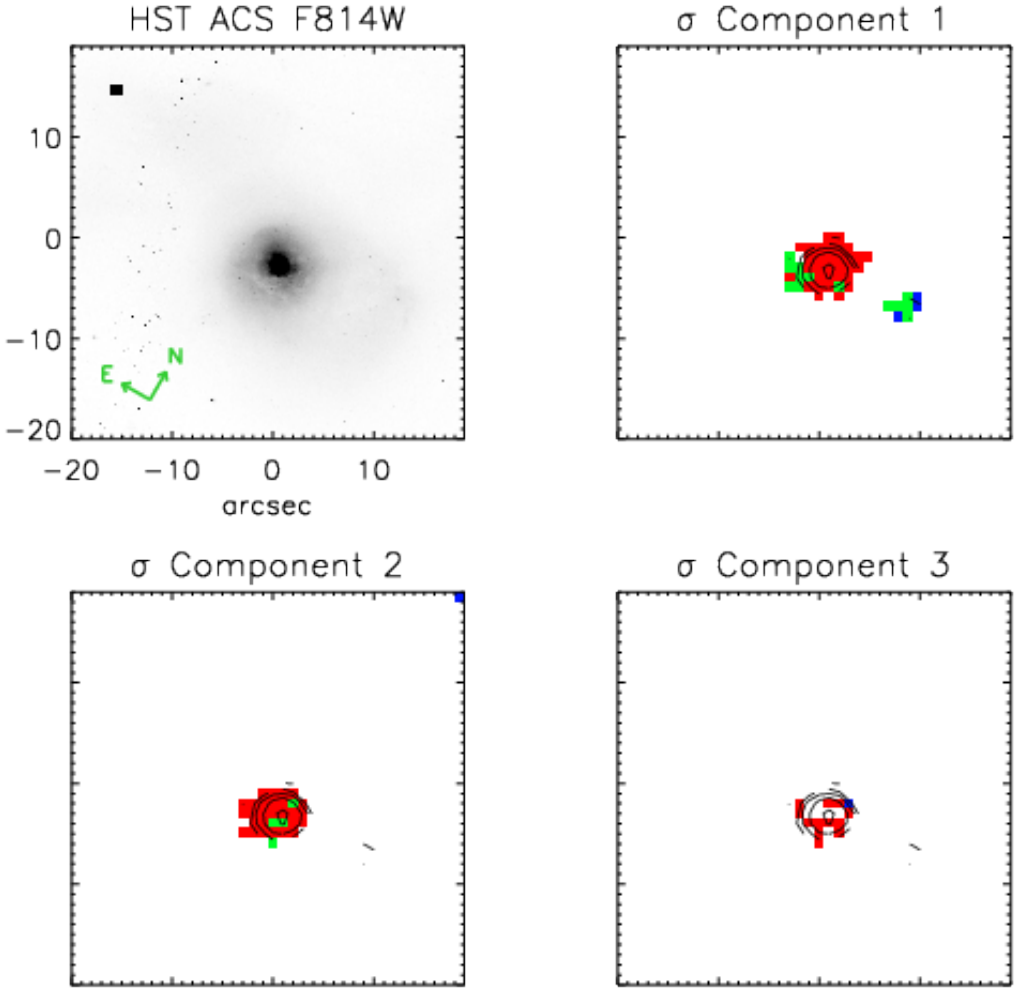

Figure C30. : Same as Figure C1, but for IRAS F22467-4906.

IRAS F23128-5919

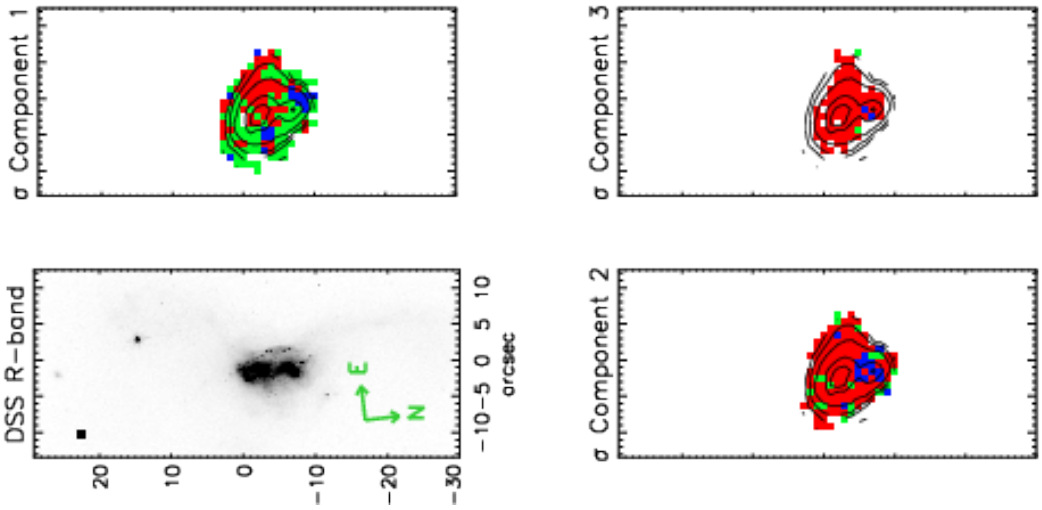

Figure C31. : Same as Figure C1, but for IRAS F23128-5919.